

ABSTRACT

Title of dissertation: THE COOL SIDE OF GALACTIC WINDS:
EXPLORATION WITH *HERSCHEL*-PACS
AND *SPITZER*-IRS

Myra Jean Stone, Doctor of Philosophy, 2020

Dissertation directed by: Professor Sylvain Veilleux
Department of Astronomy

Galactic-scale outflows driven by starbursts and/or active galactic nuclei (AGN) are key ingredients to theoretical models and numerical simulations of galaxy assembly and evolution. The feedback induced by the presence of these outflows (or winds) may affect the evolution and formation of a galaxy by regulating the amount of cold, dense gas responsible for star formation and black hole accretion.

We present the results from a systematic search for galactic-scale, molecular (OH 119 μm) outflows in a sample of 52 Local Volume ($d < 50$ Mpc) Burst Alert Telescope detected active galactic nuclei (BAT AGN) with *Herschel*-PACS. We combine the results from our analysis of the BAT AGN with the published *Herschel*/PACS data of 43 nearby ($z < 0.3$) galaxy mergers, mostly ultraluminous infrared galaxies (ULIRGs) and QSOs. Our data show that both the starburst and AGN contribute to driving OH outflows, but the fastest OH winds require AGN with quasar-like luminosities.

We also analyze *Spitzer* InfraRed Spectrograph (IRS) observations of the

OH 35 μm feature in 15 nearby ($z \lesssim 0.06$) (ultra-)luminous infrared galaxies (U/LIRGs). The measured OH 35 μm equivalent widths are used to compute an average OH column density which is then compared to the hydrogen column density for a typical optical depth at 35 μm of ~ 0.5 and gas-to-dust ratio of 125 to derive an OH-to-H abundance ratio of $X_{\text{OH}} = 1.01 \pm 0.15 \times 10^{-6}$. The OH 35 μm line profiles predicted from published radiative transfer models constrained by observations of OH 65, 79, 84, and 119 μm in five objects are found to be consistent with the IRS OH 35 μm spectra.

Finally, we analyze *Herschel*-PACS observations of five atomic fine-structure transition lines ([O I] 63 μm , [O III] 88 μm , [N II] 122 μm , [O I] 145 μm , and [C II] 158 μm) in seven nearby ($d < 16$ Mpc) galaxies with well-known galactic-scale outflows (Cen A, Circinus, M 82, NGC 253, NGC 1068, NGC 3079, and NGC 4945). With this suite of atomic emission lines, we investigate the cool neutral atomic ($T \sim 10^3$ K) and warm ionized ($T \sim 10^4$ K) gas phases within each outflow. The outflows in the *Herschel* data are spatially isolated from the galactic disk based on the kinematic signatures of the outflows. The spatial distribution and physical properties of the outflows detected in the *Herschel* data are compared with published results at other wavelengths. For completeness, an analysis of the molecular gas traced by OH 119 μm is also presented.

THE COOL SIDE OF GALACTIC WINDS:
EXPLORATION WITH *HERSCHEL*-PACS AND *SPITZER*-IRS

by

Myra Jean Stone

Dissertation submitted to the Faculty of the Graduate School of the
University of Maryland, College Park in partial fulfillment
of the requirements for the degree of
Doctor of Philosophy
2020

Advisory Committee:
Professor Sylvain Veilleux, Chair/Advisor
Professor Alberto Bolatto
Professor Bill Dorland
Dr. Marcio Meléndez
Professor Stuart Vogel

© Copyright by
Myra Jean Stone
2020

Preface

Much of the work in this thesis has been published and is presented here with minimal modification and the rest is in preparation for submission.

Chapter 2 has been published in *The Astrophysical Journal* under the title “*The Search for Molecular Outflows in Local Volume AGNs with Herschel-PACS*” (Stone, M., Veilleux, S., Meléndez, M., Sturm, E., Graciá-Carpio, J., & González-Alfonso, E., 2016, ApJ, 826,111).

Chapter 3 has been published in *The Astrophysical Journal* under the title “*Constraints on the OH-to-H Abundance Ratio in Infrared-bright Galaxies Derived from the Strength of the OH 35 μm Absorption Feature*” (Stone, M., Veilleux, S., González-Alfonso, E., Spoon, H., & Sturm, E., 2018, ApJ, 853, 132).

Chapter 4 is currently in preparation for submission to *The Astrophysical Journal* (Stone, M. & Veilleux, S.).

Acknowledgments

I would not have made it this far and completed this thesis without the immense support from the people around me. I am very grateful to my advisor, Sylvain Veilleux, for his advice and guidance in my research and his enduring ability to keep me from getting too far down into many a rabbit hole.

I am indebted to Marcio Meléndez for always being available to chat about life, the universe, and everything (mostly universe related though). His invaluable assistance with my research and coding throughout my entire graduate career was one of the main propellers that kept me moving forward. His obvious excitement about astronomy and his cheerful eagerness to share his knowledge about it has always been a reminder to me as to why I too loved the field.

I thank Blake and Zeeve for our many take-out dinners and TV watching after long days of work. These outings always kept me sane ... and looking forward to food. Their support both personal and professional has meant a great deal to me. I would like to thank Alex who was a constant source of advice, laughter, and unwavering support which kept me afloat early on in these uncharted waters. I'd like to thank Qian and Tiara for our food adventures while seeking out new and interesting restaurants. I thank Drew for our many chats which helped me navigate the ins and outs of the department and for the many chats which just helped brighten my mood.

I would like to thank my old roommates Tanya and Paulo who endured with me a very interesting 2.5 year stint in an apartment whose description would cause

your brow to furrow and your eyes to squint. I'm grateful for our little traditions such as RenFest and BBQ, Blues, and Brews which were always great ways to relax and reset. To my more recent roommates, Aaron, Lauren, Silvy and Chris, I am grateful for the welcoming home we made which was such a comfort during hard times. I'm grateful for our dinners and cocktail hours which kept me fueled for another day of research.

Last but not least, I'd like to thank my boyfriend Chris who has been amazing during this last leg of my graduate school journey. You've pushed me to strive for the best and set me back on course if ever I faltered. Your belief in me has helped me maintain belief in myself, something for which I will always be grateful for.

Table of Contents

Preface	ii
Acknowledgements	iii
Table of Contents	v
List of Tables	viii
List of Figures	ix
List of Abbreviations	xvi
1 Introduction	1
1.1 Background	1
1.2 Starburst and Active Galaxies	5
1.2.1 Starburst-Driven Winds	5
1.2.2 AGN-Driven Winds	8
1.3 The Multiphase ISM in Outflows	11
1.3.1 General Considerations	11
1.3.2 The OH Molecule	14
1.3.3 Atomic Fine-Structure Lines	15
1.4 Observatories and Instruments	17
1.4.1 <i>Herschel</i> -PACS	18
1.4.2 <i>Spitzer</i> -IRS	19
1.5 Outline of Thesis	20
2 Search for Molecular Outflows in Local Volume AGN with <i>Herschel</i> -PACS	22
2.1 Introduction	22
2.2 BAT AGN Sample Selection	29
2.3 ULIRG and PG QSO Sample	36
2.4 Properties of the Sample Galaxies	36
2.5 Observations, Data Reduction, and Spectral Analysis	44
2.5.1 OH 119 μm Feature	44
2.5.1.1 OH Observations	44
2.5.1.2 OH Data Reduction	45
2.5.1.3 Spectral Analysis of the OH Doublet	46
2.5.2 The 9.7 μm Silicate Feature	49

	2.5.2.1	Data Reduction of the 9.7 μm Silicate Feature	49
	2.5.2.2	Spectral Analysis of the 9.7 μm Silicate Feature	50
2.6	Results		51
	2.6.1	The OH 119 μm Feature	52
	2.6.2	The $S_{9.7\mu\text{m}}$ Feature	58
	2.6.3	OH Kinematics	59
2.7	Discussion		70
	2.7.1	Outflows	70
	2.7.1.1	BAT AGN with Molecular Outflows	70
	2.7.1.2	Driving Mechanisms of Molecular Outflows	74
	2.7.2	Inflows	77
	2.7.3	The 9.7 μm Silicate Feature	78
2.8	Conclusions		82
3	Constraints on the OH-to-H Abundance Ratio in Infrared-Bright Galaxies Derived from the Strength of the OH 35 μm Absorption Feature		85
	3.1	Introduction	85
	3.2	Background: The OH Molecule	90
	3.3	Sample Selection, Data Reduction, and Spectral Analysis	91
	3.3.1	The Sample	91
	3.3.2	Data Reduction	92
	3.3.3	Spectral Analysis	96
	3.4	Results	97
	3.4.1	OH Column Density	102
	3.4.2	X_{OH}	104
	3.5	Discussion	106
	3.5.1	X_{OH} : Comparison with the Literature	106
	3.5.2	X_{OH} : A Check on Radiative Transfer Models	107
	3.6	Summary	109
4	Far-Infrared Integral-Field Spectroscopy of Nearby Galactic Winds with Herschel-PACS		110
	4.1	Introduction	110
	4.2	Atomic Fine-Structure Emission Lines	113
	4.3	The Sample	116
	4.4	Observations, Archival Data, and Spectral Analysis	126
	4.5	Velocity-Integrated Emission Line Flux and Ratio Maps	128
	4.5.1	Constraints from the Emission Line Ratios	129
	4.5.2	Results from the Emission Line Ratios	130
	4.6	Gas Kinematics	138
	4.7	PDR Modeling	138
	4.7.1	[C II] 158 Emission	142
	4.7.2	[O I] 63 Emission	142
	4.7.3	Total Infrared Emission	143
	4.7.4	Hydrogen Density and UV Radiation Field	144

4.7.5	Caveats	145
4.8	Methods to Derive the Outflow Properties	146
4.8.1	Beam Smearing	146
4.8.2	Tilted Ring Model	147
4.8.3	Defining the Spatial Location of the Outflow	148
4.8.4	Line Luminosities	150
4.8.5	Mass of the Neutral Atomic Wind	151
4.8.6	Mass of the Ionized Wind	152
4.8.7	Kinetic Energy of the Wind	153
4.9	Properties of the Outflows and Multi-Phase Comparisons	153
4.9.1	M 82	155
4.9.2	Cen A	160
4.9.3	Circinus	164
4.9.4	NGC 253	167
4.9.5	NGC 1068	171
4.9.6	NGC 3079	176
4.9.7	NGC 4945	179
4.10	Summary	183
5	Summary and Future Work	187
5.1	Main Results	187
5.2	Future Work	190
A	<i>Spitzer</i> MIR SPECTRA	192
B	Results on OH 119 μm	199
	Bibliography	222

List of Tables

2.1	Herschel Observations of BAT AGN	23
2.1	Herschel Observations of BAT AGN	24
2.2	Galaxy Properties	33
2.2	Galaxy Properties	34
2.2	Galaxy Properties	35
2.3	Properties of the OH 119 μm Profiles	39
2.3	Properties of the OH 119 μm Profiles	40
2.3	Properties of the OH 119 μm Profiles	41
2.4	$S_{9.7\mu\text{m}}$ Continuum Parameters and Measured Values of the BAT AGN Sample	55
2.4	$S_{9.7\mu\text{m}}$ Continuum Parameters and Measured Values of the BAT AGN Sample	56
2.4	$S_{9.7\mu\text{m}}$ Continuum Parameters and Measured Values of the BAT AGN Sample	57
2.5	$S_{9.7\mu\text{m}}$ Continuum Parameters and Measured Values of the ULIRG/PG QSO Sample	62
2.5	$S_{9.7\mu\text{m}}$ Continuum Parameters and Measured Values of the ULIRG/PG QSO Sample	63
2.6	Results from Statistical Analyses of Host Galaxy Properties	64
2.7	Results from Statistical Analyses of the Kinematics	65
2.7	Results from Statistical Analyses of the Kinematics	66
3.1	Spitzer-IRS Spectra: Observations	88
3.2	Galaxy Properties	89
3.3	OH 35 μm Profile Properties	101
4.1	Fine-structure Lines	115
4.2	Galaxy Properties	118
4.3	PACS Fine-Structure Line Observations	121
4.3	PACS Fine-Structure Line Observations	122
4.4	Wind Properties	154
B.1	PACS OH 119 μm Observations	200

List of Figures

1.1	SMBH vs galaxy properties	5
1.2	Schematic of two evolutionary phases of a wind-blown bubble	8
1.3	Schematic of a shock driven into the ISM by an AGN	10
1.4	Multiphase AGN Outflow	12
1.5	Multiphase SB Outflow in M 82	14
1.6	Grotrian diagram of OH ground state transitions	16
1.7	Grotrian diagram of the electronic transitions in atomic fine-structure lines	17
1.8	Herschel, Spitzer, model SEDs	18
2.1	BAT/AGN and ULIRG/PG QSO property distributions	24
2.2	Fits to the continuum subtracted OH 119 line profiles	27
2.2	(Continued)	28
2.2	(Continued)	29
2.2	(Continued)	30
2.2	(Continued)	31
2.3	OH 119 EW vs M_* vs α_{AGN} vs L_{AGN}	45
2.4	The apparent strength of the $9.7 \mu\text{m}$ silicate feature relative to the local mid-infrared continuum as a function of the AGN fractions. Note that $S_{9.7\mu\text{m}}$ is a logarithmic quantity and can be interpreted as the apparent silicate optical depth. The strength of silicate absorption increases upward. Sign conventions and meanings of the symbols are the same as those in Section 2.5.1.1. Crosses represent objects with a null OH detection. Vertical lines indicate objects with a null $9.7 \mu\text{m}$ silicate feature detection.	49
2.5	Title	52

2.6 Histograms showing the distributions of the 50% (median; left panels) and 84% (right panels) velocities derived from the multi-Gaussian fits to the OH profiles of the BAT AGN. Top panels show pure absorption components (blue), pure emission components (red dashed), P-cygni emission components (red, left diagonals), and inverse P-cygni emission components (red, right diagonals). Bottom panels show pure absorption components (filled grey), P-Cygni absorption components (blue, left diagonals), inverse P-cygni absorption components (blue, right diagonals), and total absorption components (pure + P-Cygni + inverse P-Cygni). 53

2.7 v_{50} and v_{84} as a function of the stellar masses. The meanings of the symbols are the same as those in Section 2.5.1.1. The data points joined by a segment correspond to F14394+5332 W and E. The smaller symbols have larger uncertainties (values followed by double colons in Table 3.3) 67

2.8 v_{50} and v_{84} as a function of the star formation rates. The meanings of the symbols are the same as those in Section 2.5.1.1. The smaller symbols have larger uncertainties (values followed by double colons in Table 3.3) 68

2.9 v_{50} and v_{84} as a function of the specific star formation rates. The meanings of the symbols are the same as those in Section 2.5.1.1. The data points joined by a segment correspond to F14394+5332 E and W. The smaller symbols have larger uncertainties (values followed by double colons in Table 3.3) The black vertical line indicates the approximate location of the Main Sequence of star-forming galaxies (Shimizu et al., 2015). 69

2.10 v_{50} and v_{84} as a function of the AGN fractions. The meanings of the symbols are the same as those in Section 2.5.1.1. The smaller symbols have larger uncertainties (values followed by double colons in Table 3.3) 70

2.11 v_{50} and v_{84} as a function of the AGN luminosities. The meanings of the symbols are the same as those in Section 2.5.1.1. The smaller symbols have larger uncertainties (values followed by double colons in Table 3.3) 71

2.12	Total (absorption + emission) equivalent widths of OH 119 μm as a function of the apparent strength of the 9.7 μm silicate feature relative to the local mid-infrared continuum. Note that $S_{9.7\mu\text{m}}$ is a logarithmic quantity and can be interpreted as the apparent silicate optical depth. The strength of this absorption feature increases to the right. Also note that objects classified as LINERs have been excluded from this plot. Filled markers refer to Type 1 and open markers refer to Type 2. Blue squares and red circles represent BAT AGN and ULIRGs/PG QSOs, respectively. Vertical lines represent objects in which OH was not detected. Horizontal lines represent objects with a null $S_{9.7\mu\text{m}}$ detection. Dotted lines and dash-dotted lines refer to Type 1 and Type 2, respectively. Blue and red lines indicate BAT AGN and ULIRGs/PG QSOs, respectively.	80
2.13	Ratio of the semi-minor axis to the semi-major axis (a proxy for the inclination of the host galaxy disk) as a function of $S_{9.7\mu\text{m}}$ for the BAT AGN sample. Squares, triangles, and circles represent BAT AGN in which OH is observed purely in absorption, purely in emission, composite absorption/emission, respectively. Diamonds represent objects in which OH was undetected. Filled points and dash-dotted lines indicate Type 1 while open points and dotted lines indicate Type 2 AGN. Horizontal lines represent objects with a null 9.7 μm silicate feature detection.	81
3.1	Example of twelve different continuum fits to the mid-infrared spectrum of IRAS F17208-0014. The black solid histograms are the data separated from each other by an arbitrary offset. Spline pivot points are anchored at wavelengths of 33.0 μm , 33.8 μm , 34.5 μm , and 35.0 μm . The blue, green, and red dots indicate the set of pivot points which are respectively the lower limits (v1), upper limits (v2), and best-fit-by-eye values (v3) used to fit a continuum spline. The top most set of fits is the result of using a third-order ($k = 3$) spline fit to each pivot point set. Below are the results for second-order ($k = 2$) and first-order ($k = 1$) spline fits. In each case, the blue, green, and red dotted lines show the results of the spline fits to the lower-limit, upper-limit, and "best-fit-by-eye" continuum flux pivot points. The last spectrum at the bottom is fit with a polynomial. The magenta regions in this spectrum indicate the regions used to fit the first (solid blue line), second (solid green line), and third (solid red line) order polynomials to the continuum. The two dotted vertical lines in grey mark the rest wavelengths of the OH 35 doublet at systemic velocity. The dotted vertical lines in red mark the locations of the emission features [S III] 33.48 μm and [Si II] 34.82 μm . The vertical light-green band shows the region where a 20% dip in the detection response in the NOD 1 position occurs.	94

3.2	Fits to the 33 – 35 μm continua for all 15 objects in the sample. The grey shaded area shows the full range of the twelve different continuum fits described in Figure 3.1. Black dots are median values of the six fluxes at each pivot point, and the dotted line is the resultant third-order spline fit to those pivot points. The grey dotted vertical lines mark the rest wavelengths of the OH 35 doublet at systemic velocity. The red dotted vertical lines mark the locations of the emission features [S III] at 33.48 μm and [Si II] at 34.815 μm . The vertical light-green band shows the region where a 20% dip in the detection response in the NOD 1 position occurs.	95
3.3	Two-Gaussian fits to the continuum-subtracted OH 35 line profiles of the 15 objects in our sample; see Section 3.3.3. In each figure, the solid black histogram is the data. Blue dashed lines indicate the two Gaussian components which best fit the line profile, and the magenta line is the sum of those two components. The grey dotted vertical lines mark the rest wavelengths of the OH 35 doublet at systemic velocity. The red dotted vertical line marks the location of the [Si II] emission line at 34.815 μm	98
3.4	Examples of OH 35 line profile fits for each of the twelve different continuum subtracted spectra in IRAS F17208-0014. Line colors and styles are the same as that for Figure 3.3. "p1, p2, p3" indicate first-, second-, and third-order polynomial fits to the continuum, respectively. "v1" refers to the "lower-limit" pivot points in Figure 3.1. "v2" refers to the "upper-limit" pivot points, and "v3" to the "best-fit-by-eye" pivot points. "k1, k2, k3" are the orders of the spline fitted to the continuum. For example, "v2k3" is the third-order spline fit to the continuum using the "upper-limit" pivot points.	99
3.5	Distributions of the measured OH 35 (a) integrated fluxes and (b) equivalent widths.	100
3.6	Distributions of the (a) OH column densities and (b) OH-to-H abundance ratios, X_{OH} , inferred from the fits of the OH 35 feature.	102
3.7	OH 35 spectra normalized to the continuum. Red and blue lines are the two Gaussian components of the fitted line and the magenta line is the sum of the two components. The green line is the profile predicted by the radiative transfer model described in González-Alfonso & Cernicharo (1999); González-Alfonso et al. (2017). The modeled line profiles are constrained by observations of four OH lines at 65, 79, 84, and 119 μm	108
4.1	Signal-to-noise ratio maps. Contours are 0.1, 0.3, 0.5, 0.7, 0.8, and 0.9 of the peak value in each image. Black crosses mark the adopted galaxy center.	124
4.2	Total integrated emission line fluxes in $10^{-17} \text{ W m}^{-2}$. Contours are 0.1, 0.3, 0.5, 0.7, and 0.9 of the peak flux in the image. Black crosses mark the adopted galaxy center.	125

4.3	Maps of the emission line ratios. Contours are 0.1, 0.3, 0.5, 0.7, 0.8, and 0.9 of the peak value in each image.	131
4.4	Maps of the median velocities, v_{50} in units of km s^{-1} . Contours are in eight equal steps between the minimum velocity and the maximum velocity in each image.	132
4.5	Maps of the $1 - \sigma$ line widths, $W_{1\sigma}$, in units of km s^{-1} . Contours are 0.4, 0.5, 0.6, 0.7, 0.8, and 0.9 of the peak width in each image.	133
4.6	Maps of the hydrogen density, n_{H} in each object. Units are in cm^{-3} . The “low” density range is defined as $0 < n_{\text{H}} < 10^4 \text{ cm}^{-3}$ and the “high” density range is defined as $10^4 < n_{\text{H}} < 10^7 \text{ cm}^{-3}$. See Section 4.7.4 for details about the determination of these density ranges and definitions of Solutions A–D. Solution A is the low density solution with only the [C II] 158 flux correction (see Section 4.7.1 and Section 4.7.4), Solution B is the low density solution with both the fluxes of [C II] 158 and [O I] 63 corrected (see Section 4.7.1, Section 4.7.2 and Section 4.7.4), Solution C is the high density solution with only the [C II] 158 flux correction, and Solution D is the high density solution with both the fluxes of [C II] 158 and [O I] 63 corrected. As discussed in Section 4.7.4, the high density PDR solutions “C” and “D” lead to unphysical ISRFs. Therefore, we have excluded them from the analysis of the outflow.	139
4.7	Maps of the strength of the UV radiation field, G_0 , for the low density and high density limits PDR solutions. Definitions of the Solutions are the same as those in Figure 4.6.	140
4.8	M 82: Results from modeling the disk velocity field with ^{3D} BAROLO (which accounts for both the instrumental spectral and spatial resolutions) and the location of the outflow based on excess line broadening. Color bar values are in units of km s^{-1} . For each line, left to right: observed data, model result, data - model residual, spatial location of the wind in regions where $\Delta W_{1\sigma} > 25 \text{ km s}^{-1}$, and spatial location of the wind in regions where $\Delta W_{1\sigma} > 50 \text{ km s}^{-1}$. Contours in (a) are in five equal steps between the minimum and maximum velocities in each image. Contours in (b) are 0.3, 0.5, 0.7, and 0.9 of the peak value in each image. The solid blue line marks the galaxy major axis. The magenta cross marks the adopted galaxy center.	156
4.9	M 82: PACS contours (magenta) overlaid on the total integrated intensity contours of SiO(2-1) (black, García-Burillo et al., 2001) and the radio continuum at 4.8 GHz (grey scale, Wills et al., 1999).	157
4.10	Mass and KE in the wind derived from the PDR solutions (see Section 4.7.4 for definitions of Solutions A, B, C, and D) and the [O III] 88 flux. Units are in $10^4 M_{\odot}$ and 10^{51} erg for the masses and KEs, respectively.	158
4.11	Cen A: Results from modeling the disk velocity field with ^{3D} BAROLO. Symbols and plots are the same as those in Figure 4.8.	161
4.12	Cen A: PACS contours overlaid on 8.4 GHz image from Hardcastle et al. (2003).	162

4.13	Mass and KE in the wind derived from the PDR solutions and the [O III] 88 flux. Symbols, units, and plots are the same as those in Figure 4.10.	162
4.14	Circinus: Results from modeling the disk velocity field with ^{3D} BAROLO. Symbols, units, and plots are the same as those in Figure 4.8.	165
4.15	Circinus does not have a discernible outflow in either the neutral or ionized gas.	166
4.16	NGC 253: Results from modeling the disk velocity field with ^{3D} BAROLO. Symbols, units, and plots are the same as those in Figure 4.8.	168
4.17	NGC 253: PACS contours (yellow), contours of receding and approaching CO outflow (magenta and blue, respectively) from Bolatto et al. (2013). Composite image from Heesen et al. (2011) which shows H α in red from Westmoquette et al. (2011), λ 20 cm continuum (green), and soft X-ray in blue from Hardcastle et al. (2010).	169
4.18	Mass and KE in the wind derived from the PDR solutions and the [O III] 88 flux. Symbols, units, and plots are the same as those in Figure 4.10.	170
4.19	NGC 1068: Results from modeling the disk velocity field with ^{3D} BAROLO. Symbols, units, and plots are the same as those in Figure 4.8.	172
4.20	NGC 1068: PACS contours overlaid on 349 GHz continuum and CO(3-2) residual mean-velocity field from García-Burillo et al. (2014).	173
4.21	Mass and KE in the wind derived from the PDR solutions and the [O III] 88 flux. Symbols, units, and plots are the same as those in Figure 4.10.	174
4.22	NGC 3079: Results from modeling the disk velocity field with ^{3D} BAROLO. Symbols, units, and plots are the same as those in Figure 4.8.	177
4.23	Top row: PACS contours of the [C II] 158 v_{50} and $W_{1\sigma}$ residuals in the wind in NGC 3079 overlaid on 1.4GHz observations from Sebastian et al. (2019). Middle row: PACS contours of the [C II] 158 v_{50} and $W_{1\sigma}$ residuals in the wind in NGC 3079 overlaid on H α + [N II] image from Cecil et al. (2001). Bottom row: <i>Chandra</i> image (blue) + <i>HST</i> (red and green).	178
4.24	NGC 4945: Results from modeling the disk velocity field with ^{3D} BAROLO. Symbols, units, and plots are the same as those in Figure 4.8.	180
4.25	Top row: PACS contours overlaid on the [NII] residual velocity field of NGC 4945 from Venturi et al. (2017). Bottom row: PACS contours overlaid on the [NII] W70 of NGC 4945 from Venturi et al. (2017).	181
4.26	Mass and KE in the wind derived from the PDR solutions and the [O III] 88 flux. Symbols, units, and plots are the same as those in Figure 4.10.	181

A.1	Mid-infrared (5-37 μm) spectra used to measure $S_{9.7\mu\text{m}}$. The dashed line is the continuum calculated from the cubic spline interpolation fitted to the pivot points shown as black dots. Red dots show $f_{cont}(9.7\mu\text{m})$ (located on dashed continuum line) and $f_{obs}(9.7\mu\text{m})$ (located on the solid black line or the observed flux density). The blue line shows the integration range used to calculate the flux and total equivalent width of the 9.7 μm silicate feature (see Table 2.4 and Table 2.5). . . .	192
A.2	(Continued)	193
A.3	(Continued)	194
A.4	(Continued)	195
A.5	(Continued)	196
A.6	(Continued)	197
A.7	(Continued)	198
B.1	Top left: PACS IFU footprint of OH 119 (black squares) overlaid on the 22 μm WISE image of M 82. The white contour marks the spatial extent of the [O III] 88 wind. The black contour outlines the PACS footprint of the [O III] 88 observation. The black cross marks the adopted galaxy center and the blue line marks the galaxy major axis. Top right: Spline fits to the OH 119 continuum (blue dashed lines). Black lines are the observed data. Magenta areas indicate the regions used to fit the continuum. Blue dots mark the pivot points used to fit the spline. Bottom left: Line profile fitting results of the continuum-subtracted spectra. Solid blue lines indicate gaussian absorption components. Solid red lines indicate gaussian emission components. Vertical dashed blue (red) lines mark the v_{16} , v_{50} , and v_{84} velocities in absorption (emission). Bottom right: Top row, from left to right shows the total velocity-integrated flux of the fitted OH line profiles, the total flux in the absorption components only, and the total flux in the emission components only. Middle row shows v_{50} for the absorption (left) and emission components (right). Bottom row shows the $1-\sigma$ line widths of the absorption (left) and emission (right) components.	202
B.2	Cen A. Lines and symbols are the same as those in Figure B.1.	203
B.3	Circinus. Lines and symbols are the same as those in Figure B.1.	204
B.4	NGC 253. Lines and symbols are the same as those in Figure B.1.	205
B.5	NGC 1068. Lines and symbols are the same as those in Figure B.1.	206
B.6	NGC 3079. Top left: The white contour marks the spatial extent of the [C II] 158 wind. Lines and symbols are the same as those in Figure B.1.	207
B.7	NGC 4945. Lines and symbols are the same as those in Figure B.1.	208

List of Abbreviations

AGN	Active Galactic Nucleus
ALMA	Atacama Large Millimeter Array
BAT	Burst Alert Telescope
CASSIS	Cornell AtlaS of Spitzer/IRS Sources
EW	Equivalent Width
FIR	Far-Infrared
HST	Hubble Space Telescope
IR	Infrared
ICM	Intracluster Medium
IGM	Intergalactic Medium
IRS	Infrared Spectrograph
ISM	Interstellar Medium
IFS	Integral Field Spectroscopy
IFU	Integral Field Unit
LF	Luminosity Function
LIRG	Luminous Infrared Galaxy
MIR	Mid-Infrared
NED	NASA/IPAC Extragalactic Database
PACS	Photodetector Array Camera and Spectrometer
PAH	Polycyclic Aromatic Hydrocarbon
PG QSO	Palomar Green Quasi-Stellar Object
RSRF	Relative Spectral Response Function
SB	Starburst
SED	Spectral Energy Distribution
SHA	Spitzer Heritage Archive
SMBH	Supermassive Black Hole
SF	Star Formation
SNe	Supernovae
sSFR	Specific Star Formation Rate
SFR	Star Formation Rate
ULIRG	Ultra-Luminous Infrared Galaxy
UV	Ultraviolet

Chapter 1: Introduction

1.1 Background

Galactic-scale outflows (or winds) are powered by stellar and/or supermassive black-hole (SMBH) accretion processes which inject energy and momentum into the interstellar medium (ISM). On a grand scale, winds may significantly affect the assembly and evolution of galaxies (Veilleux et al., 2005, 2020). Outflows are ubiquitous at any redshift and they are invoked to help explain a number of observations in the Universe. For example, they help explain some of the observable properties of galaxies (e.g. color and gas abundance; for example, red, gas-poor ellipticals) and of the intergalactic medium (IGM). Outflows can account for the correlations that exist between the physical properties of a galaxy (e.g. the tight correlation between the SMBH mass and the mass of the spheroidal bulge). Moreover, outflows may help reconcile (or mitigate) the discrepancies between predictions from cosmological simulations and models with actual observations. In the following list, I expound upon some specific scenarios where winds have been incorporated to explain a number of observations. This list is by no means exhaustive, but it does highlight how winds may provide a significant contribution to our understanding of the formation and evolution of galaxies.

- *Star formation regulation* - There are a number of ways an outflow can affect the star formation activity in a galaxy. If the outflow has enough energy to escape the gravitational potential well of its host galaxy, then the outflow may be able to empty the reservoir of gas within the system and halt star formation completely (Fabian, 2012; Veilleux et al., 2005). Winds may heat the cold ISM via shocks or from the deposition of mechanical energy, thereby preventing the gas from condensing and forming stars (e.g. Cecil et al., 2001; Heckman & Thompson, 2017; Martin, 2006). On the other hand, if the material in the outflow lacks the energy to escape its host system, it will fall back onto the disk in the form of a “galactic fountain” and may thus be recycled again for star formation.
- *Scaling relations with the SMBH mass and the host galaxy properties* - Winds may be responsible for the fueling or quenching of accretion onto the SMBH in a galaxy (Di Matteo et al., 2005). The brightness of an active galactic nucleus (AGN) is regulated by the rate of infall from surrounding material (e.g. gas and dust) while the infall rate of material is regulated by the brightness of the AGN. This feedback loop may explain the remarkable correlations observed between the mass of the SMBH (M_{BH}) and the properties of the host galaxy, such as luminosity ($M_{BH}-L$ relation), velocity dispersions in ($M_{BH}-\sigma$ relation) and masses ($M_{BH}-M_{bulge}$ relation) of the spheroidal bulge (see the review and references therein of Kormendy & Ho, 2013). These relationships indicate that SMBHs and the bulges coevolve by regulating each other’s growth. [Figure 1.1](#)

shows the three relationships.

- *Correlations with galaxy type* - Winds that can empty their host galaxies of gas may explain the bimodal color distribution between early (E, S0, and Sa) and late (Sb, Sc, and Irr) morphological types observed in large galaxy surveys (e.g. [Strateva et al., 2001](#)). These surveys indicate that disk-dominated galaxies are predominantly blue and star forming, whereas spheroid-dominated galaxies are largely red and quiescent (e.g. [Blanton & Moustakas, 2009](#)). This bimodality indicated that some sort of quenching mechanism was required to prevent gas from cooling and/or forming stars in observed gas-poor, quiescent galaxies ([Peng et al., 2010](#)). The inclusion of winds into semi-analytic models has qualitatively reproduced this observed bimodal color distribution (e.g. [Kimm et al., 2009](#)).
- *Metal enrichment of the IGM and CGM* - Outflows may not only impact individual galaxies, but they may also play a significant role in the chemical and thermal evolution of the universe. They may even influence the metal enrichment of the intergalactic medium (IGM) and the circumgalactic medium (CGM) via the regulation of gas and dust exchange into and out of galaxies ([Bertone et al., 2007](#); [Heckman & Thompson, 2017](#); [Zhang, 2018](#)). Observations of absorption systems in quasar sightlines through the IGM/CGM show that the IGM/CGM is enriched with metals to a small fraction of solar metallicity and simulations have shown how outflows may be responsible for lifting gas and metal up and out of the galaxy disk into the IGM/CGM ([Aguirre](#)

et al., 2001; Madau et al., 2001).

- *Paucity of very high and low mass galaxies* - Early attempts to predict the statistical distributions of global properties of galaxy populations have shown a mismatch in shape between the predicted distribution of dark halo masses and the observed distribution of galaxy luminosities (or equivalently, masses). Galaxy abundances at higher luminosities (e.g. those brighter than galaxies with Milky Way-like luminosities, $L_* \sim 3 \times 10^{10} L_\odot$) are observed to decline exponentially compared to CDM simulations, while the shape of galaxy abundances are observed to flatten at the fainter end. Inclusion of feedback from the SMBH appears to explain the abundance deficit at the high luminosity end (e.g. Croton et al., 2006; Somerville et al., 2008), while the inclusion of supernovae (SNe) and stellar processes is able to reproduce the shape of the luminosity function (LF) at the fainter end (e.g. Bower et al., 2006). Essentially, feedback due to stellar processes plays a crucial role in shaping the LF for dark matter halos with $M_H \lesssim 10^{12} M_\odot$ while feedback from AGN processes plays a more dominant role at halo masses $M_H \gtrsim 10^{12} M_\odot$ (Somerville & Davé, 2015).

Although we now have a better understanding of how winds may significantly impact the formation and evolution of galaxies there still exists a plethora of unanswered questions concerning the detailed physics and properties of galactic outflows. What is the primary mechanism of energy and momentum injection that powers an outflow? How can we constrain outflow properties such as energetics, morphologies,

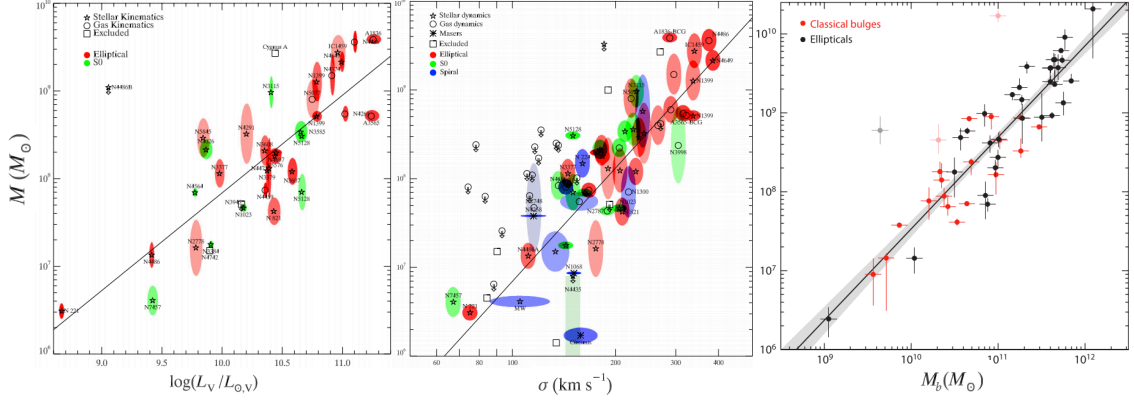


Figure 1.1 Left and Middle: $M_{BH}-L$ and $M_{BH}-\sigma$ relations, respectively (from Gültekin et al., 2009). Right: $M_{BH}-M_{\text{bulge}}$ relation (from Kormendy & Ho, 2013).

lifetimes, spatial extent, radial-dependent velocities, mass outflow rates? What is the efficiency of entraining material from the ISM and ejecting it out of the disk? The answers to these questions can fundamentally measure the impact of outflows on galaxy evolution.

In this chapter, I describe the basic physics behind outflows. In particular, the sources of energy and momentum (either starburst (SB) or AGN) and the driving mechanisms of the outflows. I also discuss the multiphase nature of outflows and the tools we used to probe different ISM phases in outflows.

1.2 Starburst and Active Galaxies

1.2.1 Starburst-Driven Winds

SB galaxies contain regions (typically nuclear or circumnuclear) that are undergoing intense and spatially concentrated star formation activity; much higher than the rate of star formation in galaxies similar to the Milky Way. Such a SB can

be triggered when gas rapidly accumulates into a small volume, say from a merger of two gas-rich galaxies [Barnes & Hernquist \(1996\)](#), or from gas funneled into the nuclear region of a galaxy by dynamical processes associated with bar instabilities [Combes & Charmandaris \(2000\)](#). The SB regions host large numbers of young, hot, massive stars that ionize their environment and evolve quickly to form supernovae. Outflows can be driven by the powerful energy reservoirs in these SB regions.

[Chevalier & Clegg \(1985, hereafter, C85\)](#) was first to establish a conceptual picture of how a SB-driven wind would work. The evolution of a bubble in the interstellar medium (ISM) evolves in several stages. First, kinetic energy is launched from a collection of stellar processes such as winds from high-mass, high-luminosity stars and explosions from supernovae (SNe). The ejecta from the winds and explosions intersect and collide with each other creating shocks that rapidly thermalize the kinetic energy of the ejecta, thus producing hot ($T \sim 10^7$ K), high pressure ($P/k \sim 10^7$ K cm⁻³), low density gas ([Strickland & Stevens, 2000](#)). The wind-shocked material creates an over-pressurized cavity (or bubble) that adiabatically expands as a free wind with $v_{\text{wind}} \sim$ several thousand km s⁻¹ ([García-Burillo et al., 2001](#)). During this “energy-conserving” phase, little energy is lost to radiation due to the high post-shock temperatures and low densities. In the next phase, the free wind passes through an internal wind shock where the ejecta is decelerated and reheated to $T \sim 10^7$ K. The pressure of the shocked wind continues to inflate a bubble which is collimated by the density gradient between the galactic disk and its halo. The bubble preferentially propagates along the direction of the steepest pressure gradient. This forms a bipolar flow which sweeps up cooler, denser, ambient disk or

halo gas that is accelerated to $v_{\text{gas}} \sim \text{few hundreds km s}^{-1}$. A shell of accumulated ISM gas then forms at the edge of the bubble. Once the velocity of the shell has decelerated enough so that the cooling time is shorter than the expansion time, the shell will begin to cool radiatively. The bubble then enters the pressure-driven snowplow phase in which the internal thermal energy of the bubble cannot be neglected. The bubble leaves the snowplow phase once the thermal energy has been radiated away. The total momentum of the inner wind is transferred to the gas and the bubble enters a “momentum-conserving” phase. Assuming a stratified halo, once the bubble diameter is comparable with the scale height of the disk, the ambient gas density will be low enough that the bubble can accelerate and fragment into clumps and filaments through Rayleigh-Taylor instabilities (Schiano, 1985). During this “break-out” phase, the freely flowing and shocked wind is injected into the galaxy halo.

In summary, the structure of a bubble expanding into an ISM due to a SB includes (a) the energy injection zone, (b) hot, freely-expanding wind, (c) wind material that has been shocked, (d) a thin, dense shell of post-shock gas that has been accumulated by the wind and is now radiatively cooling, and finally (e) undisturbed ISM material. A schematic displaying the essential features of a wind-blown bubble is shown in [Figure 1.2](#).

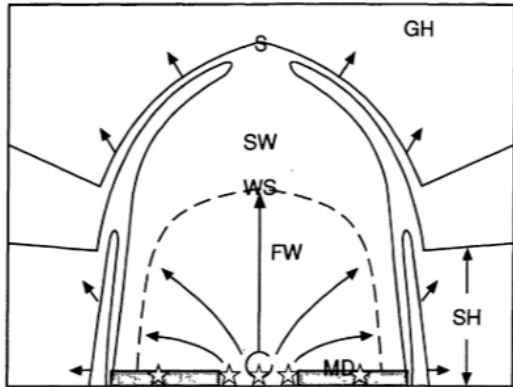


FIG. 1a

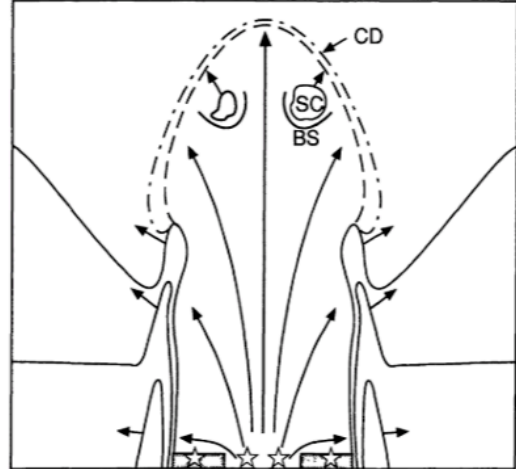


FIG. 1b

Figure 1.2 A schematic showing two evolutionary phases of a wind-blown bubble. Panel (a) shows the radiative phase where the energy injection zone from the SB is indicated by open stars, the free wind (FW, long arrows) expands outward at several thousand km s^{-1} where it passes through an internal wind shock (WS) creating shocked wind material (SW). The expanding bubble will sweep up ambient gas and accelerate it to a few hundred km s^{-1} (short arrows). The shocked gas will then radiatively cool into a thin shell (S). Eventually, when the diameter of the bubble is comparable to the scale height of the disk, it will fragment, panel (b), where the freely expanding wind fluid will flow into the halo. Bow shocks (BS) can form around shocked clouds (SC) which may be accelerated outward (from Heckman et al., 1990).

1.2.2 AGN-Driven Winds

An active galaxy contains a core of bright emission that is embedded in the nuclear region of an otherwise normal galaxy. This core is typically brighter than the rest of the galaxy, shows variations in luminosity, and is known as an AGN. Spectral energy distributions (SEDs) of this higher-than-normal luminosity core indicate that the excess brightness is non-stellar in origin. It is generally accepted that the source of energy from an AGN is the accretion of matter (e.g. gas or dust) onto the SMBH, where the accreted material loses its gravitational potential energy via conversion into heat and is partly radiated away. This accretion disk is mostly seen in the

ultra-violet (UV) and in X-rays.

In AGN, the nature of the energy outflow near the SMBH differentiates AGN feedback into two modes: “radiative” or “quasar” mode which is powered by radiation and “radio” or “kinetic” mode which is powered by mechanical jets (Cielo et al., 2018). Radiative mode feedback is typically observed in high-luminosity AGN that are radiatively efficient and close to the Eddington limit (within about one or two orders of magnitude). It is most concerned with pushing cold gas about (Fabian et al., 2013). This mode is the most likely explanation for the observed black hole mass–stellar velocity dispersion relation (the so-called “ $M_{BH}-\sigma$ ” relation). This mode was probably most effective at $z \sim 2 - 3$ when quasar activity was more common and galaxies were more rich in gas. The radio mode AGN are radiatively inefficient and typically host the most massive SMBH. These low-luminosity AGN ($L_{AGN} < 0.01 L_{Edd}$; Combes, 2014) typically harbor light relativistic radio jets and are surrounded by hot halos. They typically correspond to massive early type galaxies (e.g. radio ellipticals). If feedback successfully empties a galaxy of its gas, eventually stellar mass loss and/or intracluster plasma will inevitably refill the gas reservoir. Maintaining an empty reservoir, or at least heating the gas enough to prevent star formation, appears to be a consequence of the radio mode feedback.

In general, an AGN-driven wind will collide with the surrounding ISM, driving a reverse shock into the wind and a forward shock into the ISM. If the shocked wind cools efficiently, the outflow is “momentum-conserving” (or “momentum-driven”) and transfers only its ram pressure (and, hence, momentum flux) to the ISM (Zubovas & Nayakshin, 2014). If, on the other hand, the shocked wind cools inefficiently,

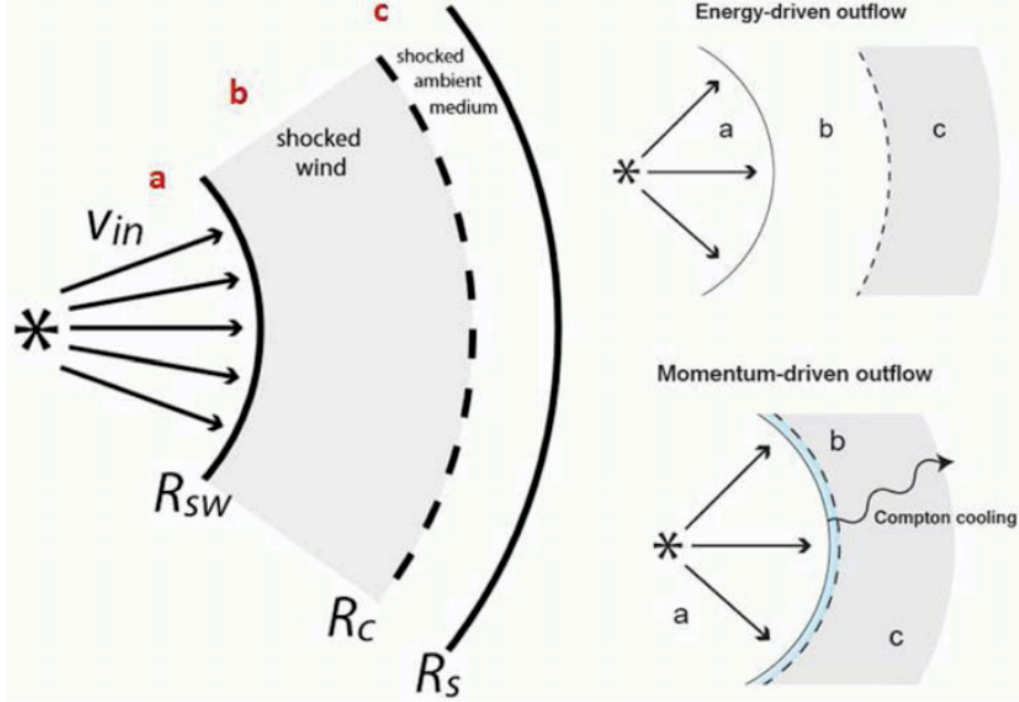


Figure 1.3 A schematic view of the shock driven into the ISM by a wind launched from an AGN is displayed in the left image where (a) is the wind region, delimited by the reverse wind shock (R_{SW}), (b) is the shocked wind that ends at the discontinuity surface (R_C), and (c) is the shocked ISM, bounded by the forward shock (R_S). The top right image shows a schematic of the “energy-conserving” outflow where the hot and thick region (b) cools inefficiently and expands adiabatically. The bottom right image shows the “momentum-conserving” outflow where the shocked wind (light blue region (b)) cools efficiently, experiences a drop in pressure, and becomes thin (from [Costa et al., 2014](#)).

the outflow is “energy-conserving” (or “energy-driven”) and transfers most of its kinetic luminosity ($L_{kin} \simeq 0.05 L_{AGN}$; [Zubovas & Nayakshin, 2014](#)) to the ambient medium. This hot outflow may create a bubble in the galaxy disk that thermally expands after the shock. This phenomenon is analogous to the adiabatic phase in a SB-driven bubble described in [Section 1.2.1](#). This kind of wind can drive outflows to velocities greater than 1000 km s^{-1} ([King et al., 2011](#)). A schematic view of the shock driven into the ISM by a wind launched from an AGN is displayed in the left image of [Figure 1.3](#). The two images on the right of [Figure 1.3](#) show the two

different driving modes.

The bubble scenario described above is valid for an AGN driving a wide-angle outflow from the accretion disk or for a low energy AGN jet where all of the kinetic energy of the jet is deposited to the ISM. If the jet is powerful and highly collimated, the jet will simply “drill” through the ISM without imparting much energy or momentum to the surrounding gas (e.g. [Scheuer, 1974](#)).

1.3 The Multiphase ISM in Outflows

1.3.1 General Considerations

It is well established that outflows are of a multiphase nature (as revealed in observations and expected from simulations), spanning from the cold and dense molecular clouds to the very hot highly ionized medium. This multiphase structure complicates the calculations for the masses and energetics in outflows because we must concurrently analyze the outflow in multiple wavelength regimes, otherwise, measurements based on a single-phase will most likely result in misleading and incomplete conclusions. However, if we wish to assess the degree to which galactic winds impact the evolution and formation of galaxies, a fundamental understanding of the dynamic, energetic, and physical properties of the outflow must be established. Therefore, it is essential to consider all phases of the ISM in outflows in order to gain an understanding of the cosmological significance of outflows.

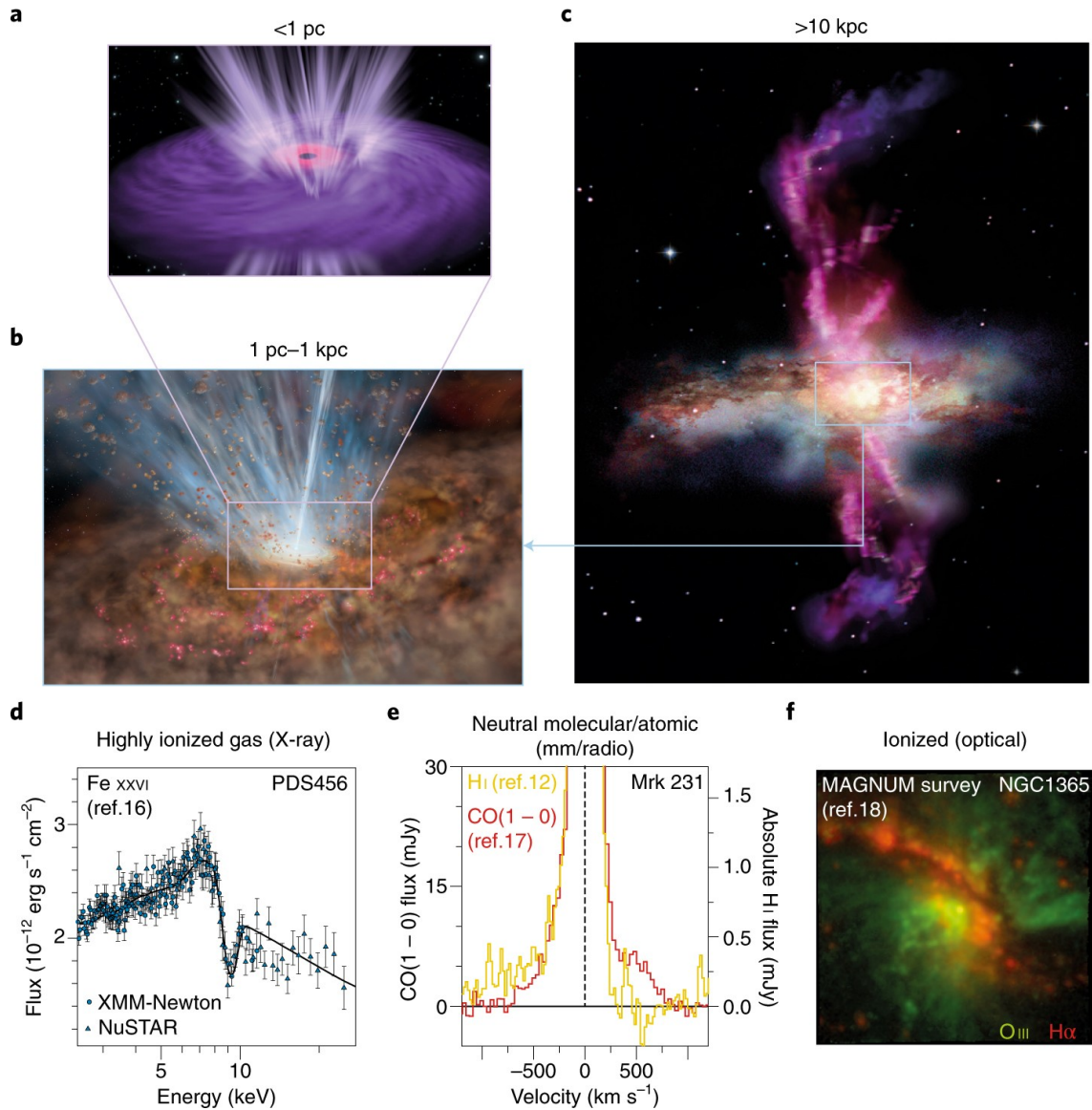


Figure 1.4 Artistic and observational views of AGN-driven winds in different ISM phases and at different physical scales. The cartoon in panels a, b, and c depicts the multiphase outflow based on observations and AGN feedback models. The outflow is launched from the galaxy nucleus (< 1 pc; panel a), propagates through the surrounding host galaxy ISM (1 pc – 1 kpc; panel b), and extends out into the galaxy halo (> 10 kpc; panel c). Observations of different outflow phases at different physical scales in three well known AGN are shown in panels d, e, and f. Panel d shows the highly ionized accretion disk wind observed in X-ray from PDS456 (Nardini et al., 2015). Panel e shows the neutral atomic and molecular outflow phases traced by the mm and radio in Mrk 231 on a scale of \sim few hundreds pc (Cicone et al., 2012; Morganti et al., 2016). Finally, panel f shows the ionized optical outflow of NGC 1365 extending out a few kpc (Venturi et al., 2017). (Figure is reproduced from (Cicone et al., 2018)).

Multiwavelength observations from the radio to the γ -ray have shown that the multiphase structure of an outflow are generally divided into four gas phases: hot (highly ionized, $T_{\text{gas}} \sim 10^6\text{--}10^7$ K; $n_{\text{gas}} \sim 10^6\text{--}10^8$ cm $^{-3}$), warm (ionized, $T_{\text{gas}} \sim 10^3\text{--}10^4$ K; $n_{\text{gas}} \sim 10^2\text{--}10^4$ cm $^{-3}$), cool (neutral atomic, $T_{\text{gas}} \sim 10^2\text{--}10^3$ K; $n_{\text{gas}} \sim 1\text{--}10^2$ cm $^{-3}$), and cold (molecular, $T_{\text{gas}} \sim 10\text{--}10^2$ K; $n_{\text{gas}} \geq 10^3$ cm $^{-3}$). These phases have been studied in several objects through various techniques which span the length of the electromagnetic spectrum. I will elucidate how these ISM phases have been traced in previous studies and I note that this list is by no means exhaustive or complete.

Chandra and XMM-Newton have been used to observe the highly ionized X-ray emitting gas (e.g. [Bravo-Guerrero & Stevens, 2017](#); [Strickland & Heckman, 2007](#); [Strickland & Stevens, 2000](#)). Optical emission (e.g. $\text{H}\alpha$, $[\text{N II}]$, $[\text{O III}]$) and absorption (e.g. Na I D and Mg II) lines have been used to trace the warm ionized ([Cecil et al., 2002](#); [Heckman et al., 2015](#); [Martin et al., 2013](#); [Rubin et al., 2014](#); [Shoppell & Bland-Hawthorn, 1998](#); [Weiner et al., 2009](#)) and neutral atomic ([Heckman et al., 2000](#); [Kornei et al., 2013](#); [Martin, 2005](#); [Rupke et al., 2002, 2005a,b,c](#); [Rupke & Veilleux, 2015](#)) gas phases in outflows. The warm molecular phase in outflows has been traced with H_2 (e.g. [Veilleux et al., 2009](#)). Cold molecular gas has been traced using OH , CO , HCN , and HCO^+ (e.g. [Bolatto et al., 2013](#); [Leroy et al., 2015](#); [Veilleux et al., 2013](#); [Walter et al., 2017](#); [Westmoquette et al., 2013](#)). Dust has also been traced in outflows (e.g. [Hutton et al., 2014](#); [McCormick et al., 2018](#); [Meléndez et al., 2015](#)). [Figure 1.4](#) shows artistic representations and observational data of different phases of AGN-driven outflows at different physical scales. [Figure 1.5](#) shows

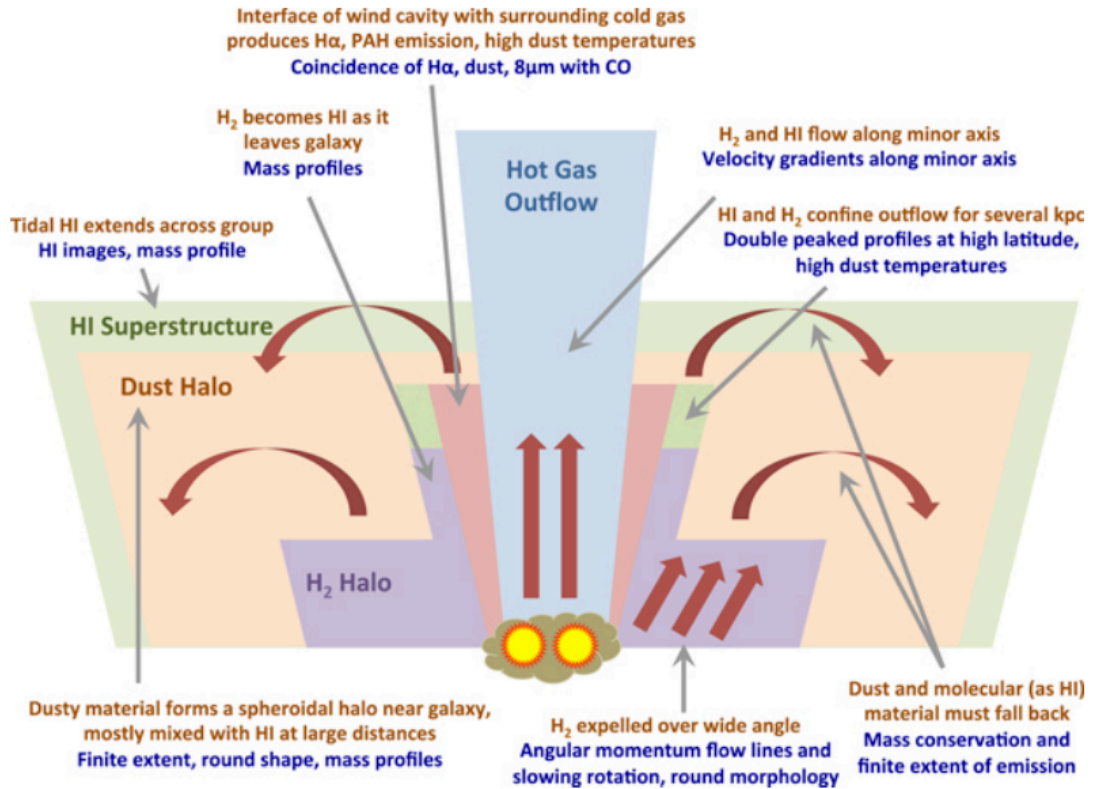


Figure 1.5 A schematic of the multiphase outflow in the SB galaxy M 82. The red statements are supported by the observational evidence described in blue (from Leroy et al., 2015).

the multiphase SB-driven outflow in M 82.

1.3.2 The OH Molecule

We use the FIR lines of the hydroxyl molecule (OH) as a tracer of the molecular gas component in an outflow. Furthermore, these lines can be used as powerful diagnostics of molecular winds because of their operative excitation mechanisms and their range in optical depths. These properties (e.g. OH is mainly excited by the absorption of FIR) also allow OH to probe nuclear regions and star forming complexes within galaxies where the FIR radiation density is strong. Within the 34

μm to $163 \mu\text{m}$ FIR wavelength range, a total of 14 lines (exhibiting both optically thick and optically thin features) arise from the eight lowest rotational levels of OH.

In this thesis, we focus on two of the OH transitions. The first is the ground-state OH ${}^2\Pi_{3/2} J = 5/2 - 3/2$ rotational Λ -doublet at $119.233 \mu\text{m}$ and $119.441 \mu\text{m}$ (hereafter, OH 119). It is the strongest of these FIR OH transitions (therefore it is more likely to be detected) and its wavelength is conveniently positioned at the peak sensitivity range of *Herschel*-PACS. Previous studies have already demonstrated the powerful diagnostic capability of OH 119 to determine wind characteristics (e.g. [Fischer et al., 2010](#); [Spoon et al., 2013](#); [Sturm et al., 2011](#); [Veilleux et al., 2013](#)). Moreover, these studies have shown that the molecular gas can dominate the mass and energy budget of the galactic outflow.

We also look at the cross ladder OH ${}^2\Pi_{3/2} \rightarrow {}^2\Pi_{5/2}$ Λ -doublet transition at 34.60 and $34.63 \mu\text{m}$ (hereafter, OH 35). OH 35 is optically thin compared to the other FIR OH transitions and because only 4% of all $35 \mu\text{m}$ absorption events result in re-emission at $35 \mu\text{m}$, OH 35 absorption line can be used to provide a meaningful constraint on the true column density.

See [Figure 1.6](#) for a schematic of the OH energy levels. Transitions analyzed in this thesis are outlined in red.

1.3.3 Atomic Fine-Structure Lines

Fine-structure line emission from neutral and ionized carbon atoms, as well as other species such as oxygen and nitrogen, is an important key to understanding the

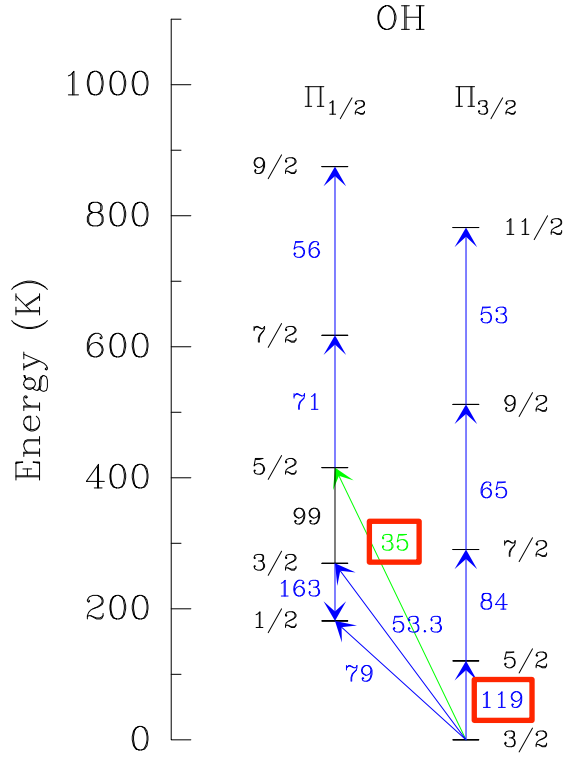


Figure 1.6 OH Λ -doublet transitions. Transitions analyzed in this thesis are outlined in red.

properties of the ISM in the region from which they originate, as it provides almost all of the gas cooling.

Warm, ionized, and relatively tenuous gas can be traced by [O III] 88, [N II] 122, and (to a smaller extent) [C II] 158. Warm, neutral, dense gas is exclusively traced by [O I] 63 and [O I] 145, but [C II] 158 emission also predominately occurs in the atomic medium. The observed lines cover a range in density and temperature behavior, which probe different phases of the ISM and are expected to probe different regions of their host galaxies. Figure 1.7 shows a schematic of the energy levels for the five atomic fine structure lines.

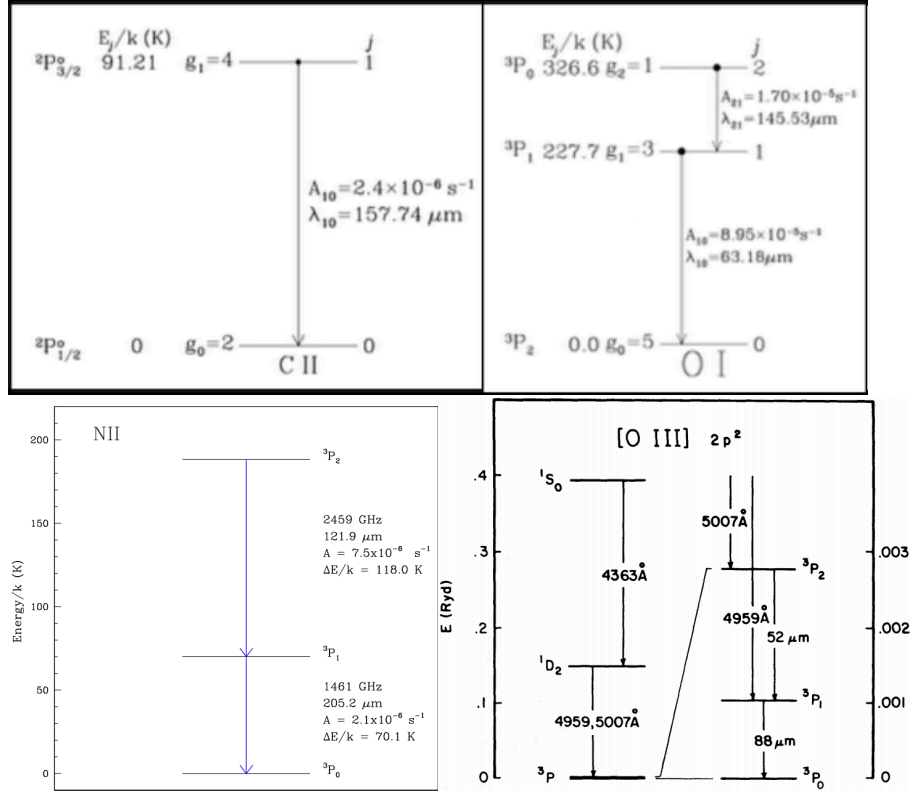


Figure 1.7 Energy level diagrams of the transitions in the electronic ground states of the atomic fine-structure lines. Top left: C⁺ (Draine, 2011). Top right: Neutral O (Draine, 2011). Bottom left: N⁺ ion (Goldsmith et al., 2015). Bottom right: O⁺⁺ ion. The optical transitions are on the left and the fine-structure transitions are on an expanded scale on the right (Dinerstein et al., 1985).

1.4 Observatories and Instruments

The online archival data presented in this thesis were acquired with the *Herschel* Space Observatory and the *Spitzer* Space Telescope. Both telescopes have run through their cryogenic fuel and are no longer in operation. In this section, I detail these observatories and the instruments used to obtain the data analyzed in this thesis. Chapter 2 utilizes PACS and Spitzer. Chapter 3 utilizes only Spitzer data. Chapter 4 utilizes only PACS data.

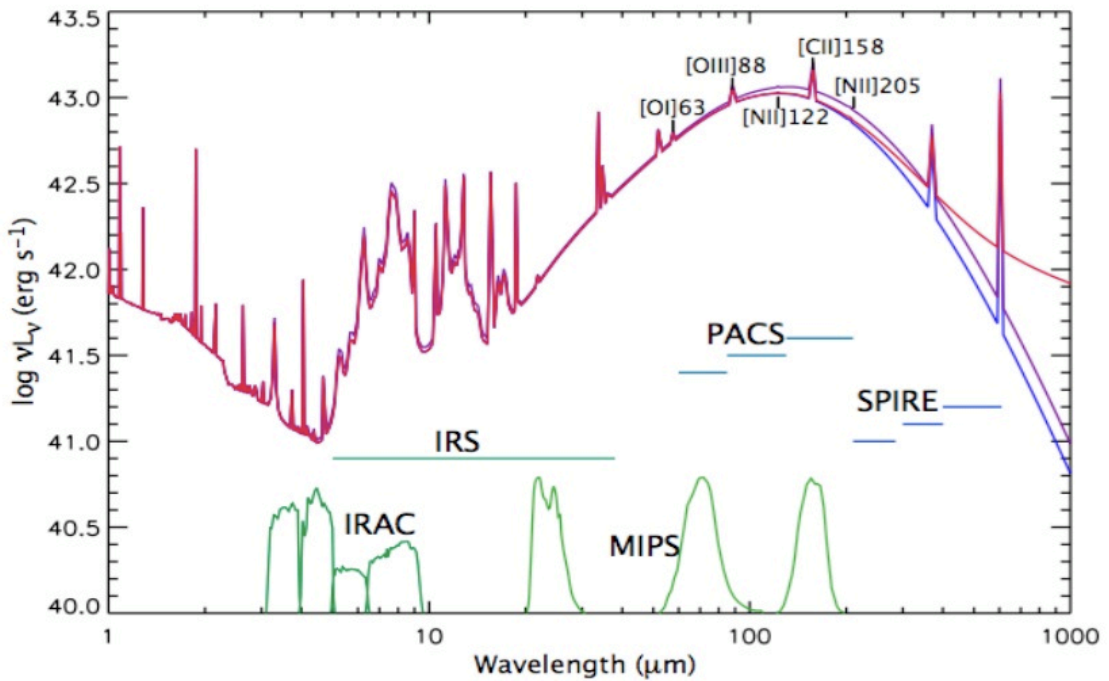


Figure 1.8 Top left: *Herschel* Space Observatory that carried PACS. Top right: *Spitzer* Space Telescope carried IRS. Bottom: Image shows a series of model spectral energy distributions (SEDs) for a star-forming galaxy. Wavelength coverage is indicated for other IR instruments. PACS covers the principal FIR atomic fine structure cooling lines of the ISM: [O I] 63 , [O III] 88 , [N II] 122 , [O I] 145 , and [C II] 158 . Notice that OH 119 falls at the peak sensitivity of PACS.

1.4.1 *Herschel*-PACS

The bulk of the data in this thesis are FIR observations from the *Herschel* Space Observatory (Pilbratt et al., 2010) which carries a 3.5 m diameter Cassegrain

telescope. It is the largest infrared space telescope to have ever been launched. Spectroscopic data was taken with the Photodetector Array Camera and Spectrometer (PACS; [Poglitsch et al., 2010](#)) on board the *Herschel*. PACS covers a field of view of $47'' \times 47''$ with a 5×5 squared spaxel (spatial pixel) integral field unit spectrograph. It has a wavelength dependent spectral resolving power that ranges from $R = 1000 - 4000$ ($\delta v \approx 75 - 300 \text{ km s}^{-1}$). PACS sampled the $\sim 50 - 210 \mu\text{m}$ FIR wavelength range with an unprecedented combination of sensitivity and spatial resolution ($\sim 6 - 11''$; this is about $4\times$ higher than previous infrared space missions). PACS covers the principal FIR fine-structure cooling lines (see bottom panel of [Figure 1.8](#)). Archival *Herschel*-PACS data were retrieved via the Herschel Science Archive (HSA).

1.4.2 *Spitzer*-IRS

Launched in 2003 *The Spitzer Space Telescope* ([Werner et al., 2004](#)), operated by the Jet Propulsion Laboratory and the *Spitzer* Science Center (SSC), incorporates a 0.85 m diameter primary mirror and has a wavelength coverage from 3.6 to $160 \mu\text{m}$. The mid-infrared ($5 - 37 \mu\text{m}$), “high-resolution” ($R \approx 600$) data presented in this thesis were obtained with the Long High (LH) module of the Infrared Spectrograph (IRS; [Houck et al., 2004](#)). The data were retrieved from The Cornell AtlaS of Spitzer/IRS Sources (CASSIS) or from the Spitzer Heritage Archive (SHA).

1.5 Outline of Thesis

This thesis focuses on the study of cool galactic winds in SBs and AGNs. Chapters 2 and 3 focus on the molecular phase in outflows. Chapter 4 is a multiphase study of outflows that looks at the neutral atomic, ionized, and molecular phases of the ISM.

In Chapter 2, we study molecular outflows and inflows in a combined sample of local *Burst Alert Telescope*-detected AGN (BAT AGN)+ULIRGs+QSOs. We measure the wind detection rate in the BAT AGN and compare it with the rate of detection in the higher luminosity ULIRGs+QSOs. We also explore what relationships exist between the properties of the outflows and the properties of their host galaxies. We then perform statistical tests to measure the strength of the correlations.

In Chapter 3, we analyze *Spitzer*-IRS data of 15 U/LIRGs and constrain the OH-to-H abundance ratio, X_{OH} , by taking advantage of the optically thin OH 35 μm transition in the MIR. We compare our value with those in the literature and evaluate the accuracy of radiative transfer models to predict absorption line profile properties.

Chapter 4 explores the multiphase nature of outflows. We analyze *Herschel*–PACS data of seven nearby galaxies with well-known winds. We mainly study the neutral atomic and ionized gas phases, but also include the molecular phase. After delineating the winds from their host galaxy disks, we estimate the spatial (e.g. location, extent, morphology) and kinematic (e.g. radial velocities, $1\text{-}\sigma$ line widths) proper-

ties of the neutral atomic and ionized gas phases in the outflows. We compare our results with data in other wavelengths. We also present the results of the analysis of the molecular gas traced by OH 119 μm .

In Chapter 5, we summarize the main results of each chapter in this thesis and discuss future work.

Chapter 2: Search for Molecular Outflows in Local Volume AGN with *Herschel*-PACS

2.1 Introduction

Massive, galactic-scale outflows driven by star formation and/or active galactic nuclei (AGNs) may be the dominant form of feedback in galaxies (Fabian, 2012; Veilleux et al., 2005). These outflows (or winds) likely affect the evolution of galaxies by regulating star formation and black hole (BH) accretion activity. These winds may shut off the gas feeding process and stop the growth of both the BH and the spheroidal component (Di Matteo et al., 2005), thereby explaining the tight “bulge–BH mass relation” (e.g. Fabian, 2012; Kormendy & Ho, 2013; Kormendy & Richstone, 1995; Marconi & Hunt, 2003). They may also quench star formation altogether and help explain the presence of “red-and-dead,” gas-poor ellipticals, and the bimodal color distribution observed in large galaxy surveys (e.g. Baldry et al., 2004; Strateva et al., 2001). Winds may also be the primary mechanism by which metals are transferred from galaxies to their surrounding halos and, to a lesser extent, to the intergalactic medium.

Table 2.1. *Herschel* Observations of BAT AGN

Name	OBSID	t_{exp} [sec]	Program
(1)	(2)	(3)	(4)
CenA	1342225989	976	OT1_shaileyd_1
Circinus	1342225147	958	OT1_shaileyd_1
ESO 005–G004	1342245457	746	OT2_sveilleu_6
ESO 137–34	1342252089	1452	OT2_sveilleu_6
IC 5063	1342241848	2897	OT2_sveilleu_6
IRAS 04410+2807	1342249997	2897	OT2_sveilleu_6
IRAS 19348–0619	1342241495	1452	OT2_sveilleu_6
MCG–05.23.16	1342245454	14251	OT2_sveilleu_6
MCG–06.30.15	1342247813	14251	OT2_sveilleu_6
Mrk18	1342253541	4309	OT2_sveilleu_6
NGC 1052	1342247734	14251	OT2_sveilleu_6
NGC 1068	1342191154	3944	SHINING target
NGC 1125	1342247722	4309	OT2_sveilleu_6
NGC 1365	1342247546	746	OT2_sveilleu_6
NGC 1566	1342244440	746	OT2_sveilleu_6
NGC 2110	1342250314	2158	OT2_sveilleu_6
NGC 2655	1342246552	1452	OT2_sveilleu_6
NGC 2992	1342246246	746	OT2_sveilleu_6
NGC 3079	1342221391	8045	DDT_esturm_4
NGC 3081	1342245955	2897	OT2_sveilleu_6
NGC 3227	1342197796	2923	GT1_lspinogl_4
NGC 3281	1342248310	746	OT2_sveilleu_6
NGC 3516	1342245980	3128	GT1_lspinogl_6
NGC 3718	1342253721	7129	OT2_sveilleu_6
NGC 3783	1342247816	2897	OT2_sveilleu_6
NGC 4051	1342247512	1452	OT2_sveilleu_6
NGC 4102	1342247002	746	OT2_sveilleu_6
NGC 4138	1342256950	1452	OT2_sveilleu_6
NGC 4151	1342247511	746	OT2_sveilleu_6
NGC 4258	1342257242	746	OT2_sveilleu_6
NGC 4388	1342197911	3453	GT1_lspinogl_4
NGC 4395	1342247533	1452	OT2_sveilleu_6
NGC 4579	1342248535	746	OT2_sveilleu_6
NGC 4593	1342248372	1452	OT2_sveilleu_6
NGC 4939	1342248509	1452	OT2_sveilleu_6
NGC 4941	1342248508	2862	OT2_sveilleu_6
NGC 4945	1342247792	958	OT1_shaileyd_1
NGC 5033	1342247011	746	OT2_sveilleu_6
NGC 5273	1342246800	14251	OT2_sveilleu_6
NGC 5290	1342247535	2158	OT2_sveilleu_6
NGC 5506	1342247811	746	OT2_sveilleu_6
NGC 5728	1342249309	2508	GT1_lspinogl_6
NGC 5899	1342247007	746	OT2_sveilleu_6

Table 2.1 (cont'd)

Name	OBSID	t_{exp} [sec]	Program
(1)	(2)	(3)	(4)
NGC 6221	1342252088	746	OT2_sveilleu.6
NGC 6300	1342253357	746	OT2_sveilleu.6
NGC 6814	1342241849	746	OT2_sveilleu.6
NGC 7172	1342218490	2933	GT1_lspinogl.4
NGC 7213	1342245961	1452	OT2_sveilleu.6
NGC 7314	1342245225	746	OT2_sveilleu.6
NGC 7465	1342245963	1452	OT2_sveilleu.6
NGC 7479	1342258846	746	OT2_sveilleu.6
NGC 7582	1342257273	746	OT2_sveilleu.6

Note. — Column 1: Galaxy name. Column 2: Observation ID. Column 3: Exposure time. Column 4: Program.

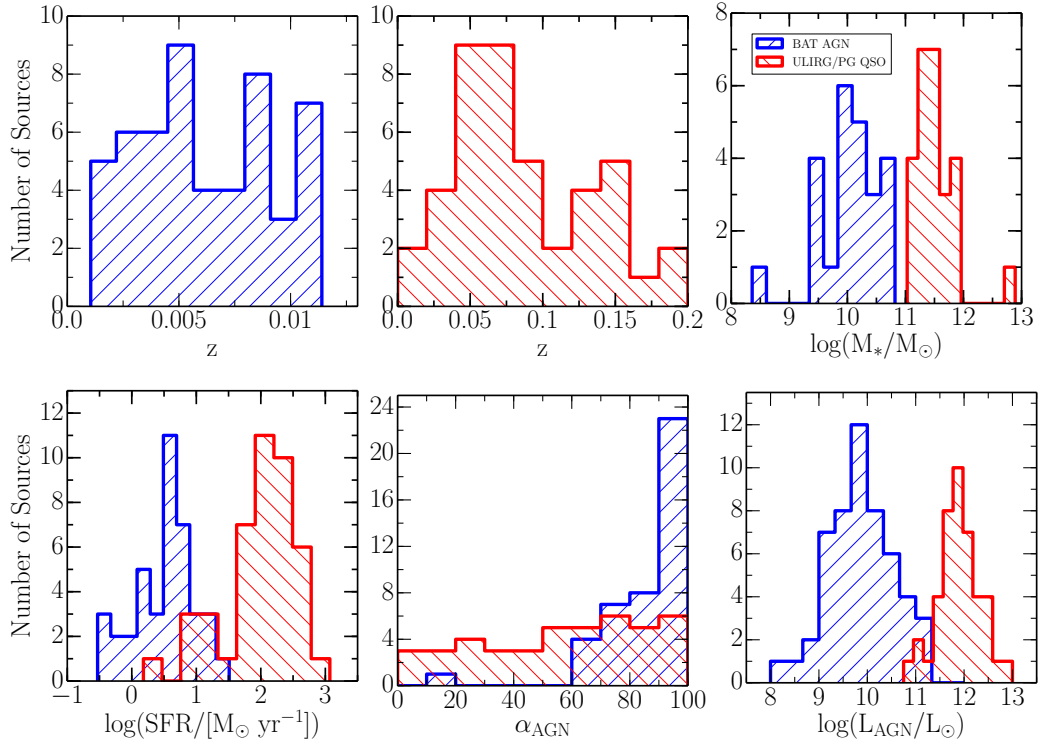


Figure 2.1 Histograms showing the distributions of the BAT AGN and ULIRG/PG QSO properties: redshifts, stellar masses, star formation rates (SFR), AGN fractions, and AGN luminosities.

Until recently, searches for galactic-scale outflows have focused on the brightest sources in bands often affected by obscuration and/or contamination from the host galaxy light (e.g. [Lehnert & Heckman, 1996](#)). These searches have generally been directed at either the ionized phase (e.g. [Crenshaw et al., 1999](#); [Dunn et al., 2008](#); [Rubin et al., 2010](#)) or the neutral phase (e.g. [Heckman et al., 2000](#); [Krug et al., 2010](#); [Martin, 2005](#); [Rupke et al., 2005a,b,c](#); [Rupke & Veilleux, 2011, 2013](#); [Schwartz & Martin, 2004](#)) of the ISM. If winds are to inhibit star formation in the host galaxy, then the mass outflow must affect the phase of the ISM from which stars form (i.e. the cold molecular gas). Our knowledge of molecular outflows is quickly improving. Recent studies of galactic-scale winds have effectively demonstrated that far infrared (FIR) spectroscopy of the hydroxyl molecule (OH) with *Herschel*-PACS is well suited to identify molecular outflows in the nearby universe ([Spoon et al., 2013](#); [Sturm et al., 2011](#); [Veilleux et al., 2013](#), hereafter, S11, V13, and S13 respectively). S11 reported preliminary evidence of a correlation between AGN luminosity (L_{AGN}) and OH terminal velocity in six ultra-luminous infrared galaxies (ULIRGs; i.e. ULIRGs with higher terminal velocities hosted AGNs with higher luminosities). V13 and S13 later confirmed this correlation via the analyses of larger samples (43 and 24 ULIRGs, respectively). In particular, V13 reported a nonlinear relationship between $\log(L_{AGN}/L_{\odot})$ and outflow velocity, but noted that better statistics were required at lower AGN luminosities in order to confirm this nonlinearity. These *Herschel*-based studies, supplemented with millimeter-wave, interferometric studies, have also shown that the molecular gas often dominates the mass and energy budget of these outflows (e.g. [Alatalo et al., 2011](#); [Cicone et al., 2014](#); [Feruglio et al., 2010](#); [Fischer](#)

et al., 2010; González-Alfonso et al., 2014b; Morganti et al., 2013; Sturm et al., 2011; Veilleux et al., 2013).

There is thus a clear need to extend this type of study to lower AGN luminosities and star formation rates (SFRs). For this, we examine *Herschel* observations of a complete sample of local *Swift*-BAT selected AGNs. Since stellar processes contribute negligibly to the 14-195 keV emission, the Burst Alert Telescope detected active galactic nucleus (BAT AGN) survey is not sensitive to star formation activity within the host galaxy. Additionally, this survey is unbiased to column densities of $N_H \lesssim 10^{24} \text{ cm}^{-2}$. The characteristics and host galaxy properties of these ultra-hard X-ray detected BAT AGNs have been studied extensively across most wavelengths (e.g. Koss et al., 2013, 2011; Matsuta et al., 2012; Meléndez et al., 2014; Mushotzky et al., 2014; Shimizu et al., 2016, 2015; Vasudevan & Fabian, 2009; Vasudevan et al., 2010; Winter et al., 2012). By combining the results of our analysis on 52 BAT AGNs with those of V13 on 43 ULIRGs, we extend the range of AGN luminosities, SFRs, and stellar masses sampled in this study by 1-2 orders of magnitude, from which we can draw stronger statistical conclusions on the driving mechanisms of these outflows. We also examine mid-infrared (MIR; 5–37 μm) spectra from the Infrared Spectrograph (IRS) on board the *Spitzer Space Telescope* of the combined BAT AGN + ULIRG + PG QSO sample in an attempt to constrain the distributions of the dust, as measured by the strength of the 9.7 μm silicate feature, and OH gas within these systems. We note that although robust, statistical conclusions can only be drawn from a well-defined sample, valuable insight into molecular winds may still be obtained by combining these two samples which are distinct in their

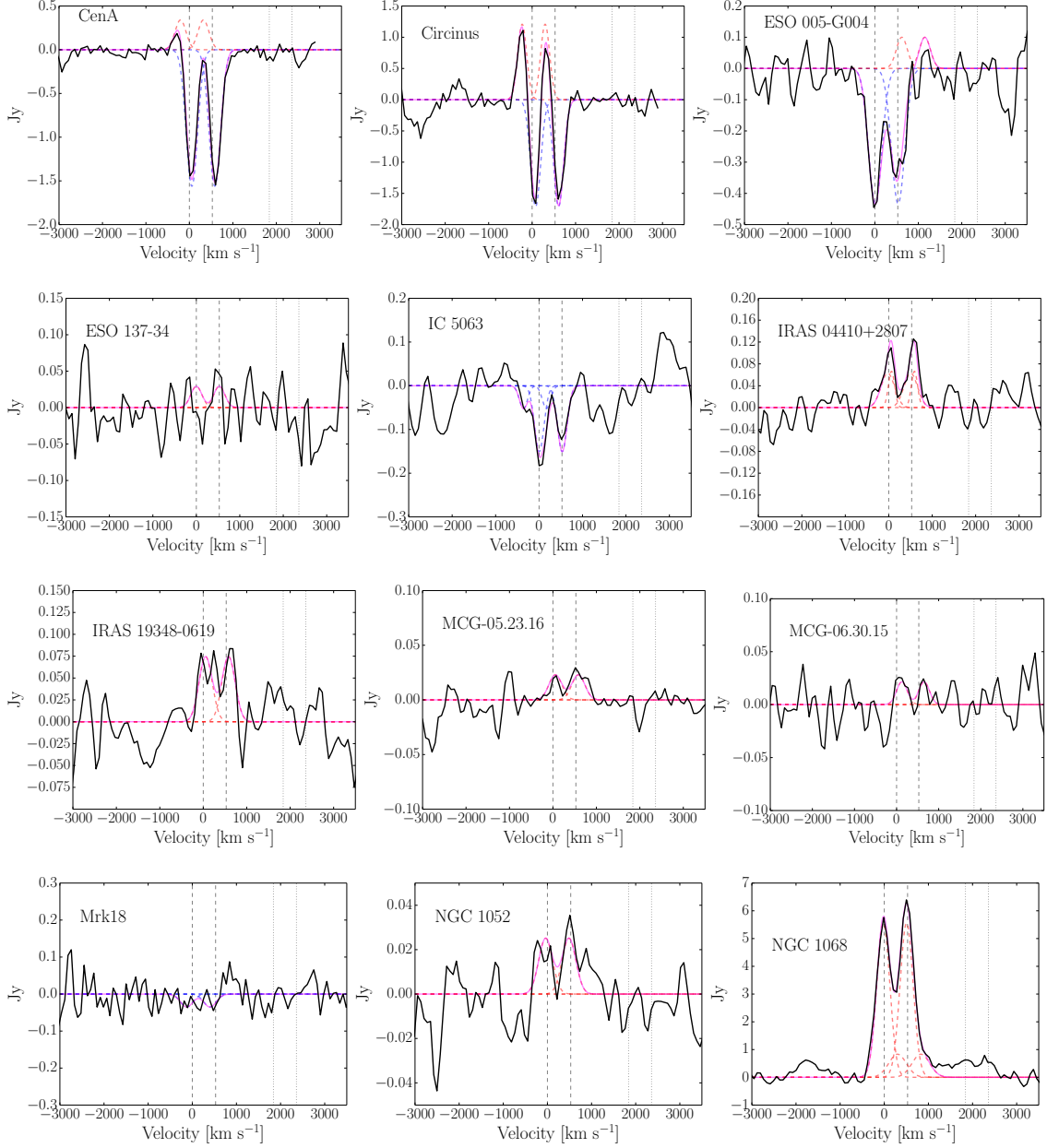


Figure 2.2 Fits to the central spaxel, continuum subtracted OH 119 μm profiles of the 52 objects in our sample; see Section 2.5.1.3. In each figure, the solid black line represents the data and the magenta line is the best fit to the data. The blue and red dashed lines represent the Gaussian components of the fits. The origin of the velocity scale corresponds to OH 119.233 μm at the systemic velocity. The two vertical dashed and dotted lines mark the positions of ^{16}OH and ^{18}OH , respectively.

selection methods and in their properties.

The samples used in this analysis are described in Section 2. The observations

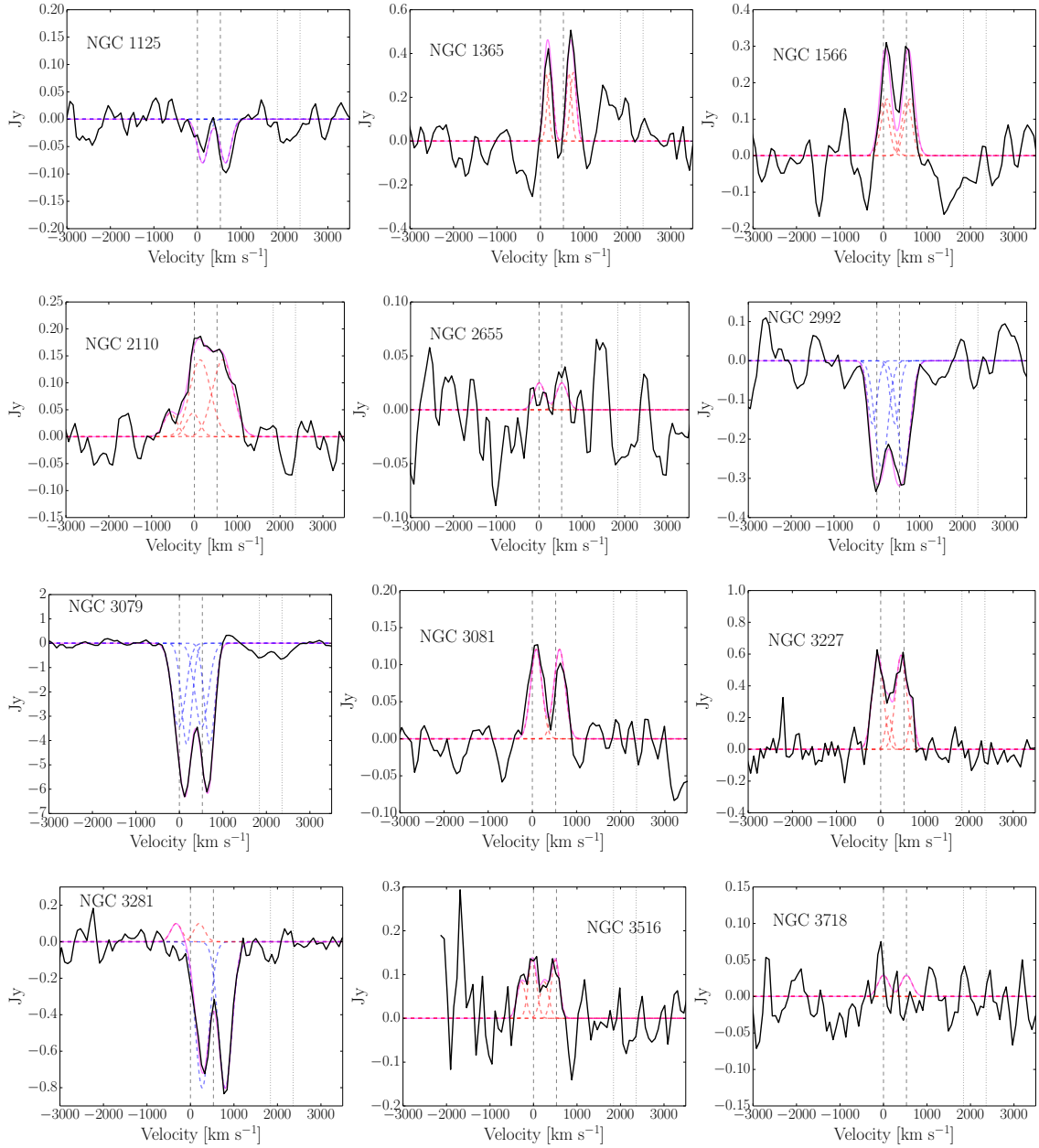


Figure 2.2 (Continued)

and data reduction techniques are outlined in Section 3. The results of the analysis are presented in Section 4, while the implications of these results are reported in Section 5. The conclusions are summarized in Section 6.

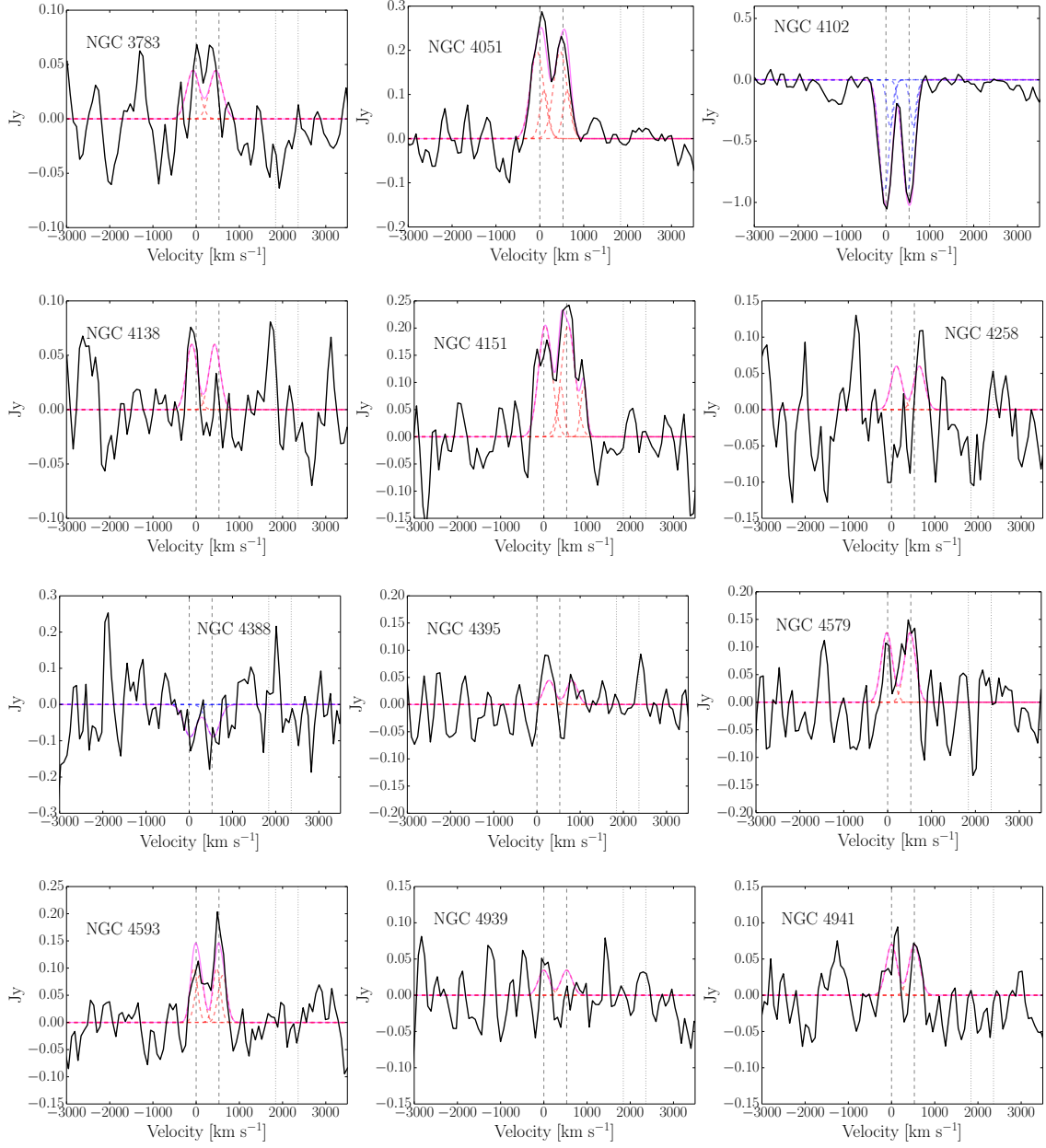


Figure 2.2 (Continued)

2.2 BAT AGN Sample Selection

The BAT AGN in our sample were selected using three criteria: (1) all targets are from the very hard X-ray selected (14-195 keV) 58-month *Swift*-BAT Survey (Baumgartner et al., 2011) of local AGN. Since the 14-195 keV flux is solely produced

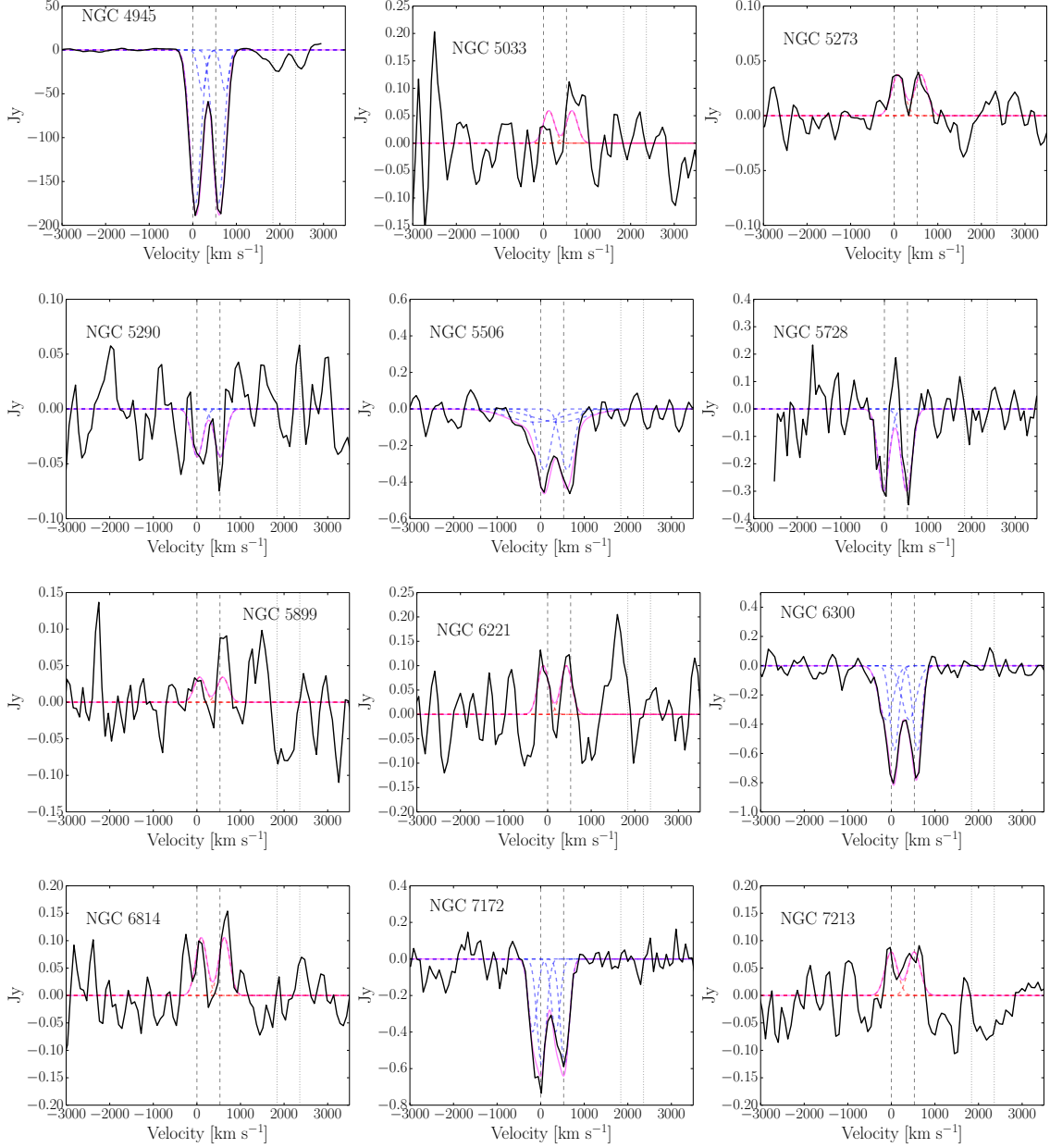


Figure 2.2 (Continued)

by the AGN and unaffected by the host galaxy light or obscuration along the line-of-sight ($N_H \lesssim 10^{24} \text{ cm}^{-2}$, this criterion removes any ambiguity as to the power of the AGN. Thus, the *Swift*-BAT survey is arguably superior to soft X-ray, UV, optical, IR, or radio surveys for understanding the role of AGN-driven winds in galaxies. (2) All targets have a total integrated flux at $120 \mu\text{m}$ of $S_{120}^{\text{tot}} \gtrsim 1 \text{ Jy}$ so

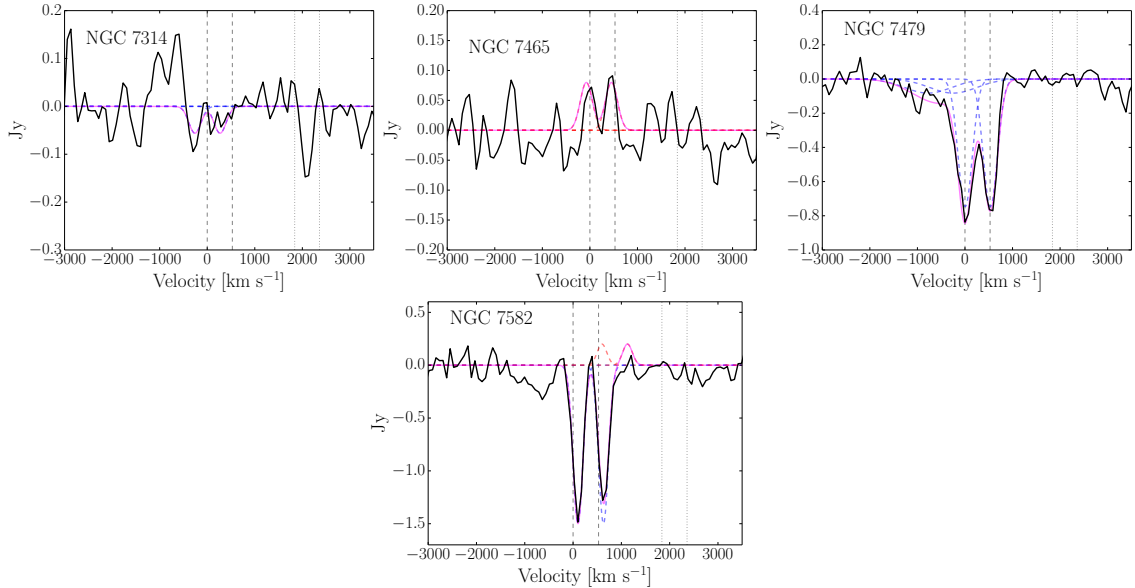


Figure 2.2 (Continued)

that high S/N in the continuum can be reached in a reasonable amount of time with PACS. (3) Finally, all targets are located within 50 Mpc. The low redshifts in this sample provide the best possible scale ($\sim 0.02\text{-}0.2$ kpc arcsec $^{-1}$) for spatially separating star-formation emission from the nuclear component. This distance is also large enough to properly sample the AGN luminosity function up to quasar-like values ($\log L_{\text{BAT}} \sim 43.5$; $\log L_{\text{BOL}} \sim 45$), without favoring IR-bright systems due to criterion #2.

We find that 52 targets meet these three requirements. Of these targets, 42 objects are from the cycle 2 open-time program OT2_sveilleu_6 (PI: S. Veilleux), 3 objects are from the guaranteed time program GT1_lspinogl_4 (PI: L. Spinoglio), 2 objects are from the guaranteed time program GT1_lspinogl_6 (PI: L. Spinoglio), 3 objects are from the cycle 1 open-time program OT1_shaileyd_1 (PI: S. Hailey-Dunsheath), 1 object is from the Director’s Discretionary Time DDT_esturm_4 (PI:

E. Sturm), and 1 object is from the guaranteed time key program Survey with Herschel of the ISM in Nearby Infrared Galaxies (SHINING; PI: E. Sturm) (see [Table 2.1](#)).

Table 2.2. Galaxy Properties

(Name)	z	Distance (Mpc)	α_{AGN} (%)	$\log L_{\text{AGN}}$ (L_{\odot})	$\log M_{*}$ (M_{\odot})	$\log \text{SFR}$ ($M_{\odot} \text{ yr}^{-1}$)	$f_{\text{cen}}/f_{\text{tot}}$	$f_{30\mu\text{m}}/f_{15\mu\text{m}}$	Type
(1)	(2)	(3)	(4)	(5)	(6)	(7)	(8)	(9)	(10)
CenA	0.001901 ^a	3.7	93.2	9.78	0.14	2.44	Type 2
Circinus	0.001573 ^a	4.2	86.6	9.19	0.22	3.32	Type 1
ESO 005–G004	0.006379 ^b	22.4	89.4	9.73	...	0.72	0.15	2.95	Type 2
ESO 137–34	0.009144	33	...	9.99	...	0.5	0.2	...	Type 2
IC 5063	0.011198 ^c	49	93.3	10.75	...	0.61	0.38	2.43	Type 2
IRAS 04410+2807	0.011268	48.7	...	10.61	...	0.43	0.37	...	Type 2
IRAS 19348–0619	0.010254	44.3	...	10.17	...	0.66	0.29	...	Type 1
MCG–05.23.16	0.008486	36.6	96.9	10.94	9.56	–0.53	0.59	1.97	Type 2
MCG–06.30.15	0.007749	33.4	99.9	10.36	...	–0.4	0.57	1.60	Type 1
Mrk18	0.011345 ^d	47.9	79.0	9.96	9.57	0.41	0.48	4.40	Type 2
NGC 1052	0.005037	19.5	95.7	9.56	10.35	...	0.46	2.12	Type 2
NGC 1068	0.003931 ^a	12.7	100	9.26	0.14	1.20	Type 2
NGC 1125	0.010931	47.2	60.8	10.1	...	0.39	0.42	7.31	Type 2
NGC 1365	0.005349 ^a	17.9	75.3	9.82	...	1.51	0.18	4.96	Type 1
NGC 1566	0.005017	12.2	...	9.01	0.21	...	Type 1
NGC 2110	0.007789	35.6	94.0	11.11	10.63	0.49	0.43	2.34	Type 2
NGC 2655	0.00467	24.4	91.8	9.41	...	–0.1	0.25	2.63	Type 2
NGC 2992	0.00771	31.6	92.1	9.94	10.31	0.75	0.38	2.59	Type 2
NGC 3079	0.003797 ^d	19.1	68.7	9.59	9.98	1.22	0.29	5.99	Type 2
NGC 3081	0.007976	26.5	93.8	10.27	10.31	0.12	0.35	2.37	Type 2
NGC 3227	0.004001 ^a	18.7	88.6	10.09	9.98	0.55	0.33	3.05	Type 1
NGC 3281	0.010674	46.1	92.7	10.77	10.24	0.84	0.46	2.51	Type 2
NGC 3516	0.008889 ^e	52.5	95.5	11.02	10.46	0.19	0.44	2.15	Type 1
NGC 3718	0.003312	17	...	9.05	9.98	–0.3	0.23	...	LINER
NGC 3783	0.009791 ^f	47.8	95.2	11.12	...	0.68	0.11	2.19	Type 1

Table 2.2 (cont'd)

(Name)	z	Distance (Mpc)	α_{AGN} (%)	$\log L_{\text{AGN}}$ (L_{\odot})	$\log M_{\star}$ (M_{\odot})	$\log \text{SFR}$ ($M_{\odot} \text{ yr}^{-1}$)	$f_{\text{cen}}/f_{\text{tot}}$	$f_{30\mu\text{m}}/f_{15\mu\text{m}}$	Type
(1)	(2)	(3)	(4)	(5)	(6)	(7)	(8)	(9)	(10)
NGC 4051	0.002490 ^a	14.3	95.2	9.41	9.44	0.57	0.34	2.19	Type 1
NGC 4102	0.002823	20.4	61.7	9.57	9.68	1.02	0.51	7.15	LINER
NGC 4138	0.002962	20.7	99.3	9.62	9.61	0.04	0.05	1.67	Type 1
NGC 4151	0.003502 ^a	9.9	100	10.23	...	-0.38	0.24	1.48	Type 1
NGC 4258	0.001494	7.5	98.4	8.59	0.07	1.79	Type 2
NGC 4388	0.008467 ^a	21	84.3	10.6	10.53	0.58	0.14	3.64	Type 2
NGC 4395	0.001064	4.5	72.7	8.21	8.28	...	0.1	5.34	Type 1
NGC 4579	0.00506	19.6	...	9.11	0.21	...	Type 2
NGC 4593	0.008455 ^a	30.8	76.5	10.43	10.75	...	0.4	4.78	Type 1
NGC 4939	0.010374	44.8	90.2	10.21	...	0.82	0.06	2.84	Type 2
NGC 4941	0.003707 ^d	18.7	89.5	9.36	...	-0.19	0.22	2.93	Type 2
NGC 4945	0.001836 ^g	4.1	10.4	9.18	0.41	18.96	Type 2
NGC 5033	0.003211 ^a	19.6	...	8.84	...	0.95	0.1	...	Type 1
NGC 5273	0.003619	16	77.4	9.06	9.64	...	0.55	4.64	Type 1
NGC 5290	0.008583	35	...	9.88	10.23	0.62	0.12	...	Type 2
NGC 5506	0.006228 ^a	23.8	93.3	10.64	10.02	0.25	0.52	2.43	Type 1
NGC 5728	0.009475 ^a	30.6	70.4	10.43	10.78	0.78	0.41	5.71	Type 2
NGC 5899	0.008546	38.1	91.0	9.97	10.28	0.95	0.13	2.73	Type 2
NGC 6221	0.004999	12.2	65.4	8.99	...	0.76	0.24	6.53	Type 2
NGC 6300	0.003699	14.4	87.0	9.82	...	0.63	0.31	3.27	Type 2
NGC 6814	0.005214	22.8	98.0	10.11	10.3	0.6	0.05	1.83	Type 1
NGC 7172	0.009180 ^e	33.9	92.4	10.8	...	0.83	0.24	2.54	Type 2
NGC 7213	0.005983 ^d	22	100	9.82	...	0.25	0.12	1.46	Type 1
NGC 7314	0.004839 ^h	18.6	89.0	9.77	10.06	...	0.13	3.00	Type 1
NGC 7465	0.006666 ⁱ	27.2	...	9.54	...	0.21	0.35	...	Type 2

Table 2.2 (cont'd)

(Name)	z	Distance (Mpc)	α_{AGN} (%)	$\log L_{\text{AGN}}$ (L_{\odot})	$\log M_{*}$ (M_{\odot})	$\log \text{SFR}$ ($M_{\odot} \text{ yr}^{-1}$)	$f_{\text{cen}}/f_{\text{tot}}$	$f_{30 \mu\text{m}}/f_{15 \mu\text{m}}$	Type
(1)	(2)	(3)	(4)	(5)	(6)	(7)	(8)	(9)	(10)
NGC 7479	0.007942	33.9	83.7	9.88	...	1.14	0.37	3.73	Type 2
NGC 7582	0.005541 ^j	20.9	73.8	10.06	...	1.2	0.49	5.18	Type 2

^aRedshift is calculated using the [OI] 63.18 μm , [OI] 145.53 μm , [CII] 157.74 μm , and [NII] 121.90 μm emission lines.

^bRedshift is calculated using the [OI] 145.53 μm emission line.

^cRedshift is calculated using the [OI] 63.18 μm and [CII] 157.74 μm emission lines.

^dRedshift is calculated using the [CII] 157.74 μm emission line.

^eRedshift is calculated using the [CII] 157.74 μm and [NII] 121.90 μm emission lines.

^fRedshift is calculated using the [OI] 63.18 μm and [OI] 145.53 μm emission lines.

^gRedshift is calculated using the [OI] 63.18 μm , [OI] 145.53 μm , and [CII] 157.74 μm emission lines.

^hRedshift is calculated using the [OI] 145.53 μm and [CII] 157.74 μm emission lines.

ⁱRedshift is calculated using the [OI] 63.18 μm , [CII] 157.74 μm , and [NII] 121.90 μm emission lines.

^jRedshift is calculated using the [OI] 14.53 μm , [CII] 157.74 μm , and [NII] 121.90 μm emission lines.

Note. — Column 1: Galaxy name. Column 2: Redshift value (When available, redshift is calculated from emission lines. Otherwise, redshifts are from NED). Column 3: When available mean, redshift-independent distance is obtained from NED. Otherwise, the luminosity distance is calculated via [Wright \(2006\)](#). Column 4: α_{AGN} , fractional contribution of the AGN to the bolometric luminosity; see [Section 2.4](#). Column 5: AGN luminosity. Column 6: stellar masses are adopted from [Koss et al. \(2011\)](#). Column 7: star formation rate; see [Section 2.4](#). Column 8: Continuum flux density ratio at 119 μm of the central spaxel to all 25 spaxels. For reference, the average continuum ratio for a point source calculated from the five PG QSOs in our ULIRG sample is $f_{\text{cen}}/f_{\text{tot}} = 0.56$. Column 9: 30 μm to 15 μm continuum flux density ratio. Column 10: Spectral type.

2.3 ULIRG and PG QSO Sample

We include in our analysis the *Herschel*/PACS spectra of the ULIRGs and PG QSOs from V13. Of the 43 objects (38 ULIRGs + 5 QSOs) from that sample, 23 targets are from the key program SHINING (PI: E. Sturm), 15 targets are from the cycle 1 open-time program OT1_sveilleu_1 (PI: S. Veilleux), and 5 are from the cycle 2 open-time program OT2_sveilleu_4 (PI: S. Veilleux).

This sample spans a broad range of merger stages. 20 objects are cool ($f_{25}/f_{60} \leq 0.2$) pre-merger ULIRGs, 18 objects are warm ($f_{25}/f_{60} > 0.2$) quasar-dominated, late-stage, fully coalesced ULIRGs, and 5 objects are “classic” IR-faint QSOs. These QSOs are in a late merger phase in which the quasar has finally shed its natal “cocoon” of dust and gas and feedback effects may be receding (Veilleux et al., 2009, V13)

2.4 Properties of the Sample Galaxies

The properties of our BAT AGN sample are listed in Table 2.2. The notes to Table 2.2 briefly explain the meaning of each of these quantities. Some quantities, however, require further clarification. We apply the bolometric correction from Winter et al. (2012) to our BAT AGN luminosities, which are derived from the fluxes from the *Swift* BAT 70-month survey. Since the *Swift*-BAT bandpass is at high enough energies (14-195 keV) to be unaffected by all but the highest levels of obscuration, the luminosities in this bandpass should be the direct unobscured

signature from the AGN. Thus, it is assumed to be a good proxy for the bolometric luminosity of the AGN. The correction is a scale factor derived from the correlation between the bolometric luminosity, which is determined from simultaneous broad-band fitting of the spectral energy distribution of 33 sources in the optical, UV, and X-ray (Vasudevan & Fabian, 2007, 2009), and the *Swift* BAT band 14-195 keV luminosities of those sources. The ordinary least-squares line through these data of Winter et al. (2012) yields the following correction:

$$L_{\text{AGN}} = 10.5 \times L_{14-195\text{keV}}, \quad (2.1)$$

where L_{AGN} is the bolometric luminosity of the AGN and $L_{14-195\text{keV}}$ is the *Swift* BAT luminosity in the 14-195 keV band.

For the ULIRGs, we adopt the starburst and AGN luminosities from V13, which were calculated as follows: the bolometric luminosities were estimated to be $L_{\text{BOL}} = 1.15 L_{\text{IR}}$, where L_{IR} is the infrared luminosity over 8 – 1000 μm (Sanders & Mirabel, 1996), and $L_{\text{BOL}} = 7L(5100 \text{ \AA}) + L_{\text{IR}}$ for the PG QSOs (Netzer et al., 2007). Here, $L(5100 \text{ \AA})$ corresponds to λL_{λ} at 5100 \AA .

The starburst and AGN luminosities were next calculated from

$$L_{\text{BOL}} = L_{\text{AGN}} + L_{\text{SB}} \quad (2.2)$$

$$= \alpha_{\text{AGN}} L_{\text{BOL}} + L_{\text{SB}}, \quad (2.3)$$

where α_{AGN} is the fractional contribution of the AGN to the bolometric luminosity,

hereafter called the ‘‘AGN fraction’’ for short. For the BAT AGN sample, we derive the AGN fractions from the rest frame $f_{30\mu m}/f_{15\mu m}$ continuum flux density ratio, which was found by [Veilleux et al. \(2009\)](#) to be more tightly correlated with the PAH-free, silicate-free MIR/FIR ratio and the AGN contribution to the bolometric luminosity than any other *Spitzer*-derived continuum ratio. The fraction of the $15\mu m$ flux produced by the AGN is defined as:

$$\begin{aligned} \frac{\text{AGN}\%(f_{15})}{100} &\equiv \frac{(f_{30}/f_{15})_{agn}}{(f_{30}/f_{15})_{agn} + (f_{30}/f_{15})_{sb}} \\ &= \frac{(f_{30}/f_{15})_{obs} - (f_{30}/f_{15})_{sb}}{(f_{30}/f_{15})_{agn} - (f_{30}/f_{15})_{sb}}, \end{aligned} \tag{2.4}$$

where $(f_{30}/f_{15})_{obs}$ is the observed flux density ratio. $(f_{30}/f_{15})_{agn}$ and $(f_{30}/f_{15})_{sb}$ are the flux density ratios due to the AGN and starburst, respectively. We adopt from Table 9 of [Veilleux et al. \(2009\)](#) the zero-point values of $\log (f_{30}/f_{15})_{agn} = 0.2$ and $\log (f_{30}/f_{15})_{sb} = 1.35$.

Table 2.3. Properties of the OH 119 μm Profiles

(Name)	v_{50} (abs) (km s^{-1})	v_{84} (abs) (km s^{-1})	Flux_{abs} (Jy km s^{-1})	EQW_{abs} (km s^{-1})	v_{50} (emi) (km s^{-1})	v_{84} (emi) (km s^{-1})	Flux_{emi} (Jy km s^{-1})	EQW_{emi} (km s^{-1})	$\text{EQW}_{\text{Total}}$ (km s^{-1})
(1)	(2)	(3)	(4)	(5)	(6)	(7)	(8)	(9)	(10)
CenA	63	195	521.1	27	-201:	-327:	-107.9	-6	21
Circinus	81	201	494.3	8	-225	-327:	-313.9:	-5:	3
ESO 005-G004	9	-141	167.1	70	622	754	-32	-14	55
ESO 137-34	-9.4	-14	-14
IC 5063	-33::	-309::	53.7:	16	16
IRAS 04410+2807	21::	135::	-36.8::	-37::	-37::
IRAS 19348-0619	57	207	-28.5	-25:	-25:
MCG-05-23-016	57::	207::	-8.6::	-21::	-21::
MCG-06-30-015	129::	255::	-6.9::	-8::	-8::
Mrk 18	12.4:	6:	6
NGC 1052	-39::	117::	-9.9::	-27::	-27::
NGC 1068	15	213	-2479.1	-70	-70
NGC 1125	123:	-3:	24.8:	20	20
NGC 1365	177:	267:	-104.8:	-4:	-4:
NGC 1566	51	177	-93.6	-36	-36
NGC 2110	75	351	-103.9	-38	-38
NGC 2655	9::	135::	-8::	-9::	-9::
NGC 2992	45	-129	146.9	33	33
NGC 3079	87	-93	2580.2	119	119
NGC 3081	93	219	-38.7	-33	-33
NGC 3227	-27	147	-225.3	-53	-53
NGC 3281	273	429	313.9	99	-321	-453	-32	-10	-86
NGC 3516	-99	39	-52.4	-78	-78
NGC 3718	-9.3:	-15:	-15:
NGC 3783	-69::	81::	-16.8::	-33::	-33::

Table 2.3 (cont'd)

(Name)	v_{50} (abs) (km s ⁻¹)	v_{84} (abs) (km s ⁻¹)	Flux _{abs} (Jy km s ⁻¹)	EQW _{abs} (km s ⁻¹)	v_{50} (emi) (km s ⁻¹)	v_{84} (emi) (km s ⁻¹)	Flux _{emi} (Jy km s ⁻¹)	EQW _{emi} (km s ⁻¹)	EQW _{Total} (km s ⁻¹)
(1)	(2)	(3)	(4)	(5)	(6)	(7)	(8)	(9)	(10)
NGC 4051	-9:	141:	-102.2:	-57:	-57:
NGC 4102	-3	-135	343.4	12:	12:
NGC 4138	-99::	33::	-19.2::	-81::	-81::
NGC 4151	75	333:	-96.7	-82	-82
NGC 4258	-19.2	-18	-18
NGC 4388	32.7	18	18
NGC 4395	-14.2::	-254::	-254::
NGC 4579	-15::	111::	-40.3::	-36::	-36::
NGC 4593	15	141	-44.4	-26:	-26:
NGC 4939	-11.1	-45	-45
NGC 4941	3::	129::	-22.4::	-40::	-40::
NGC 4945	87	-51	66839.9	171	171
NGC 5033	-15.1	-4	-4
NGC 5273	87:	231:	-13.6:	-30:	-30:
NGC 5290	9::	-117::	14::	25::	25::
NGC 5506	45::	-357::	234:	59:	59:
NGC 5728	-15::	-141::	96::	20::	20::
NGC 5899	-11:	-15:	-15:
NGC 6221	-99::	33::	-32::	-4::	-4::
NGC 6300	-3	-201	301.5	70	70
NGC 6814	105::	231::	-33.8::	-82::	-82::
NGC 7172	-51:	-207::	252.6	85	85
NGC 7213	-3::	141::	-28.3::	-42::	-42::
NGC 7314	18	24	24
NGC 7465	-69::	57::	-25.6::	-13::	-13::

Table 2.3 (cont'd)

(Name)	v_{50} (abs) (km s ⁻¹)	v_{84} (abs) (km s ⁻¹)	Flux _{abs} (Jy km s ⁻¹)	EQW _{abs} (km s ⁻¹)	v_{50} (emi) (km s ⁻¹)	v_{84} (emi) (km s ⁻¹)	Flux _{emi} (Jy km s ⁻¹)	EQW _{emi} (km s ⁻¹)	EQW _{Total} (km s ⁻¹)
(1)	(2)	(3)	(4)	(5)	(6)	(7)	(8)	(9)	(10)
NGC 7479	-51	-658::	379.6	73	73
NGC 7582	105	3	383.6	13	604:	700::	-50.1::	-2	11

Note. — Column 1: galaxy name. Column 2: v_{50} (abs) is the median velocity of the fitted absorption profile *i.e.* 50% of the absorption takes place at velocities above - more positive than - v_{50} . Column 3: v_{84} (abs) is the velocity above which 84% of the absorption takes place. Column 4: the total integrated flux for the absorption component(s). Column 5: the total equivalent width for the absorption component(s). Column 6: v_{50} (emi) is the median velocity of the fitted emission profile. Column 7: v_{84} (emi) is the velocity below which 84% of the emission takes place. Column 8: the total integrated flux for the emission component(s). Column 9: the total equivalent width for the emission component(s). Column 10: The total equivalent width for the sum of the two components for one line of the OH doublet. Fluxes followed by a colon indicate uncertainties between 20% and 50%. Velocities followed by a colon indicate uncertainties between 50 – 150 km s⁻¹. Fluxes followed by a double colon indicate uncertainties > 50%. Velocities followed by a double colon indicate uncertainties > 150 km s⁻¹.

The fraction of the bolometric luminosity produced by the AGN is then calculated from:

$$\begin{aligned} \alpha_{\text{AGN}} &\equiv \frac{\text{AGN}(L_{\text{bol}})}{100} = \frac{L(\text{bol})^{\text{agn}}}{L(\text{bol})^{\text{agn}} + L(\text{bol})^{\text{sb}}} \\ &= \frac{1}{1 + \left[\frac{100}{\text{AGN}\% (f_{15})} - 1 \right] \left[\frac{(L_{\nu}(15 \mu\text{m})/L(\text{bol}))_{\text{agn}}}{(L_{\nu}(15 \mu\text{m})/L(\text{bol}))_{\text{sb}}} \right]} \end{aligned} \quad (2.5)$$

where we adopt the bolometric corrections of

$$\log [L_{\nu}(15 \mu\text{m})/L(\text{bol})]_{\text{agn}} = -14.33$$

$$\log [L_{\nu}(15 \mu\text{m})/L(\text{bol})]_{\text{sb}} = -14.56$$

from Table 10 of [Veilleux et al. \(2009\)](#). As a check, we compare the AGN fractions derived via this method with those found in [Tommasin et al. \(2010\)](#). For the few objects in common (i.e. NGC 1125, NGC 3516, NGC 4388, NGC 7172, and NGC 7582), we find good agreement between the two methods. For the ULIRGs and QSOs, we adopt the AGN fractions from V13 which are calculated using the same method applied to the BAT AGN.

BAT AGN stellar masses are adopted from [Koss et al. \(2011\)](#). ULIRG stellar masses are calculated by adopting H -band absolute magnitudes from V13. We then assume $M_H^* = -23.7$ (the H -band absolute magnitude of a L^* galaxy in a Schechter function description of the local field galaxy luminosity function ([Bell & de Jong, 2001](#); [Cole et al., 2001](#))) and $m_* = 1.4 \times 10^{11} M_{\odot}$ (the mass of an early-type galaxy

at the knee of the Schechter distribution (Cole et al., 2001; Veilleux et al., 2002)).

BAT AGN SFRs are derived from equation [25] of Calzetti et al. (2010):

$$\text{SFR}(160)(M_{\odot} \text{ yr}^{-1}) = \frac{L(160) [\text{erg s}^{-1}]}{4.8 \times 10^{42}}, \quad (2.6)$$

where $L(160)$ is λL_{λ} at $160 \mu\text{m}$ and the factor 4.8×10^{42} assumes a Kennicutt (1998) calibration for SFR. SFRs for ULIRGs and PG QSOs are calculated from equation [1] of Rupke et al. (2005b):

$$\text{SFR} = \frac{L_{\text{SB}}}{5.8 \times 10^9 L_{\odot}}, \quad (2.7)$$

where $L_{\text{SB}} = L_{\text{BOL}}(1 - \alpha_{\text{AGN}})$.

Table 2.1 shows the distributions of redshifts, stellar masses, SFRs, AGN fractions, and AGN luminosities for all 52 BAT AGN in our sample (blue diagonals) and for all 43 objects (38 ULIRGs + 5 PG QSOs; red diagonals) from V13. The AGN fractions of the BAT AGN are typically higher than the fractions of the V13 sample of objects. The AGN luminosities and SFRs of the BAT AGN, however, are typically lower by two orders of magnitude than those of the ULIRGs and QSOs.

2.5 Observations, Data Reduction, and Spectral Analysis

2.5.1 OH 119 μm Feature

2.5.1.1 OH Observations

The OH observations were obtained with the PACS FIR spectrometer (Poglitsch et al., 2010) on board *Herschel* (Pilbratt et al., 2010). We focus our efforts on the ground-state OH 119 μm ${}^2\Pi_{3/2} J = 5/2 - 3/2$ rotational Λ -doublet. This feature is the strongest transition in ULIRGs and is positioned near the peak spectroscopic sensitivity of PACS. Fischer et al. (2010), S11, and V13 have demonstrated the efficacy of using the OH 119 μm feature to determine wind characteristics.

The data for OT2_sveilleu_6 were obtained in a similar fashion as those in SHINING (S11) and OT1_sveilleu_1 (V13). PACS was used in range scan spectroscopy mode in high sampling centered on the redshifted OH 119 μm + ${}^{18}\text{OH}$ 120 μm complex with a velocity range of $\sim \pm 4000 \text{ km s}^{-1}$ (rest-frame 118-121 μm) to provide enough coverage on both sides of the OH complex for reliable continuum placement. As a result, the PACS spectral resolution is $\sim 270 \text{ km s}^{-1}$. The total amount of observation time (including overheads) for OT2_sveilleux_6 was 35.3 hours. The program ID and observing time for each target, including all overheads, are listed in Table 2.2. A large chopper throw of $3'$ is used in all cases.

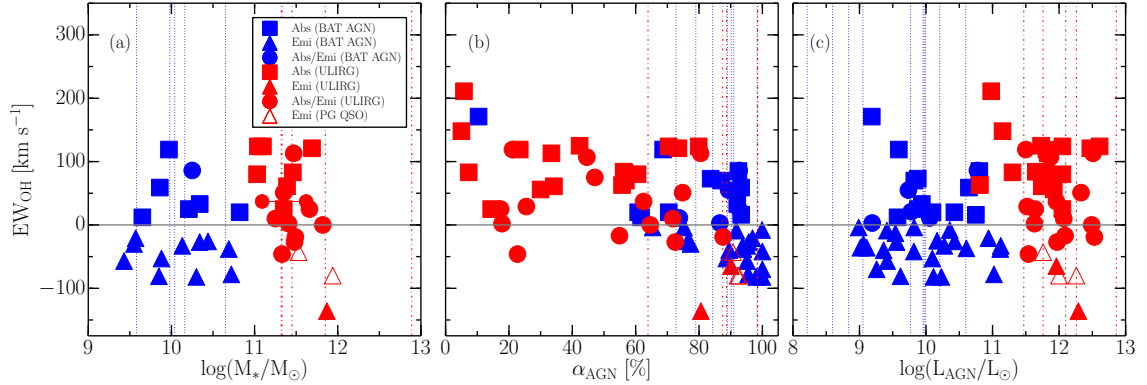


Figure 2.3 Total (absorption + emission) equivalent widths of OH $119 \mu\text{m}$ (positive values indicate absorption and negative values indicate emission) as a function of the (a) stellar masses, (b) AGN fractions, (c) AGN luminosities. The colors blue and red refer to BAT AGN and ULIRGs/PG QSOs, respectively. Filled squares, triangles, and circles represent BAT AGN or ULIRGs in which OH $119 \mu\text{m}$ is seen purely in absorption, purely in emission, or with composite absorption/emission, respectively. Open triangles represent PG QSOs in which OH $119 \mu\text{m}$ is seen purely in emission. The blue, vertical, dotted lines refer to BAT AGN in which OH $119 \mu\text{m}$ is not detected. Similarly, the red, vertical, dash-dotted lines represent ULIRGs/PG QSOs with undetected OH $119 \mu\text{m}$. The gray, horizontal line marks the null OH equivalent width.

2.5.1.2 OH Data Reduction

The reduction of the OH data on the BAT AGN sample was carried out using the standard PACS reduction and calibration pipeline (ipipe) included in HIPE 6.0. For the final calibration, fainter sources were normalized to the telescope flux (which dominates the total signal) and recalibrated using a reference telescope spectrum obtained from dedicated Neptune observations during the *Herschel* performance verification phase. [Sturm et al. \(2011\)](#) demonstrated that this telescope background technique can reliably recover the continuum from faint sources. In the following, we use the spectrum of the central $9.4'' \times 9.4''$ spatial pixel (spaxel) only, without the application of a point source flux correction. In a few objects we note that the

OH emission is extended. These objects will be the focus of a future paper.

The reduced spectra were next smoothed using a Gaussian kernel of width $0.05 \mu\text{m}$ (i.e. about half a resolution element) to reduce the noise in the data before the spectral analysis. A spline was fit to the continuum emission and subtracted from the spectra. Subsequently, spectral fitting was carried out on these continuum-subtracted spectra.

2.5.1.3 Spectral Analysis of the OH Doublet

Line profile fits of the OH 119.233, 119.441 μm doublet were computed by using *PySpecKit*, a spectroscopic analysis and reduction toolkit for optical, infrared, and radio spectra (Ginsburg & Mirocha, 2011). The toolkit uses the Levenberg-Marquardt technique to solve the least-squares problem in order to find the best fit for the observations. Profile fitting of the OH doublet followed a similar procedure as that outlined in V13, in which the doublet profile was modeled using four Gaussian components (two components for each line of the doublet), each characterized by their amplitude (either negative or positive), peak position, and standard deviation (or, equivalently FWHM). However, many of the OH profiles observed here were fit with only two Gaussian components (one component for each line of the doublet), since a fit with four Gaussian components often led to spurious results (i.e. skinny components with $\text{FWHM} \sim 10 \text{ km s}^{-1}$, values too small to be considered real). The separation between the two lines of the doublet was set to $0.208 \mu\text{m}$ in the rest frame ($\sim 520 \text{ km s}^{-1}$) and the amplitude and standard deviation were fixed to be

the same for each component in the doublet. In cases where OH was not detected, two Gaussian components, characterized by an amplitude consistent with the 1σ level of the noise and a FWHM (300 km s^{-1}) approximately equal to the resolution of PACS, were fit and maximum values for the OH flux and equivalent width were derived.

Four distinct scenarios apply to our data: (1) pure OH absorption, (2) pure OH emission, (3) P Cygni profiles, and (4) inverse P Cygni profiles. In scenario 1, there is no evidence of OH emission and each line of the OH doublet is fitted with 1-2 absorption components. In the case of the two-component fit, one component traces the stronger low-velocity component of the outflow, while the other component traces the fainter high-velocity component. In the case of the single-component fit, only the low-velocity component is captured. Scenario 2 is treated similarly. In this scenario, there is no evidence for any OH absorption and 1-2 Gaussian components are used to model each line of the OH doublet. In scenario 3, each line of the doublet is modeled with a single blueshifted absorption and a single redshifted emission component. In scenario 4, each line of the doublet is modeled with a single blueshifted emission component and a single redshifted absorption component. In scenarios 3 and 4, just as in the one-component fits of Scenarios 1 and 2, only the low-velocity component of the outflow is captured.

These fits were first used to quantify the strength and nature (absorption versus emission) of the OH feature: (1) the total flux and equivalent width of the OH $119.441 \mu\text{m}$ line, adding up all of the absorption and emission components, (2) the flux and equivalent width of the absorption component(s) used to fit this line,

and (3) the flux and equivalent width of the emission component(s) used to fit this line.

Following the same method as that outlined in V13, we also characterize the OH profile by measuring velocities: (1) $v_{50}(\text{abs})$ is the median velocity of the fitted absorption profile, i.e., 50% of the absorption takes place at velocities above (more positive than) $v_{50}(\text{abs})$, (2) $v_{84}(\text{abs})$ is the velocity above which 84% of the absorption takes place, (3) $v_{50}(\text{emi})$ is the median velocity of the fitted emission profile, i.e., 50% of the emission takes place at velocities below (less positive than) $v_{50}(\text{emi})$, and (4) $v_{84}(\text{emi})$ is the velocity below which 84% of the emission takes place. We note that three objects are fitted with inverted P-Cygni profiles, suggesting inflow. Circinus is an unambiguous fit while Centaurus A and NGC 3281 are marginally fit with inverted P-Cygni profiles. The velocities from the inverted P-Cygni profile fits are measured as thus: $v_{50}(\text{abs})$ and $v_{84}(\text{abs})$ are the velocities *below* which 50% and 84% of the absorption takes place, respectively, and $v_{50}(\text{emi})$ and $v_{84}(\text{emi})$ are the velocities *above* which 50% and 84% of the emission takes place, respectively.

We note that the OH emission is extended in some of our BAT AGN sources. While a full analysis of the 5×5 spaxels spectrum is outside the scope of this paper, we provide the ratio of the central spaxel 119 μm continuum flux density to that of the summed 25 spaxels (f_{cen}/f_{tot}) to quantify the degree to which some of our BAT AGN are spatially extended (see [Table 2.2](#)). For reference, the average value of f_{cen}/f_{tot} for a point source (derived from the five PG QSOs in our sample) is 0.56. Note that the continuum is often considerably more extended than the OH 119 μm feature.

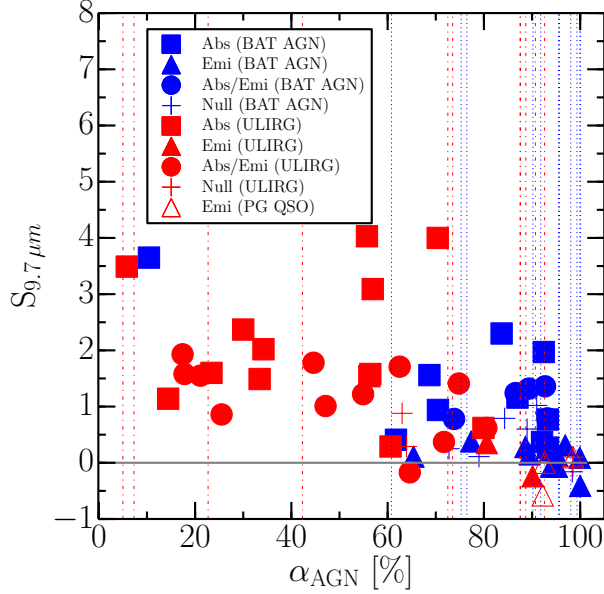


Figure 2.4 The apparent strength of the $9.7 \mu\text{m}$ silicate feature relative to the local mid-infrared continuum as a function of the AGN fractions. Note that $S_{9.7 \mu\text{m}}$ is a logarithmic quantity and can be interpreted as the apparent silicate optical depth. The strength of silicate absorption increases upward. Sign conventions and meanings of the symbols are the same as those in Section 2.5.1.1. Crosses represent objects with a null OH detection. Vertical lines indicate objects with a null $9.7 \mu\text{m}$ silicate feature detection.

2.5.2 The $9.7 \mu\text{m}$ Silicate Feature

2.5.2.1 Data Reduction of the $9.7 \mu\text{m}$ Silicate Feature

Mid-infrared (MIR; $5\text{--}37 \mu\text{m}$) low resolution spectra ($R \sim 60 - 127$) used to measure the $9.7 \mu\text{m}$ silicate feature for the BAT AGN, ULIRG, and PG QSO samples were extracted from The Cornell AtlaS of Spitzer/IRS Sources (CASSIS¹).

The archival data were obtained with the Infrared Spectrograph (IRS; Houck et al. (2004)) on board the Spitzer Space Telescope (Werner et al., 2004). There were two objects however (NGC 7479 and NGC 4945), in which the MIR spectrum was

¹<http://www.cassis.sirtf.com/atlas>

extracted from the Spitzer Heritage Archive (SHA²).

The *Spitzer* observations were made with the Short-Low (SL, 5.2-14.5 μm) and Long-Low (LL, 14.0-38.0 μm) modules of the IRS. The orders were stitched to LL order 2, requiring order-to-order scaling adjustments of less than $\sim 15\%$.

2.5.2.2 Spectral Analysis of the 9.7 μm Silicate Feature

We have measured the strength of the 9.7 μm silicate feature for sources in our BAT AGN sample and in the ULIRG/QSO sample. The calculation of the mid-infrared continuum loosely follows the method of [Spoon et al. \(2007\)](#). For a majority of the sources, the mid-infrared continuum (e.g. the continuum flux density f_{cont}) is determined from a cubic spline interpolation to continuum pivots at 5.2, 5.6, 14.0, 27.0, and 31.5 μm . For objects in which the 9.7 μm silicate feature dominates the spectrum (i.e. there is very little PAH emission), an additional pivot point is added at 7.8 μm . The pivot points are adopted from [Spoon et al. \(2007\)](#), however we have placed a pivot point at 27 μm instead of at 25 μm due to the proximity of the [OIV] emission line at 25.89 μm which is common in BAT AGN. Due to the diversity of our BAT AGN sample, the wavelength range in which the 9.7 μm silicate feature is determined differs slightly from source to source (see [Table 2.4](#)). Typically, however, the observed flux density (e.g. f_{obs}) is determined from a cubic spline interpolation to the data between $\sim 8\mu\text{m}$ and $\sim 14\mu\text{m}$. This interpolation skips the H₂ line at 9.6 μm , [S IV] line at 10.51 μm , PAH feature at 11.25 μm , H₂ line at 12.28 μm , and [NeII] at 12.68 μm .

²<http://sha.ipac.caltech.edu/applications/Spitzer/SHA/>

The apparent strength of the 9.7 μm silicate feature is then defined as:

$$S_{9.7\ \mu\text{m}} = -\ln\left(\frac{f_{\text{obs}}(9.7\ \mu\text{m})}{f_{\text{cont}}(9.7\ \mu\text{m})}\right). \quad (2.8)$$

Here, we adopt the sign convention consistent with our OH 119 μm analysis (e.g. positive $S_{9.7\ \mu\text{m}}$ values indicate absorption while negative $S_{9.7\ \mu\text{m}}$ values indicate emission). Note that this convention is different from previous studies (e.g. [Spoon et al., 2007](#)).

For sources with a silicate absorption feature, $S_{9.7\ \mu\text{m}}$ can be interpreted as the the apparent silicate optical depth. [Table 2.4](#) and [Table 2.5](#) lists pivot points, integration ranges, and measured equivalent widths and fluxes of the 9.7 μm silicate feature for our samples. MIR spectra showing these pivot points and integration ranges may be found in the Appendix.

2.6 Results

[Figure 2.1](#) shows the fits to the OH 119 μm profiles for our BAT AGN targets. The OH 119 μm parameters for all targets derived from these fits are listed in [Table 3.3](#). The meaning of each parameter is discussed in [Section 2.5.1.3](#) and in the notes to [Table 3.3](#). Note that the fluxes and equivalent widths in [Table 3.3](#) need to be multiplied by a factor of two when considering both lines of the doublet.

In this section we compare the OH 119 μm and $S_{9.7\ \mu\text{m}}$ results listed in [Table 3.3](#), [Table 2.4](#), and [Table 2.5](#), with the galaxy properties listed in [Table 2.2](#).

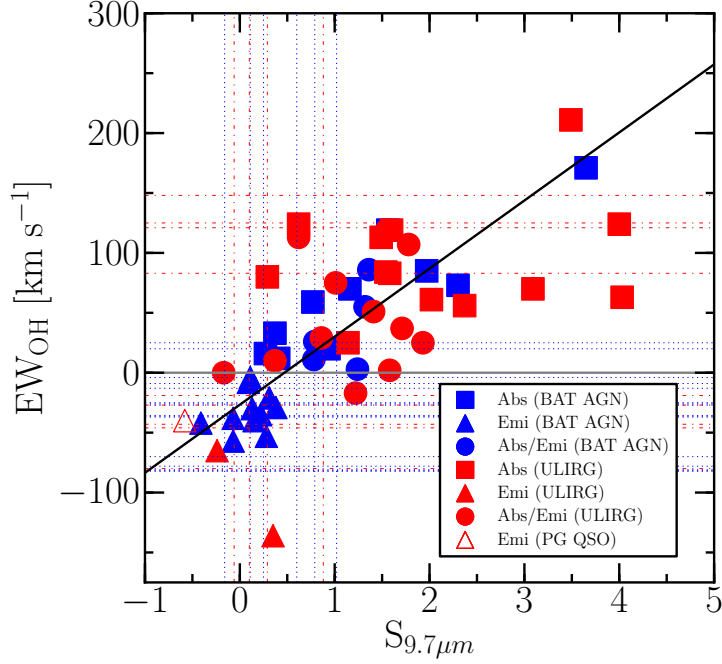


Figure 2.5 Total (absorption + emission) equivalent widths of OH $119 \mu\text{m}$ as a function of the apparent strength of the $9.7 \mu\text{m}$ silicate feature relative to the local mid-infrared continuum. Note that $S_{9.7\mu\text{m}}$ is a logarithmic quantity and can be interpreted as the apparent silicate optical depth. The strength of this absorption feature increases to the right. Sign conventions and meanings of the symbols are the same as those in Section 2.5.1.1. Horizontal, blue, dotted lines represent BAT AGN in which the $9.7 \mu\text{m}$ silicate feature is not detected. Similarly, horizontal, red, dash-dotted lines represent ULIRGs/PG QSOs with a null $9.7 \mu\text{m}$ silicate feature detection. The black diagonal line shows the ordinary least squares bisector linear regression: $\text{EW}_{\text{OH}} = 56.81 \times S_{9.7\mu\text{m}} - 26.7 \text{ km s}^{-1}$. The Pearson r null probability for the linear relationship between $S_{9.7\mu\text{m}}$ and the total OH equivalent width is $P[\text{null}] = 1.2 \times 10^{-9}$ for the BAT AGN sample and $P[\text{null}] = 0.003$ for the ULIRG + QSO sample. When the samples are combined, we find $P[\text{null}] = 3.9 \times 10^{-9}$.

2.6.1 The OH $119 \mu\text{m}$ Feature

The OH $119 \mu\text{m}$ doublet is detected in 42 of the 52 objects in our BAT AGN sample. Of the 42 detections, 25 are seen purely in emission, 12 are seen purely in absorption, and 5 are seen with absorption+emission composite profiles. For comparison, in the ULIRG + QSO sample (V13), 37 objects showed OH $119 \mu\text{m}$ detections,

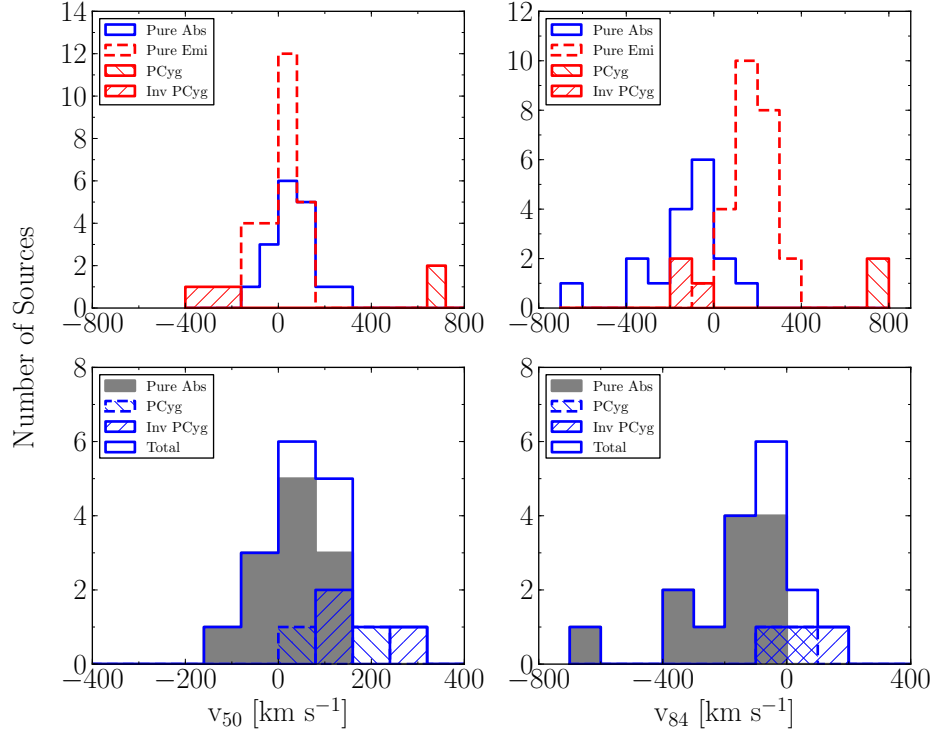


Figure 2.6 Histograms showing the distributions of the 50% (median; left panels) and 84% (right panels) velocities derived from the multi-Gaussian fits to the OH profiles of the BAT AGN. Top panels show pure absorption components (blue), pure emission components (red dashed), P-cygni emission components (red, left diagonals), and inverse P-cygni emission components (red, right diagonals). Bottom panels show pure absorption components (filled grey), P-Cygni absorption components (blue, left diagonals), inverse P-cygni absorption components (blue, right diagonals), and total absorption components (pure + P-Cygni + inverse P-Cygni).

17 of which were seen purely in absorption, 15 showed absorption+emission composite profiles, and 5 were seen purely in emission. [Section 2.5.1.1a](#), [Section 2.5.1.1c](#) plot the OH equivalent width with the stellar mass and AGN luminosity, respectively. For these properties, we see no discernible correlation in either the individual samples (i.e. BAT AGN only and ULIRG + PG QSO only) or in the combined sample. There is however a weak trend between EW_{OH} and AGN fraction ([Section 2.5.1.1b](#)) when the samples are combined. A more formal statistical analysis of these parameters indeed indicates a statistically significant correlation between

these quantities when all objects are considered (see [Table 2.6](#)).

For the BAT AGN in which OH 119 μm is seen purely in emission, we find that the AGN is dominant (i.e. $\alpha_{\text{AGN}} > 50\%$) in these objects. In agreement with V13, the low luminosities ($\log(L_{\text{AGN}}/L_{\odot}) \lesssim 12$) of these 20 AGN-dominated objects with pure OH emission suggest that the AGN fraction is more important than AGN luminosity in setting the character (i.e. strength of emission relative to absorption) of the OH feature. Therefore, we see that dominant AGN in our sample can excite the OH molecule (via radiative pumping or collisional excitation) and produce the ${}^2\Pi_{3/2} J = 5/2 \rightarrow 3/2$ rotational emission line. This trend was noted in V13.

Table 2.4. $S_{9.7\mu\text{m}}$ Continuum Parameters and Measured Values of the BAT AGN Sample

(Name)	Pivot Points (μm)	Integration Range (μm)	Flux $_{S_{9.7\mu\text{m}}}$ (Jy μm)	EQW $_{S_{9.7\mu\text{m}}}$ (μm)	$S_{9.7\mu\text{m}}$
(1)	(2)	(3)	(4)	(5)	(6)
CenA	5.2, 5.6, 14.0, 27.0, 31.5	8.3, 11.3	1.06	1.01	0.79
Circinus	5.2, 5.6, 14.0, 31.5	7.8, 14	23.38	2.06	1.24
ESO 005–G004	5.2, 5.6, 14.0, 27.0, 31.5	8.6, 11.19	0.34	1.55	1.32
ESO 137–34
IC 5063	5.2, 5.6, 14.0, 27.0, 31.5	8.15, 12.3	0.37	0.55	0.27
IRAS 00410+2807
IRAS 19348–0619
MGC–05.23.16	5.2, 5.6, 14.0, 27.0, 31.5	8, 12.45	0.32	0.64	0.31
MGC–06.30.15	5.2, 5.6, 14.0, 27.0, 31.5	8.09, 10.4	0.05	0.16	0.09
Mrk 18	5.2, 5.6, 14.0, 27.0, 31.5	9, 10.4	0.01	0.12	0.11
NGC 1052
NGC 1068
NGC 1125
NGC 1365
NGC 1566
NGC 2110	5.2, 5.6, 14.0, 27.0, 31.5	7.8, 14	0.17	0.74	–0.07
NGC 2655
NGC 2992	5.2, 5.6, 14.0, 27.0, 31.5	8.75, 11.1	0.13	0.48	0.37
NGC 3079	5.2, 5.6, 14.0, 27.0, 31.5	8.8, 11.13	0.66	1.5	1.56
NGC 3081	5.2, 5.6, 14.0, 27.0, 31.5	8, 11.3	0.09	0.44	0.22
NGC 3227	5.2, 5.6, 14.0, 27.0, 31.5	8.75, 11.09	0.15	0.46	0.28
NGC 3281	5.2, 5.6, 7.8, 14.0, 27.0, 31.5	7.8, 14	1.98	2.27	1.36
NGC 3516
NGC 3718
NGC 3783	5.2, 5.6, 14.0, 27.0, 31.5	7.9, 11.3	0.17	0.33	0.13

Table 2.4 (cont'd)

(Name)	Pivot Points (μm)	Integration Range (μm)	Flux $_{S_{9.7\mu\text{m}}}$ (Jy μm)	EQW $_{S_{9.7\mu\text{m}}}$ (μm)	$S_{9.7\mu\text{m}}$
(1)	(2)	(3)	(4)	(5)	(6)
NGC 4051	5.2, 5.6, 14.0, 21.9, 24.9	8, 10.8	0.07	0.24	-0.07
NGC 4102	5.2, 5.6, 14.0, 27.0, 31.5	9, 10.95	0.23	0.52	0.41
NGC 4138
NGC 4151	...	7.8, 14
NGC 4258	5.2, 5.6, 14.0, 27.0, 31.5	7.8, 13.39	0.14	1.15	-0.16
NGC 4388	5.2, 5.6, 14.0, 27.0, 31.5	8.2, 12.2	0.43	1.35	0.79
NGC 4395	5.2, 5.6, 14.0, 27.0, 31.5	7.8, 11.09	0.004	0.67	0.25
NGC 4579
NGC 4593
NGC 4939
NGC 4941	5.2, 5.6, 7.8, 14.0, 27.0, 31.5	8, 11.13	0.02	0.33	0.15
NGC 4945	7.8, 14.0, 27.0, 31.5	7.8, 11.09	1.95	2.72	3.65
NGC 5033
NGC 5273	4.6, 14.0, 27.0, 31.5	7.7, 11.05	0.01	0.66	0.38
NGC 5290
NGC 5506	5.2, 5.6, 14.0, 27.0, 31.5	8.35, 12.15	1.2	1.16	0.77
NGC 5728	5.2, 5.6, 14.0, 27.0, 31.5	8.63, 11.16	0.15	1.17	0.94
NGC 5899	5.2, 5.6, 14.0, 27.0, 31.5	8.1, 11.15	0.08	1.44	1.02
NGC 6221	5.2, 5.6, 14.0, 27.0, 31.5	9.2, 10.7	0.03	0.13	0.11
NGC 6300	5.2, 5.6, 14.0, 27.0, 31.5	8.58, 12.2	0.67	1.71	1.16
NGC 6814
NGC 7172	5.2, 5.6, 14.0, 27.0, 31.5	8.15, 12.52	0.68	2.37	1.97
NGC 7213	5.2, 5.6, 14.0, 27.0, 31.5	8.76, 13.3	0.36	2.26	-0.41
NGC 7314	5.2, 5.6, 7.8, 14.0	7.8, 14	0.09	1.38	0.6
NGC 7465

Table 2.4 (cont'd)

(Name)	Pivot Points (μm)	Integration Range (μm)	Flux $_{S_{9.7\mu\text{m}}}$ (Jy μm)	EQW $_{S_{9.7\mu\text{m}}}$ (μm)	$S_{9.7\mu\text{m}}$
(1)	(2)	(3)	(4)	(5)	(6)
NGC 7479	4.6, 7.8, 14.0, 27.0, 31.5	7.8, 12.9	1.98	3.09	2.3
NGC 7582	5.2, 5.6, 14.0, 27.0, 31.5	8.8, 11.05	0.81	0.95	0.78

Note. — Column 1: galaxy name. Column 2: Pivot points in microns used for the continuum interpolation. Column 3: Integration range of the 9.7 μm silicate feature. Column 4: Total integrated flux of the 9.7 μm silicate feature. Column 5: total equivalent width for the 9.7 μm silicate feature. Column 6: $S_{9.7\mu\text{m}}$; see [Section 2.5.2.2](#).

2.6.2 The $S_{9.7\mu\text{m}}$ Feature

[Figure 2.4](#) plots the apparent strength of the $9.7\ \mu\text{m}$ silicate absorption feature versus the AGN fraction α_{AGN} . Here, larger, more positive values of $S_{9.7\mu\text{m}}$ indicate stronger silicate absorption features. We see no discernible trend between the strength of this silicate feature and AGN fraction. This is surprising since the AGN fractions should be inversely proportional to the equivalent widths of the PAH features ([Veilleux et al., 2009](#)). Thus, [Figure 2.4](#) should look similar to Figure 1 of [Spoon et al. \(2007\)](#) which plots the $6.2\ \mu\text{m}$ PAH emission feature and $S_{9.7\mu\text{m}}$. We find that our data do not show the bifurcation observed in [Spoon et al. \(2007\)](#) because only two of our ULIRGs (F08572+3915 and F15250+3608) lie on the upper branch of the bifurcation, and none of our BAT AGN populate the upper branch. The two objects in [Figure 2.4](#) which display $\alpha_{\text{AGN}} \sim 10\%$ and high $S_{9.7\mu\text{m}}$ are NGC 4945 and F15327+2340. Both of these objects show weak PAH emission and are therefore not displayed in Figure 1 of [Spoon et al. \(2007\)](#).

[Figure 2.5](#) shows a positive correlation between the measured OH equivalent width and the $9.7\ \mu\text{m}$ silicate optical depth. The black diagonal line shows the ordinary least squares bisector linear regression for the entire sample (BAT AGN + ULIRGs + PG QSOs):

$$\text{EW}_{\text{OH}} = 56.81 \times S_{9.7\mu\text{m}} - 26.7 \text{ [km s}^{-1}\text{]}. \quad (2.9)$$

The Pearson correlation coefficient of the linear relationship for $S_{9.7\mu\text{m}}$ and the

total OH equivalent width is $\rho_{S_{9.7\mu m}, EW_{OH}} = 0.7$ with a $P[\text{null}]$ (the probability of an uncorrelated system producing datasets that have a Pearson correlation at least as extreme as the one computed from these datasets) of 3.9×10^{-9} for the combined sample. If we restrict this analysis to the BAT AGN only, we find $\rho_{S_{9.7\mu m}, EW_{OH}}(\text{BAT AGN}) = 0.89$ with a $P[\text{null}]$ of 1.2×10^{-9} . Restricting the analysis to ULIRGs and PG QSOs only yields $\rho_{S_{9.7\mu m}, EW_{OH}}(\text{ULIRG/PG QSO}) = 0.5$ with a $P[\text{null}]$ of 0.003.

In [Figure 2.5](#) we also see that objects with OH in emission show either weak silicate absorption or silicate emission. Objects with OH P-Cygni profiles show moderate silicate absorption features, while the strongest silicate absorption features are seen in objects in which OH is observed purely in absorption. We return to this result in [Section 3.5](#).

2.6.3 OH Kinematics

We quantify the visual trends observed (or not observed) in our kinematic investigation of the individual samples (i.e. BAT AGN only or ULIRG/QSO only) and of the combined sample by calculating the correlational significances between the observed OH velocities (v_{50} and v_{84}) and the host galaxy properties (stellar masses, SFRs, specific star formation rates (sSFRs; i.e. the rate at which stars are formed divided by the stellar mass of the galaxy), and AGN fractions and luminosities. Since the spatial location of the OH emission is unknown, physical interpretations of the observed OH velocities in these cases will be ambiguous (e.g., blueshifted

velocities may correspond to outflow or inflow if the OH emission region is located in front or behind the continuum source, respectively). We therefore exclude from our analysis objects in which OH is detected purely in emission. The results of our statistical analyses on all objects with either redshifted or blueshifted absorption profiles are listed in [Table 2.7](#).

[Section 2.6](#) shows the distributions of velocities derived from both the OH absorption and emission line features ($v_{50}(\text{abs})$, $v_{84}(\text{abs})$, $v_{50}(\text{emi})$, and $v_{84}(\text{emi})$, as defined in [Section 2.5.1.3](#) and listed in [Table 3.3](#)). In V13, we adopted [Rupke et al. \(2005a\)](#)'s conservative definition of an outflow as having an OH absorption feature with a median velocity (v_{50}) more negative than -50 km s^{-1} . Similarly, we can define an inflow as having an OH absorption feature with a median velocity (v_{50}) more positive than 50 km s^{-1} . This cutoff is used to avoid contamination due to systematic errors and measurement errors in wavelength calibration, line fitting (see [Section 2.5.1.3](#)), and redshift determination. We find that only two objects in our BAT AGN sample meet this outflow criterion, and just barely: NGC 7172 and NGC 7479 (both have $v_{50} = -51 \text{ km s}^{-1}$). The presence of a significant blue wing in the absorption profile of OH $119 \mu\text{m}$ in NGC 7479 with $v_{84} = -658 \text{ km s}^{-1}$ adds considerable support to this interpretation. An extended blue wing with $v_{84} < -300 \text{ km s}^{-1}$ may also be present in the OH absorption profile of IC 5063, NGC 5506, and NGC 7172, although these detections are more tentative than in NGC 7479. In contrast, seven objects have OH absorption features with median velocities larger than $+50 \text{ km s}^{-1}$: Centaurus A, Circinus, NGC 1125, NGC 3079, NGC 3281, NGC 4945, and NGC 7582. The clear detection of an inverted P-Cygni profile in Circinus

provides unambiguous evidence for the presence of an inflow in this object. The inverted P-Cygni profiles in Centaurus A and NGC 3281 are much less secure. We return to these objects in [Section 3.5](#).

Table 2.5. $S_{9.7\mu\text{m}}$ Continuum Parameters and Measured Values of the ULIRG/PG QSO Sample

(Name)	Pivot Points (μm)	Integration Range (μm)	Flux $_{S_{9.7\mu\text{m}}}$ (Jy μm)	EQW $_{S_{9.7\mu\text{m}}}$ (μm)	$S_{9.7\mu\text{m}}$
(1)	(2)	(3)	(4)	(5)	(6)
07251–0248	5.2, 14.0, 27.0, 31.5	8.45, 12.7	0.21	3.4	2.37
09022–3615	5.2, 5.6, 14.0, 27.0, 31.5	8.3, 12.6	0.43	1.84	1.22
13120–5453	5.2, 5.6, 14.0, 27.0, 31.5	8.7, 12.0	0.5	1.72	1.49
19542+1110	5.2, 5.6, 14.0, 27.0, 31.5	8.74, 11.14	0.05	1.12	0.86
F00509+1225	5.2, 5.6, 14.0, 27.0, 31.5	7.8, 14.0	0.31	0.82	–0.24
F01572+0009	5.2, 5.6, 14.0, 27.0, 31.5	8.1, 14.0	0.06	0.75	–0.17
F05024–1941	5.2, 5.6, 10.8, 18.5	7.8, 12.6	0.01	1.65	0.22
F05189–2524	5.2, 5.6, 14.0, 27.0, 31.5	8.37, 14.0	0.54	1.01	0.37
F07598+6508	5.2, 5.6, 14.0, 27.0, 31.5	7.2, 14.0	0.11	0.49	–0.15
F08572+3915	5.2, 5.6, 7.8, 14.0, 27.0, 31.5	7.8, 13.0	2.55	3.39	4.00
F09320+6134	5.2, 5.6, 14.0, 27.0, 31.5	8.65, 12.1	0.33	1.91	1.58
F10565+2448	5.2, 5.6, 14.0, 27.0, 31.5	8.76, 11.17	0.16	1.21	1.01
F11119+3257	5.2, 5.6, 7.8, 14.0, 27.0, 31.5	7.8, 12.6	0.17	1.21	0.62
F12072–0444	5.2, 5.6, 14.0, 27.0, 31.5	8.1, 12.6	0.22	2.36	1.41
F12112+0305	5.2, 5.6, 14.0, 27.0, 31.5	8.6, 12.4	0.13	2.42	1.58
F12243–0036	5.2, 5.6, 7.8, 14.0, 27.0, 31.5	8.15, 12.8	4.73	3.95	4.03
F12265+0219	5.2, 5.6, 14.0, 27.0, 31.5	8.8, 14.0	0.08	0.26	–0.06
F12540+5708	5.2, 5.6, 14.0, 27.0, 31.5	8.4, 12.6	2.62	1.49	0.62
F13305–1739
F13428+5608	5.2, 5.6, 14.0, 27.0, 31.5	8.2, 12.6	0.73	2.77	2.02
F13451+1232	5.2, 5.6, 7.8, 14.0, 27.0, 31.5	7.8, 12.2	0.06	0.61	0.35
F14348–1447	5.2, 5.6, 14.0, 27.0, 31.5	8.3, 12.4	0.15	2.66	1.93
F14378–3651	5.2, 5.6, 14.0, 27.0, 31.5	8.7, 12.1	0.06	1.76	1.55
F14394+5332	5.2, 5.6, 14.0, 27.0, 31.5	8.5, 12.3	0.18	2.26	1.71
F15206+3342	5.2, 5.6, 14.0, 27.0, 31.5	9.0, 11.1	0.02	0.47	0.29

Table 2.5 (cont'd)

(Name)	Pivot Points (μm)	Integration Range (μm)	Flux $_{S_{9.7\mu\text{m}}}$ (Jy μm)	EQW $_{S_{9.7\mu\text{m}}}$ (μm)	$S_{9.7\mu\text{m}}$
(1)	(2)	(3)	(4)	(5)	(6)
F15250+3608	5.2, 5.6, 7.8, 14.0, 27.0, 31.5	7.8, 14.0	0.94	3.54	3.42
F15327+2340	5.2, 5.6, 7.8, 14.0, 27.0, 31.5	7.8, 12.6	2.87	3.57	3.49
F15462-0450	5.2, 5.6, 14.0, 27.0, 31.5	8.6, 12.4	0.06	0.78	0.29
F16504+0228	5.2, 5.6, 14.0, 27.0, 31.5	8.65, 12.2	0.72	2.06	1.54
F17208-0014	5.2, 5.6, 14.0, 27.0, 31.5	8.6, 12.4	0.37	2.38	1.96
F19297-0406	5.2, 5.6, 14.0, 27.0, 31.5	8.6, 12.5	0.12	2.48	1.60
F20551-4250	5.2, 5.6, 7.8, 14.0, 27.0, 31.5	7.8, 14.0	1.52	3.43	3.09
F22491-1808	5.2, 5.6, 14.0, 27.0, 31.5	8.65, 12.4	0.07	2.2	1.14
F23128-5919	5.2, 5.6, 14.0, 27.0, 31.5	8.65, 12.2	0.23	1.45	0.88
F23233+2817
F23365+3604	5.2, 5.6, 14.0, 27.0, 31.5	8.65, 12.4	0.17	2.49	1.78
F23389+0300
PG 1126-041
PG 1351+640	5.2, 5.6, 14.0, 27.0, 31.5	8.1, 14.0	0.24	2.31	-0.58
PG 1440+356
PG 1613+658	5.2, 5.6, 14.0, 27.0, 31.5	7.2, 14.0	0.03	0.38	-0.01
PG 2130+099	5.2, 5.6, 14.0, 27.0, 31.5	7.75, 14.0	0.05	0.29	0.10
Z11598-0114

Note. — Column 1: galaxy name. Column 2: Pivot points in microns used for the continuum interpolation. Column 3: Integration range of the $9.7\ \mu\text{m}$ silicate feature. Column 4: Total integrated flux of the $9.7\ \mu\text{m}$ silicate feature. Column 5: total equivalent width for the $9.7\ \mu\text{m}$ silicate feature. Column 6: $S_{9.7\ \mu\text{m}}$; see [Section 2.5.2.2](#).

Table 2.6. Results from Statistical Analyses of Host Galaxy Properties

Parameter	Number of Objects	ρ_s	P_ρ	τ	P_τ	r	P_r
(1)	(2)	(3)	(4)	(5)	(6)	(7)	(8)
$\log M_*$ - EW _{OH} (ULIRGs Only)	21	-0.49	2.5e-02	-0.34	3.3e-02	-0.56	8.4e-03
$\log M_*$ - EW _{OH} (BAT AGN only)	18	0.04	8.8e-01	0.04	8.2e-01	-0.00	9.9e-01
$\log M_*$ - EW _{OH} (Combined Sample)	39	0.13	4.3e-01	0.09	4.0e-01	0.13	4.2e-01
α_{AGN} - EW _{OH} (ULIRGs Only)	37	-0.42	1.1e-02	-0.29	1.0e-02	-0.47	3.7e-03
α_{AGN} - EW _{OH} (BAT AGN only)	38	-0.11	5.2e-01	-0.08	5.0e-01	-0.27	1.0e-01
α_{AGN} - EW _{OH} (Combined Sample)	75	-0.42	1.8e-04	-0.29	2.3e-04	-0.44	7.0e-05
$\log L_{\text{AGN}}$ - EW _{OH} (ULIRGs Only)	37	-0.25	1.3e-01	-0.19	9.7e-02	-0.31	6.4e-02
$\log L_{\text{AGN}}$ - EW _{OH} (BAT AGN only)	42	0.03	8.5e-01	0.02	8.6e-01	-0.03	8.7e-01
$\log L_{\text{AGN}}$ - EW _{OH} (Combined Sample)	79	0.26	2.0e-02	0.18	2.1e-02	0.25	2.4e-02

Note. — Column 1: quantities considered for the statistical test. Column 2: number of objects in which OH 119 μm is detected. Column 3: Spearman rank order correlation coefficient. Column 4: null probability of the Spearman rank order correlation coefficient. Column 5: Kendall's correlation coefficient. Column 6: null probability of Kendall's correlation. Column 7: Pearson's linear correlation coefficient. Column 8: Two-tail area probability of Pearson's linear correlation. Null probabilities $\lesssim 10^{-3}$ (shown in bold-faced characters) indicate statistically significant trends.

Table 2.7. Results from Statistical Analyses of the Kinematics

Parameter	Number of Objects	ρ_s	P_ρ	τ	P_τ	r	P_r
(1)	(2)	(3)	(4)	(5)	(6)	(7)	(8)
ULIRGs Only							
$\log M_* - v_{50}$	18	-0.15	5.6e-01	-0.15	3.8e-01	-0.04	8.7e-01
$\log M_* - v_{84}$	18	-0.10	7.0e-01	-0.08	6.4e-01	0.01	9.6e-01
$\log SFR - v_{50}$	32	0.28	1.2e-01	0.22	8.2e-02	0.06	7.6e-01
$\log SFR - v_{84}$	32	0.19	2.9e-01	0.14	2.4e-01	0.07	7.1e-01
sSFR - v_{50}	18	0.37	1.3e-01	0.26	1.3e-01	0.54	2.2e-02
sSFR - v_{84}	18	0.26	3.0e-01	0.21	2.3e-01	0.57	1.4e-02
$\alpha_{AGN} - v_{50}$	32	-0.52	2.4e-03	-0.37	3.2e-03	-0.48	5.5e-03
$\alpha_{AGN} - v_{84}$	32	-0.46	7.4e-03	-0.31	1.2e-02	-0.46	7.6e-03
$\log L_{AGN} - v_{50}$	32	-0.50	3.3e-03	-0.37	2.8e-03	-0.56	8.0e-04
$\log L_{AGN} - v_{84}$	32	-0.44	1.1e-02	-0.32	9.8e-03	-0.54	1.6e-03
BAT AGN Only							
$\log M_* - v_{50}$	6	-0.23	6.6e-01	-0.14	7.0e-01	-0.34	5.1e-01
$\log M_* - v_{84}$	6	0.09	8.7e-01	-0.07	8.5e-01	0.27	6.1e-01
$\log SFR - v_{50}$	13	-0.11	7.3e-01	-0.11	6.2e-01	-0.04	8.9e-01
$\log SFR - v_{84}$	13	0.24	4.4e-01	0.17	4.2e-01	-0.02	9.5e-01
sSFR - v_{50}	6	0.32	5.4e-01	0.28	4.4e-01	0.17	7.4e-01
sSFR - v_{84}	6	0.54	2.7e-01	0.33	3.5e-01	0.34	5.1e-01
$\alpha_{AGN} - v_{50}$	13	-0.50	8.4e-02	-0.32	1.3e-01	-0.50	8.1e-02
$\alpha_{AGN} - v_{84}$	13	-0.69	9.4e-03	-0.50	1.7e-02	-0.44	1.3e-01
$\log L_{AGN} - v_{50}$	14	-0.27	3.6e-01	-0.18	3.7e-01	-0.39	1.7e-01
$\log L_{AGN} - v_{84}$	14	-0.36	2.1e-01	-0.27	1.9e-01	-0.29	3.2e-01
Combined Sample							
$\log M_* - v_{50}$	24	-0.58	2.8e-03	-0.44	2.5e-03	-0.13	5.5e-01
$\log M_* - v_{84}$	24	-0.53	7.9e-03	-0.38	9.9e-03	-0.08	7.0e-01
$\log SFR - v_{50}$	45	-0.34	2.3e-02	-0.21	3.9e-02	-0.44	2.3e-03
$\log SFR - v_{84}$	45	-0.30	4.3e-02	-0.18	7.8e-02	-0.40	6.8e-03

Table 2.7 (cont'd)

Parameter	Number of Objects	ρ_s	P_ρ	τ	P_τ	r	P_r
(1)	(2)	(3)	(4)	(5)	(6)	(7)	(8)
sSFR $- v_{50}$	24	0.13	5.6e-01	0.10	4.8e-01	0.34	1.1e-01
sSFR $- v_{84}$	24	0.10	6.3e-01	0.09	5.2e-01	0.38	6.7e-02
$\alpha_{\text{AGN}} - v_{50}$	45	-0.04	8.1e-01	-0.03	7.8e-01	-0.08	6.1e-01
$\alpha_{\text{AGN}} - v_{84}$	45	-0.09	5.6e-01	-0.06	5.7e-01	-0.12	4.5e-01
$\log L_{\text{AGN}} - v_{50}$	46	-0.70	6.8e-08	-0.51	5.7e-07	-0.67	3.3e-07
$\log L_{\text{AGN}} - v_{84}$	46	-0.61	8.2e-06	-0.45	8.9e-06	-0.63	2.9e-06

Note. — Column 1: quantities considered for the statistical test. Column 2: number of objects in which OH 119 μm is detected in either redshifted or blueshifted absorption. Column 3: Spearman rank order correlation coefficient. Column 4: null probability of the Spearman rank order correlation coefficient. Column 5: Kendall’s correlation coefficient. Column 6: null probability of Kendall’s correlation. Column 7: Pearson’s linear correlation coefficient. Column 8: Two-tail area probability of Pearson’s linear correlation. Null probabilities $\lesssim 10^{-3}$ (shown in bold-faced characters) indicate statistically significant trends.

Figure 2.7, Figure 2.8, and Figure 2.9 plot the OH velocities (v_{50} and v_{84}) as a function of the stellar masses, star formation rates, and specific star formation rates. If we consider our two samples individually, a visual inspection of these plots does not show a correlation between these properties. However, once the samples are combined we see a negative correlation between the observed OH velocities and the stellar mass or star formation rate of the galaxy (i.e. galaxies with larger stellar masses or star formation rates exhibit more negative v_{50} and v_{84} values). The strengths of these correlations are quantified in Table 2.7. No obvious trend is seen with sSFR for the combined sample. These results remain quantitatively the same if instead of using the global star formation rates we use the star formation rates from the central spaxel (scaled by the ratio of the continuum flux from the central

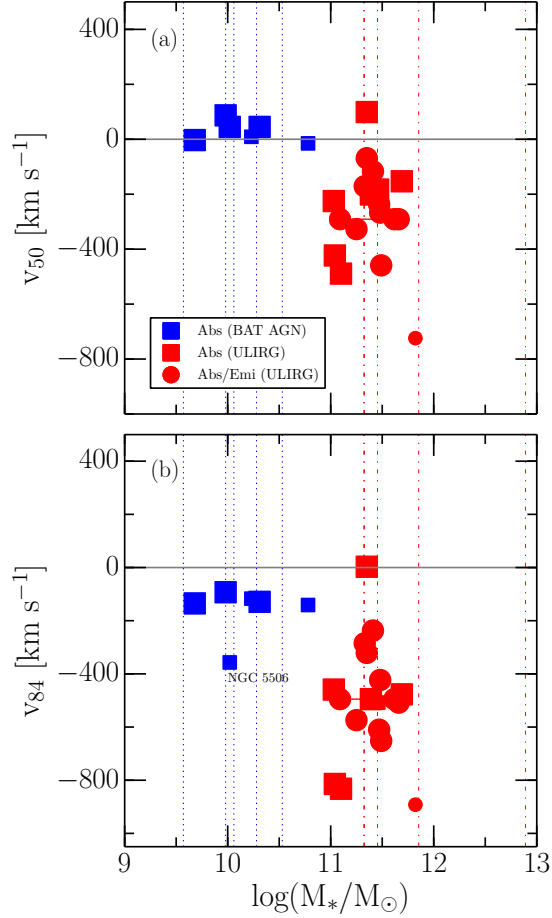


Figure 2.7 v_{50} and v_{84} as a function of the stellar masses. The meanings of the symbols are the same as those in Section 2.5.1.1. The data points joined by a segment correspond to F14394+5332 W and E. The smaller symbols have larger uncertainties (values followed by double colons in Table 3.3)

spaxial to that of all 25 spaxels, as listed in column (8) of Table 2.2).

Figure 2.10 plots the OH velocities (v_{50} and v_{84}) as a function of the AGN fractions α_{AGN} , where α_{AGN} is derived from the f_{30}/f_{15} continuum flux density ratios. As described in V13, ULIRGs/PG QSOs with dominant AGN ($\alpha_{\text{AGN}} \geq 50\%$) appear to have larger negative velocities than ULIRGs/PG QSOs with dominant starbursts ($\alpha_{\text{AGN}} \leq 50\%$), but a K-S test between velocity distributions of dominant AGN and dominant starburst systems indicated no statistically significant difference. A K-S

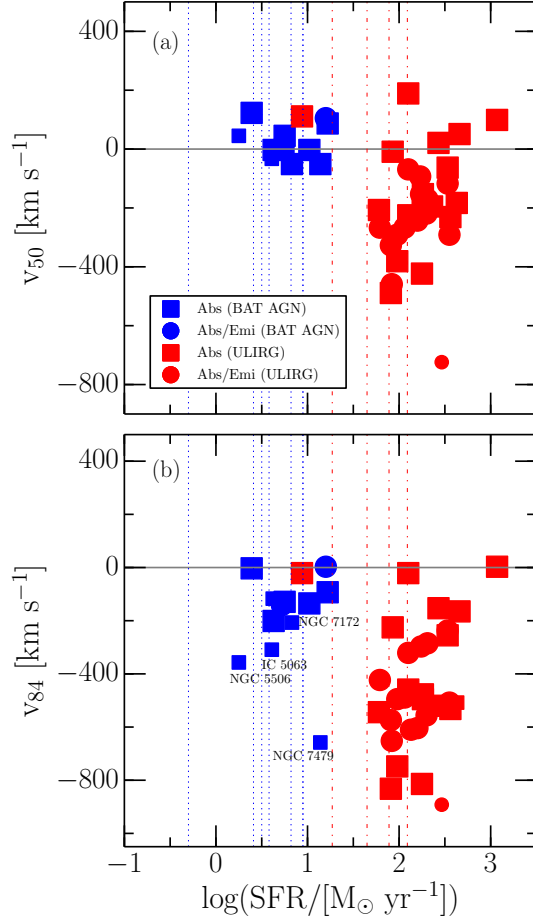


Figure 2.8 v_{50} and v_{84} as a function of the star formation rates. The meanings of the symbols are the same as those in Section 2.5.1.1. The smaller symbols have larger uncertainties (values followed by double colons in Table 3.3)

test on the combined BAT AGN and ULIRG + QSO sample also does not show a significant trend between the measured OH velocity and AGN fraction.

Figure 2.11 shows the OH velocities (v_{50} and v_{84}) versus the AGN luminosities, $L_{\text{AGN}} = 10.5 \times L_{14-195\text{keV}}$ for our BAT AGN sample and $L_{\text{AGN}} = \alpha_{\text{AGN}} L_{\text{BOL}}$ for the ULIRG/QSO sample; see Section 2.4. A correlation between these quantities is not observed in the BAT AGN sample, but clear trends are seen in the ULIRG/QSO sample and in the combined sample (see Table 2.7). Objects with $\log(L_{\text{AGN}}/L_{\odot}) \lesssim 11.5$ show no evidence for fast outflows. This suggests that AGN

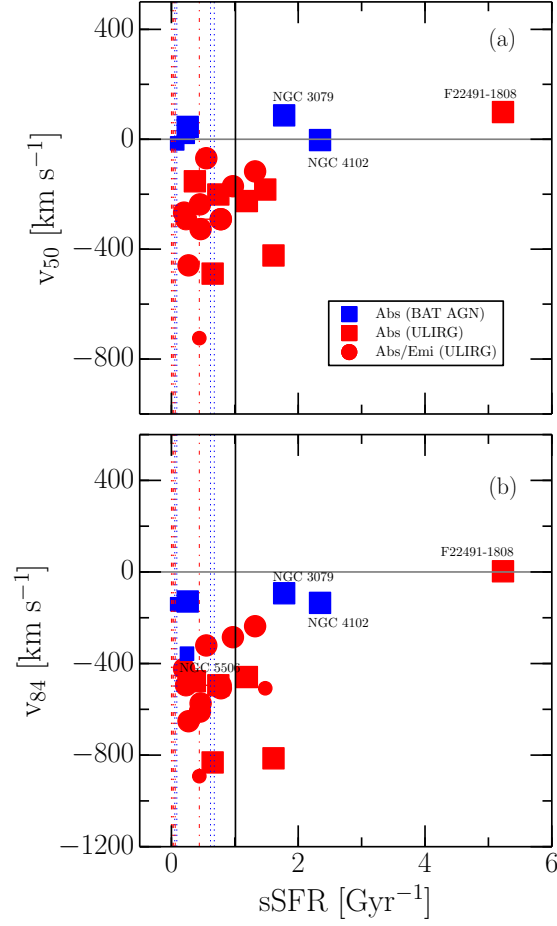


Figure 2.9 v_{50} and v_{84} as a function of the specific star formation rates. The meanings of the symbols are the same as those in Section 2.5.1.1. The data points joined by a segment correspond to F14394+5332 E and W. The smaller symbols have larger uncertainties (values followed by double colons in Table 3.3) The black vertical line indicates the approximate location of the Main Sequence of star-forming galaxies (Shimizu et al., 2015).

of lower luminosities are not able to drive significant molecular winds.

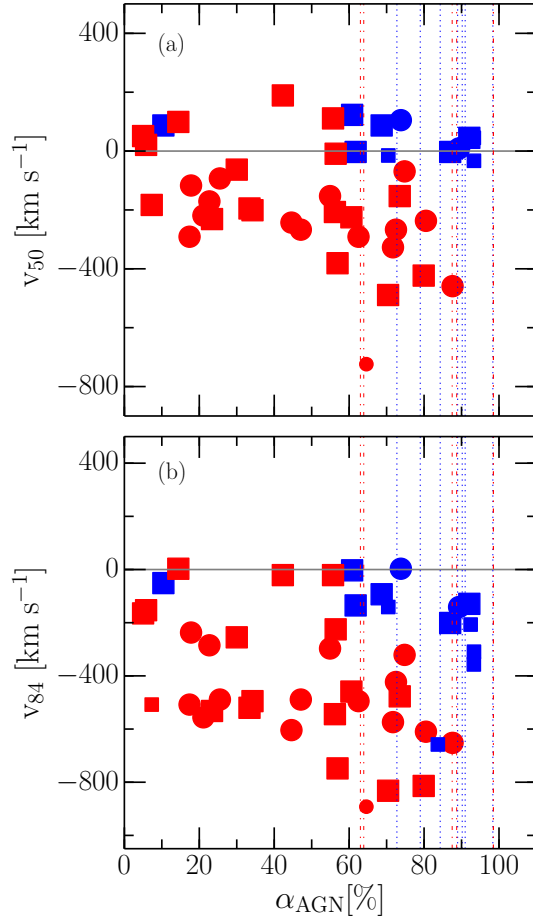


Figure 2.10 v_{50} and v_{84} as a function of the AGN fractions. The meanings of the symbols are the same as those in Section 2.5.1.1. The smaller symbols have larger uncertainties (values followed by double colons in Table 3.3)

2.7 Discussion

2.7.1 Outflows

2.7.1.1 BAT AGN with Molecular Outflows

As mentioned above, only (one) four objects in our BAT AGN sample shows (unambiguous) evidence of a molecular outflow (NGC 7479 is the unambiguous case, while NGC 5506, NGC 7172, and IC 5063 are more uncertain; see Figure 2.8 and

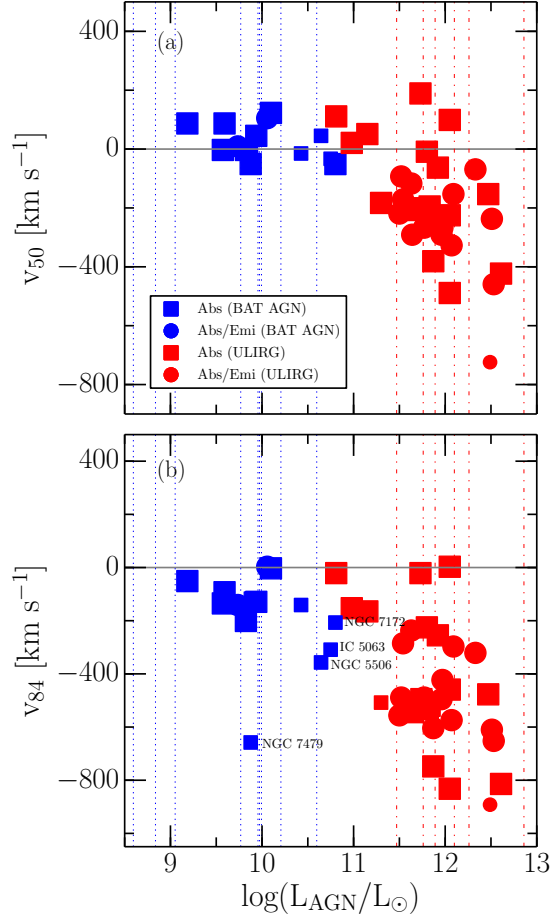


Figure 2.11 v_{50} and v_{84} as a function of the AGN luminosities. The meanings of the symbols are the same as those in Section 2.5.1.1. The smaller symbols have larger uncertainties (values followed by double colons in Table 3.3)

Figure 2.11). This corresponds to an outflow detection rate of (6%) 24%, if we take into account that this search for outflows was possible only in the 17 sources with OH 119 μm in absorption. This outflow detection rate is significantly smaller than that found in ULIRGs ($\sim 70\%$). We note, however, that outflow detection may be easier in the ULIRGs due to their higher gas fractions.

NGC 7479 is the best case for an outflow in our sample of BAT AGN. NGC 7479 is a barred galaxy with the faint broad line emission at $\text{H}\alpha$ but not at $\text{H}\beta$ of a Seyfert 1.9 galaxy (Véron-Cetty & Véron, 2006). To quantify the uncertainty

of the OH blue-wing detection in NGC 7479, we have refit the continuum for this object with a third order polynomial and then refit the OH doublet via the method outlined in [Section 2.5.1.3](#). Although we find a shift in the velocities measured with this different continuum ($v_{50}(\text{abs}) = -45 \text{ km s}^{-1}$ and $v_{84}(\text{abs}) = -513 \text{ km s}^{-1}$), this shift (a measure of the error in our velocity estimates) is not large enough to account for the location of NGC 7479 in [Figure 2.11b](#). The origin for the high outflow velocity in NGC 7479 may lie in its unusually high far-infrared surface density ([Lutz et al., 2015](#)). The high wind velocity observed in NGC 7479 may thus be due to its unusually high SFR surface density (e.g. [Diamond-Stanic et al., 2012](#)). However, we cannot exclude the possibility that the OH outflow in NGC 7479 is driven by the radio jet detected by [Laine & Beck \(2008\)](#).

NGC 5506 is an edge-on disk galaxy optically classified as a Seyfert 1.9 galaxy, just like NGC 7479. In the very hard X-ray regime, NGC 5506 is one of the most luminous and brightest Seyferts in the local universe ($L_{14-195 \text{ keV}} \sim 10^{43} \text{ erg s}^{-1}$; [Baumgartner et al., 2011](#)), and its obscuring column ($N_{\text{H}} = 3.4 \times 10^{22} \text{ cm}^{-2}$; [Bassani et al., 1999](#)) is intermediate between typical values for Seyfert 1s and 2s. Mid-infrared $8 - 13 \mu\text{m}$ observations of NGC 5506 ([Roche et al., 1984](#)) suggest that the nuclear region of NGC 5506 within 5 arcsec is powered by highly obscured AGN activity with little starburst activity. The OH $119 \mu\text{m}$ line profile of NGC 5506 shows a very broad, secondary gaussian component, suggestive of an outflow (see [Figure 2.1](#)), but the velocities of this component are uncertain (see [Table 3.3](#)). Interestingly, the optical forbidden emission lines of NGC 5506 also exhibit distinct blue wings extending to -1000 km s^{-1} ([Veilleux, 1991a,b,c](#)), giving credence to the

idea that a fast outflow is indeed present in this object.

IC 5063 is a massive ($M_* \approx 10^{11} M_\odot$) early-type galaxy which hosts a powerful double-lobed radio source ($P_{1.4\text{GHz}} = 3 \times 10^{23} \text{ W Hz}^{-1}$). The presence of this strong radio source is contrary to the weakly collimated jets found in the BAT AGN of [Middelberg et al. \(2004\)](#). Observations of high velocity ($\sim 600 \text{ km s}^{-1}$) warm molecular hydrogen gas in the western lobe of IC 5063 suggests that molecules may be shock-accelerated by the expanding radio jets ([Tadhunter et al., 2014](#)). Thus, the presence of this powerful jet may explain the additional boost observed in the (uncertain) outflow velocity v_{84} .

NGC 7172 is an obscured ($N_{\text{H}} \sim 10^{23} \text{ cm}^{-2}$; [Turner & Pounds, 1989](#)), almost edge-on Type 2 Seyfert galaxy which belongs to the Hickson compact group HCG 90. [Smajić et al. \(2012\)](#) derive the two-dimensional velocity field and velocity distribution of the central $4'' \times 4''$ region of NGC 7172 using several emission lines (i.e. $\text{Pa}\alpha$, $\text{H}_2(1-0)\text{S}(1)$, and $[\text{Si VI}]$) and two CO stellar absorption features. All measurements indicate disk rotation from east to west with amplitude of at least $\pm 100 \text{ km s}^{-1}$. Comparison of HST F606W imaging ([Malkan et al., 1998](#)) with 2MASS images in J -, H -, and K -bands ([Jarrett et al., 2003](#)) shows a shift of the nucleus by more than $1''$ going from the visible to the J -, H -, and K -band. The central spaxel aperture ($9.4'' \times 9.4''$) of *Herschel* does not have the resolution to detect such a shift, but if the central spaxel is not centered on the galaxy nucleus, and if the velocity structure for OH 119 μm is comparable to that seen in the near-infrared, then it is possible that the blueshifted absorption we detect is due to incomplete sampling of the rotation curve rather than a molecular outflow.

This last object emphasizes the fact that the poor spatial resolution of *Herschel* makes the interpretation of the OH spectra challenging. We have tried to err on the side of being cautious by utilizing a centroid velocity threshold of -50 km s^{-1} and/or the detection of blue wings with $v_{84} < -300 \text{ km s}^{-1}$. The *Herschel* data are not always sensitive to small-scale winds. Indeed, small-scale molecular winds are known to exist in some of our sources. For instance, [García-Burillo et al. \(2014\)](#) detect AGN-driven CO(3-2), CO(6-5), HCN(4-3), HCO⁺(4-3), and CS(7-6) outflows in NGC 1068 on spatial scales of $\sim 20 - 35 \text{ pc}$ ($\sim 0.3'' - 0.5''$), while OH is observed purely in emission in the *Herschel* data and is therefore ambiguous regarding the existence of a large-scale outflow until a full analysis of the velocity field is carried out. Additionally, molecular outflows (or inflows) may be present, but not centered on the central spaxel. For example, *Herschel* observations of OH 79, 84, and 65 μm , as well as HCN suggest the existence of a spatially resolved outflow outside of the central spaxel in NGC 3079 even though the central spaxel apparently displays an OH inflow. A detailed discussion of these objects is outside the scope of this work, but these issues will be addressed in a future paper.

2.7.1.2 Driving Mechanisms of Molecular Outflows

Correlations between the observed OH outflow velocities and the stellar masses, star formation rates, and AGN luminosities of the host galaxies can shed light upon the physical mechanisms responsible for driving molecular winds. There are good reasons to believe that energy and momentum injection from star formation ac-

tivity plays a role in driving massive, galactic-scale outflows. For example, the observed spatial coincidence between H- α filaments and the X-ray emission from galactic winds suggests a close physical connection between the origins of these features (Cooper et al., 2008). Additionally, previous studies (e.g. Cicone et al., 2014; Martin, 2005; Rupke et al., 2005a; Schwartz & Martin, 2004; Weiner et al., 2009) have shown the existence of a positive trend between SFRs and outflow velocities. Curiously, V13 found no such trend in their ULIRGs + QSO sample. It appears, as V13 surmised, that the lack of a trend between these quantities was due to the limited range in SFR of the V13 sample, which spans only ~ 2 dex. As seen in Figure 2.8, when the BAT AGN are combined with the ULIRGs of V13, the sample spans a range ~ 3 dex in SFR, and a positive correlation between outflow velocities and SFRs becomes apparent.

Positive correlations between stellar masses and outflow velocities in the neutral and ionized phases of the ISM have also been reported in the literature (e.g. Martin, 2005; Rupke et al., 2005a; Weiner et al., 2009). V13 did not see this trend in the molecular data of their ULIRG + QSO sample, but again attributed this negative result to the small range in stellar masses of their sample (~ 1 dex). Our BAT AGN + ULIRG + QSO sample now extends over a stellar mass range of ~ 2 dex and reveals a significant trend (see Figure 2.7). However, note that this trend may be of secondary origin since a positive correlation is well known to exist between stellar mass and SFR in galaxies, both locally (e.g. $0.015 \leq z \leq 0.1$; Elbaz et al., 2007; Renzini & Peng, 2015; Shimizu et al., 2015) and at high redshift (e.g. $0.7 < z < 1.5$; Rubin et al., 2010; Whitaker et al., 2014) – the so-called Main

Sequence of star-forming galaxies.

V13 reported a weak trend between wind velocities (v_{50} and v_{84}) and AGN fractions in their ULIRG sample. They cautioned that the correlation could be merely an obscuration effect where both the AGN and central high-velocity outflowing material are more easily detectable when the dusty material has been swept away or is seen more nearly face-on. Indeed, by adding our BAT AGN sample to the ULIRG sample, we find that this weak correlation disappears. AGN fractions are thus not a good predictor of molecular outflows. On the other hand, a convincing causal connection was presented in V13 between AGN luminosities and molecular outflow velocities with a possible steepening of the relation above $\log(L_{\text{AGN}}^{\text{break}}/L_{\odot}) = 11.8 \pm 0.3$. Our results do indeed strongly suggest that at higher AGN luminosities ($\log(L_{\text{AGN}}/L_{\odot}) \gtrsim 11.5$) the AGN dominates over star formation in driving the outflow. At lower luminosities ($\log(L_{\text{AGN}}/L_{\odot}) \lesssim 11.5$) the AGN may not have the energetics required to drive fast molecular winds.

Statistically, the correlation between wind velocity and AGN luminosity is stronger than the correlation between wind velocity and SFR (see [Table 2.7](#)). However, while the AGN may be the dominant source for driving the winds observed in our sample, it is clear that SFR also plays a role in driving these winds. The presence of an AGN seems to boost the observed velocity over that which would be observed in purely star forming systems ([Cicone et al., 2014](#)), although large scatter is observed (see [Figure 2.11](#)). This scatter may have multiple origins: (1) If the outflow is not spherically symmetric, projection effects will produce scatter in the observed velocities. (2) The efficiency to entrain material in the outflow depends on

several complex factors associated with the acceleration mechanisms and the multi-phase nature of these processes. For instance, if radiation pressure is the dominant mechanism driving the outflow, radiative transfer effects are probably important so that not all of the OH-detected gas is “seeing” the same radiation field and therefore not experiencing the same radiation force. Similarly, if the dominant driving mechanism is ram pressure of a fast diffuse medium on dense cloudlets, one might expect to observe a range of velocities depending on the characteristics (e.g., sizes and densities) of the cloudlets entrained in the flow and their survival timescales (e.g. [Cooper et al., 2008, 2009](#)). (3) The AGN luminosity is measured from the 14 – 195 keV flux and therefore represent the current value of the AGN luminosity. In contrast, the observed outflow was likely produced ~ 1 to several $\times 10^6$ years ago based on the measured OH velocities and inferred outflow sizes (≤ 1 kpc; [González-Alfonso et al. \(2014b, 2015\)](#); [Sturm et al. \(2011\)](#)). AGN variability may therefore cause considerable scatter in [Figure 2.11](#).

2.7.2 Inflows

Seven objects (Centaurus A, Circinus, NGC 1125, NGC 3079, NGC 3281, NGC 4945, and NGC 7582) have OH absorption features with median velocities larger than 50 km s^{-1} , corresponding to an inflow detection rate of $\sim 40\%$. By far the best case for inflow in our sample is Circinus where OH 119 μm shows an inverted P-Cygni profile. Inverted P-Cygni profiles are also tentatively detected in Centaurus A and NGC 3281.

Interestingly, previous searches for neutral-gas (Na I D) outflows/inflows in IR-faint Seyfert galaxies have also shown distinctly higher detection rates of inflows than outflows. Specifically, in an analysis of 35 IR-faint Seyferts ($10^{9.9} < L_{\text{IR}}/L_{\odot} < 10^{11.2}$), [Krug et al. \(2010\)](#) reported an inflow detection rate of $\sim 37\%$ and an outflow detection rate of only $\sim 11\%$. These numbers are similar to those derived here, and considerably different from those measured in (U)LIRGs using OH ($\sim 10\%$; V13) and Na I D (e.g. $\sim 15\%$ inflow detection rate for 78 starbursting galaxies with $\log(L_{\text{IR}}/L_{\odot}) = 10.2 - 12.0$; [Rupke et al., 2005a,b](#)). The origin of this difference is unknown. The fast winds in (U)LIRGs may disturb the neutral-molecular gas and prevent it from infalling to the center. On average, IR-bright sources are also richer in gas and dust than IR-faint galaxies. This material may be masking the central regions where inflow is taking place.

2.7.3 The 9.7 μm Silicate Feature

The analysis of the strength of the $S_{9.7\mu\text{m}}$ feature can provide insight into the mechanism responsible for the excitation of OH 119 μm observed in our sample. As seen in [Figure 2.5](#), the comparison of the OH 119 μm equivalent width, EW_{OH} , and the strength of the silicate feature, $S_{9.7\mu\text{m}}$, implies a rather tight connection between OH gas and mid-infrared obscuration (a correlation is also found between OH 65 μm and $S_{9.7\mu\text{m}}$; see also [González-Alfonso et al. \(2015\)](#)). The clear trend of deeper OH 119 μm absorption and fainter OH 119 μm emission with increasing silicate obscuration (more positive values of $S_{9.7\mu\text{m}}$) suggests that OH 119 μm emission is

strongly affected by the obscuring geometry. Our results expand on those of V13 and S13 who found a similar trend with OH equivalent width and the strength of the $9.7 \mu\text{m}$ feature among ULIRGs.

S13 argue that the OH $119 \mu\text{m}$ emission region often lies within the buried nucleus and that radiative excitation is the dominant source of OH $119 \mu\text{m}$ emission. In reality, the geometry of the silicate obscuration and the source of the OH $119 \mu\text{m}$ emission may be more complex. [Figure 2.12](#) plots the total equivalent width of OH $119 \mu\text{m}$ as a function of $S_{9.7 \mu\text{m}}$ and distinguishes between AGN spectral type for each object. Note that objects classified as LINERs have been excluded from this plot due to the ambiguous energy source in these objects ([Sturm et al., 2006](#)). None of the Type 1 galaxies (BAT AGN or ULIRGs) show a strong silicate absorption ($S_{9.7 \mu\text{m}} \gtrsim 1.5$). Interestingly, we see that OH $119 \mu\text{m}$ for some Type 2 BAT AGN and ULIRGs is observed in emission ($\text{EW}_{\text{OH}} < 0 \text{ km s}^{-1}$) while the silicate feature, $S_{9.7 \mu\text{m}}$, is seen in absorption. It is possible that the OH $119 \mu\text{m}$ emission region is not nuclear, but is instead distributed throughout a circumnuclear starburst where the number density ($n(\text{H}_2) \sim \text{a few times } 10^5 \text{ cm}^{-3}$), temperature ($\sim 100 \text{ K}$), and OH abundance ($X(\text{OH}) \sim 2 \times 10^{-6}$) are sufficient for collisional rather than radiative excitation of the upper level of OH $119 \mu\text{m}$ (e.g. NGC 1068; [Spinoglio et al., 2005](#)). Until we examine in detail all 5×5 spaxels of the PACS data, the location of the OH emission in our objects will remain unclear. This type of analysis can be done in just a few select objects; this will be discussed in a future paper.

Determining the origin of the silicate feature is also a challenge. The dust responsible for this feature may reside in the AGN torus, or on larger scale in the

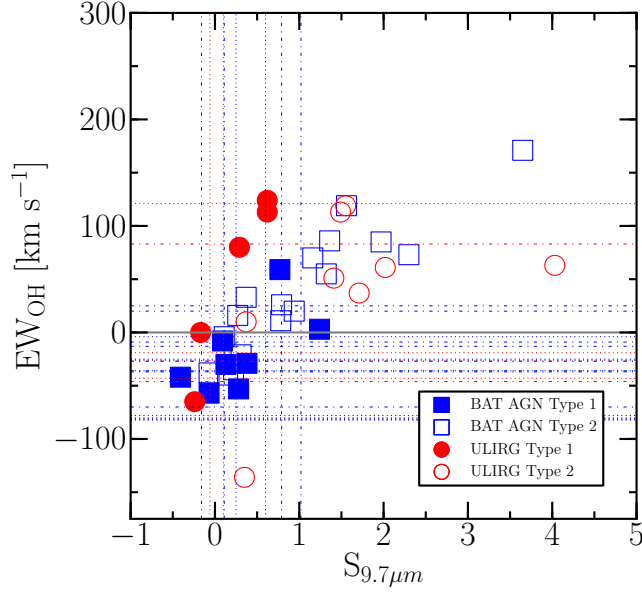


Figure 2.12 Total (absorption + emission) equivalent widths of OH 119 μm as a function of the apparent strength of the 9.7 μm silicate feature relative to the local mid-infrared continuum. Note that $S_{9.7\mu\text{m}}$ is a logarithmic quantity and can be interpreted as the apparent silicate optical depth. The strength of this absorption feature increases to the right. Also note that objects classified as LINERs have been excluded from this plot. Filled markers refer to Type 1 and open markers refer to Type 2. Blue squares and red circles represent BAT AGN and ULIRGs/PG QSOs, respectively. Vertical lines represent objects in which OH was not detected. Horizontal lines represent objects with a null $S_{9.7\mu\text{m}}$ detection. Dotted lines and dash-dotted lines refer to Type 1 and Type 2, respectively. Blue and red lines indicate BAT AGN and ULIRGs/PG QSOs, respectively.

disk of the host galaxy, or some combination of these two.

Figure 2.13 plots the ratio of the semi-minor and semi-major axes (a proxy for the inclination of the host galaxy disk) as a function of $S_{9.7\mu\text{m}}$ for BAT AGN. We have excluded the ULIRG/PG QSO sample from this particular analysis because these objects are undergoing or have undergone a major merger, and therefore, do not have a well-defined galactic plane or inclination. Visual inspection of Figure 2.13 suggests a weak trend between the inclination of the BAT AGN host galaxy and the depth of the 9.7 μm silicate feature. First, we see that OH for nearly face-on

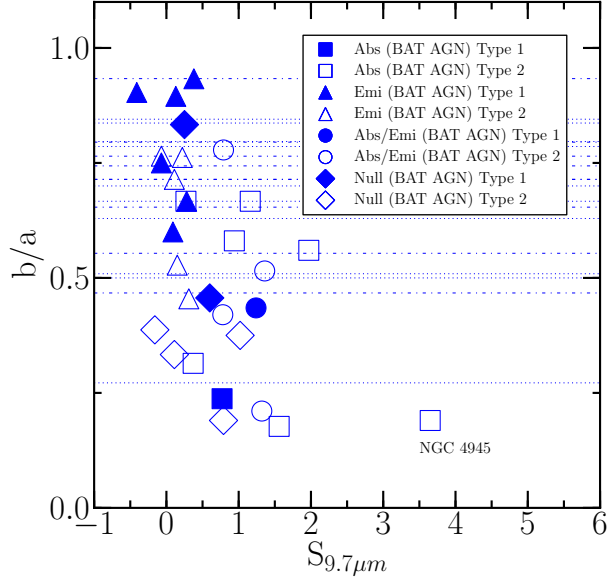


Figure 2.13 Ratio of the semi-minor axis to the semi-major axis (a proxy for the inclination of the host galaxy disk) as a function of $S_{9.7\mu\text{m}}$ for the BAT AGN sample. Squares, triangles, and circles represent BAT AGN in which OH is observed purely in absorption, purely in emission, composite absorption/emission, respectively. Diamonds represent objects in which OH was undetected. Filled points and dash-dotted lines indicate Type 1 while open points and dotted lines indicate Type 2 AGN. Horizontal lines represent objects with a null $9.7\mu\text{m}$ silicate feature detection.

hosts ($b/a \gtrsim 0.8$) is seen only in pure emission and the strength of $S_{9.7\mu\text{m}}$ is weak. Second, we find that nearly edge-on galaxies show the broadest range of silicate absorption strengths, including the most extreme case of NGC 4945. However, the lack of a strong trend between inclination and $S_{9.7\mu\text{m}}$ strength suggests that the dust responsible for the $9.7\mu\text{m}$ silicate feature is located not only in the plane of the host galaxy, but also in the nuclear torus. Our results are qualitatively consistent with [Goulding et al. \(2012\)](#), who invoke a clumpy torus paradigm of many individual optically thick clouds ([Nenkova et al., 2002, 2008](#)) and suggest that deeper silicate features ($S_{9.7\mu\text{m}} \gtrsim 0.5$) are due to dust distributed at radii much larger ($\gg \text{pc}$) than that predicted for a torus.

2.8 Conclusions

We present the results of our analysis of *Herschel*/PACS spectroscopic observations of 52 nearby ($d < 50$ Mpc) BAT AGN selected from the very hard X-ray (14-195 keV) *Swift*-BAT Survey of local AGN. We also include in our analysis the *Herschel*/PACS data on 38 ULIRGs and 5 PG QSOs from V13. The depth of the silicate feature at $9.7 \mu\text{m}$ feature in all these objects is measured from archival Spitzer/IRS data. Our combined BAT AGN + ULIRG + QSO sample covers a range of AGN luminosity and SFR of $\gtrsim 3$ dex and ~ 3 dex, respectively. The main results from our analysis are:

1. The OH $119 \mu\text{m}$ feature is detected in 42 of the 52 objects in our BAT AGN sample. Of these detections, OH $119 \mu\text{m}$ is observed purely in emission for 25 targets, purely in absorption for 12 targets, and absorption+emission composite for 5 targets.
2. Evidence for molecular outflows (absorption profiles with median velocities more blueshifted than -50 km s^{-1} and/or blueshifted wings with 84-percentile velocities less than -300 km s^{-1}) is seen in only four objects (NGC 7479, NGC 5506, NGC 7172, and IC 5063), corresponding to 24% of all targets where this search for outflows was possible. This outflow detection rate is significantly smaller than that found in ULIRGs by V13 ($\sim 70\%$). The best case for outflow is NGC 7479, an object with one of the highest infrared surface densities among our BAT AGN.

3. We find evidence for molecular inflows (absorption profiles with median velocities more redshifted than 50 km s^{-1}) in seven objects (Circinus, NGC 1125, NGC 3079, NGC 3281, and NGC 4945), corresponding to an inflow detection rate of $\sim 40\%$, considerably higher than the rate measured among ULIRGs ($\sim 10\%$) but similar to the detection rate of neutral-gas (Na I D) inflows among IR-faint Seyfert galaxies. By far the best case for OH inflow among our BAT AGN is Circinus, where OH $119 \mu\text{m}$ shows a distinct inverted P-Cygni profile.
4. The positive correlation between OH velocities and AGN luminosities reported in V13 is strengthened in the combined sample, but it is not seen in the BAT AGN sample. This suggests that luminous AGN play a dominant role in driving the fastest winds, but stellar processes will dominate when the AGN is weak or absent.
5. We confirm that the absorption strength of OH $119 \mu\text{m}$ is a good proxy for dust optical depth in these systems. Our findings are consistent with most, but not all, of the OH $119 \mu\text{m}$ emission originating near the AGN. Spatially resolved OH emission is seen in a few objects in our sample (e.g., NGC 1068) and may originate from a circumnuclear starburst where the number density and temperature are sufficiently high to collisionally excite the upper level of OH $119 \mu\text{m}$.
6. A comparison of the strength of the $9.7 \mu\text{m}$ silicate feature with the inclination of the host galaxy disk and spectral type of the AGN confirm earlier results that the dust responsible for this feature is located not only in the nuclear

component, but also in the disk of the host galaxy.

Chapter 3: Constraints on the OH-to-H Abundance Ratio in Infrared-Bright Galaxies Derived from the Strength of the OH 35 μm Absorption Feature

3.1 Introduction

Galactic-scale outflows are driven by the collective effects of supernovae, winds from massive stars, and winds or jets from active galactic nuclei (AGN; e.g. [Veilleux et al., 2005](#), and references therein). These outflows can disperse heavy elements, interstellar dust, and energy throughout a galaxy and into the galaxy halo; they may therefore play a significant (if not dominant) role in galaxy evolution (e.g. [Benson et al., 2003](#); [Bower et al., 2006](#); [Croton et al., 2006](#); [Fabian, 2012](#); [Hopkins et al., 2008, 2006](#); [King, 2010](#); [Springel, 2005](#)). They have been detected ubiquitously in both low- and high-redshift systems (e.g. [Alexander et al., 2010](#); [Banerji et al., 2011](#); [Brusa et al., 2016](#); [Cano-Díaz et al., 2012](#); [Carniani et al., 2015, 2016](#); [Cicone et al., 2015](#); [Cresci et al., 2015](#); [Förster Schreiber et al., 2014](#); [Genzel et al., 2014](#); [Greene et al., 2012](#); [Harrison et al., 2014, 2012, 2016](#); [Kornei et al., 2012](#); [Maiolino et al., 2012](#); [Martin et al., 2012](#); [McElroy et al., 2015](#); [Nesvadba et al., 2011](#); [Tremonti et al., 2007](#); [Veilleux et al., 2005](#); [Weiner et al., 2009](#); [Zakamska et al., 2016](#)). They are

particularly significant in infrared luminous galaxy mergers where both starbursts and luminous AGN often co-exist together (e.g. [Cicone et al., 2014](#); [González-Alfonso et al., 2017](#); [Janssen et al., 2016](#); [Martin, 2005, 2006](#); [Rupke et al., 2017, 2002, 2005a,b,c](#); [Rupke & Veilleux, 2011](#); [Spoon et al., 2013](#); [Sturm et al., 2011](#); [Veilleux et al., 2017, 2013](#)). However, the central regions of these mergers are generally enshrouded in dust so infrared tracers are needed to peer through the dusty veil.

Numerous studies have demonstrated that the infrared transitions of the hydroxyl molecule, OH, are a powerful diagnostic tool with which to investigate the nature of cool molecular outflows. [Fischer et al. \(2010\)](#) first reported the remarkable detection of OH 79 and 119 μm (hereafter, the OH λ -doublet transitions will be referred for short only by their rounded wavelengths: OH 79 and OH 119) with P-Cygni profiles (incontrovertible evidence of the presence of an outflow) in the nearby QSO, Mrk 231. Results from [Sturm et al. \(2011\)](#) revealed the detection of massive molecular outflows traced by OH 79 for six galaxies and a tentative correlation between OH outflow velocities and AGN luminosities. This correlation was confirmed by [Veilleux et al. \(2013\)](#) (and [Spoon et al., 2013](#)) who reported the detection of OH outflows in $\sim 70\%$ of 43 (24) ULIRGs + QSOs, and further strengthened when [Stone et al. \(2016\)](#) combined the 43 ULIRGs + QSOs of [Veilleux et al. \(2013\)](#) with OH 119 observations of 52 Swift/Burst Alert Telescope (BAT)-detected AGN.

In order to evaluate the impact of these outflows on the evolution of their host galaxies, it is necessary to measure the sizes and energetics (e.g., mass-outflow rate, momentum flux, and mechanical power) of these outflows. Multi-transitional OH analyses have had considerable success constraining these quantities and the

dominant mechanisms driving these winds (González-Alfonso et al., 2014b, 2017). All of the dynamical quantities depend on the hydrogen column densities inferred from the OH features. These in turn depend on the OH-to-H abundance ratio, X_{OH} , needed to infer the H column densities from the measured OH column densities. This abundance ratio is generally *assumed* to be $\sim 2.5 \times 10^{-6}$, based on the value inferred from multitransition observations of OH in the Galactic Sgr B2, the Orion KL outflow, and in buried nuclei, as well as predictions of chemical models of photodissociation regions and of cosmic-ray- and X-ray-dominated regions (see González-Alfonso et al., 2017, and references therein).

In this paper, we provide an independent constraint on X_{OH} . We focus our attention on the OH 35 μm (hereafter, OH 35) absorption feature covered by *Spitzer*-IRS. OH 35 is optically thinner than the other OH doublets in the far-infrared, and although it is more sensitive to extinction effects, OH 35 remains a reliable indicator of OH column densities. OH is assumed to be mixed with dust and given the high continuum optical depths (even in the far-IR; González-Alfonso et al., 2014b), the absorption is restricted to a “skin” of matter. Our OH column densities therefore also provide a constraint on the abundance of OH relative to the dust, from which X_{OH} (relative to H nuclei) is derived, assuming a gas-to-dust ratio. We are able to carry out this analysis on 15 local ($z \sim 0.06$) (ultra-)luminous infrared galaxies (U/LIRGs), which have both *Herschel*-PACS observations of the OH 119 and/or 79 μm transitions as well as *Spitzer*-IRS observations of the OH 35 μm transition.

Background information on the structure of the OH molecule is presented in Section 3.2. The galaxy sample, data reduction, and spectral analysis are described

Table 3.1. *Spitzer*-IRS Spectra: Observations

Name	PI	AORKey(s)
(1)	(2)	(3)
Arp 220	Houck, James	16910080, 21247232
IRAS F04454-4838	Armus, Lee	20334080
IRAS F05189-2524	Calibration, IRS	04969216
IRAS F08572+3915	Calibration, IRS	20925696, 21457920, 24568064, 27381760, 28704256
IRAS F12224-0624	Bradford, Charles	11272960
IRAS 15250+3609	Houck, James	04983040
IRAS 17208-0014	Houck, James	04986624
IRAS F20551-4250	Houck, James	04990208
IRAS F23128-5919	Houck, James	04991744
Mrk 231	Calibration, IRS	16694016, 17102592, 17202688, 19318016, 21453568, 22157312, 24915456, 34294016
Mrk 273	Houck, James	04980224
NGC 2623	Houck, James	09072896
NGC 4418	Houck, James	04935168
UGC 5101	Houck, James	04973056
Zw453.062	Sturm, Eckhard	10512128

Note. — Column 1: Galaxy name. Column 2: Principle Investigator. Column 3: AORKey.

in [Section 3.3](#). [Section 3.4](#) presents the results of the OH 35 line profile fitting. [Section 3.5](#) discusses the implications of our results. A summary of the results and conclusions is given in [Section 4.10](#).

Table 3.2. Galaxy Properties

Name	Other Name	z^a	f_{15}/f_{30}	α_{AGN} [%]	$\log L_{\text{bol}}$ [L_{\odot}]	$\log L_{\text{SB}}$ [L_{\odot}]	$\log L_{\text{AGN}}$ [L_{\odot}]	σ_* [km s^{-1}]	M_H <i>mag</i>	Type
(1)	(2)	(3)	(4)	(5)	(6)	(7)	(8)	(9)	(10)	(11)
IRAS F04454-4838		0.0529	0.09 ^b	42.0	11.84 ^c	11.61	11.47
IRAS F05189-2524		0.0426	0.198	71.7	12.22	11.67	12.07	137	-23.96	AGN 2
IRAS F08354+2555	NGC 2623	0.01846	0.07 ^b	29.6	11.58 ^c	11.05	11.43	L
IRAS F08572+3915		0.0584	0.191	70.4	12.2	11.67	12.05	...	-23.58	L
IRAS F09320+6134	UGC 5101	0.0394	0.13	56.4	12.05	11.69	11.8	L
IRAS F12224-0624		0.02636	0.04 ^b	0	11.34 ^c	...	11.34	L
IRAS F12243-0036	NGC 4418	0.00727	0.128	55.7	11.06	10.71	10.81	AGN 2
IRAS F12540+5708	Mrk 231	0.0422	0.272	80.5	12.6	11.89	12.51	120	-24.52	AGN 1
IRAS F13428+5608	Mrk 273	0.0378	0.081	34.2	12.21	12.03	11.74	285	-24.32	AGN 2
IRAS 15250+3609		0.0554	0.095	42.3	12.1	11.86	11.73	150	...	L
IRAS F15327+2340	Arp 220	0.0181	0.049	5.8	12.22	12.19	10.98	164	...	L
IRAS 17208-0014		0.0428	0.038	< 5.0	12.45	12.43	< 11.15	229	...	L
IRAS F20551-4250		0.043	0.132	56.9	12.11	11.74	11.87	140	...	L
IRAS F23024+1916	Zw453.062	0.02510	0.07 ^b	30.0	11.36 ^c	10.84	11.21	L
IRAS F23128-5919	ESO 148-IG 002	0.0446	0.154	63	12.09	11.66	11.89	H

Note. — Column 1: Galaxy name. Column 2: Another name. Column 3: Redshift. Column 4: f_{15}/f_{30} values from [Veilleux et al. \(2009\)](#). Column 5: α_{AGN} , fractional contribution of the AGN to the bolometric luminosity based on the f_{15}/f_{30} ratio. Column 6: Bolometric luminosity. Column 7: Starburst bolometric luminosity. Column 8: AGN luminosity. Column 9: σ_* , stellar velocity dispersion from [Dasyra et al. \(2006a,b, 2007\)](#). Column 10: M_H , absolute H -band magnitudes from [Veilleux \(2006\)](#); [Veilleux et al. \(2009\)](#). Column 11: Optical spectral types, H for H II galaxies, L for LINER-like, AGN 2 and AGN 1 for type 2 AGN and type 1 AGN, respectively. For the spectral type, we adopted the classification from [Veilleux et al. \(1999, 2009\)](#). When not available, we used the values from NED/SIMBAD.

^aNASA/IPAC Extragalactic Database (NED); <https://ned.ipac.caltech.edu/>

^b f_{15}/f_{30} ratio is measured from low-resolution *Spitzer*-IRS spectra extracted from CASSIS.

^cValues for $L(40 - 500 \mu\text{m})$ and D_L (the luminosity distance) used to calculate $L(8 - 1000 \mu\text{m})$ and L_{bol} ([Sanders & Mirabel, 1996](#)) are adopted from [Armus et al. \(2009\)](#)

3.2 Background: The OH Molecule

The OH electronic ground state ${}^2\Pi$ is split due to spin-orbit coupling where spin angular momentum can be oriented either parallel or anti-parallel to the orbital angular momentum. Thus, the rotational states are split into two ladders: ${}^2\Pi_{3/2}$ and ${}^2\Pi_{1/2}$ (Storey et al., 1981), where the total angular momentum is given by $J = N \pm 1/2$ (N is the rotational quantum number). Additionally, the orbital angular momentum can have two orientations with respect to the molecular axis, each having a slightly different energy. This Λ -doubling further splits each J level into two levels of opposite parity.

The cross-ladder ${}^2\Pi_{3/2} \rightarrow {}^2\Pi_{1/2}$ $J = 3/2 \rightarrow 5/2$ Λ -doublet transition at 34.60 and 34.63 μm (see Fig.1 of González-Alfonso et al., 2014b) is an efficacious column density estimator. Within an optical depth region of $\tau_{35\mu\text{m}} \sim 0.5$, we expect OH 35 to remain optically thin, enabling us to calculate the OH abundance for a given gas-to-dust ratio. Indeed, the spontaneous transition probabilities (described by the Einstein- A coefficient) of the intra-ladder transitions are much larger ($\sim 0.1 \text{ s}^{-1}$ for $J = 3/2$ to $\sim 10 \text{ s}^{-1}$ for $J = 13/2$) than the cross-ladder transitions ($\sim 0.05 - 10^{-4} \text{ s}^{-1}$) from the same levels (Offer & van Dishoeck, 1992). Excitation of the cross-ladder transitions at 35 μm decay through multiple branches (i.e. 35 μm ; 15-84-119 μm ; 48-119 μm ; 99-53 μm ; 99-163-79 μm). Only 4% of all 35 μm absorption events result in re-emission at 35 μm (Bradford et al., 1999). Thus, OH 35 can provide a meaningful constraint on the true column density.

Note that observations of OH 35 have also proved useful in studies of OH

megamasers (Darling, 2007; Darling & Giovanelli, 2006). Radiative pumping from the absorption of 35 μm photons can invert the hyperfine population of the OH ground state. A 18 cm continuum source can then stimulate maser emission. Evidence in support of this radiative pump model was reported in Skinner et al. (1997) who observed OH 35 in Arp 220. They determined that the photon absorption rate in the 35 μm transition could be efficient enough to power observed OH masers.

3.3 Sample Selection, Data Reduction, and Spectral Analysis

3.3.1 The Sample

We have searched the *Herschel* Science Archive¹ (HSA) and the *Spitzer* Heritage Archive² (SHA) for objects with (1) $z \lesssim 0.06$ (the OH 35 feature of more distant objects will be redshifted out of the *Spitzer*-IRS wavelength range), (2) PACS spectra covering the redshifted OH 79 and/or 119 μm features, and (3) OH 35 μm detection in the IRS long high (LH) spectra. There were 242 objects which met the first two criteria and only 15 of those objects satisfied all three criteria. Details of the *Spitzer* observations for our sample are listed in Table 3.1 and galaxy properties may be found in Table 3.2.

All sources are morphologically classified as mergers or interacting systems (e.g. Veilleux et al., 2002). Our sample exhibits a range of interaction stages, from double nuclei systems with projected separation < 10 kpc (e.g. Mrk 273, IRAS F14348–1447, IRAS F20100–4156, IRAS F08572+3915), to mergers showing a sin-

¹<http://www.cosmos.esa.int/web/herschel/science-archive>

²<http://sha.ipac.caltech.edu/applications/Spitzer/SHA/>

gle nucleus with tidal tails (e.g. IRAS F05189–2524), to warm, quasar-dominated late stage mergers (e.g. Mrk 231).

The bolometric luminosities of the galaxies are similar ($\log(L_{\text{bol}}/L_{\odot}) \sim 12.2$), but the AGN contribution to the bolometric luminosity (i.e. the AGN fraction) essentially runs the full gamut from 0 to 1, resulting in AGN luminosities in the range of $\log(L_{\text{AGN}}/L_{\odot}) = 10.81 - 12.51$. The AGN fractions here are adopted from [Veilleux et al. \(2009\)](#), which are based on the 30-to-15 μm continuum flux ratio, f_{30}/f_{15} .

3.3.2 Data Reduction

All of the mid-infrared (5 – 37 μm), "high resolution" ($R \approx 600$) spectra used for this study were obtained with the Long High (LH) module of the Infrared Spectrograph (IRS; [Houck et al., 2004](#)) on board the *Spitzer* Space Telescope ([Werner et al., 2004](#)). These spectra were acquired using a high-accuracy blue peak-up and observed in staring mode. The spectra were extracted using either the S17.2 or the S18.7 pipeline of the *Spitzer* Science Center (SSC). Data reduction follows the procedure outlined in [Spoon et al. \(2009\)](#) and in [Spoon & Holt \(2009\)](#), and starts at the DROOP level products created by the SSC pipeline. These products have been corrected for stray-light contributions, non-linear responsivity in the pixels, and drooping, but have not been flat fielded. For some observations, sky background images were then subtracted, and interpolation over bad pixels was performed us-

ing the IDL package `IRSCLEAN`¹. The data analysis package `SMART` (Higdon et al., 2004) was then used to extract the one-dimensional target spectrum in “full slit” (11.1'' × 22.3'') mode.

The same procedure was followed for a large number of observations of the calibration star ξ Dra. The relative spectral response function (RSRF) was then created from the ratio of the observed spectrum of ξ Dra to the stellar reference spectrum (Cohen et al., 2003, Sloan et al. 2005, private communication). The final spectrum was obtained by multiplying the object spectrum by the RSRF. For objects with more than one AOR Key, the final spectrum is the result of co-adding (no special weighting applied) the high-resolution spectra from each AOR key.

For most of our objects, there is an artifact at $\sim 34.8\text{--}35.0\ \mu\text{m}$ in the observer’s frame in the NOD 1 spectrum, but the artifact is not present in the NOD 2 spectrum. Inspection of the RSRF for NOD 1 shows that there is a 20% dip in the response at these wavelengths. It is possible that the dip in the NOD 1 spectrum therefore originates in the RSRF. The vertical light-green band in Figure 3.1 shows the region in velocity space where the dip occurs. Fortunately, its location does not affect the OH 35 and [Si II] spectral line structures. The wavelength calibration of our spectra is accurate to about $100\ \text{km s}^{-1}$ (e.g. about 1/5 of an IRS resolution element of $500\ \text{km s}^{-1}$).

¹IRSCLEAN is available at <http://irsa.ipac.caltech.edu/data/SPITZER/docs/dataanalysistools/tools/irsclean/>

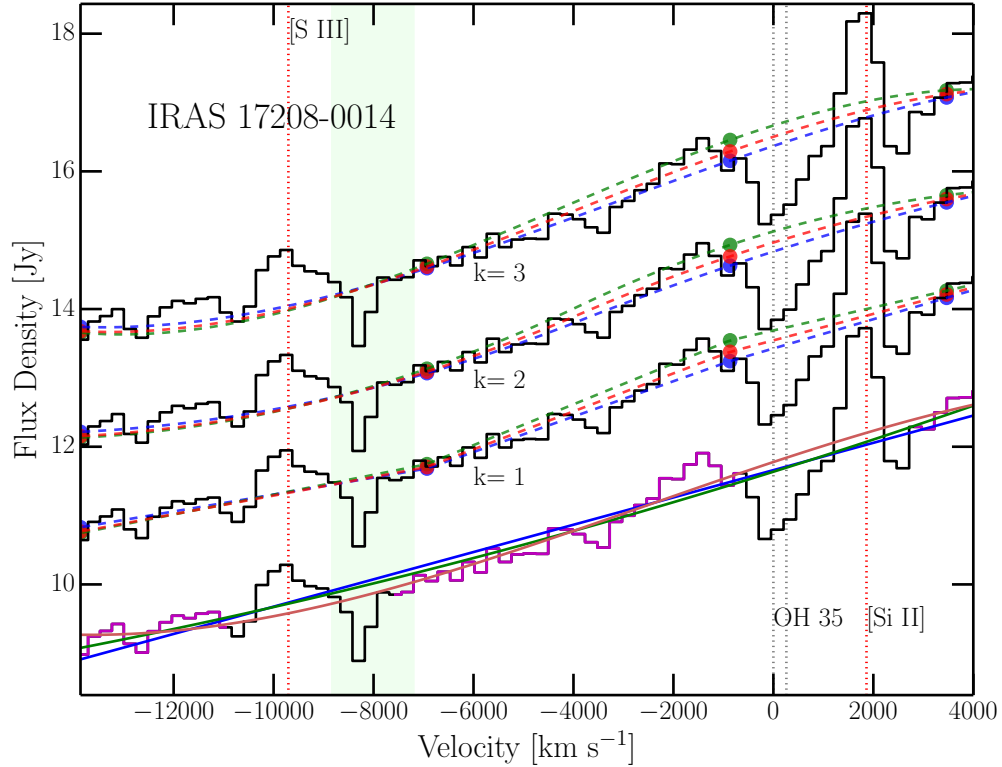


Figure 3.1 Example of twelve different continuum fits to the mid-infrared spectrum of IRAS F17208-0014. The black solid histograms are the data separated from each other by an arbitrary offset. Spline pivot points are anchored at wavelengths of $33.0 \mu\text{m}$, $33.8 \mu\text{m}$, $34.5 \mu\text{m}$, and $35.0 \mu\text{m}$. The blue, green, and red dots indicate the set of pivot points which are respectively the lower limits (v_1), upper limits (v_2), and best-fit-by-eye values (v_3) used to fit a continuum spline. The top most set of fits is the result of using a third-order ($k = 3$) spline fit to each pivot point set. Below are the results for second-order ($k = 2$) and first-order ($k = 1$) spline fits. In each case, the blue, green, and red dotted lines show the results of the spline fits to the lower-limit, upper-limit, and "best-fit-by-eye" continuum flux pivot points. The last spectrum at the bottom is fit with a polynomial. The magenta regions in this spectrum indicate the regions used to fit the first (solid blue line), second (solid green line), and third (solid red line) order polynomials to the continuum. The two dotted vertical lines in grey mark the rest wavelengths of the OH 35 doublet at systemic velocity. The dotted vertical lines in red mark the locations of the emission features [S III] $33.48 \mu\text{m}$ and [Si II] $34.82 \mu\text{m}$. The vertical light-green band shows the region where a 20% dip in the detection response in the NOD 1 position occurs.

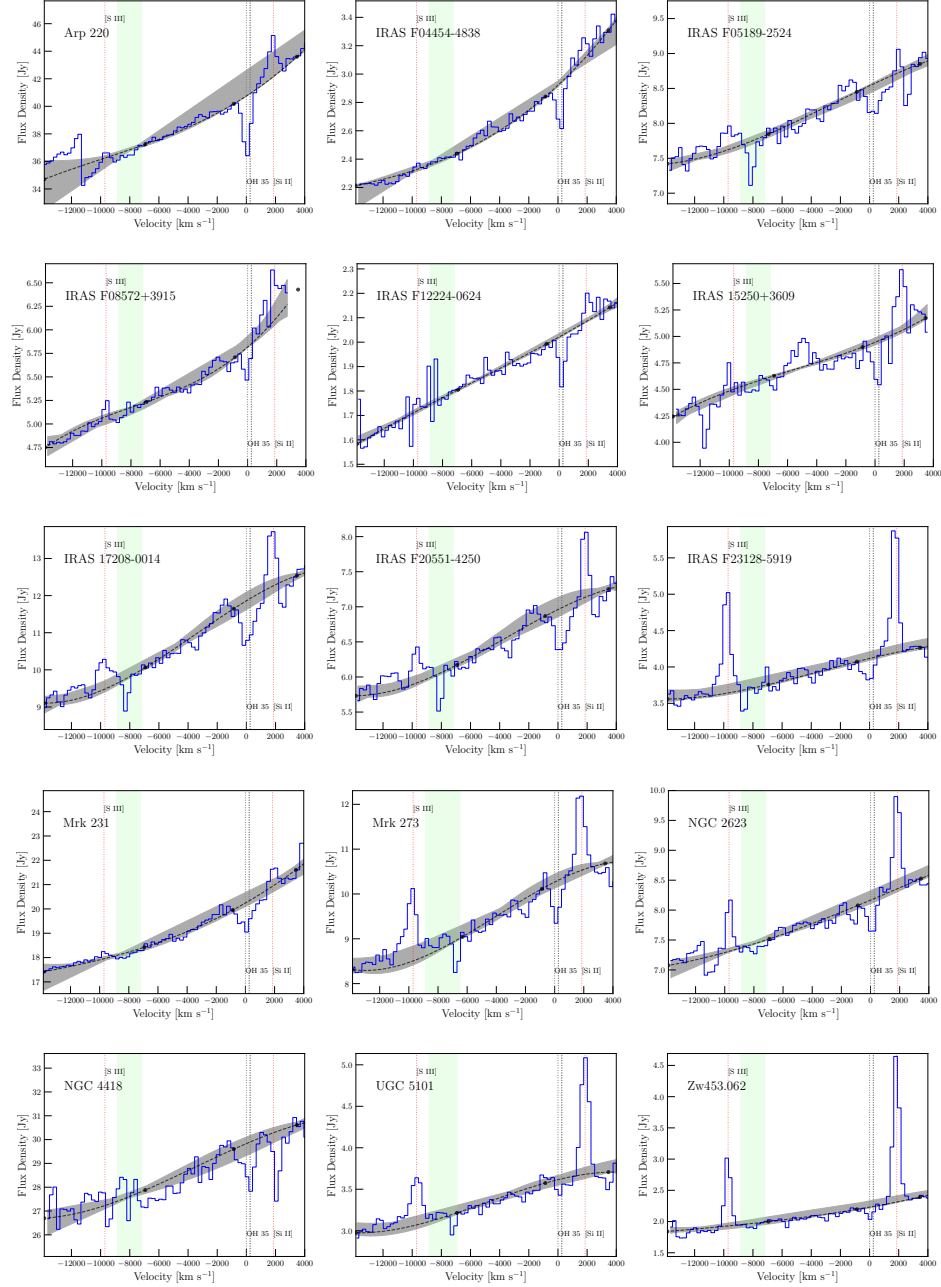


Figure 3.2 Fits to the 33 – 35 μm continua for all 15 objects in the sample. The grey shaded area shows the full range of the twelve different continuum fits described in Figure 3.1. Black dots are median values of the six fluxes at each pivot point, and the dotted line is the resultant third-order spline fit to those pivot points. The grey dotted vertical lines mark the rest wavelengths of the OH 35 doublet at systemic velocity. The red dotted vertical lines mark the locations of the emission features [S III] at 33.48 μm and [Si II] at 34.815 μm . The vertical light-green band shows the region where a 20% dip in the detection response in the NOD 1 position occurs.

3.3.3 Spectral Analysis

To determine the extent to which continuum placement affects the measured properties (e.g. total integrated flux and equivalent width) of the OH 35 feature, we have fit twelve different baselines to the spectra. First-, second-, and third-order polynomials were fit via least squares minimization using wavelength regions which avoided spectral features (e.g. emission or absorption lines) and known artifacts. Splines were also fit to the continuum via four pivot points anchored at wavelengths of $33.0 \mu\text{m}$, $33.8 \mu\text{m}$, $34.5 \mu\text{m}$, and $35.0 \mu\text{m}$. Pivot point wavelengths were chosen to avoid known spectral features within this mid-infrared region.

Three sets of continuum fluxes for the pivot points were chosen by eye. One set marks an upper limit on the continuum fluxes while another marks a lower limit on the continuum fluxes. The third set is a “best fit” by visual inspection. To each set of pivot points, a first-, second-, and third-order spline was fit. [Figure 3.1](#) shows an example of the continuum fits to IRAS F17208-0014.

[Figure 3.2](#) shows the range of continuum placements (grey shaded area) for each object. The black dots are median values of the six fluxes at each pivot point, and the dotted line is the resultant third-order spline fit to those pivot points. We choose this “median” fit as the continuum for our sources and subtract it from each spectrum. The dotted vertical lines in red mark the locations of emission features [S III] at $33.48 \mu\text{m}$ and [Si II] at $34.815 \mu\text{m}$. For both [Figure 3.1](#) and [Figure 3.2](#), the two dotted vertical lines in grey mark the rest wavelengths for both components of the OH 35 doublet at systemic velocity. These are separated by only $0.03 \mu\text{m}$ or

$\sim 250 \text{ km s}^{-1}$. Given the spectral resolution of the data ($\sim 500 \text{ km s}^{-1}$), a single blended spectral feature is detected in our sources.

Line profile fits of the OH 35 Λ -doublet were computed by using *PySpecKit*, a spectroscopic analysis and reduction toolkit for optical, infrared, and radio spectra (Ginsburg & Mirocha, 2011). The toolkit uses the Levenberg-Marquardt technique to solve the least-squares problem in order to find the best fit for the observations. Profile fitting of the OH doublet followed a similar procedure as that outlined in Veilleux et al. (2013) and in Stone et al. (2016), in which the line profile was modeled using two Gaussian components, each characterized by their negative amplitude, peak position, and standard deviation (or, equivalently FWHM). Gaussian parameters of the components were allowed to vary independently of each other. Note that these fits are only used to quantify the strength (i.e. total integrated flux and equivalent width) of the OH 35 absorption feature. The Gaussian components do not have a physical interpretation, nor do they account for each unresolved line in the doublet.

3.4 Results

Figure 3.3 shows the fits to the continuum-subtracted OH 35 feature of each galaxy. The dashed blue lines indicate the Gaussian components and the magenta line is their sum. The total integrated fluxes and equivalent widths of the OH 35 feature measured from these spectral fits and their associated $1\text{-}\sigma$ uncertainties based on the fits are listed in Table 3.3.

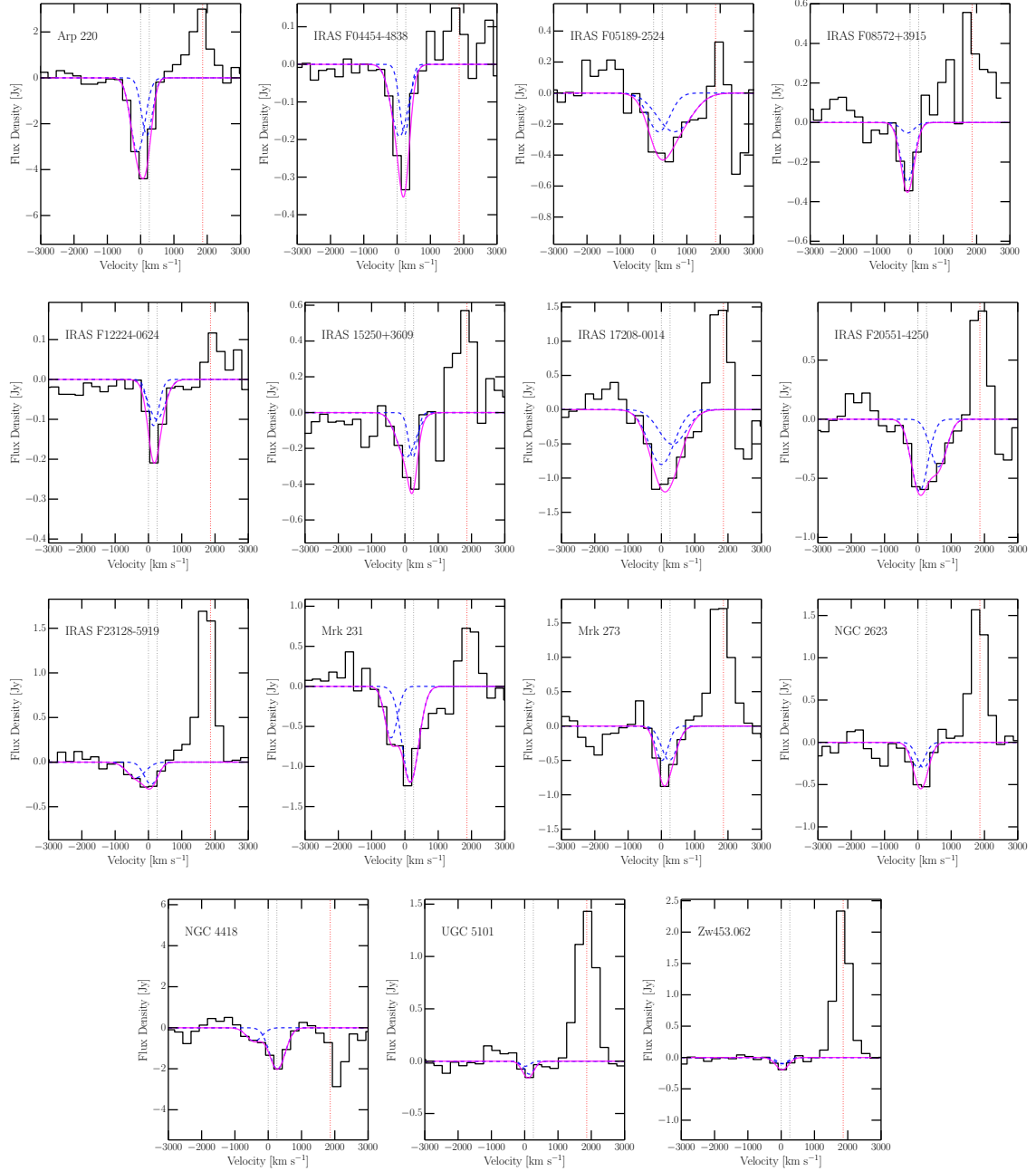


Figure 3.3 Two-Gaussian fits to the continuum-subtracted OH 35 line profiles of the 15 objects in our sample; see Section 3.3.3. In each figure, the solid black histogram is the data. Blue dashed lines indicate the two Gaussian components which best fit the line profile, and the magenta line is the sum of those two components. The grey dotted vertical lines mark the rest wavelengths of the OH 35 doublet at systemic velocity. The red dotted vertical line marks the location of the [Si II] emission line at $34.815 \mu\text{m}$.

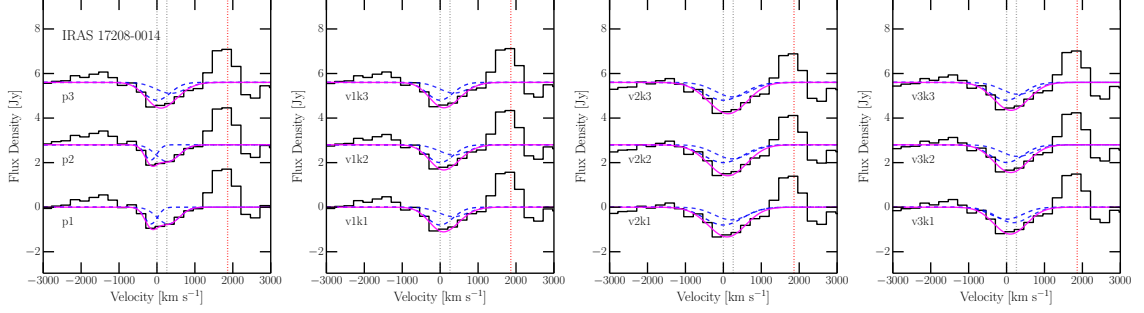


Figure 3.4 Examples of OH 35 line profile fits for each of the twelve different continuum subtracted spectra in IRAS F17208-0014. Line colors and styles are the same as that for Figure 3.3. "p1, p2, p3" indicate first-, second-, and third-order polynomial fits to the continuum, respectively. "v1" refers to the "lower-limit" pivot points in Figure 3.1. "v2" refers to the "upper-limit" pivot points, and "v3" to the "best-fit-by-eye" pivot points. "k1, k2, k3" are the orders of the spline fitted to the continuum. For example, "v2k3" is the third-order spline fit to the continuum using the "upper-limit" pivot points.

Our sources show the OH 35 line profile in absorption only. This is to be expected since essentially all OH molecules pumped to the upper ${}^2\Pi_{1/2}$, $J = 5/2$ level will relax by emitting a $99 \mu\text{m}$ photon along the ${}^2\Pi_{1/2}$ ladder instead of emitting a $35 \mu\text{m}$ photon. We note that this $99 \mu\text{m}$ emission line is not observed in the PACS observations of our sample because it is redshifted into the $100 \mu\text{m}$ gap of PACS.

Figure 3.4 shows the twelve OH 35 line profile fits to each of the continuum-subtracted spectra of IRAS F17208-0014. "p1, p2, p3" indicate first-, second-, and third-order polynomial fits to the continuum, respectively. "v1" refers to the lower limit continuum flux pivot points in Figure 3.1. "v2" refers to the upper limit continuum flux pivot points, and "v3" refers to the "best fit by eye" pivot points. "k1, k2, k3" are the orders of the spline fitted to the continuum. For example, "v2k3" is the third order spline fit to the continuum using the upper limit pivot points. The resultant fluxes and equivalent widths from all of the continuum fits

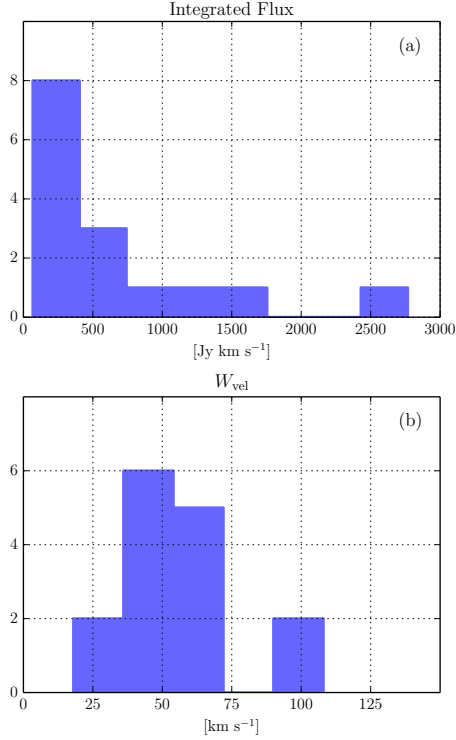


Figure 3.5 Distributions of the measured OH 35 (a) integrated fluxes and (b) equivalent widths.

are used to estimate the measurement errors. [Section 3.4](#) shows the distributions of the measured OH 35 fluxes and equivalent widths in our sample.

On average, we find that the uncertainties on the placement of the continuum translate into uncertainties of about $\pm 15\%$ on the final values of the equivalent width measurements listed in [Table 3.3](#). Since the OH column density scales linearly with the OH 35 equivalent width, the typical uncertainties on the measurements of N_{OH} and X_{OH} are also $\pm 15\%$. We note that the detection of OH 35 in UGC 05101 is marginal (with an uncertainty as high as $\pm 64\%$), so it is excluded from these calculations and from the mean OH column density and mean OH-to-H abundance ratio in the following sections.

Table 3.3. OH 35 μm Profile Properties

Name	Flux [Jy km s ⁻¹]	W_{vel} [km s ⁻¹]	N_{OH} [10 ¹⁷ cm ⁻²]	X_{OH} [10 ⁻⁶]
(1)	(2)	(3)	(4)	(5)
Arp 220	2977 \pm 362	72 \pm 9	1.69 \pm 0.21	1.64 \pm 0.20
IRAS F04454-4838	190 \pm 15	64 \pm 6	1.49 \pm 0.15	1.44 \pm 0.14
IRAS F05189-2524	524 \pm 60	61 \pm 7	1.42 \pm 0.17	1.38 \pm 0.16
IRAS F08572+3915	176 \pm 22	30 \pm 4	0.7 \pm 0.09	0.68 \pm 0.10
IRAS F12224-0624	109 \pm 7	54 \pm 4	1.26 \pm 0.08	1.22 \pm 0.08
IRAS 15250+3609	262 \pm 23	52 \pm 5	1.21 \pm 0.12	1.17 \pm 0.11
IRAS 17208-0014	1286 \pm 292	108 \pm 27	2.51 \pm 0.63	2.44 \pm 0.61
IRAS F20551-4250	633 \pm 132	90 \pm 20	2.09 \pm 0.46	2.03 \pm 0.45
IRAS F23128-5919	249 \pm 27	60 \pm 7	1.39 \pm 0.16	1.35 \pm 0.16
Mrk 231	1050 \pm 186	51 \pm 10	1.19 \pm 0.22	1.15 \pm 0.22
Mrk 273	531 \pm 118	51 \pm 12	1.19 \pm 0.28	1.15 \pm 0.28
NGC 2623	300 \pm 9	36 \pm 1	0.86 \pm 0.02	0.83 \pm 0.03
NGC 4418	1581 \pm 403	53 \pm 14	1.23 \pm 0.32	1.20 \pm 0.32
UGC 5101	67 \pm 38	18 \pm 11	0.42 \pm 0.26	0.41 \pm 0.26
Zw453.062	93 \pm 8	42 \pm 4	1 \pm 0.08	0.95 \pm 0.08

Note. — Column 1: Galaxy name. Column 2: Total integrated flux. Column 3: Equivalent width. Column 4: OH column density. Column 5: OH abundance relative to H.

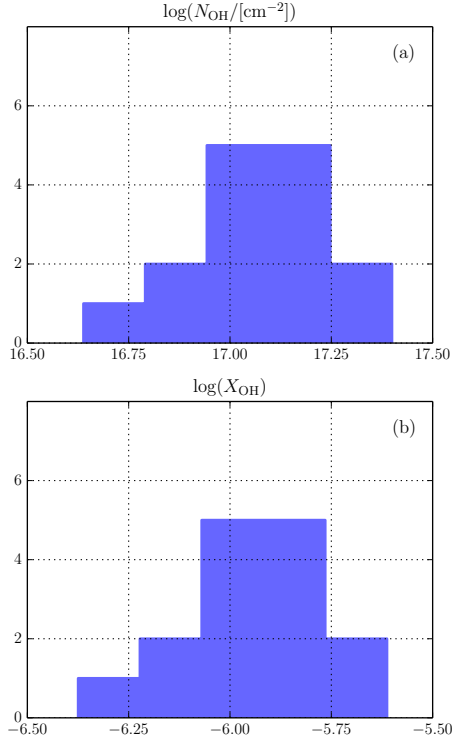


Figure 3.6 Distributions of the (a) OH column densities and (b) OH-to-H abundance ratios, X_{OH} , inferred from the fits of the OH 35 feature.

3.4.1 OH Column Density

The equivalent width of an absorption line is defined as

$$W_v = \int \frac{I_v(c) - I_v}{I_v(c)} dv, \quad (3.1)$$

where $I_v(c)$ is the intensity of the continuum and I_v is the line intensity at frequency

v . The optical depth is related to the line intensity via

$$I_v = I_v(c) e^{-\tau_v}, \quad (3.2)$$

where $\tau = \int n \sigma ds$ (n is the volume density of absorbers and σ is the cross section for absorption). Therefore, we can relate the optical depth and the equivalent width,

$$W_\nu = \int (1 - e^{-\tau_\nu}) d\nu. \quad (3.3)$$

For a foreground screen of homogeneous, isothermal gas illuminated by a background source, in the optically thin limit ($\tau \ll 1$), [Equation 3.3](#) reduces to

$$W_\nu = N_{\text{OH}} \sigma_0 \int \Phi_\nu d\nu, \quad (3.4)$$

where N_{OH} is the ground state OH column density and Φ_ν is the line profile function defined such that $\int_0^\infty \Phi_\nu d\nu = 1$ and σ_0 holds the parameters of the transition. If the Einstein coefficients A_{ul} for spontaneous emission and B_{ul} for stimulated emission are in units of $[\text{s}^{-1}]$ and $[\text{cm}^3 (\text{J s}^2)^{-1}]$, respectively (where u refers to the upper energy level and ℓ the lower energy level), we have the relations

$$A_{ul} = \frac{8\pi h}{\lambda^3} B_{ul}, \quad (3.5)$$

$$B_{ul} g_u = B_{\ell u} g_\ell, \quad (3.6)$$

where g is the degeneracy of the level and h is the Planck constant. Thus,

$$\sigma_0 = \frac{h}{\lambda} B_{\ell u} = \frac{A_{ul} \lambda^2}{8\pi} \frac{g_u}{g_\ell}. \quad (3.7)$$

Substituting σ_0 in [Equation 3.4](#) and noting that $W_{\text{vel}} [\text{cm s}^{-1}] = W_\nu [\text{s}^{-1}] \cdot \lambda [\text{cm}]$,

we see that the number of molecules per unit area along the line of sight is

$$N_{\text{OH}} = \frac{W_{\text{vel}} 8\pi}{A_{u\ell} \lambda^3} \frac{g_\ell}{g_u}. \quad (3.8)$$

Adopting $A_{u\ell} = 0.0174 \text{ s}^{-1}$ from [Destombes et al. \(1977\)](#) and [Bradford et al. \(1999\)](#), we calculate OH column densities using the empirically measured equivalent widths for our objects. Those column densities are shown in [Figure 3.6](#) and listed in [Table 3.3](#) with the associated $1\text{-}\sigma$ standard deviation of the distribution. We find a mean of $N_{\text{OH}} = 1.31 \pm 0.22 \times 10^{17} \text{ cm}^{-2}$ for the objects in our sample.

3.4.2 X_{OH}

We can now calculate X_{OH} , the OH abundance relative to H

$$X_{\text{OH}} = \frac{N_{\text{OH}}}{N_{\text{H}}}. \quad (3.9)$$

First, we estimate the column density of H nuclei for a given $\tau_{35\mu\text{m}}$ (the optical depth at $35 \mu\text{m}$ due to dust) via

$$N_{\text{H}} = \frac{(M_{\text{gas}}/M_{\text{dust}}) \tau_{35\mu\text{m}}}{\kappa_{35\mu\text{m}} m_{\text{H}}}, \quad (3.10)$$

where $(M_{\text{gas}}/M_{\text{dust}})$ is the gas-to-dust ratio by mass, $\kappa_{35\mu\text{m}}$ is the mass absorption coefficient of dust at $35 \mu\text{m}$, and m_{H} is the H mass. From Figure 2 of [González-Alfonso et al. \(2014a\)](#) we adopt $\kappa_{35\mu\text{m}} = 290 \text{ cm}^2 \text{ g}^{-1}$, and we adopt a gas-to-dust

ratio of 100, appropriate for the nuclear regions of luminous and ultraluminous infrared galaxies (e.g. [Wilson et al., 2008](#)). We adopt an optical depth $\tau_{35\mu m} = 0.5$ because, in the inner regions, the OH excitation temperature will be in near equilibrium with the dust temperature. Moreover, for $\tau_{35\mu m} > 0.5$, OH absorption becomes harder to detect due to extinction at $35\mu m$. Thus, we find $N_H \sim 1 \times 10^{23} \text{ cm}^{-2}$.

Results for the OH column density from [Equation 3.8](#) combined with the H column density from [Equation 3.10](#) provide X_{OH} . We calculate this abundance ratio for each of our sources (see [Table 3.3](#)) with the associated $1-\sigma$ standard deviation of the distribution. We find a mean of $X_{OH} = 1.27 \pm 0.21 \times 10^{-6}$ for our sample. [Figure 3.6](#) shows the OH-to-H abundance ratios resulting from these calculations.

We remark that our estimates for X_{OH} are formally only lower limits because (1) some fraction of the OH molecules are in excited levels, so N_{OH} is a lower limit to the column density of all OH states, (2) the covering fraction of the $35 \mu m$ continuum source by this obscuring material may not be 100%, and (3) some of the spectra are not background-subtracted which reduces the equivalent width of the OH 35 feature¹

¹When comparing the optimally extracted spectra available from CASSIS with the spectra presented here, we find that the background subtraction does not have a noticeable effect on the equivalent widths.

3.5 Discussion

3.5.1 X_{OH} : Comparison with the Literature

Here we compare our empirically derived values of X_{OH} with those found in the literature. Estimates of X_{OH} are typically derived by fitting radiative transfer models to multitransition observations of OH. For example, [Goicoechea & Cernicharo \(2002\)](#) modeled the first 20 rotational levels in OH and constrained the model with observations of Sgr B2. They report a range of $X_{\text{OH}} = 2 - 5 \times 10^{-6}$ (OH relative to H_2). A similar study by [Goicoechea et al. \(2006\)](#) of the Orion KL outflow derived a lower value of $X_{\text{OH}} = 0.5 - 1 \times 10^{-6}$. Following these two papers, the OH outflow studies of [Sturm et al. \(2011\)](#) and [González-Alfonso et al. \(2014b, 2017\)](#) adopted a value of $X_{\text{OH}} = 2.5 \times 10^{-6}$. Recent estimates of X_{OH} in obscured nuclei ([Falstad et al., 2015](#); [Fischer et al., 2014](#); [González-Alfonso et al., 2012](#)) seem to favor the higher OH abundances. Our empirically derived value of $X_{\text{OH}} = 1.3 \pm 0.4 \times 10^{-6}$ falls in the lower portion of this range of values. However, recall that our estimate is a lower limit, so it is formally consistent with all previously assumed and computed values of X_{OH} in the literature.

Our estimate is also consistent with [Richings & Faucher-Giguere \(2017\)](#)'s broad range of values for X_{OH} ($3.3 \times 10^{-6} - 2.2 \times 10^{-5}$), which is deduced from hydrochemical simulations of AGN-driven winds. It should be noted, however, that the X_{OH} values here and in [González-Alfonso et al. \(2014b, 2017\)](#) are relative to hydrogen nuclei in both atomic and molecular forms, while [Richings & Faucher-Giguere](#)

(2017)’s abundance ratios are relative to molecular hydrogen, hence the larger values. Finally, we note that our empirically determined values of X_{OH} are consistent with the values of chemical models of photodissociation regions (the peak value in Sternberg & Dalgarno, 1995) and of cosmic-ray- and X-ray-dominated regions (Meijerink et al., 2011).

3.5.2 X_{OH} : A Check on Radiative Transfer Models

In recent years, radiative transfer models have been used to infer the main physical parameters of molecular outflows in several infrared-bright galaxies (e.g. González-Alfonso & Cernicharo, 1999; González-Alfonso et al., 2014b, 2017), and many of these properties depend upon the inferred H column density (e.g. outflowing mass, mass outflow rate, momentum flux, and energy flux). It is therefore important to verify that these models also predict realistic OH 35.

Figure 3.7 shows the predicted OH 35 feature of the five ULIRGs (IRAS F05189-2524, IRAS F08572+3915, IRAS F20551-4250, Mrk 231, and Mrk 273) in common with the sample of González-Alfonso et al. (2017). In this paper, two ground-state lines (OH 79 and 119) and two excited lines (OH 65 and 84) were used to constrain the model. The green line is the OH 35 profile predicted by these models while the magenta line is the result from our fits to the observed feature (see Section 3.3.3). The agreement between the two is generally very good in terms of overall strength (equivalent width) of the feature. The predicted profiles are also largely consistent with the observed profiles, after taking into account the rather

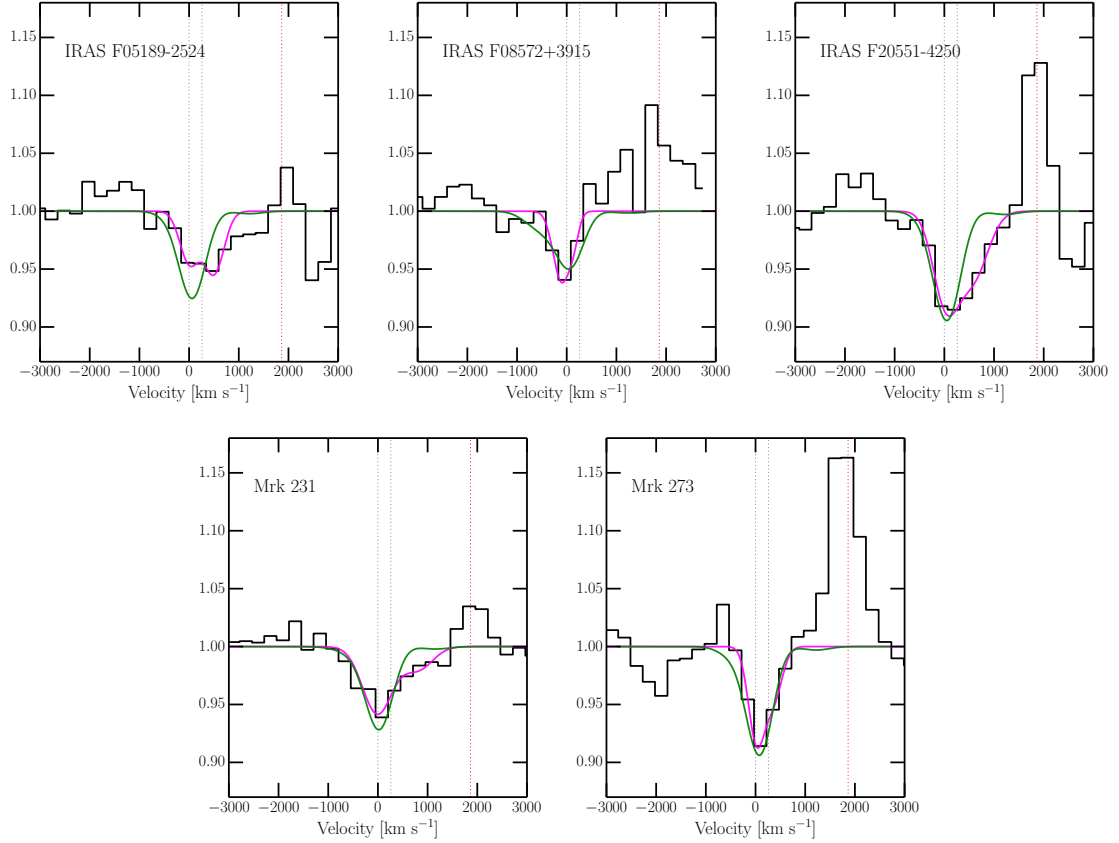


Figure 3.7 OH 35 spectra normalized to the continuum. Red and blue lines are the two Gaussian components of the fitted line and the magenta line is the sum of the two components. The green line is the profile predicted by the radiative transfer model described in [González-Alfonso & Cernicharo \(1999\)](#); [González-Alfonso et al. \(2017\)](#). The modeled line profiles are constrained by observations of four OH lines at 65, 79, 84, and 119 μm .

large uncertainties on the observed profiles associated with the continuum placement and the modest spectral resolution of the IRS data. The consistency between the model predictions and the observations adds some confidence in the energetics derived from these models.

3.6 Summary

We have analyzed mid-infrared ($5 - 37 \mu\text{m}$) *Spitzer*–IRS spectra of 15 nearby ($z \lesssim 0.06$) ULIRGs focusing on the OH $35 \mu\text{m}$ absorption feature. Several different methods were used to fit these spectra and estimate the uncertainties on the measured line parameters. The measured equivalent widths of OH $35 \mu\text{m}$ implies an average OH column density and $1\text{-}\sigma$ standard deviation to the mean of $N_{\text{OH}} = 1.31 \pm 0.22 \times 10^{17} \text{ cm}^{-2}$. We infer an OH-to-H abundance ratio of $X = 1.27 \pm 0.21 \times 10^{-6}$ when we assume a gas-to-dust ratio of 100, appropriate for the nuclear regions of luminous and ultraluminous infrared galaxies. This abundance ratio is formally a lower limit. It is consistent to within a factor of two with the value assumed in the radiative transfer models of OH outflows in these systems ($X_{\text{OH}} = 2.5 \times 10^{-6}$). We also find that the depths and profiles of OH $35 \mu\text{m}$ predicted by these models are largely consistent with the observed OH $35 \mu\text{m}$ spectra, providing support for the predicted energetics from these models.

Chapter 4: Far-Infrared Integral-Field Spectroscopy of Nearby Galactic Winds with Herschel-PACS

4.1 Introduction

Large-scale galactic outflows driven by stellar processes and/or active galactic nuclei (AGNs) play a pivotal role in the life cycle of galaxies by heating the cold interstellar medium (ISM), suppressing or triggering star formation, fueling or quenching accretion onto the central black hole, and by influencing the chemical enrichment of galaxies (e.g. [Fabian, 2012](#); [Heckman & Thompson, 2017](#); [Rupke, 2018](#); [Veilleux et al., 2005, 2020](#)). Although we now have a better understanding of how winds may significantly impact the formation and evolution of galaxies (e.g. we see this in semi-analytic, N-body, and hydrodynamical models of galaxy evolution where feedback is incorporated, (e.g. [Naab & Ostriker, 2017](#); [Somerville & Davé, 2015](#); [Zhang, 2018](#)), there still exists a plethora of unanswered questions concerning the detailed physics and properties of galactic outflows. What is the primary mechanism of energy and momentum injection that powers an outflow? How can we constrain outflow properties such as morphologies, lifetimes, spatial extent, radial-dependent velocities, mass outflow rates, and energetics? What is the efficiency of entraining material

from the ISM and ejecting it out of the disk? The answers to these questions can fundamentally measure the impact of outflows on galaxy evolution. However, it is challenging to constrain these properties because outflows involve multiple phases of the ISM (cold molecular, cool neutral atomic, warm and hot ionized; [Heckman & Thompson, 2017](#)) and hence, span a large range of temperatures ($T \sim 10 - 10^7$ K; [Zhang, 2018](#)), physical scales (a few parsecs to several kiloparsecs), and densities ($n \sim 10^{-2} - 10^6 \text{ cm}^{-3}$; [Croxall et al., 2012](#); [Draine, 2011](#)).

If we wish to gain a complete understanding of how winds contribute to the evolution of galaxies, it is crucial that we conduct detailed multi-phase ISM investigations of outflows and we must look to our local neighborhood where nearby galaxies provide us the opportunity to study spatially resolved spectroscopic observations of outflows. Integral Field Spectroscopy (IFS) of the ionized (e.g. [Harrison et al., 2014](#); [Martin & Soto, 2016](#); [Venturi et al., 2017](#)), neutral (e.g. [Rupke & Veilleux, 2011](#)), and molecular (e.g. [Pereira-Santaella et al., 2016](#); [Rupke & Veilleux, 2013](#)) ISM phases of outflows has made it possible to decompose the complex kinematics within galaxies. Not only can we utilize IFS to delineate disk rotation and outflow in a galaxy, but we can also gain insight into the spatial extent or morphological structure of the outflow.

However, star formation regions and areas near the AGN in a galaxy are heavily enshrouded in dust which severely hampers UV and optical wavelength observations. Fortunately, the far-infrared (FIR) provides us the opportunity to observe in these dusty regions without large extinction effects. We take advantage of the unprecedented combination of angular resolution, sensitivity, and spatial coverage of

the FIR spectroscopic integral field unit (IFU) of the Photodetector Array Camera and Spectrometer (Poglitsch et al., 2010, PACS;) on board the *Herschel* Space Observatory (Pilbratt et al., 2010) to peer through the dusty veil obscuring the regions where stars form and black holes grow.

In this paper, we present the main results of our analysis of the cool neutral atomic and the warm ionized ISM phases, as traced by FIR fine-structure line transitions in seven nearby ($d < 16$ Mpc) galaxies that are well known to harbor winds: Centaurus A (hereafter abbreviated as Cen A), Circinus, M 82, NGC 253, NGC 1068, NGC 3079, and NGC 4945. The proximity of these galaxies allows us to spatially resolve the morphologies and kinematics of the outflows (at the distances for our sample, the physical sizes covered by a PACS $9.7'' \times 9.7''$ spaxel are $\sim 0.2 - 1$ kpc). The OH 119 μm doublet (hereafter, OH 119) has also been observed by PACS in this galaxy sample, which we present and compare with the observations of the ionized and neutral gas.

The PACS data of the atomic gas for M 82 have been examined in detail in Contursi et al. (2013, hereafter C13). However, their observations cover a larger field of view (FOV), $2.5' \times 2.5'$, compared to our $\sim 47'' \times 47''$ FOV. Therefore, they were able to capture the outflow out to 1 kpc above and below the galaxy disk whereas we only capture the outflow out to a few hundred pc. Moreover, the majority of our FOV falls inside the starburst region of M 82. The observations from C13 were obtained in mapping mode instead of the pointed mode spectra presented here. Due to the spatial steps of the rasters used in their observations, the sky is Nyquist sampled and a spatial resolution of $6''$ ($\sim 130 - 270$ pc, depending upon wavelength)

is achieved. In pointed mode, the beam is undersampled and has a native resolution of $\sim 10''$. This is important to note because the sky will be undersampled which results in an underestimated source flux and the true morphology of an object will be degraded and difficult to reconstruct from a single pointed observation. Fortunately, we can increase confidence in the approximation in which the source morphology is reconstructed by comparing the interpolated observation with higher resolution data. Therefore, we re-examine PACS data of M 82 here for completeness and to validate our analysis on the other objects.

This paper is organized as follows: The FIR atomic fine-structure lines are discussed in [Section 4.2](#). The galaxies in our sample are described in [Section 4.3](#). Descriptions of the observations, archival data, and data reductions are found in [Section 4.4](#). We present the results of our analysis in [Section 4.5](#) and [Section 4.6](#). [Section 4.7](#) and [Section 4.8](#) outline the methods used to derive the gas outflow properties. The interpretation of the results and their implications are discussed in [Section 4.9](#). [Section 4.10](#) outlines our main conclusions. [Appendix B](#) contains the analysis of the molecular gas traced by OH 119. In this paper we adopt the standard convention that negative velocities with respect to systemic indicate approaching material.

4.2 Atomic Fine-Structure Emission Lines

The gas phases in the PACS FIR range (55–210 μm) cool through strong emission lines arising from atomic fine-structure transitions and molecular transitions,

with the strongest atomic emission originating from carbon, nitrogen, and oxygen and their various ions. These atoms are collisionally excited and then de-excite through forbidden transitions, emitting photons and thus removing thermal energy from the gas. Indeed, the cooling radiation from these emission lines are so powerful that they provide almost all of the gas cooling in the cold neutral and warm ionized phases of the ISM, and hence the emission is easily detectable over large distances (for example, [O III] 88 has been observed out to $z = 9.11$; [Hashimoto et al., 2018](#)). The importance of these fine-structure transitions cannot be understated since they are the dominant mechanism for gas cooling and can therefore directly impact the star formation in a galaxy. Here we observe five atomic fine-structure line transitions within the PACS FIR waveband: [O I] 63 μm , [O III] 88 μm , [N II] 122 μm , [O I] 145 μm , and [C II] 158 μm (hereafter, we drop the wavelength unit, μm , for brevity). Because this suite of FIR lines span a wide range of ionization potentials (IP = 11.26 – 35.12 eV), critical densities ($n_{\text{crit}} \sim 40 - 10^5 \text{ cm}^{-3}$), and excitation temperatures ($T_{\text{ex}} = 91 - 326 \text{ K}$), the combination of these lines allows us to investigate the physical conditions of the multiple phases of an outflow and probe the different regions of a galaxy from which these emission lines originate (see [Table 4.1](#) for more details of the fine-structure lines).

The low-excitation atomic lines ([O I] 63, [O I] 145, [C II] 158) sample photodissociation regions (PDRs) at the interfaces between molecular, atomic, and ionized gas phases in star-forming regions where intense far-ultra-violet (FUV) radiation photodissociates CO, resulting in bright emission of [O I] and [C II]

Table 4.1. Fine-structure Lines

Line	Transition	λ [μm]	ν [GHz]	IP [eV]	T_{ex} [K]	$n_{\text{crit,H}}$ [cm^{-3}]	$n_{\text{crit,e}}$ [cm^{-3}]
(1)	(2)	(3)	(4)	(5)	(6)	(7)	(8)
[O I] 63	$^3\text{P}_1 - ^3\text{P}_2$	63.18	4744.77	0.0 – 13.62	227	2×10^5	...
[O III] 88	$^3\text{P}_1 - ^3\text{P}_0$	88.36	3393.01	35.12 – 54.94	163	...	510
[N II] 122	$^3\text{P}_2 - ^3\text{P}_1$	121.89	2459.38	14.53 – 29.60	188	...	375
[O I] 145	$^3\text{P}_0 - ^3\text{P}_1$	145.52	2060.07	0.0 – 13.62	326	5×10^4	...
[C II] 158	$^2\text{P}_{3/2} - ^2\text{P}_{1/2}$	157.74	1900.54	11.26 – 24.38	91	2×10^3	47

Note. — The information in Table 4.1 is based on [Herrera-Camus et al. \(2018a\)](#), [Israel et al. \(2017\)](#), [Farrah et al. \(2013\)](#) and the Leiden Atomic and Molecular Database ([Schöier et al., 2005](#)). Column 1: Atomic fine-structure line, Column 2: Electronic energy level transition, Column 3: Rest wavelength, Column 4: Rest frequency, Column 5: Ionization potential to create the species and the ionization potential to ionize the species, Column 6: Excitation temperature, Column 7: Critical density for collisions with H I and H₂, Column 8: Critical density for collisions with electrons.

([Hollenbach & Tielens, 1997](#); [Sternberg & Dalgarno, 1995](#); [Tielens & Hollenbach, 1985](#)). [C II] 158 arises from both ionized and neutral gas due to its ionization potential of 11.2 eV. [C II] 158 is the dominant coolant in regions with densities $n_{\text{H}} \sim 10 - 10^5 \text{ cm}^{-3}$ and temperatures $T \sim 100 - 300 \text{ K}$, and is the strongest emission line from cooler gas ($T < 10^4 \text{ K}$) in galaxies ([Carilli & Walter, 2013](#)). In PDRs, the [O I] 63 and [O I] 145 line emission originates solely in the neutral regime. [O I] 145 is the faintest of the fine-structure lines, but its advantage is that it does not suffer from self-absorption like [O I] 63, which can be affected by self-absorption by relatively small amounts of foreground gas ($N_{\text{H}} \sim 2 \times 10^{20} \text{ cm}^{-2}$; [Liseau et al., 2006](#)). [O I] 63 line emission can also originate in X-ray dominated regions (XDRs) near AGN ([Dale et al., 2004](#)). At higher densities ($n_e \sim 10^5 \text{ cm}^{-3}$) and higher temperatures ($T > 200 \text{ K}$), [O I] 63 becomes the dominant cooling line

for neutral atomic gas instead of [C II] 158 (Meijerink et al., 2007). [O I] 63 line emission may also arise from shocks (Lutz et al., 2003).

The high-excitation ionic emission line [O III] 88 traces moderate density ($\sim 100 \text{ cm}^{-3}$) clouds, H II regions of photoionization from young, massive stars (Spinoglio & Malkan, 1992; Voit, 1992), and the narrow line region (NLR) excited by AGN (Díaz-Santos et al., 2017). The high abundance of oxygen makes [O III] 88 a primary coolant of the warm ionized phase of the ISM, and its high ionization potential (35.12 eV) predominantly traces very energetic conditions near AGN (Ferkinhoff et al., 2010), hot OB stars, or shocks (Stasińska et al., 2015). [N II] 122, a low-excitation line, also originates in H II regions and is solely excited in ionized gas due to its ionization potential of 14.53 eV, a value just above the ionization energy of hydrogen, 13.6 eV. Moreover, its low critical density ($\sim 350 \text{ cm}^{-3}$) means that it can easily be excited in the diffuse ionized phase of the ISM (Goldsmith et al., 2015; Herrera-Camus et al., 2016).

4.3 The Sample

The seven galaxies in our sample (see Table 4.2 for more details about the galaxy sample) are well known to harbor winds and have been studied intensively across the entire accessible electromagnetic spectrum. The spatial scale of these studies span a range of a few pc to several hundred kpc. Two of our sample are classified as pure starbursts (“H II galaxies” in the table; M 82 and NGC 253) while the other five (Cen A, Circinus, NGC 1068, NGC 3079, and NGC 4945) harbor both

a narrow-line AGN and a starburst.

M 82 is considered to be the archetypal starburst galaxy, hosting a substantial population of supernova remnants (Pedlar et al., 1999) and several star clusters (de Grijs, 2001). It is the energy from these populations' stellar processes that drives the well-known kpc-scale bipolar conically-shaped outflow along the galaxy's minor axis. The inclination of M82 provides a direct sight line to the S part of the disk which makes the approaching S outflow cone clearer in visibility. The N outflow cone is receding from us and lies behind the galaxy disk where emission in the base of the outflow may be extinguished by the disk itself. Hard X-ray ($E \sim 6.7$ keV) emission inside the central $|r| < 200$ pc, $|z| < 100$ pc of the galaxy arises from the wind fluid that drives the larger scale outflow (Griffiths et al., 2000). UV (e.g. Hoopes et al., 2005), mid-infrared (Engelbracht et al., 2006), and far-infrared/sub-mm (e.g. Alton et al., 1999; Roussel et al., 2010) images provide evidence of dust entrained in the hotter outflowing gas. Confined to the cone walls, warm ionized gas is seen as optical filamentary emission in $H\alpha$, [N II], and [S II] (Shopbell & Bland-Hawthorn, 1998). Warm molecular hydrogen in the near-infrared roughly traces the $H\alpha$ and warm dust emission (Veilleux et al., 2009). Observations of CO show molecular line splitting along the minor axis providing further evidence of a conical outflow morphology (Leroy et al., 2015).

Table 4.2. Galaxy Properties

Galaxy Name	RA [h m s]	Dec [$^{\circ}$ ' "]	Distance [Mpc]	SFR [$M_{\odot} \text{ yr}^{-1}$]	$\log L_{\text{FIR}}$ [L_{\odot}]	i [$^{\circ}$]	PA [$^{\circ}$]	Type	Morph.
(1)	(2)	(3)	(4)	(5)	(6)	(7)	(8)	(9)	(10)
M 82	09 55 52.2	+69 40 46.60	3.6	10	10.67	81	65	SB	I0
Cen A	13 25 27.62	-43 01 08.81	3.8	2	9.91	75	278	AGN & SB	S0 pec
Circinus	14 13 09.95	-65 20 11.87	4.2	4.7	9.92	65	216	AGN & SB	SAb
NGC 253	00 47 33.12	-25 17 17.59	3.9	3	10.35	76	230	SB	SABc
NGC 1068	02 42 40.71	-00 00 47.81	14.4	18	11.13	40	278	AGN & SB	S0 pec
NGC 3079	10 01 57.80	+55 40 47.24	16		10.64	84	166	AGN & SB	SBc
NGC 4945	13 05 27.48	-49 28 05.57	3.8	0.4	10.28	75	45	AGN & SB	SBcd

Note. — Column 1: Galaxy name, Column 2: Adopted RA of the galaxy center, Column 3: Adopted Dec of the galaxy center, Column 4: Luminosity distance, Column 5: Star formation rate, Column 6: FIR luminosity, Column 7: Galaxy inclination, Column 8: Position angle of the galaxy major axis, Column 9: Type, Column 10: Morphology classification.

Cen A is the prototypical Fanaroff-Riley I-type low-luminosity galaxy, and at a distance of 3.8 Mpc (Harris et al., 2010), it is the nearest active radio galaxy. In the radio, Cen A hosts a collimated subparsec-scale jet and counterjet (Burns et al., 1983; Tingay et al., 1998), parsec-scale inner lobes (Clarke et al., 1992; Schreier et al., 1981), a kpc-scale middle lobe (Morganti et al., 1999), and giant outer radio lobes on scale of hundreds of kpc (McKinley et al., 2013). Optical images show evidence of a bipolar outflow on scales of ~ 10 kpc (McKinley et al., 2018). $H\alpha$ (Blanco et al., 1975; McKinley et al., 2018) and [O III] $\lambda 5007$ filaments are also seen on scales of the middle lobe.

Circinus is the closest Seyfert 2 galaxy at 4.2 Mpc (Tully et al., 2009) and the second brightest AGN in the mid-infrared (after NGC 1068). The prominent ionization cone located NW of the galaxy nucleus contains extended optical filaments with outflowing velocities $\sim 100 - 200$ km s $^{-1}$ out to ~ 1 kpc (e.g. Marconi et al., 1994; Sharp & Bland-Hawthorn, 2010; Veilleux & Bland-Hawthorn, 1997; Veilleux et al., 2003). The ionization cone and outflow are traced on parsec scale in the NIR (Maiolino et al., 2000) and on kiloparsec scale in the X-Ray (Mingo et al., 2012). CO observations detect a “NW cloud” spatially coincident with the ionized outflow cone with a blue-shifted velocity of ~ 150 km s $^{-1}$ and a “far W cloud” moving along an $H\alpha$ filament (Zschaechner et al., 2016). Edge-brightened bipolar lobes are also seen in the radio which extend up to more than 2 kpc on either side of the galaxy plane (Elmouttie et al., 1998a).

NGC 253 is a starburst-dominated galaxy at a distance of 3.9 Mpc (Westmoquette et al., 2011), making it one of the two closest nuclear starburst galaxies

(M 82 being the other). *Chandra* observations (Strickland et al., 2002; Strickland & Stevens, 2000) show a limb-brightened conical outflow to the SE of the galaxy nucleus which is spatially aligned with the $\sim 100\text{--}300 \text{ km s}^{-1}$ outflow observed in $\text{H}\alpha$ (Westmoquette et al., 2011), and a northern X-ray outflow lobe that lies behind the disk of the galaxy. Outflows have been observed in Na I D (Heckman et al., 2000) and in OH (Sturm et al., 2011; Turner, 1985). A prominent molecular wind has been traced in CO with a mass outflow rate between $\sim 3 - 9 M_{\odot}\text{yr}^{-1}$ (assuming optically thin CO emission; Bolatto et al., 2013) and $\sim 25 - 50 M_{\odot}\text{yr}^{-1}$ (assuming optically thick CO emission; Krieger et al., 2019; Zschaechner et al., 2018). Even at the lower limit, these outflow rates (when compared to NGC 253’s star formation rate) are large enough to substantially affect the galaxy’s star formation activity.

NGC 1068 is the archetypal Type 2 Seyfert galaxy and contains an AGN and a circumnuclear starburst. NGC 1068 also harbors a kiloparsec-scale radio jet (e.g. Wilson & Ulvestad, 1987). The NLR gas has been observed as an outflow with a biconical morphology (Cecil et al., 1990; Das et al., 2006). The northeast side of the cone is in front of the galactic disk (oriented towards us) while the Southwest side is behind (oriented away from us) and obscured by the galactic disk (Barbosa et al., 2014). Sub-mm interferometry of molecular lines in the circumnuclear disk strongly suggests the existence of a giant, AGN-driven outflow extending to ~ 100 pc with a velocity of $\sim 100 - 200 \text{ km s}^{-1}$ (García-Burillo et al., 2014; Krips et al., 2011).

Table 4.3. PACS Fine-Structure Line Observations

Object Name	ObsId	Line	Spec. Res. ^a	Ang. Res. ^b	t_{exp} ^d	AOT	Chop Throw	Program ID
(1)	(2)	(3)	(4)	(5)	(6)	(7)	(8)	(9)
M 82	1342186799	[O I] 63	90	9.5	582	line	large	SDP_esturm_3
M 82	1342186798	[O III] 88	125	9.5	986	line	large	SDP_esturm_3
M 82	1342186798	[N II] 122	290	10.0	986	line	large	SDP_esturm_3
M 82	1342186798	[O I] 145	250	11.0	986	line	large	SDP_esturm_3
M 82	1342186798	[C II] 158	240	11.5	986	line	large	SDP_esturm_3
Cen A	1342202590	[O I] 63	90	9.5	873	line	large	KPGT_esturm_1
Cen A	1342202588	[O III] 88	125	9.5	11291	range	med	KPGT_rguesten_1
Cen A	1342203444	[N II] 122	290	10.0	5663	range	large	KPGT_rguesten_1
Cen A	1342202589	[O I] 145	250	11.0	2341	line	large	KPGT_esturm_1
Cen A	1342202589	[C II] 158	240	11.5	2341	line	large	KPGT_esturm_1
Circinus	1342191298	[O I] 63	90	9.5	1281	line	large	KPGT_esturm_1
Circinus	1342191297	[O III] 88	125	9.5	1948	line	large	KPGT_esturm_1
Circinus	1342191297	[N II] 122	290	10.0	1948	line	large	KPGT_esturm_1
Circinus	1342191297	[O I] 145	250	11.0	1948	line	large	KPGT_esturm_1
Circinus	1342191297	[C II] 158	240	11.5	1948	line	large	KPGT_esturm_1
NGC 1068	1342191153	[O I] 63	90	9.5	3671	range	large	KPGT_esturm_1
NGC 1068	1342203124	[O III] 88	125	9.5	3386	range	large	KPGT_esturm_1
NGC 1068	1342191154	[N II] 122	290	10.0	3944	range	large	KPGT_esturm_1
NGC 1068	1342191154	[O I] 145	250	11.0	3944	range	large	KPGT_esturm_1
NGC 1068	1342203121	[C II] 158	240	11.5	3456	range	large	KPGT_esturm_1
NGC 253	1342199414	[O I] 63	90	9.5	873	line	large	KPGT_esturm_1
NGC 253	1342199415	[O III] 88	125	9.5	1975	line	large	KPGT_esturm_1
NGC 253	1342199415	[N II] 122	290	10.0	1975	line	large	KPGT_esturm_1
NGC 253	1342199415	[O I] 145	250	11.0	1975	line	large	KPGT_esturm_1
NGC 253	1342199415	[C II] 158	240	11.5	1975	line	large	KPGT_esturm_1

Table 4.3 (cont'd)

Object Name	ObsId	Line	Spec. Res. ^a	Ang. Res. ^b	t_{exp} ^d	AOT	Chop Throw	Program ID
(1)	(2)	(3)	(4)	(5)	(6)	(7)	(8)	(9)
NGC 3079	1342221391	[C II] 158	240	11.5	8045	range	med	DDT_esturm.4
NGC 4945	1342212218	[O I] 63	90	9.5	2939	range	large	KPGT_esturm.1
NGC 4945	1342212220	[O III] 88	125	9.5	1975	line	large	KPGT_esturm.1
NGC 4945	1342212220	[N II] 122	290	10.0	1975	line	large	KPGT_esturm.1
NGC 4945	1342212220	[O I] 145	250	11.0	1975	line	large	KPGT_esturm.1
NGC 4945	1342212220	[C II] 158	240	11.5	1975	line	large	KPGT_esturm.1

^aSpectral resolutions are in units of km s^{-1} .

^bAngular resolutions are in units of arcsec.

^cEstimated from Fig.8 in the PACS Spectroscopy Performance and Calibration Guide Issue 3.0.

^dExposure times are in units of seconds.

Note. — Column 1: Galaxy name, Column 2: Observation ID, Column 3: Atomic fine-structure line, Column 4: Spectral Resolution of PACS at the emission line wavelength, Column 5: Angular resolution of PACS at the emission line wavelength, Column 6: Exposure time, Column 7: PACS Astronomical Observation Template, Column 8: Size of observation chopper throw, Column 9: Program ID.

NGC 3079 is well known for its spectacular super-bubbles. In the optical (e.g. Cecil et al., 2001; Veilleux et al., 1994), only the eastern bubble of NGC 3079’s double-lobed radio structure (Irwin et al., 2019) is visible. The galaxy disk is inclined such that the E side is nearest to us (Filippenko & Sargent, 1992; Yamauchi et al., 2004) and the counter bubble is located behind the disk where optical line emission is extinguished. The ionized outflow originating from the nucleus reaches velocities of up to $\sim 1500 \text{ km s}^{-1}$ (Cecil et al., 2001). $\text{H}\alpha + [\text{N II}]$ emission is observed in alignment with the bridges and loops seen in radio (Duric et al., 1983; Filippenko & Sargent, 1992). There is a slow-moving ($v \sim 0.1c$) parsec-scale radio jet (Middelberg et al., 2005) and copious amounts of hot X-ray gas that are aligned with the optical emission-line filaments (Cecil et al., 2002).

NGC 4945 harbors a radio-quiet AGN and a nearly edge-on circumnuclear starburst disk with ~ 83 pc radius (Marconi et al., 2000a). It is known for its high obscuration along the line of sight ($N_{\text{H}} \sim 3.5 \times 10^{24} \text{ cm}^{-2}$; Puccetti et al., 2014) and is the brightest Seyfert 2 galaxy in the hard X-ray range ($> 20 \text{ keV}$; Itoh et al., 2008), radiating at a variable rate of $L/L_{\text{Edd}} \sim 0.1$ (Madejski et al. 2000). $\text{H}\alpha$ emission tracing a central outflow cone was detected by Lehnert (1992); the cone has been imaged in both optical and near-infrared emission lines by Moorwood et al. (1996). In the soft X-ray ($\sim 0.6 \text{ keV}$), the plume is interpreted as a mass-loaded wind launched from the nuclear starburst (Schurch et al., 2002). Heckman et al. (1990) detected line splitting in optical spectroscopic data and found the line emission to originate from the surface of an expanding conical structure. Line splitting starts around 70 pc and extends out to 700 pc.

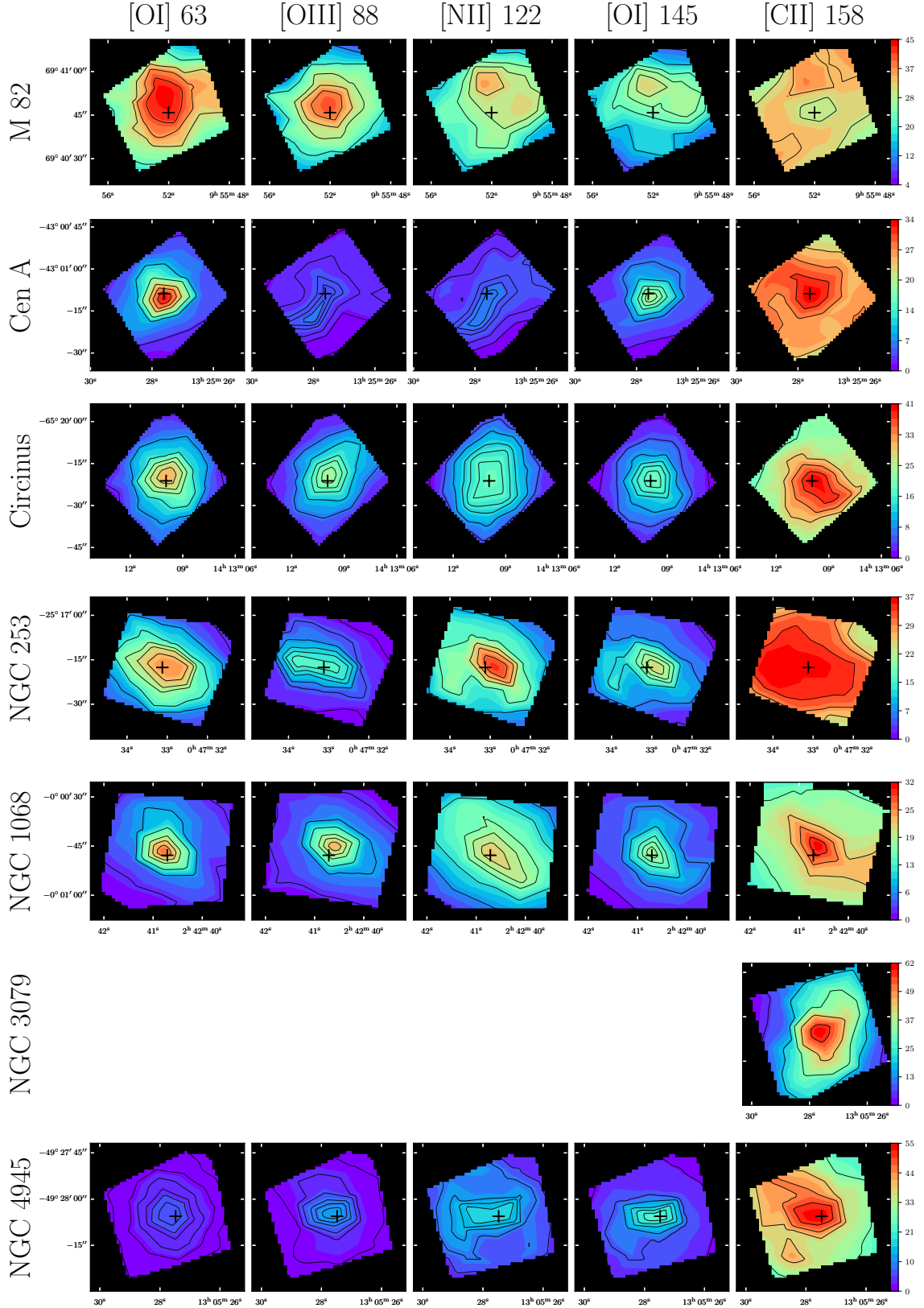


Figure 4.1 Signal-to-noise ratio maps. Contours are Contours are 0.1, 0.3, 0.5, 0.7, 0.8, and 0.9 of the peak value in each image. Black crosses mark the adopted galaxy center.

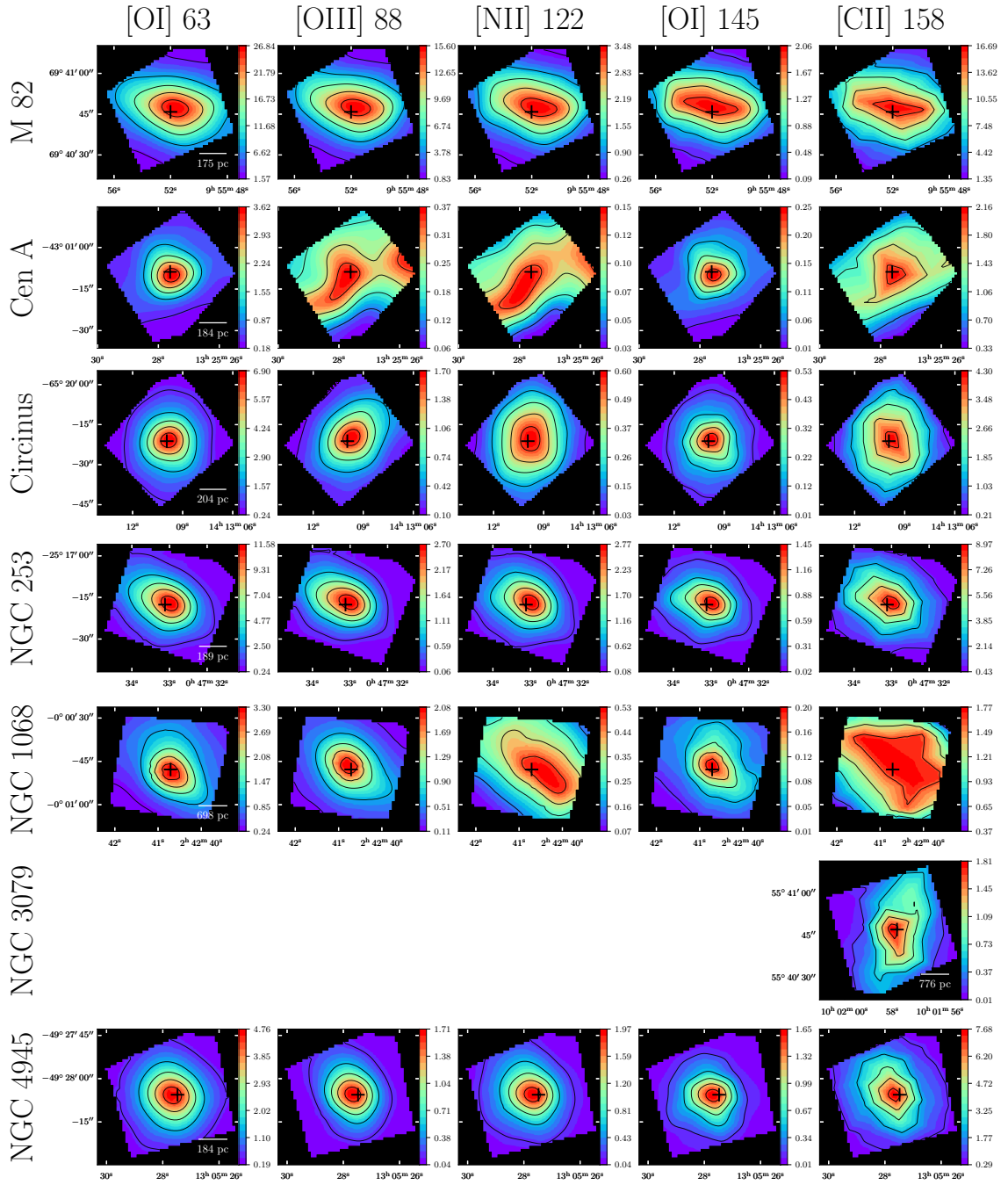


Figure 4.2 Total integrated emission line fluxes in $10^{-17} \text{ W m}^{-2}$. Contours are 0.1, 0.3, 0.5, 0.7, and 0.9 of the peak flux in the image. Black crosses mark the adopted galaxy center.

4.4 Observations, Archival Data, and Spectral Analysis

The observations of the fine-structure lines, [O I] 63, [O III] 88, [N II] 122, [O I] 145, and [C II] 158 were performed with the Photoconductor Array Camera and Spectrometer (PACS; Poglitsch et al., 2010) on board the ESA Herschel Space Observatory (Pilbratt et al., 2010). These observations were done in pointed observing mode with PACS line and range scan spectroscopy astronomical observing templates (AOTs). A large chopper throw is used for a majority of the observations (two medium throws were used for Cen A ObsID 134220258 and NGC 3079 ObsID 134221391). Observations of M 82 are from the Science Demonstration Phase SDP_esturm_3 (PI: E. Sturm). Observations of Cen A, Circinus, NGC 253, and NGC 4945 are from Guaranteed Time Key Programs KPGT_esturm_1 (PI: E. Sturm) and KPGT_rguesten_1 (PI: R. Güsten). NGC 3079 is from the Director’s Discretionary Time DDT_estrum_4 (PI: E. Sturm). More specific observation details are listed in Table 4.3.

The FIR data were retrieved from the Herschel Science Archive (HSA)¹ via the Herschel Interactive Processing Environment (HIPE v15.0.0; Ott, 2010). These data have been pipeline-processed at the Herschel Science Centre with the Standard Product Generation (SPG) software v14.2.0 up to the *rebinnedCube* task. The standard reduction steps include glitch masking, bad and noisy pixel masking, dark and background subtraction, spectral flatfielding, and flux calibration to Jy per spaxel. The uncertainty on the absolute flux calibration is of the order $\sim 6\%$ and

¹<http://www.archives.esac.esa.int/hsa/whsa/>

the wavelength calibration uncertainties for the red and blue channel are ~ 20 km s^{-1} and ~ 40 km s^{-1} , respectively (Poglitsch et al., 2010).

For each spaxel in an observation, a second-order polynomial is fit to the continuum and subtracted from the spectrum. Two Gaussian components were then fit to the continuum-subtracted spectrum and line profile properties are estimated using the sum of the two components. It should be noted that NGC 1068 needed three Gaussian components to more accurately capture the broad wings exhibited in its emission lines, and in this case, the sum of the three Gaussian components is used to estimate line profile properties. Signal-to-noise ratio maps are presented in [Table 4.3](#), where in general, the largest SNRs are observed in [C II] 158 and [O I] 63 . The velocity-integrated emission line flux and ratio maps are discussed in [Section 4.5](#) and the kinematic analysis of these data is presented in [Section 4.6](#).

We note that the observed wavelength range of [N II] 122 contains a second pass ghost in most of the non-central PACS spectrometer spaxels. This ghost originates from the [C II] 158 line and appears as a broad spectral feature shifted redward of the [N II] 122 line profile. This ghost lies close to the [N II] 122 line profile and leaves a small amount of observable continuum redward of [N II] 122 making continuum placement difficult. Therefore, we exclude the analysis of [N II] 122 in our discussion of the outflows in [Section 4.9](#).

4.5 Velocity-Integrated Emission Line Flux and Ratio Maps

Figure 4.2 and Figure 4.3 show the maps of the velocity-integrated line fluxes and line ratios, respectively. These emission line ratios are useful diagnostic tools that can probe the physical properties of the ISM. The spatial distribution of emission ratios can reveal the excitation and ionization conditions in different regions of a galaxy. Moreover, it is possible to infer the ionization or excitation source of the gas. Line ratios constrain physical gas properties such as the strength of the surrounding radiation field, chemical abundances, local temperatures, and gas densities. To compute these line ratio maps, the total integrated flux maps were first smoothed to the same resolution and aligned to a common pixel grid. Here, we first briefly summarize the physical conditions traced by the following emission line ratios: [O I] 63/[C II] 158, [O III] 88/[O I] 63, [O III] 88/[N II] 122, [O III] 88/[C II] 158, [O I] 145/[O I] 63, and [C II] 158/[N II] 122, before discussing the results.

It should be noted that [O I] 63 can be affected by self-absorption from cold foreground gas with column densities as low as $N_{\text{H}} \sim 2 \times 10^{20} \text{ cm}^{-2}$ (Liseau et al., 2006). Therefore, any conclusions drawn from ratio values dependent upon the [O I] 63 emission line flux should be made with care. In the ratios listed below, if self-absorption is present in the [O I] 63 spectrum, then the [O I] 63 / [C II] 158 values will be underestimated while the [O III] 88 / [O I] 63 and [O I] 145 / [O I] 63 values will be overestimated. In this galaxy sample, [O I] 63 self-absorption is only obvious in the spectra along the NE portion of the galaxy major axis of NGC 4945 (absorption is not obviously detected above and below the disk).

4.5.1 Constraints from the Emission Line Ratios

[O I] 63 / [C II] 158 – [C II] 158 and [O I] 63 are the dominant coolants in PDRs, so the relative strength of their emission is a proxy for the FUV heating intensity (a measure of how many FUV photons contribute to the gas heating) in these regions (Parkin et al., 2014). This ratio can also be used to discriminate between XDRs near AGN and classical PDRs. PDR emission is produced at the outer edges of molecular clouds, but at high densities ($n \sim 10^5 \text{ cm}^{-3}$) in XDRs, the deeply penetrating X-ray photons can ionize [O I] in a larger volume of the molecular cloud, thereby enhancing the [O I] 63 emission (Meijerink et al., 2007). In XDRs, the [O I] 63 line emission can substantially exceed the emission of [C II] 158 and become the dominant cooling mechanism in the neutral gas (Herrera-Camus et al., 2018b). Thus, the ionization effects of the AGN can be traced by high ratios of [O I] 63 / [C II] 158 .

[O III] 88 / [O I] 63 – This ratio yields the ionized to neutral gas ratio in a region, but the ratio alone does not distinguish whether the source of ionization is the AGN or SB (Fernández-Ontiveros et al., 2016). Low ratios indicate the dominance of the [O I] 63 line emission from dense, neutral gas.

[O III] 88 / [N II] 122 – [O III] 88 and [N II] 122 line emission can arise in the NLR of AGN. Thus, their line ratio is a sensitive indicator of the strength of the ionization parameter, U , (the number of incident ionizing photons divided by the hydrogen gas density within the NLR of an AGN; Abel et al., 2009) of the NLR. In stellar H II regions, this ratio directly measures the effective temperature of the

stars responsible for ionization. The ratio reveals the stellar classification of the youngest stars in the region (Ferkinhoff et al., 2011).

[O III] 88 / [C II] 158 – This ratio is an excitation sensitive indicator. [O III] 88 line emission arises in the NLR of AGN or in H II regions where hot O and B stars produce photons energetic enough to ionize [O III] 88. Therefore it traces regions of high radiation fields and gives a measure of the relative ionized to neutral gas abundances.

[O I] 145 / [O I] 63 – In the optically thin limit ([O I] 145 / [O I] 63 values $\lesssim 0.1$; Tielens & Hollenbach, 1985), and in the temperature range 100 – 400 K and density range $n_{\text{H}} \lesssim 10^4 \text{ cm}^{-3}$, the [O I] 145 / [O I] 63 line ratio is an effective temperature tracer for the neutral gas in PDRs (Liseau et al., 2006; Tielens & Hollenbach, 1985). Higher values of this ratio indicates high gas temperatures (Fernández-Ontiveros et al., 2016; Kaufman et al., 1999). The gas temperature traced by this ratio is anti-correlated with the gas density traced by [S III] 33 μm / [S III] 18 μm (Spinoglio et al., 2015).

[C II] 158 / [N II] 122 – [N II] 122 line emission arises solely from low-excitation photoionized gas, so the [C II] 158 / [N II] 122 ratio can quantify the fraction of [C II] 158 emission originating from the neutral gas in PDRs.

4.5.2 Results from the Emission Line Ratios

M 82: Emission in all lines (see Figure 4.2) show elongation from E to W, however, [O I] 63 and [O III] 88 show a slightly more compact nuclear morphology.

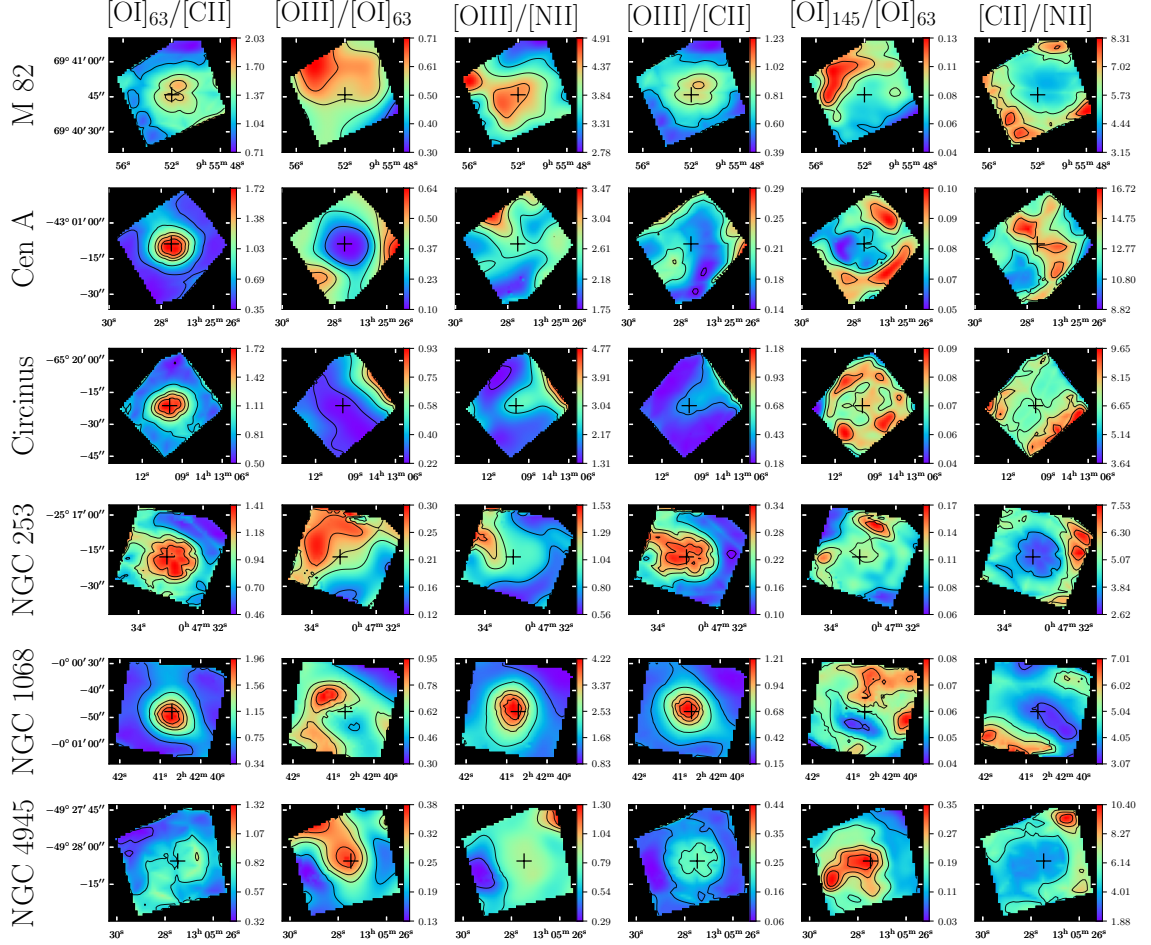


Figure 4.3 Maps of the emission line ratios. Contours are 0.1, 0.3, 0.5, 0.7, 0.8, and 0.9 of the peak value in each image.

This morphology is emphasized in Figure 4.3 where high ratios of $[\text{O I}] 63 / [\text{C II}] 158$, $[\text{O III}] 88 / [\text{N II}] 122$, and $[\text{O III}] 88 / [\text{C II}] 158$ are in a compact region around the galaxy nucleus. The emission line ratios also indicate that the neutral gas traced by $[\text{O I}] 63$ and the ionized gas traced by $[\text{O III}] 88$ and $[\text{N II}] 122$ is typically stronger near the galaxy center, but further from the center, $[\text{O I}] 145$ and $[\text{C II}] 158$ emission begin to dominate.

C13 shows that the bipolar outflow is best determined from the $[\text{O III}] 88 / [\text{O I}] 63$ ratio. Our smaller FOV makes a direct morphological compar-

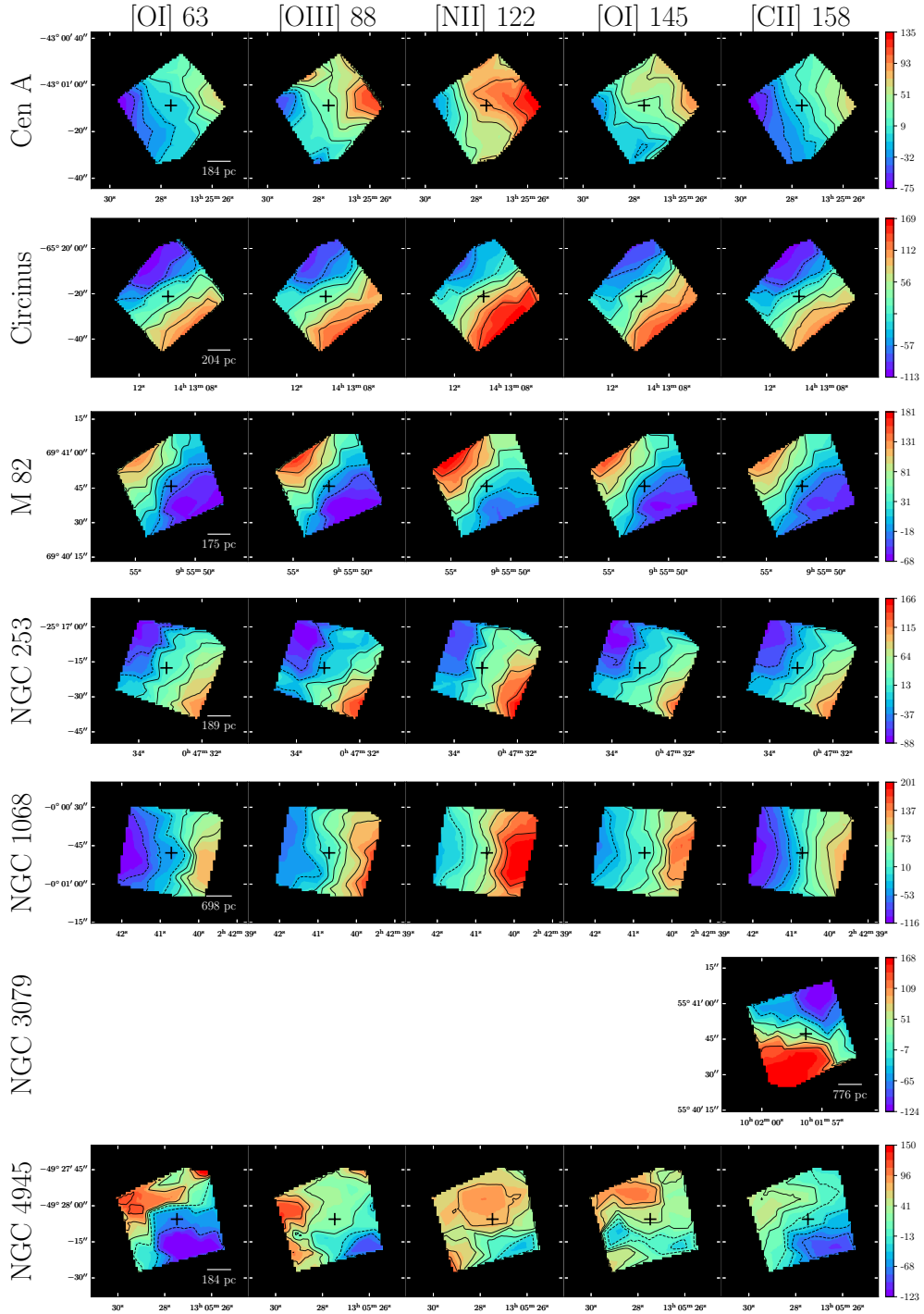


Figure 4.4 Maps of the median velocities, v_{50} in units of km s^{-1} . Contours are in eight equal steps between the minimum velocity and the maximum velocity in each image.

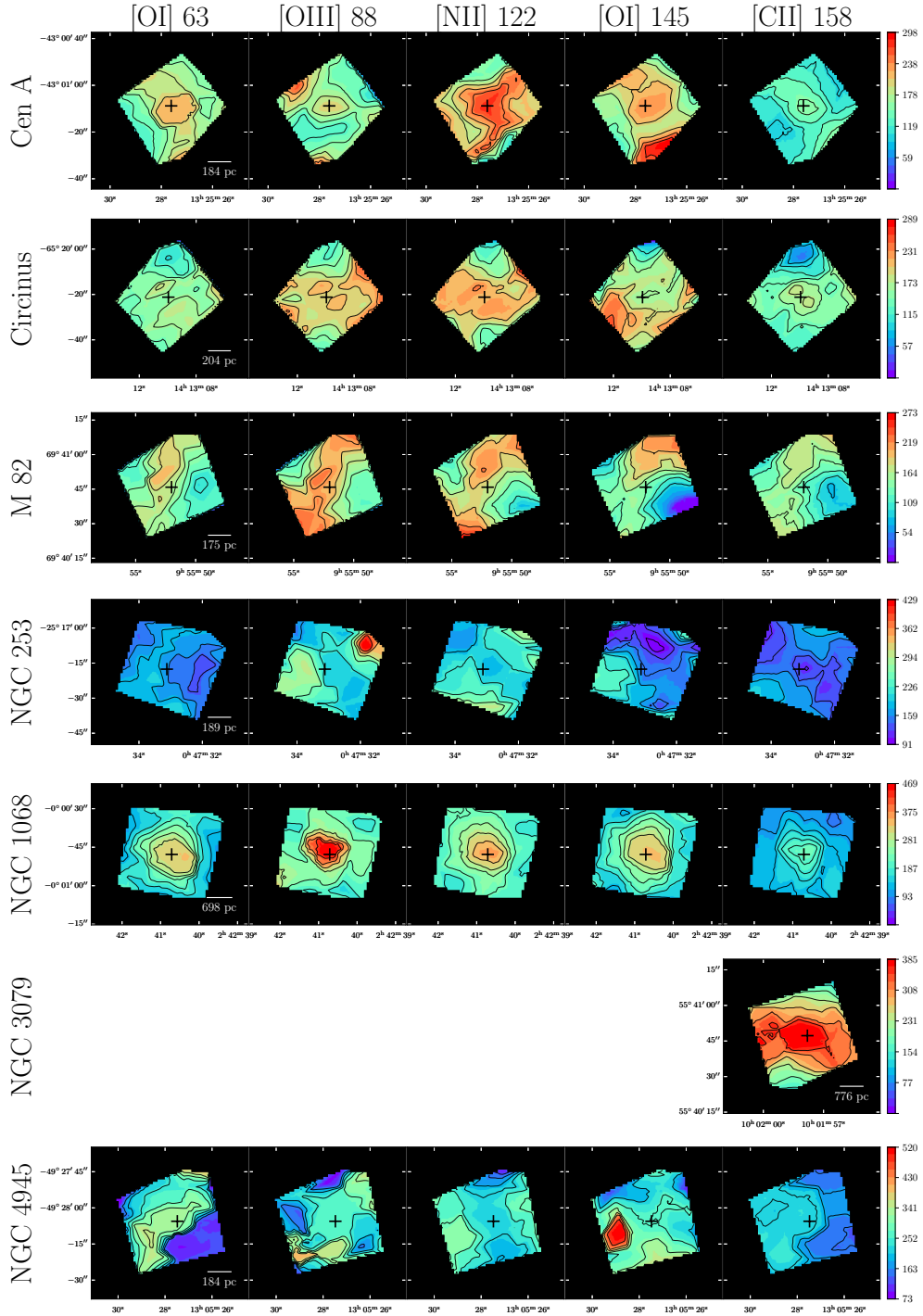


Figure 4.5 Maps of the $1 - \sigma$ line widths, $W_{1\sigma}$, in units of km s^{-1} . Contours are 0.4, 0.5, 0.6, 0.7, 0.8, and 0.9 of the peak width in each image.

ison difficult because our FOV encapsulates mostly the base of the outflow cones. C13 reports that the highest [O III] 88 / [O I] 63 ratios are highest in the N portion of the SB region, which is consistent with our findings. C13 also reports an asymmetry in the disk in the [O I] 145 / [O I] 63 line ratios. Our results are consistent with their findings with the higher ratios relegated to the E portion of the disk and the smaller ratios in the W portion of the disk.

Cen A: In [Figure 4.2](#) the adopted galaxy center of Cen A is spatially coincident with the peak emission in all lines. Cen A exhibits a centrally condensed nuclear emission of neutral gas with a slightly shallower flux gradient towards the NE of the nucleus, as seen in the [O I] 63 and [O I] 145 maps. On the other hand, the ionized gas traced by [O III] 88 and [N II] 122 shows bright, elongated nuclear emission (oriented SE to NW) surrounded by diffuse emission that extends to the edges of the PACS FOV. Although [C II] 158 is seen as diffuse emission outside of the galaxy center similar to [O III] 88 and [N II] 122, the brightest contours of [C II] 158 are not elongated SE to NW as seen in the ionized gas. Instead, the brightest contours of [C II] 158 emission are closer in morphology to the compact nuclei seen in the neutral gas.

NE of the galaxy nucleus, in a location spatially coincident with “Knot A”, there is a compact region of high [O III] 88 / [C II] 158 ratios. The highest [O I] 63 / [C II] 158 ratios in [Figure 4.3](#) for Cen A are localized to the galaxy center, but there is some slight extension of higher ratios to the NE in the direction of the jet. There is also elongation of higher [C II] 158 / [N II] 122 ratios to the NE in the direction of the jet. In general, the neutral gas traced by [O I] 63 dominates the central re-

gions (as seen in the low $[\text{O III}] 88 / [\text{O I}] 63$ ratios and the high $[\text{O I}] 63 / [\text{C II}] 158$ ratios).

Circinus: The nuclear neutral gas emission seen in $[\text{O I}] 63$ and $[\text{O I}] 145$ shows a compact spatial distribution with a shallower flux gradient extending to the SW of the galaxy center. The ionized gas traced by $[\text{O III}] 88$ in contrast shows elongated emission with a shallower flux gradient extending to the NW. We see that the emission in $[\text{N II}] 122$ and $[\text{C II}] 158$ are the most spatially extended of all the lines and show a preferential elongation along the north – south axis.

The well-known ionization cone in Circinus is most clearly identified in the $[\text{O III}] 88 / [\text{N II}] 122$, $[\text{O III}] 88 / [\text{C II}] 158$, and $[\text{C II}] 158 / [\text{N II}] 122$ emission line ratio maps shown in [Figure 4.3](#). The $[\text{O III}] 88 / [\text{N II}] 122$ ratios are, on average, a factor of 2 greater inside the cone than those in the disk. The high $[\text{O I}] 63 / [\text{C II}] 158$ ratios localized to the central region of Circinus reveals the effects of the AGN on the nearby gas ($[\text{O I}] 63$ line emission can be particularly strong in XDRs or NLRs near AGN).

NGC 253: The emissions for all of the fine-structure lines in NGC 253 lie in a elongated morphology along the NE – SW axis, coincident with the 2.2 μmm stellar bar detected by [Scoville et al. \(1985\)](#). There is a steep flux gradient for all lines towards the SW. Most of the $[\text{O I}] 63$, $[\text{O III}] 88$, and $[\text{O I}] 145$, emission is concentrated within the central $10'' \times 10''$. In contrast, the $[\text{C II}] 158$ and $[\text{N II}] 122$ emission distributions extend further above and below the galaxy major axis.

Again we see the effects of the AGN radiation on the gas in the elevated values of the line ratios of $[\text{O I}] 63 / [\text{C II}] 158$ and $[\text{O III}] 88 / [\text{C II}] 158$ (although

these ratios also show some elongation towards the E along the galaxy disk) and the low ratios of $[\text{C II}] 158 / [\text{N II}] 122$ found in compact nuclear regions in NGC 253. The $[\text{O I}] 63 / [\text{C II}] 158$ and $[\text{O III}] 88 / [\text{C II}] 158$ ratios also indicate the presence of neutral gas (as traced by $[\text{C II}] 158$) in the N outflow cone of NGC 253.

NGC 1068: All line emission in NGC 1068 is elongated along the NE – SW axis and aligned with the galaxy’s 2.5 kpc near-infrared nuclear bar (Schinnerer et al., 2000). The peak line emission for $[\text{O I}] 63$, $[\text{O III}] 88$, and $[\text{O I}] 145$ are localized to a compact region near the galaxy nucleus while $[\text{C II}] 158$ and $[\text{N II}] 122$ emission is much more diffuse.

The outflow in NGC 1068 is most obvious in the $[\text{O III}] 88 / [\text{O I}] 63$ ratio (see Figure 4.3) where the largest ratios are in a compact region NE of the galaxy nucleus in the direction of the known ionization cone and outflow. The effects of the AGN radiation are seen in the nuclear compact morphologies of high ratios in $[\text{O I}] 63 / [\text{C II}] 158$, $[\text{O III}] 88 / [\text{N II}] 122$, and $[\text{O III}] 88 / [\text{C II}] 158$. Also clear from those ratios is that the neutral gas traced by $[\text{C II}] 158$ increases in emission further away from the galaxy center. The higher ratios in $[\text{O I}] 145 / [\text{O I}] 63$ N of the nucleus and the higher ratios of $[\text{C II}] 158 / [\text{N II}] 122$ S of the nucleus appear to trace molecular arms in NGC 1068.

NGC 3079: $[\text{C II}] 158$ line emission in NGC 3079 is diffuse and elongated in the direction of the galaxy major axis. East of the nucleus, a steep flux gradient is observed along the galaxy minor axis in the direction of the optical bubble (Cecil et al., 2001; Veilleux et al., 1994).

NGC 4945: For all lines in NGC 4945, peak line emission is in a compact

region near the nucleus. The [O III] 88, [N II] 122, and [C II] 158 line emission is elongated N to S where [N II] 122 and [C II] 158 are more diffuse than [O III] 88 . The neutral gas traced by [O I] 63 is diffuse but the flux decreases more uniformly with increasing distance from the nucleus, whereas the steeper flux gradients of [O III] 88, [N II] 122, and [C II] 158 lie in the direction of the galaxy minor axis. The [O I] 145 emission is elongated to the S and the SE of the nucleus. It should be noted that there is significant self-absorption in [O I] 63 for NGC 4945. We do not correct for this absorption, so the [O I] 63 fluxes reported here should be considered lower limits.

The [O III] 88 / [N II] 122 ratios in NGC 4945 (see [Figure 4.3](#)) show high values in a compact region inside the NW outflow cone and low ratios in the SE cone, indicating a higher ionization in the NW cone. The [O III] 88 / [O I] 63 ratios are highest in the disk along the NE direction. As mentioned earlier in this section, the [O I] 63 spectrum of NGC 4945 suffers from self-absorption along the NE portion of the disk. So the higher [O III] 88 / [O I] 63 values are most likely due to the self-absorption as opposed to higher ionization. The [O I] 145 / [O I] 63 ratio shows high values in a compact region around the nucleus which also extends SE in the direction of the outflow. Lower [O I] 145 / [O I] 63 ratios in the NW cone suggest a lower temperature for the neutral gas compared to the SE cone. The [O I] 63 self-absorption is not obviously observed in regions above and below the galaxy disk. Therefore, even though the [O I] 145 / [O I] 63 values near the nucleus are most likely overestimates, there is greater confidence in the accuracy of the [O I] 145 / [O I] 63 values in the NW and SE outflow cones of NGC 4945. The [O III] 88 / [C II] 158 ratios show

low values in a compact region around the galaxy center indicating higher ionization near the AGN with [C II] 158 line emission increasing with distance from the nucleus. The [C II] 158 / [N II] 122 ratios are lower in a compact region around the nucleus compared to a compact region in the NW outflow cone with higher values, indicating a higher [C II] 158 emission in the NW outflow.

4.6 Gas Kinematics

The widths and velocities of the emission line profiles in each spaxel are described by the non-parametric characteristics v_{50} and $W_{1\sigma}$. v_{50} is the median velocity of the fitted emission line profile, i.e. 50% of the emission is produced at velocities below v_{50} . Zero velocity corresponds to the rest wavelength at the galaxy's systemic velocity. $W_{1\sigma}$ is the width of the line profile within 1- σ standard deviation of v_{50} .

Figure 4.4 and Figure 4.5 show the v_{50} and $W_{1\sigma}$ maps of the sample galaxies, respectively. These maps are analyzed in Section 4.8 and the results of this analysis are discussed in Section 4.9 where they are compared to the multi-phase outflows known to exist in these galaxies.

4.7 PDR Modeling

It is possible that the emission of the neutral ISM component in the outflows of our galaxies originate from photodissociation regions (PDRs). PDRs are the warm, dense surfaces of molecular clouds that are exposed to the far-ultraviolet (FUV) photons ($6 \text{ eV} < h_\nu < 13.6$, Hollenbach & Tielens, 1997, 1999) that escape from H II

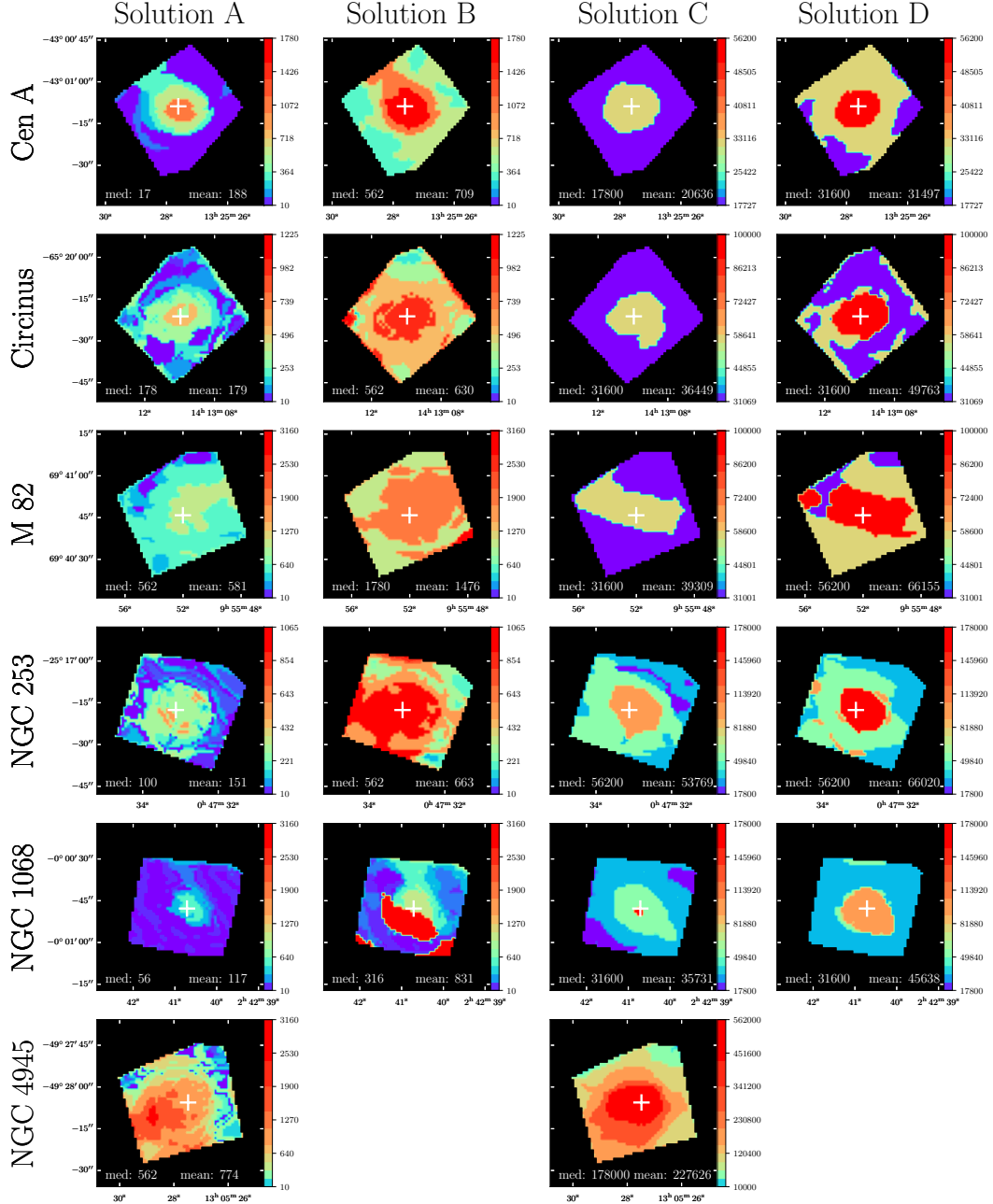


Figure 4.6 Maps of the hydrogen density, n_{H} in each object. Units are in cm^{-3} . The “low” density range is defined as $0 < n_{\text{H}} < 10^4 \text{ cm}^{-3}$ and the “high” density range is defined as $10^4 < n_{\text{H}} < 10^7 \text{ cm}^{-3}$. See Section 4.7.4 for details about the determination of these density ranges and definitions of Solutions A–D. **Solution A** is the low density solution with only the [C II] 158 flux correction (see Section 4.7.1 and Section 4.7.4), **Solution B** is the low density solution with both the fluxes of [C II] 158 and [O I] 63 corrected (see Section 4.7.1, Section 4.7.2 and Section 4.7.4), **Solution C** is the high density solution with only the [C II] 158 flux correction, and **Solution D** is the high density solution with both the fluxes of [C II] 158 and [O I] 63 corrected. As discussed in Section 4.7.4, the high density PDR solutions “C” and “D” lead to unphysical ISRFs. Therefore, we have excluded them from the analysis of the outflow.

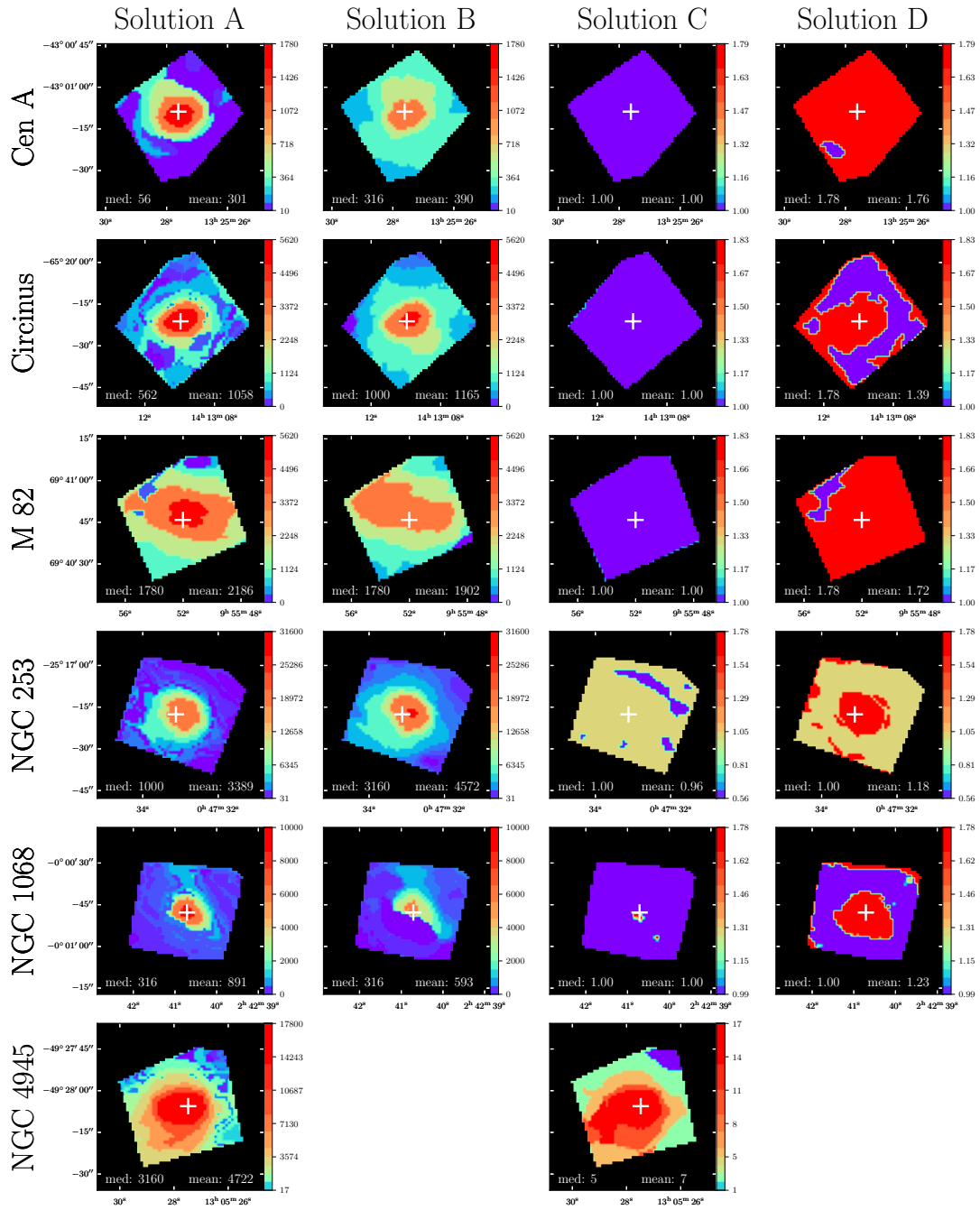


Figure 4.7 Maps of the strength of the UV radiation field, G_0 , for the low density and high density limits PDR solutions. Definitions of the Solutions are the same as those in Figure 4.6.

regions in star-forming regions or the accretion disks in AGN. The absorption of FUV photons by gas and dust is converted to FIR radiation including intense emission of [C II] 158 and [O I] 63 transitions, mainly excited by collisions with H₂ molecules and H I ($n_{\text{H}} \gtrsim 10^3 - 10^4 \text{ cm}^{-3}$; Liseau et al., 2006), whose line emissions dominate the gas cooling in PDRs (Tielens & Hollenbach, 1985). These two transitions are the brightest PDR emission lines in the *Herschel*-PACS spectral range and thus, are sensitive probes to the physical conditions of the gas in a PDR.

In this section, we use the fluxes of [O I] 63, [O I] 145, and [C II] 158 and the total infrared continuum emission (TIR $\sim 30 - 1000 \mu\text{m}$) to derive simple PDR models and infer the spatially-averaged properties of the gas by comparing observed emission line ratios to theoretically predicted line ratios. The models we employ here were first presented by Hollenbach et al. (1991); Tielens & Hollenbach (1985); Wolfire et al. (1990). Kaufman et al. (2006, 1999) has since updated these models to include more recent values of atomic and molecular data, current chemical rate coefficients, and grain photoelectric heating rates. These models assume that the light-emitting material is a plane-parallel, semi-infinite slab illuminated from one side. We use the PDR Toolbox¹ (Pound & Wolfire, 2008), a publicly available implementation of the model diagnostics to constrain the intensity of the ambient UV radiation field (G_0 or ISRF; conventionally expressed in units of the local Galactic FUV flux = $1.6 \times 10^{-3} \text{ erg cm}^{-2} \text{ s}^{-1}$, a.k.a Habing flux, Habing, 1968) and the hydrogen nucleus density (n_{H}). Before we can estimate the PDR parameters of our sample, we must first consider a flux correction for [C II] 158 and [O I] 63 .

¹<http://dustem.astro.umd.edu/pdrt/>

4.7.1 [C II] 158 Emission

The [C II] 158 line emission originates from both the ionized and neutral ISM phases due to the transition’s low ionization potential (11.26 eV), low transition temperature (91 K), and low critical density for collisions ($2 \times 10^3 \text{ cm}^{-3}$). The PDR model, however, only considers the [C II] 158 flux arising from the neutral gas. Therefore, we must correct for the fraction of [C II] 158 flux that is emitted from the ionized gas. We can derive this fraction using the [N II] 122 flux whose higher ionization potential (14.53 eV) implies that the nitrogen emission originates solely from the ionized gas. We assume that the [C II] 158 flux from the ionized gas scales directly with that of the [N II] 122 line using the relation valid for dense HII regions and for a Milky Way C/N abundance ratio equal to 3.8 (Rubin et al., 1993, 1988):

$$[\text{CII}]_{\text{ionized}} = 1.1 \times [\text{NII}]. \quad (4.1)$$

4.7.2 [O I] 63 Emission

The PDR models employed here assume that the line emission originating from the irradiated side of a cloud is optically thin. However, when a spectral line is optically thick, as is the case with [O I] 63, and the cloud is lit from behind, we will not observe emission of that line. This means we only see the [O I] 63 flux if the irradiated side of a cloud is facing us. Kaufman et al. (1999) states that we will observe half of the [O I] 63 emission produced with the other half radiating away from our line of sight. We therefore correct for this geometrical effect by multiplying

the observed [O I] 63 flux by a factor of two. Most likely, the true [O I] 63 flux correction factor lies somewhere between one and two. Therefore, we estimate the PDR solutions with and without the [O I] 63 flux correction. The final PDR results represent the range of values that the observed gas may have.

As mentioned in [Section 4.5](#), [O I] 63 can suffer from self-absorption which would also affect the amount of the emission detected. There is heavy absorption in [O I] 63 in NGC 4945 (see [Section 4.5.2](#)), therefore we do not compute a PDR solution for NGC 4945 using the [O I] 63 flux. The other objects do not show obvious absorption in [O I] 63, therefore we apply only a geometrical correction to the [O I] 63 emission.

4.7.3 Total Infrared Emission

We estimate the TIR emission ($8 - 1000 \mu\text{m}$) using the specific flux values at [O I] 63, [O III] 88, [O I] 145, and [C II] 158 from the continua fitted in [Section 4.4](#).

Assuming optically thin emission and a fixed grain emissivity ($\beta = 1$), we fit the continuum fluxes with a modified blackbody and extract the calculated flux density at $60 \mu\text{m}$ and $100 \mu\text{m}$. We then compute the FIR emission using the equation from [Helou et al. \(1988\)](#) :

$$\begin{aligned}
 FIR [Wm^{-2}] &= 1.26 \times 10^{-14} \\
 &\times (2.58 \times I_{60 \mu\text{m}} [Jy] + I_{100 \mu\text{m}} [Jy]) .
 \end{aligned}
 \tag{4.2}$$

Using the IR bolometric correction from [Dale et al. \(2001\)](#) we approximate

the TIR emission via:

$$\log\left(\frac{\text{TIR}}{\text{FIR}}\right) = a_0 + a_1x + a_2x^2 + a_3x^3 + a_4x^4, \quad (4.3)$$

where $x = \log[I_{60\mu\text{m}}/I_{100\mu\text{m}}]$ and $a \approx [0.2738, -0.0282, 0.7281, 0.6208, 0.9118]$ assuming a redshift $z = 0$.

4.7.4 Hydrogen Density and UV Radiation Field

The solutions from the PDR toolbox are degenerate. Therefore, a predicted emission line ratio may be produced by either a low density environment with a strong radiation field or a high density environment with a weak radiation field. For our sample of galaxies, inspection of the χ^2 map in the $n_{\text{H}}-G_0$ parameter space shows a delineation between the degenerate solutions of the PDR modeling. Therefore, we also modeled the PDR regions within a “low” density range, $0 < n_{\text{H}} < 10^4 \text{ cm}^{-3}$ and a “high” density range, $10^4 < n_{\text{H}} < 10^7 \text{ cm}^{-3}$

Here we present the hydrogen density (n_{H} ; see [Figure 4.6](#)) and far-ultraviolet interstellar radiation field (ISRF; G_0 ; see [Figure 4.5.2](#)) solutions from the PDR modeling. Hereafter, for brevity and clarity, the four PDR solutions will be referred to as Solutions A, B, C, and D. **Solution A** is the low density solution with only the [C II] 158 flux correction. The [C II] 158 flux correction attempts to remove the portion of [C II] 158 emission that originates from ionized gas by using [Equation 4.1](#). **Solution B** is the low density solution with both the fluxes of [C II] 158 and [O I] 63 corrected. The [O I] 63 flux is corrected using a geometrical

factor of two as described in [Section 4.7.2](#). **Solution C** is the high density solution with only the [C II] 158 flux correction. **Solution D** is the high density solution with both the fluxes of [C II] 158 and [O I] 63 corrected.

Setting a high density limit ($n_{\text{H}} > 10^4 \text{ cm}^{-3}$) results in a ISRF $\sim 1 G_0$ across the entire FOV in the galaxy sample (NGC 4945 is the exception with a peak ISRF of $\sim 17 G_0$ around the galaxy center). Radiation fields this weak and this extended in the central regions of these galaxies are not physical since much higher radiation fields are expected near an AGN or a circumnuclear starburst. Although NGC 4945 does show a higher ISRF ($\lesssim 17 G_0$) around the nucleus compared to the other galaxies, it is still too small to be realistic. Because the radiation fields modeled at a high density limit produce unrealistic ISRFs, we will only discuss the low-density solutions A and B in the following analysis.

4.7.5 Caveats

We have derived the spatially-averaged neutral gas properties of our galaxy sample via a simple and uniform treatment of the integrated line emission fluxes. However, the physical parameters inferred from any PDR model should not be taken too literally, since they are dependent upon the assumptions adopted and the microphysics implemented in a model that oversimplifies a much more complex set of physical conditions. Moreover, due to the discretization of the parameter space in the PDR models, we are wary of the pixel-to-pixel variations in the final (n_{H}, G_0) solutions. In particular, if the input flux uncertainties had been lower, it is possible

that the final (n_{H}, G_0) results would have been different than the results presented here. This is seen in the final PDR solution maps as a hot/cold pixel in the middle of an otherwise well defined morphological structure. This is corrected by interpolating these pixels with surrounding neighbors.

4.8 Methods to Derive the Outflow Properties

In this section the methods for estimating the physical and kinematic outflow properties in the galaxy sample are outlined. The spectral observation cubes are first used to model the disk rotation in each galaxy. The resulting velocity field is then subtracted from the observed emission line profile properties and the residuals are used to define the spatial location of the outflow. The emission line fluxes within the wind region are used to estimate line luminosities. The line luminosities in turn, are used to compute the masses and kinetic energies in the neutral and ionized gas in the outflow.

4.8.1 Beam Smearing

One of the greatest difficulties in deriving galaxy kinematics from velocity fields is overcoming the effect of beam smearing ([Bosma, 1978](#)). The radial velocities in a galaxy vary on spatial scales smaller than the beam size of the observing instrument. Effectively, this means that the velocities at different radii will be blended, thus flattening the observed velocity field gradients, decreasing the slope of the derived rotation curve at the galaxy center, and broadening the width of the observed line

profiles. This is a significant problem since the broadening effect can be incorrectly attributed to the gas velocity dispersion.

Fortunately, we can employ methods that utilize the full 3D data cube (two spatial dimensions and one spectral dimension) of a galaxy and build a model that directly incorporates the instrument’s 2D point spread function and spectral resolution. To do this we use the software package ^{3D}BAROLO¹ (Di Teodoro & Fraternali, 2015) which simulates the observational data in a cube by building a “tilted-ring” model that best fits the data. Accounting for the instrumental contribution to the observed data will result in a disk model which more accurately captures the true kinematics of the gas. The details of the “tilted-ring” model and the employment of ^{3D}BAROLO are discussed in the following section.

4.8.2 Tilted Ring Model

The velocity field of a disk galaxy can be described by a “tilted-ring” model (Rogstad et al., 1974), where the disk is built from a series of concentric annuli that increase in radius with the distance from the galaxy center. This model assumes that the line emitting material is confined to a thin disk and that the kinematics are dominated by rotational motion. Emission of the gas in each ring is described by geometric parameters (centroid, radius, width, scale height, inclination angle along the line of sight of the observer, and position angle of the major axis) and kinematic parameters (systemic velocity, rotational velocity, and velocity dispersion). For ^{3D}BAROLO, the instrumental spectral and spatial resolutions are also inputs so that

¹<http://editeodoro.github.io/Bbarolo/>, version 1.4

the final model accounts for both instrumental effects.

In reproducing the observed data cube, ^{3D}BAROLO assumes that all of the velocity dispersion is due to rotation and turbulence. Outflows are known to exist along the minor axes of the sample galaxies, so this assumption means that the velocity dispersion of the disk model will be overestimated, with the largest errors at the center of the galaxy where line broadening suffers the most from beam smearing.

We attempt to mitigate this effect by assuming a constant velocity dispersion across the disk and estimate the value of this velocity dispersion using data outside the galaxy center where the beam smearing is the least severe. The data are fit in two stages. In the first stage, the gas velocity dispersion and the rotational velocity are left as free parameters. The remaining parameters are input as “correct” values and held constant. Afterwards, the mean of the fitted gas velocity dispersions of the three outmost rings is then computed. For the second stage, this mean dispersion is input as a fixed parameter and only the rotational velocity is left free. The resultant disk model is the assumed galaxy velocity field.

4.8.3 Defining the Spatial Location of the Outflow

The kinematics of the outflow can be delineated from those of the disk by examining the residuals in v_{50} and in $W_{1\sigma}$ between the observed data and the modeled disk (Δv_{50} and $\Delta W_{1\sigma}$, respectively). Recall from [Section 4.8.2](#), the modeled galaxy velocity field accounts for the instrumental spatial and spectral resolutions. Therefore, in the residuals, the instrumental effects have been removed. In this

galaxy sample, excess line widths are a more reliable indicator of outflow than the v_{50} residuals. For example, the outflow of M 82 is known to lie along the galaxy minor axis. Inspection of the $\Delta W_{1\sigma}$ maps (see Column 3 in [Figure 4.8b](#)) shows an obvious SE to NW trend consistent with the direction of the outflow, but no such trend is observed in the Δv_{50} maps (see Column 3 in [Figure 4.8a](#)). For this reason $\Delta W_{1\sigma}$ is used to define the spatial location of the wind.

The excess line widths are assumed to trace non-circular motions in the gas. These motions can be due to the presence of morphological features in a galaxy, such as spiral arms, a nuclear bar, a warped disk, and/or an outflow. Ideally, in the absence of such features, save the outflow, the spatial location of the wind would be defined as those regions where $\Delta W_{1\sigma} > 0 \text{ km s}^{-1}$. However, these features do exist in our galaxy sample and for some, the projected morphologies of those features overlap with each other, making decomposition of the wind from the features difficult. Therefore, when defining the spatial location of the wind, it is important to carefully choose a minimum threshold in $\Delta W_{1\sigma}$ which would account for gas motions not related to the outflow.

For various thresholds, features in the $\Delta W_{1\sigma}$ maps were compared to the physical features of the galaxies observed at other wavelengths. For example, for [C II] 158 in NGC 1068, a region of excess line width SW of the nucleus more likely traces a molecular spiral arm because the region is elongated N to S along the arm (see Column 3 of [Figure 4.19b](#)) and because the S outflow cone lies behind the galaxy disk where even in the FIR the S cone may be extinguished. A threshold of $\Delta W_{1\sigma} > 25 \text{ km s}^{-1}$ was chosen to minimize the inclusion of regions where

excess line widths were spatially coincident with features unrelated to the known outflow. Ultimately, this threshold does mitigate the detection of gas motions unrelated to the wind, but it does not remove those motions completely. Although a higher threshold would more effectively exclude gas motions unrelated to the outflow, such a threshold might also exclude the outflow all together. For example, the detection of a [C II] 158 outflow in M 82 disappears completely with a threshold of $\Delta W_{1\sigma} > 50 \text{ km s}^{-1}$ (see Column 5 of [Figure 4.8b](#)), however, [C II] 158 is known to exist in the outflow of M 82 (C13). This is a probable indicator that a threshold of $\Delta W_{1\sigma} > 50 \text{ km s}^{-1}$ is too harsh a limit. We include $W_{1\sigma}$ residual maps with $\Delta W_{1\sigma} > 50 \text{ km s}^{-1}$ as reference for a lower limit to the spatial extent of the wind in the sample galaxies (see Column 5 of subfigure (b) in [Figure 4.8](#), [Figure 4.11](#), [Figure 4.14](#), [Figure 4.16](#), [Figure 4.19](#), [Figure 4.22](#), [Figure 4.24](#)), but the following analysis defines the spatial location of the wind as those regions where $\Delta W_{1\sigma} > 25 \text{ km s}^{-1}$.

4.8.4 Line Luminosities

The relation from [Solomon et al. \(1992\)](#) is used to estimate the emission line luminosities from the observed line fluxes via

$$\frac{L_{\text{line}}}{L_{\odot}} = 1.04 \times 10^{-3} S_{\text{line}} \Delta v (1+z)^{-1} \nu_{\text{rest}} D_L^2, \quad (4.4)$$

where $S_{\text{line}} \Delta v$ is the velocity integrated flux in Jy km s^{-1} , $\nu_{\text{rest}} = \nu_{\text{obs}}(1+z)$ is the rest frequency in GHz, and D_L is the luminosity distance in Mpc (see [Table 4.2](#) for

galaxy details).

4.8.5 Mass of the Neutral Atomic Wind

We follow [Hailey-Dunsheath et al. \(2010\)](#) to estimate the neutral atomic gas mass in the outflow by using the inferred [C II] 158 luminosity and the PDR solutions (see [Section 4.7](#)). Assuming the line emission is optically thin, the minimum atomic gas mass can be estimated by

$$\frac{M_{\text{atomic}}}{M_{\odot}} = 0.77 \left(\frac{L_{[\text{C II}] 158}}{L_{\odot}} \right) \left(\frac{1.4 \times 10^{-4}}{X_{\text{C}^+}} \right) \times \left(\frac{1 + 2e^{-91\text{K}/T} + n_{\text{crit}}/n}{2e^{-91\text{K}/T}} \right), \quad (4.5)$$

where $L_{[\text{C II}] 158}$ is the [C II] 158 line luminosity in solar units, X_{C^+} is the carbon abundance per hydrogen atom, n is the gas density, and n_{crit} is the critical density. We assume that the PDR surface temperature, T_{S} , derived in [Section 4.7](#) is representative of the region's gas temperature and we adopt $X_{\text{C}^+} = 1.6 \times 10^{-4}$ ([Sofia et al., 2004](#)) which assumes a C^+ abundance typical of PDRs in the Milky Way.

The atomic outflow mass estimated here (see [Table 4.4](#)) is derived only from the gas associated with [C II] 158 emission and is not an estimate of the total neutral atomic gas in the outflow. Also, a lower X_{C^+} value will result in a more massive wind. Therefore, we emphasize that these mass estimates should be considered lower limits.

4.8.6 Mass of the Ionized Wind

Following [Ferkinhoff et al. \(2010\)](#), the minimum ionized gas mass required to produce the observed [O III] 88 line emission can be estimated in the high-density ($n_{\text{crit}}/n \ll 1$), high-temperature ($T_{\text{eff}} > 40,000$ K) limit via

$$\frac{M_{\text{ionized}}}{M_{\odot}} = F_{\text{line}} \cdot \frac{g_t}{g_u} \frac{4\pi \cdot D_L^2}{A h\nu} \frac{m_{\text{H}}}{X_{\text{element}}} \frac{1}{X_{\text{ion}}}, \quad (4.6)$$

where F_{line} is the emission line flux, $g_t = \sum g_i \exp(-\delta E_i/kT)$ is the partition function, g_u is the statistical weight of the upper transition level, D_L is the source luminosity distance, A is the Einstein A coefficient, ν is the rest frequency of the emission line, m_{H} is the mass of hydrogen, X_{element} is the relative abundance of the emission line species to hydrogen (e.g. O^{++}/H^+ , which, for a minimum mass is the total abundance ratio O/H), and X_{ion} is the fractional abundance of a given species in a particular ionization state (e.g. O^{++}/O). We adopt the gas-phase abundance ratio $X_{\text{O}} = 5.9 \times 10^{-4}$ from [Savage & Sembach \(1996\)](#).

It is important to note that in our gas mass calculations we are assuming that all of the oxygen is in the form of O^{++} . The ionization potential of O^{++} (in this case, 35.12 eV for [O III] 88) is much higher than that of O^+ so it is unlikely that all of the oxygen will be doubly ionized. Therefore, we include an ionization correction term, X_{ion} , to estimate a more realistic gas-phase abundance ratio, $X_{\text{O}^{++}}$. For example, if the stellar $T_{\text{eff}} \sim 36,000$ K, the fraction of O^{++} to the total oxygen abundance will only be $\sim 15\%$, and the ionized wind mass will be about 7 times larger. The

computed masses of the ionized gas in the wind are listed in [Table 4.4](#).

4.8.7 Kinetic Energy of the Wind

The kinetic energy in the wind may be described as the sum of the “bulk” kinetic energy and the “turbulent” kinetic energy of the outflowing gas ([Rupke et al., 2005a](#); [Veilleux et al., 2020](#)) via:

$$KE_{\text{wind}} = \frac{1}{2} M_{\text{wind}} \left[v_{50, \text{wind}}^2 + 3 \left(\frac{W_{1\sigma, \text{wind}}}{2} \right)^2 \right]. \quad (4.7)$$

The estimates of the kinetic energies in the wind are listed in [Table 4.4](#).

4.9 Properties of the Outflows and Multi-Phase Comparisons

In this section we discuss the results from [Section 4.8](#) and directly compare the physical properties of the neutral and ionized outflows within each sample galaxy. For each object, the first figure shows the observed velocity field and $1-\sigma$ line width (v_{50} and $W_{1\sigma}$, respectively) measured from the line profile fitting outlined in [Section 4.4](#) and [Section 4.6](#). This figure also shows the modeled v_{50} and $W_{1\sigma}$ results from [Section 4.8.2](#), followed by the residuals between the data and the model. Lastly, the figure shows the regions where the $1-\sigma$ line width residuals ($\Delta W_{1\sigma}$) exceed 25 and 50 km s^{-1} to delineate where the outflow is believed to be significant. Hereafter, the residual velocities and line widths inside the regions where $\Delta W_{1\sigma} > 25 \text{ km s}^{-1}$ are defined as $\Delta v_{50 \text{ wind}}$ and $\Delta W_{1\sigma \text{ wind}}$, respectively. The second figure for each object

Table 4.4. Wind Properties

Galaxy Name	Solution A		Solution B		[O III] 88	
	M	KE	M	KE	M	KE
(1)	(2)	(3)	(4)	(5)	(6)	(7)
Outflow Definition: $\Delta W_{1\sigma} > 25 \text{ km s}^{-1}$						
M 82	86.1	34.7	17.4	6.13	3.56	1.62
Cen A	18.2	4.35	1.57	0.27	0.05	0.02
Circinus
NGC 253	106	35.9	10.9	3.57	0.40	0.32
NGC 1068	8.95	20.8
NGC 4945	0.36	0.22
Outflow Definition: $\Delta W_{1\sigma} > 50 \text{ km s}^{-1}$						
M 82	1.22	0.70
Cen A	0.01	0.01
Circinus
NGC 253	23.6	12.9	1.62	0.93	0.26	0.28
NGC 1068	5.49	19.0
NGC 4945	0.07	0.13

Note. — Masses of the wind are in units of $10^6 M_{\odot}$. Kinetic energies of the wind are in units of 10^{53} erg. “Solution A” and “Solution B” refer to the low density limit ($n_{\text{H}} < 10^4 \text{ cm}^{-3}$) PDR results from Section 4.7.4 used to compute the neutral outflow mass (see Section 4.8.5) and kinetic energy (see Section 4.8.7). Outflow masses and kinetic energies listed in the top table are estimated using fluxes, radial velocities, and $1-\sigma$ line widths in the spatial regions where the $1-\sigma$ line width residuals between the observed and modeled velocity field ($\Delta W_{1\sigma}$) is larger than 25 km s^{-1} (see Section 4.8.3 for further details). The bottom table is the same as that above except the $1-\sigma$ line width residual threshold is 50 km s^{-1} . This higher threshold illustrates the lower limit of the outflow masses and kinetic energies. Column 1: Galaxy Name. Column 2: Neutral gas mass in the outflow derived in the low density limit with only the [C II] 158 flux corrected, Column 3: Kinetic energy of the neutral gas in the outflow derived in the low density limit with only the [C II] 158 flux corrected, Column 4: Neutral gas mass in outflow derived in the low density limit with the [C II] 158 and [O I] 63 fluxes corrected, Column 5: Kinetic energy of the neutral gas in the outflow derived in the low density limit with the [C II] 158 and [O I] 63 fluxes corrected, Column 6: Ionized gas mass in the outflow estimated from the [O III] 88 flux (see Section 4.8.6). Column 7: Kinetic energy of the ionized gas in the outflow estimated from the [O III] 88 flux (see Section 4.8.7).

compares these outflow maps with existing photometric and kinematic data at other wavelengths. The final figure for each object presents maps of the neutral and ionized gas masses and the corresponding kinetic energies associated with the outflows.

As mentioned in [Section 4.4](#), the continuum placement of [N II] 122 is difficult due to the proximity of the second pass ghost to the [N II] 122 line profile. Therefore, [N II] 122 is excluded from the following analysis because of the high uncertainty in its line profile measurements. Also, [O I] 63 is not used to model the NGC 4945 galaxy disk due to the presence of strong self-absorption in the line profiles which is not seen in the other galaxies. Additionally, the wind kinematics for NGC 3079 only include the gas traced by [C II] 158 since this is the only fine structure line observed in NGC 3079.

4.9.1 M 82

The M 82 v_{50} maps in all lines (see [Figure 4.8a](#), Column: 1) show that the E side of the disk is receding from us (largest velocity at $\sim 145 \text{ km s}^{-1}$) and the W side of the disk is approaching us (largest velocity at $\sim -55 \text{ km s}^{-1}$). Although the direction of the disk rotation and the lower approaching radial velocity in this PACS data is consistent with the analysis in C13, the maximum receding velocity reported here is $\sim 45 \text{ km s}^{-1}$ greater than that reported in C13. The M 82 $\Delta v_{50 \text{ wind}}$ maps (see Column 4 of [Figure 4.8a](#)) show the NW outflow in all lines and indicate that the cone is receding from us with $\Delta v_{50 \text{ wind}}$ up to $\sim 65 \text{ km s}^{-1}$ (the largest recession velocity is in [O I] 145). The S outflow is approaching us, but is seen only in the ionized

M 82

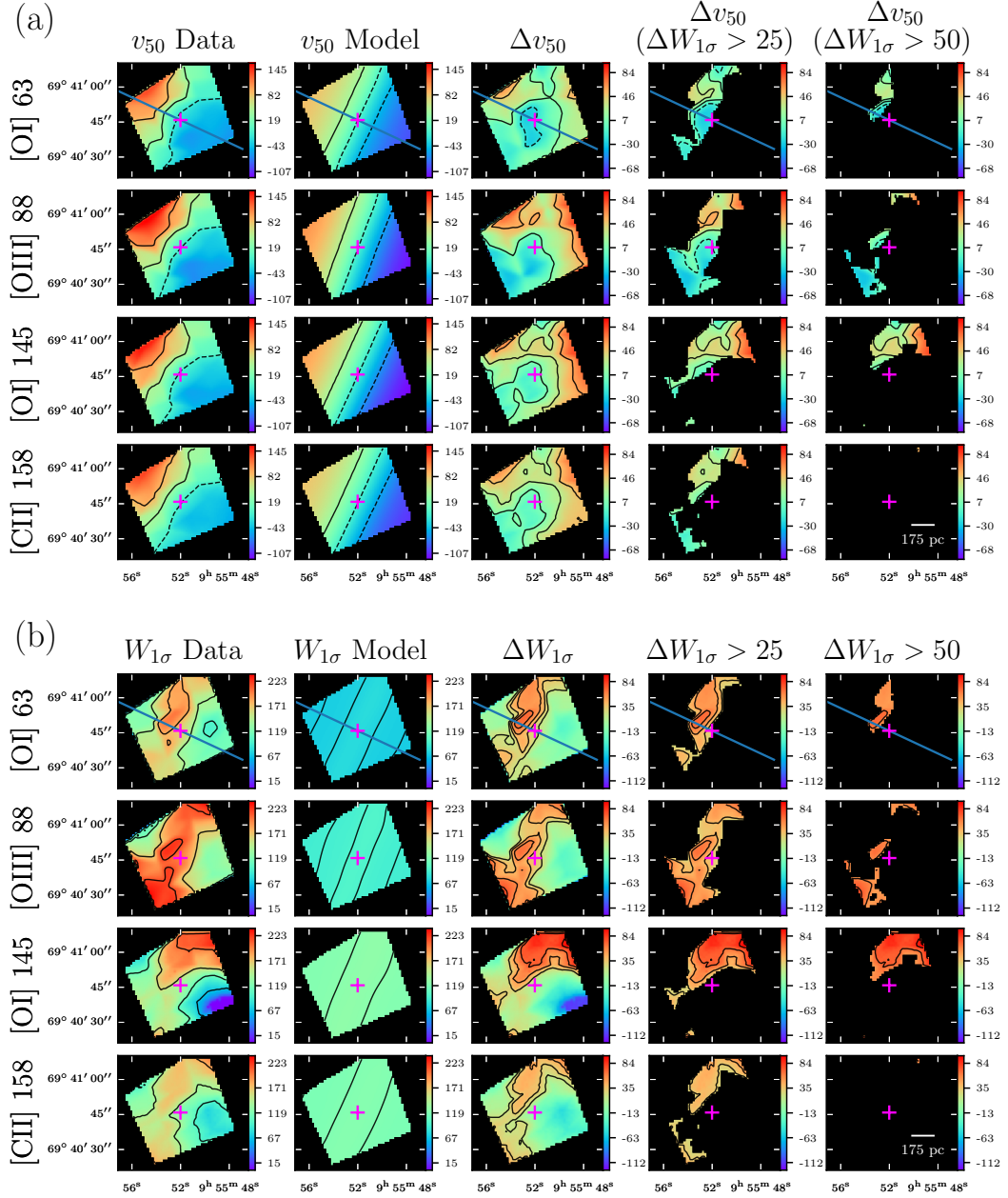


Figure 4.8 M 82: Results from modeling the disk velocity field with $3D$ BAROLO (which accounts for both the instrumental spectral and spatial resolutions) and the location of the outflow based on excess line broadening. Color bar values are in units of km s $^{-1}$. For each line, left to right: observed data, model result, data - model residual, spatial location of the wind in regions where $\Delta W_{1\sigma} > 25$ km s $^{-1}$, and spatial location of the wind in regions where $\Delta W_{1\sigma} > 50$ km s $^{-1}$. Contours in (a) are in five equal steps between the minimum and maximum velocities in each image. Contours in (b) are 0.3, 0.5, 0.7, and 0.9 of the peak value in each image. The solid blue line marks the galaxy major axis. The magenta cross marks the adopted galaxy center.

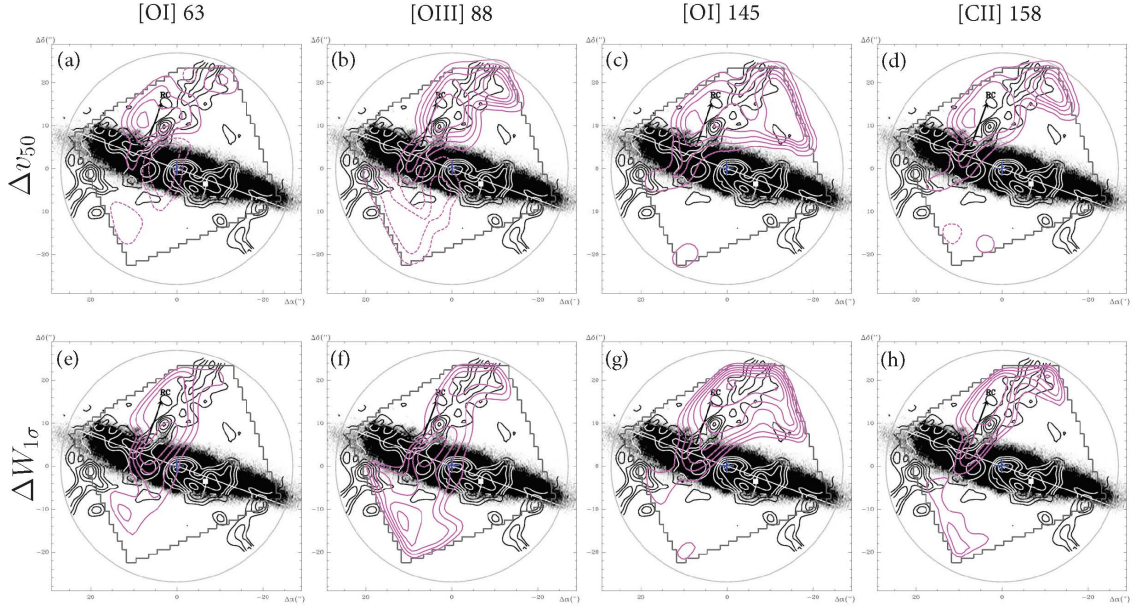


Figure 4.9 M 82: PACS contours (magenta) overlaid on the total integrated intensity contours of SiO(2-1) (black, [García-Burillo et al., 2001](#)) and the radio continuum at 4.8 GHz (grey scale, [Wills et al., 1999](#)).

gas traced by [O III] 88 with $\Delta v_{50 \text{ wind}}$ velocities ranging from $\sim -30 \text{ km s}^{-1}$ to $\sim -10 \text{ km s}^{-1}$. In general, the $\Delta v_{50 \text{ wind}}$ velocities increase with increasing (projected) distance from the galaxy nucleus in [O III] 88, [O I] 145, and [C II] 158. This is not the case with [O I] 63, however, where the $\Delta v_{50 \text{ wind}}$ velocities are greatest near the nucleus and decrease further up above the disk.

The largest residual velocity dispersions in the wind region (Column 4 of [Figure 4.8b](#)) are in [O I] 145 with $\Delta W_{1\sigma \text{ wind}}$ ranging from $\sim 25 - 85 \text{ km s}^{-1}$, where the velocity dispersions increase as the (projected) distance from the nucleus increases. The range of $\Delta W_{1\sigma \text{ wind}}$ velocities is similar between [O I] 63 and [O III] 88 ($\Delta W_{1\sigma \text{ wind}} \sim 30 - 65 \text{ km s}^{-1}$). Unlike [O I] 145, the largest residual velocity dispersions in [O I] 63 are localized in a compact area near the galaxy center and decrease with increasing distance from the center. [O III] 88 contains a similar compact region near

M 82

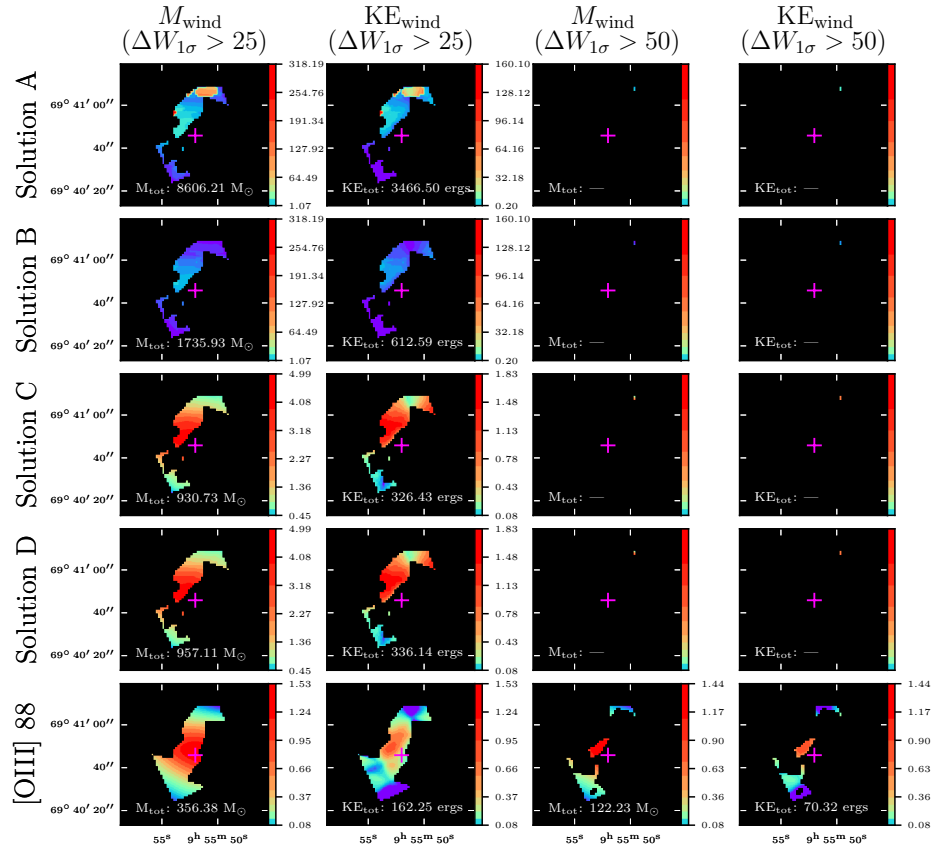


Figure 4.10 Mass and KE in the wind derived from the PDR solutions (see Section 4.7.4 for definitions of Solutions A, B, C, and D) and the [O III] 88 flux. Units are in $10^4 M_{\odot}$ and 10^{51} erg for the masses and KEs, respectively.

the nucleus as seen in [O I] 63 , however, although the dispersions in [O III] 88 initially decrease with increasing distance from the nucleus, at about $r \sim 10''$, $\Delta W_{1\sigma \text{ wind}}$ increases at larger radii. [C II] 158 appears to have a near constant $\Delta W_{1\sigma \text{ wind}} \sim 40 \text{ km s}^{-1}$ along the entire length of the collimated structure.

C13 estimate the velocity dispersions are $\sim 50 - 100 \text{ km s}^{-1}$ larger inside the outflow cones compared to the disk. Our observed data (even in its smaller FOV) are consistent with this assessment.

The sputtering of dust grains by shocks will release gas-phase silicon. The silicon is rapidly oxidized and forms SiO (Flower et al., 1996). Therefore, SiO is a good tracer of shocks, since it is thought to be formed in shocks. Figure 4.9 shows PACS contours (magenta) overlaid on the SiO (black and white contours) observed by García-Burillo et al. (2001) and the 4.8 GHz continuum (greyscale) observed by Wills et al. (1999). The SiO chimney appears to originate in the galaxy disk and extends to the NE beyond the PACS FOV. All lines trace this chimney out to $\sim 20''$ ($\sim 350 \text{ pc}$) above the disk and consistently indicate it is receding from us (see Figure 4.9a - Figure 4.9d). Residuals in [O III] 88 are the most tightly spatially correlated with the chimney while in [O I] 145 the residuals are the most extended W and E of the chimney. The residuals in the wind of M 82 are consistent with the idea that at the base of the outflow, gas flows out of the galaxy disk in filamentary channels instead of being launched uniformly across the starburst region.

The largest masses and KEs in the neutral outflow lie on the N edge of the outflow for Solution A, while the largest masses and KEs from Solution B lie inside the galaxy disk (see Figure 4.10). The morphology of the ionized mass distribution

follows that of the [O III] 88 flux distribution (i.e. the overall morphology of the ionized gas mass in the outflow is ellipsoidal and lies spatially coincident with the galaxy disk). The highest KEs in the ionized outflow coincide with the portion of the SiO chimney that intersects the galaxy plane.

C13 estimate the mass of the neutral gas in the outflow to be $2 - 8 \times 10^7 M_{\odot}$; a value $\sim 4 - 15$ times lower than the cold molecular gas reported in [Walter et al. \(2002, \$3.3 \times 10^8 M_{\odot}\$ \)](#) and 3 orders of magnitude higher than the warm molecular gas reported in [Veilleux et al. \(2009\)](#). C13 estimated a KE of $\sim 1 - 5 \times 10^{54}$ erg in the neutral outflow; an order of magnitude lower than that of H α ([Shopbell & Bland-Hawthorn, 1998, \$3 \times 10^{55}\$ erg](#)) and 2 orders of magnitude larger than the KE measured in H $_2$.

4.9.2 Cen A

The velocity field shown in the first column of [Figure 4.11a](#) indicates that the E side of the gaseous disk at the center of Cen A is approaching us, while the W side of the disk is receding from us, consistent with the velocity field observed in the optical ionized ([Bland et al., 1987](#)) and molecular gas ([Espada et al., 2009](#)). The velocities range from $v_{50} \sim -60$ to $+105 \text{ km s}^{-1}$ for all lines.

The wind region in this object, defined by the excess line broadening or residual velocity dispersions, lies along the galaxy minor axis in the direction of the well-known radio jet. Bulk velocities of the gas near the galaxy nucleus are mostly systemic with $\Delta v_{50 \text{ wind}} \sim \pm 10 \text{ km s}^{-1}$ for all lines (see [Figure 4.11a.1](#) -

Cen A

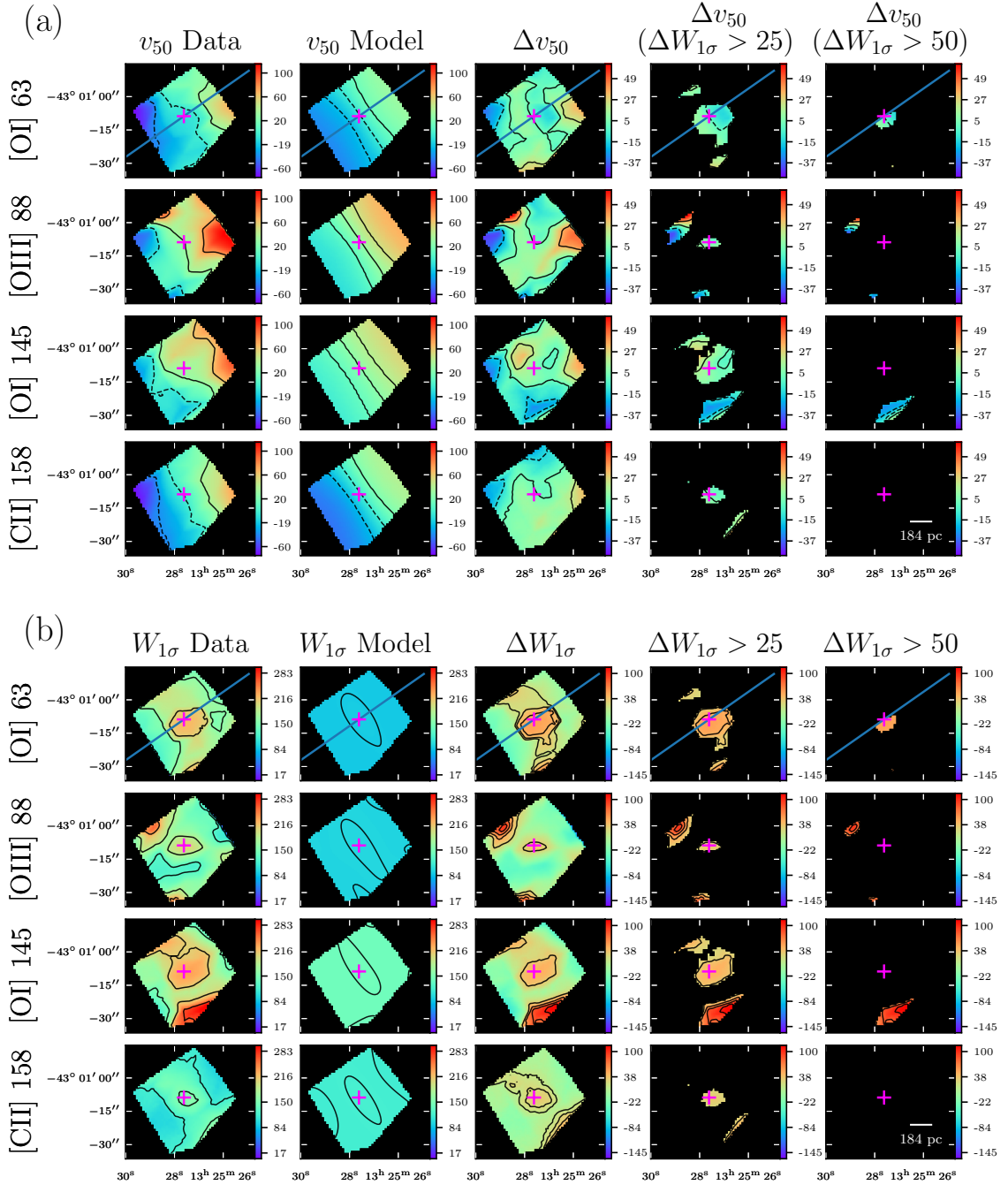


Figure 4.11 Cen A: Results from modeling the disk velocity field with 3^{D} BAROLO. Symbols and plots are the same as those in Figure 4.8.

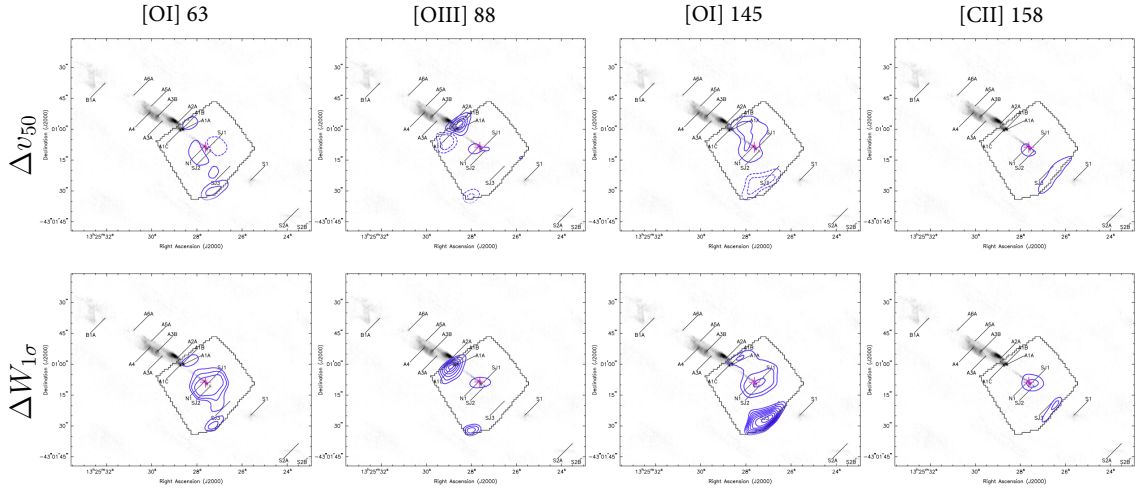


Figure 4.12 Cen A: PACS contours overlaid on 8.4 GHz image from [Hardcastle et al. \(2003\)](#).

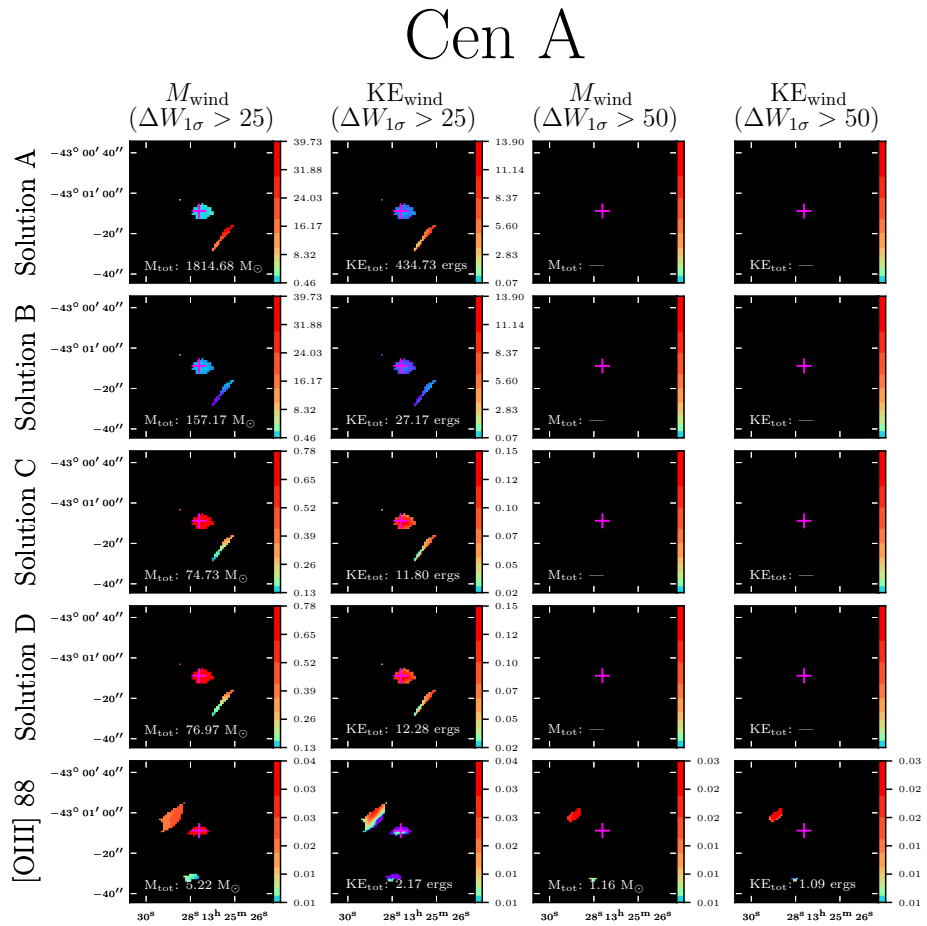


Figure 4.13 Mass and KE in the wind derived from the PDR solutions and the [O III] 88 flux. Symbols, units, and plots are the same as those in [Figure 4.10](#).

Figure 4.11a.4). In [O III] 88 , there is a compact feature $\sim 15''$ NE of the nucleus with v_{50} residuals $\sim -30 \text{ km s}^{-1}$ in the E and $\sim +45 \text{ km s}^{-1}$ in the W. This feature is not seen in [C II] 158 and shows little bulk motion in either [O I] 63 or [O I] 145 ($\Delta v_{50 \text{ wind}} \sim +10 \text{ km s}^{-1}$).

The residual velocity dispersions in the wind region (Figure 4.11b.1 - Figure 4.11b.4) near the galaxy nucleus for [O III] 88 and [C II] 158 are spatially compact with $\Delta W_{1\sigma \text{ wind}} \lesssim 30 \text{ km s}^{-1}$. Also near the nucleus, the residual velocity dispersions in [O I] 63 and [O I] 145 are elongated towards the NW in the direction of the jet with $\Delta W_{1\sigma \text{ wind}} \sim 30 - 50 \text{ km s}^{-1}$. The wind region observed in [O I] 145 is the most extended along the major axis compared to the wind region mapped by the other three emission lines. The largest residual velocity dispersions in the compact feature NE of the nucleus is $\Delta W_{1\sigma \text{ wind}} \sim 90 \text{ km s}^{-1}$ in [O III] 88 , while moderate velocity dispersions of $\sim 30 \text{ km s}^{-1}$ are seen in [O I] 63 and [O I] 145 .

In [O I] 145 an elongated feature is seen S of the galaxy nucleus with $\Delta v_{50 \text{ wind}} \sim 25 \text{ km s}^{-1}$ and $\Delta W_{1\sigma \text{ wind}} \sim 95 \text{ km s}^{-1}$. It is unlikely that this feature is a component of the outflowing gas as it spatially coincides with the edge of the putative warped disk seen in CO, Pa- α , and the MIR (Espada et al., 2009; Marconi et al., 2000b; Quillen et al., 2006; Radomski et al., 2008).

Figure 4.12 shows PACS contours of $\Delta v_{50 \text{ wind}}$ (top row) and $\Delta W_{1\sigma \text{ wind}}$ (bottom row) overlaid on the 8.4 GHz images of Cen A from Hardcastle et al. (2003). NE of the nucleus, within $r \lesssim 1 \text{ kpc}$, a compact feature is seen in [O I] 63 , [O III] 88 , and [O I] 145 . This feature is spatially coincident with a complex of bright emission knots seen in the radio and X-ray and which are known to be associated with the

outflow (e.g. [Hardcastle et al., 2003](#); [Kraft et al., 2002](#)).

For PDR Solution A (see [Figure 4.13](#)), the largest neutral outflow masses ($\sim 4 \times 10^5 M_{\odot}$) are located to the SW of the nucleus in a thin structure elongated from NW to SE. This is in striking contrast to PDR Solution B where the largest neutral masses ($\sim 4 \times 10^3 M_{\odot}$) are compact and localized around the galaxy nucleus.

[Figure 4.13](#) also shows a compact region of ionized gas around the nucleus that contains $\sim 50 M_{\odot}$ and a structure to the NE with mass $\sim 30 M_{\odot}$. The largest KE of 9×10^{48} erg lies in a concentrated region to the NE with more moderate energies of $\sim 2 \times 10^{48}$ centered close to the nucleus. This region of large energy spatially corresponds to knot “A” found in [Kraft et al. \(2002\)](#).

4.9.3 Circinus

The v_{50} maps of Circinus (see Column 1 of [Figure 4.14a](#)) range in velocity between $\pm 100 \text{ km s}^{-1}$ and confirm data at other wavelengths that the N side of the disk is approaching us and the S side of the disk is receding from us consistent with observations in $\text{H}\alpha$ ([Elmouttie et al., 1998b](#)) and in CO ([Zschaechner et al., 2016](#)).

Circinus lacks a significant detection of an outflow in any of the fine-structure lines. Although the [O III] 88 residuals NW of the nucleus lie within the ionization cone, the residuals also overlap with a molecular spiral arm seen in CO ([Izumi et al., 2018](#)). Lying on the PACS FOV and spatially coincident with the molecular spiral arm, it is difficult to attribute this residual line width to the outflow. [O I] 145 residuals in the wind lie SE of the nucleus and are more likely associated

Circinus

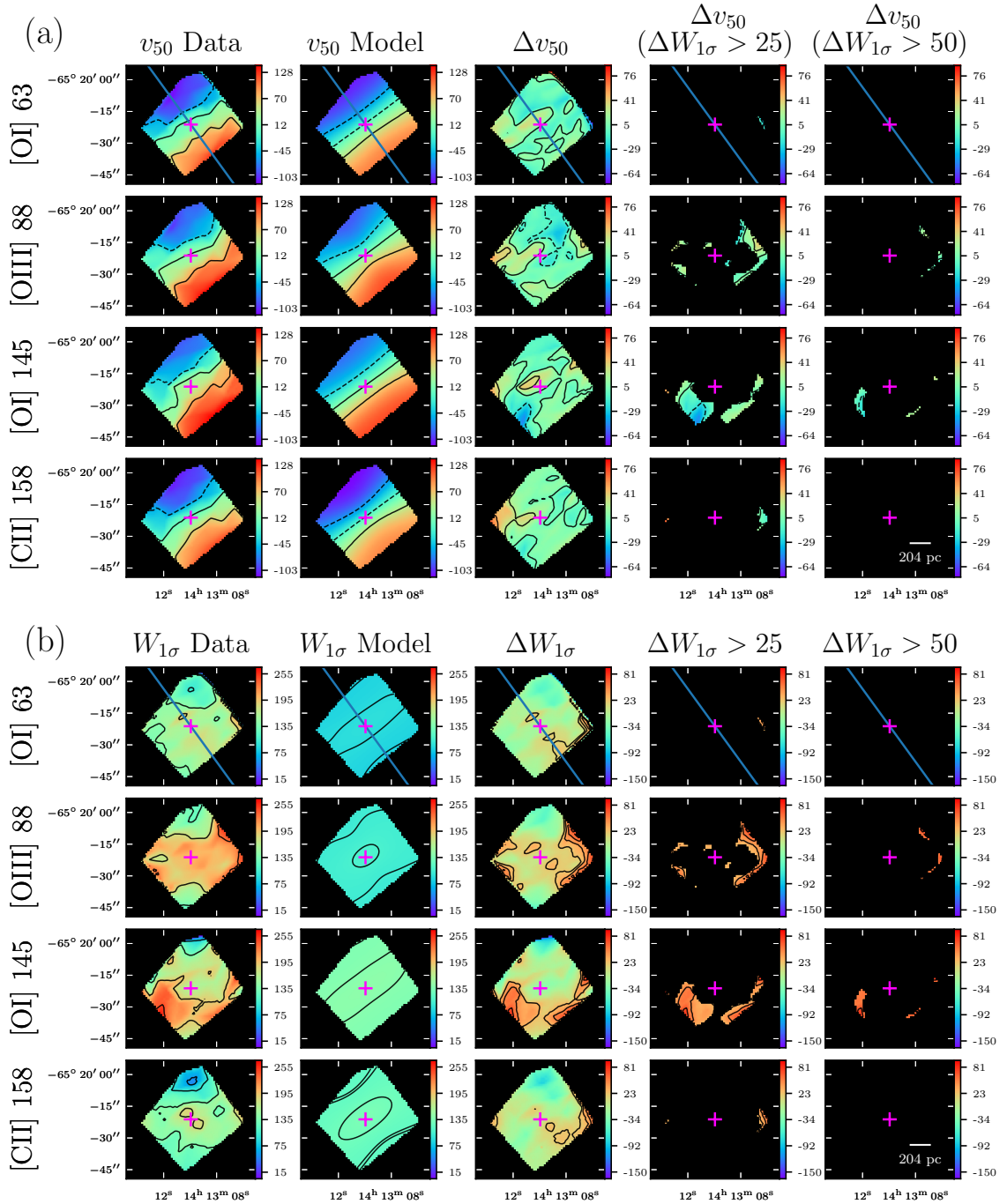


Figure 4.14 Circinus: Results from modeling the disk velocity field with 3^{D} BAROLO. Symbols, units, and plots are the same as those in Figure 4.8.

Circinus

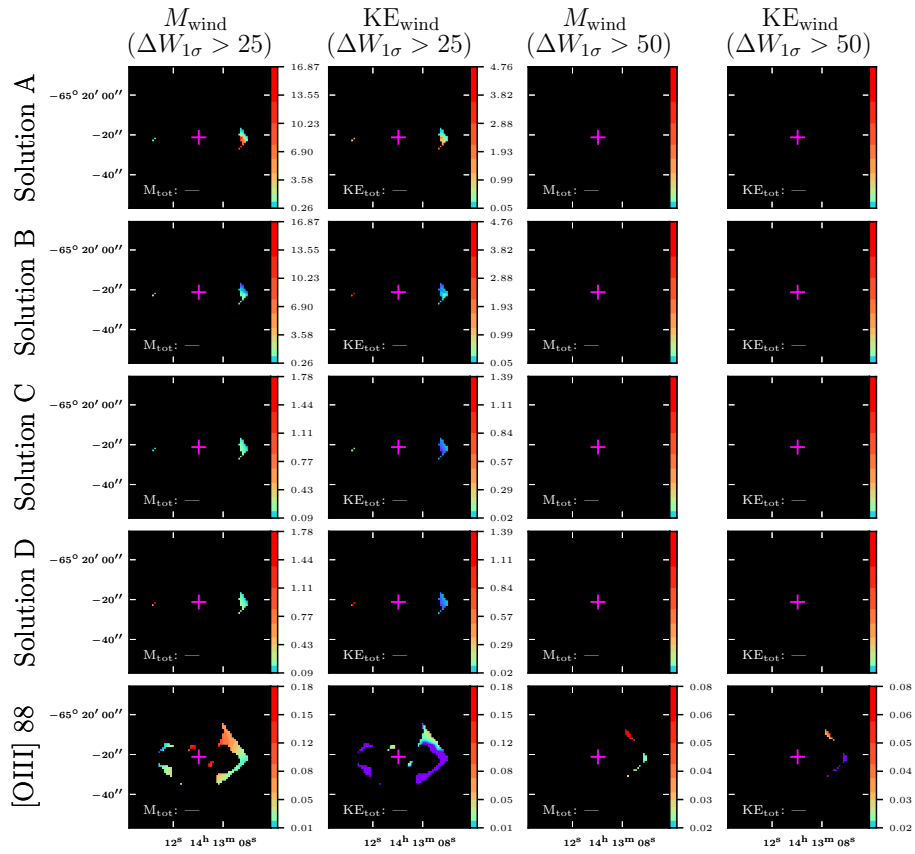


Figure 4.15 Circinus does not have a discernible outflow in either the neutral or ionized gas.

with the circumnuclear starburst ring (see Figure 5 of [Mingo et al., 2012](#)).

4.9.4 NGC 253

For NGC 253, the v_{50} maps (see Column 1 of [Figure 4.16a](#)) range in velocity from $\sim -80 \text{ km s}^{-1}$ to $\sim 130 \text{ km s}^{-1}$ for all lines. The E side of the disk is approaching us while the W side of the disk is receding from us, consistent with observations in $\text{H}\alpha$ ([Hlavacek-Larrondo et al., 2011](#)).

In [Figure 4.16\(a, b\)](#), the wind traced by [O I] 63 is a column oriented along the galaxy minor axis. The column is approximately $\sim 5''$ wide to the NE of the nucleus. That width increases as distance from the nucleus increases, with maximum widths of $\sim 15''$ and $\sim 30''$ for the regions N and S of the galaxy center, respectively. The largest v_{50} ($\sim 40 \text{ km s}^{-1}$) are located in the S portion of the column while the v_{50} in the N portion of the column are nominal ($\sim 0 - 5 \text{ km s}^{-1}$). This suggests that the S cone traced by [O I] 63 is receding but there is little (if any) bulk motion of the gas in the N cone along the line of sight. The velocity dispersion across the column is nearly uniform with $W_{1\sigma} \sim 20 \text{ km s}^{-1}$.

The wind in [O III] 88 lies in two distinct regions to the NW and SE of the nucleus. The NW feature with diameter $\sim 15''$ is located $\sim 10''$ from the galaxy center while the W edge of the $\sim 20'' \times 15''$ SE feature is adjacent to the nucleus. [Figure 4.16a](#) shows the largest approaching velocities ($\sim -40 \text{ km s}^{-1}$) are concentrated in the NW feature. The largest velocity dispersions ($\sim 200 \text{ km s}^{-1}$) are prominent in the NW feature while more moderate velocity dispersions ($\lesssim 90$

NGC 253

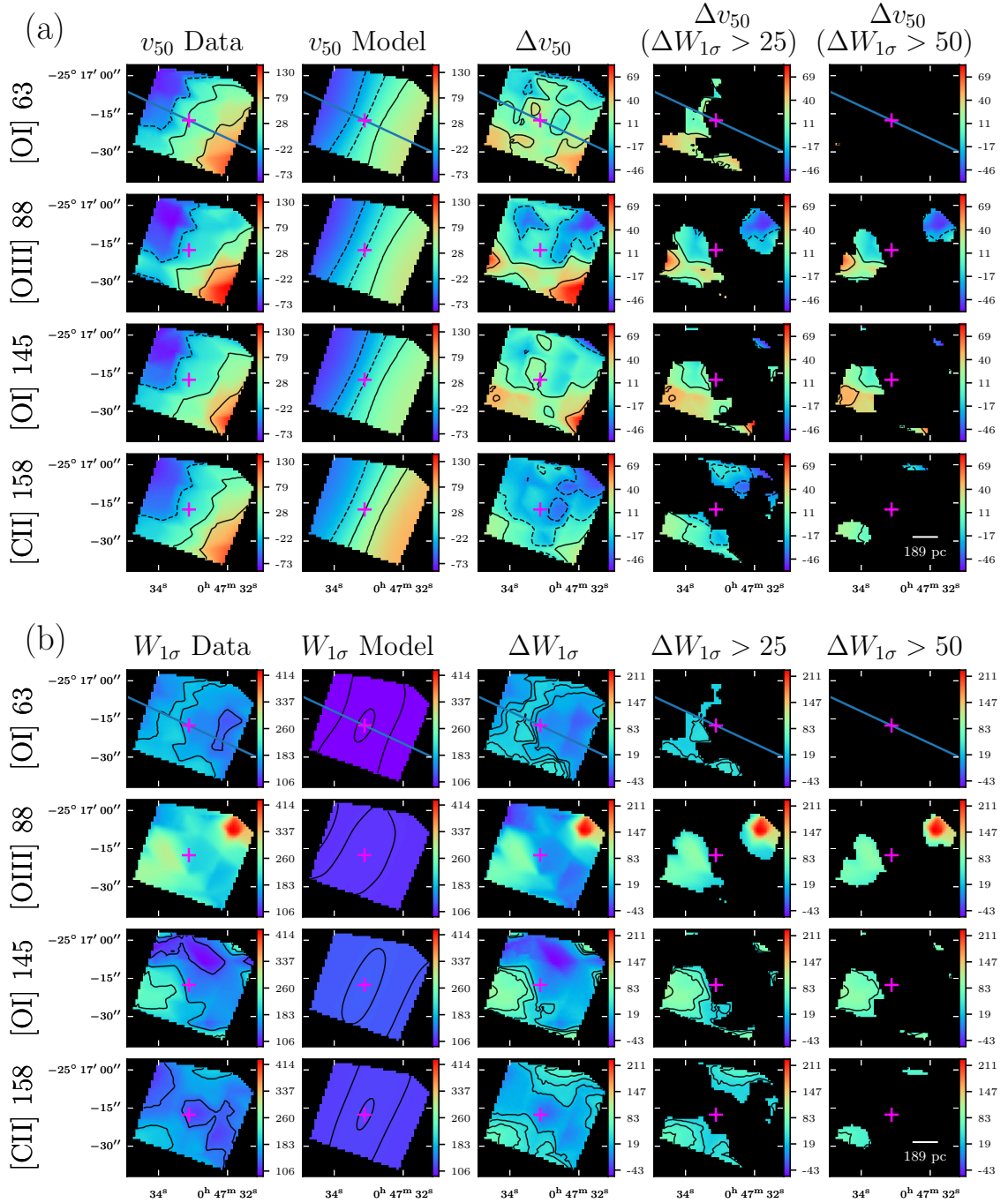


Figure 4.16 NGC 253: Results from modeling the disk velocity field with ^{3D}BAROLO. Symbols, units, and plots are the same as those in Figure 4.8.

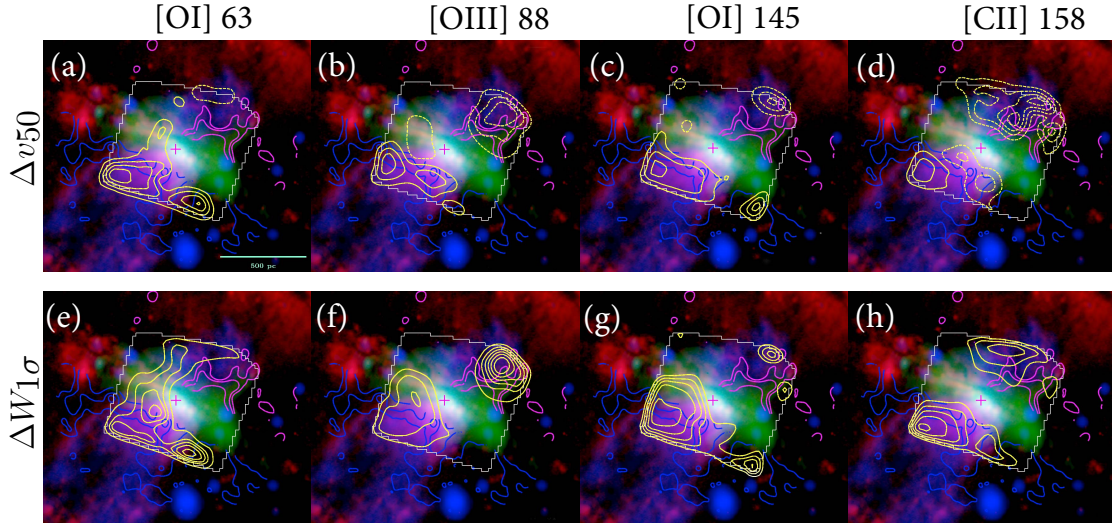


Figure 4.17 NGC 253: PACS contours (yellow), contours of receding and approaching CO outflow (magenta and blue, respectively) from Bolatto et al. (2013). Composite image from Heesen et al. (2011) which shows H α in red from Westmoquette et al. (2011), λ 20 cm continuum (green), and soft X-ray in blue from Hardcastle et al. (2010).

km s $^{-1}$) are found in the SE feature.

The wind traced by [O I] 145 is concentrated to the SE of the nucleus with receding velocities $50 \gtrsim v_{50} \gtrsim 0$ km s $^{-1}$ (see Figure 4.16a) and velocity dispersions $W_{1\sigma} \lesssim 115$ km s $^{-1}$ (see Figure 4.16b). The feature is $\sim 20''$ in diameter on the E side while the W side tapers to the SW for $\sim 8''$. As seen in [O III] 88, the W edge of the [O I] 145 SW feature lies adjacent to the nucleus. Interestingly, not only does this SW feature contain similar velocity dispersions (~ 115 km s $^{-1}$) in [O III] 88 and in [O I] 145, but the extent and location of those velocity dispersions are spatially coincident in the emission lines. No feature is seen in the NW in [O I] 145.

Figure 4.16a shows that the majority of [C II] 158 is approaching us with the largest velocities ($v_{50} \sim -45$) located NW of the nucleus. The velocity dispersions of [C II] 158 are moderate ($\sim 40 - 80$ km s $^{-1}$; see Figure 4.16b) in the NW and SE

NGC 253

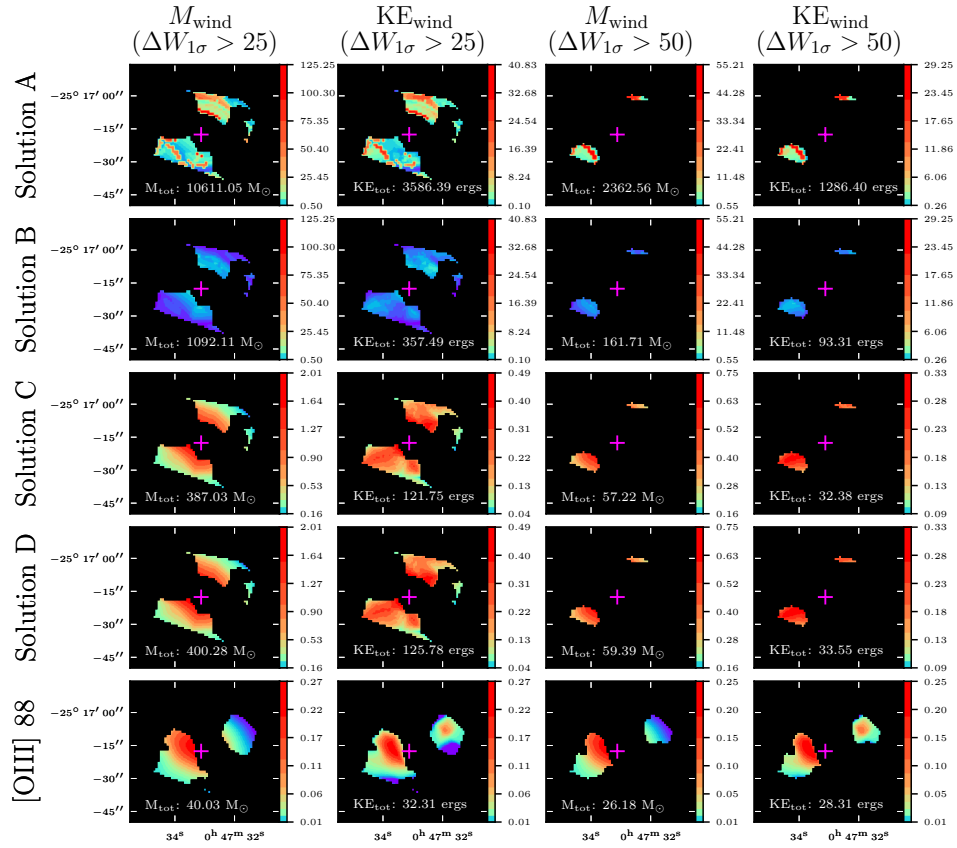


Figure 4.18 Mass and KE in the wind derived from the PDR solutions and the [O III] 88 flux. Symbols, units, and plots are the same as those in Figure 4.10.

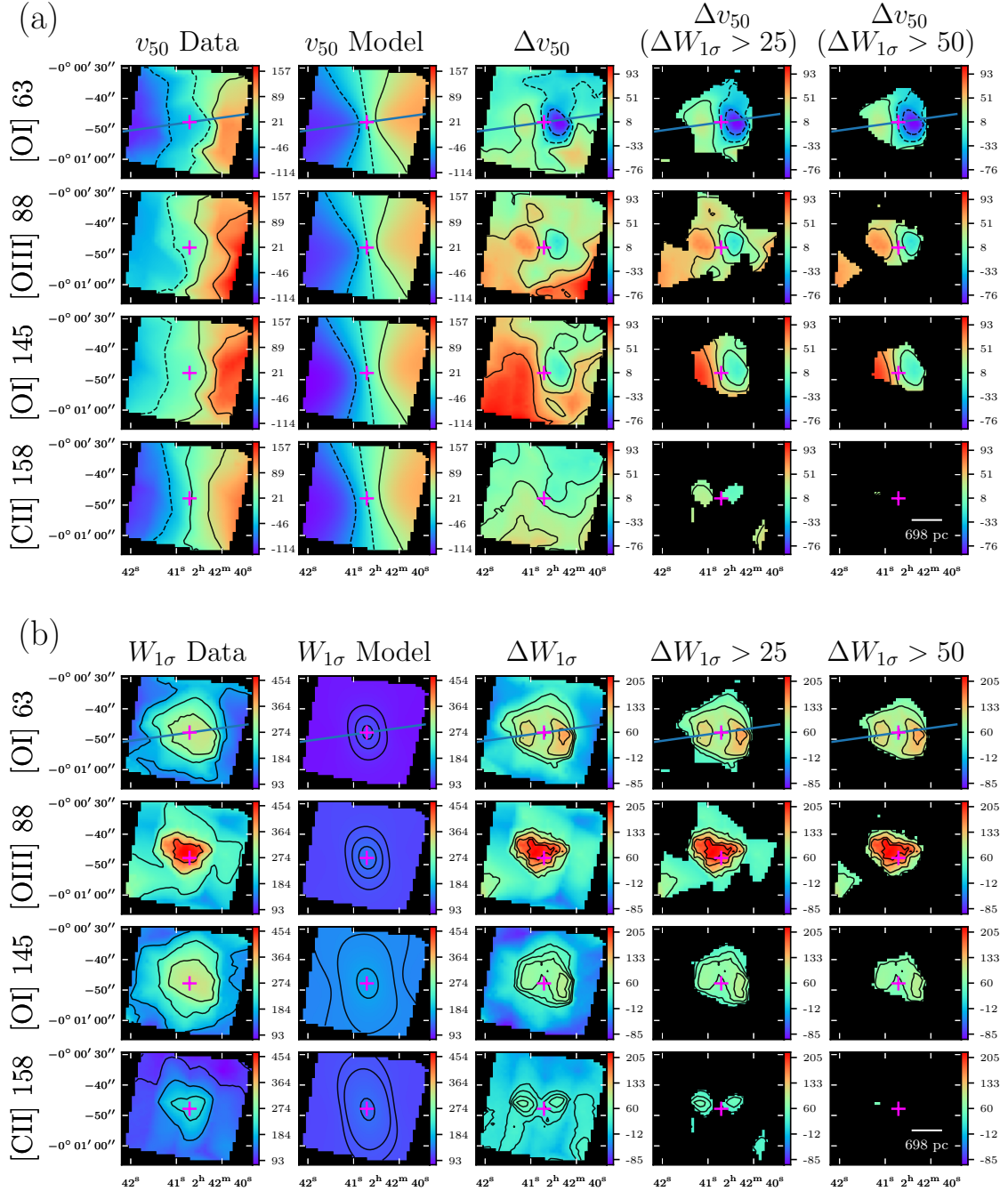
features. The length of the SE feature is detected along the entire S edge of the FOV while the width of the feature tapers from the largest width of $\sim 10''$ and decreases towards the SE. The NW feature is roughly $15'' \times 10''$ and lies along the edge of the N FOV. Unlike the [O I] 63 and [O I] 145 the SE feature traced by [C II] 158 does not lie adjacent to the galaxy center.

The greatest amount of ionized gas is found in the SE lobe with masses at $\sim 350 M_{\odot}$ near the galaxy center and then decreasing in the SE direction with increasing radius from the nucleus. The ionized gas masses in the NW lobe are considerably smaller than in the southern lobe, with masses ranging from ~ 10 to $\sim 80 M_{\odot}$. We see that the largest energies ($\sim 2 \times 10^{49}$ ergs) in the ionized wind are located in long, thin structure in the SE lobe. We see that the moderate KE are more extended in the SE lobe.

4.9.5 NGC 1068

The v_{50} maps of NGC 1068 (see Column 1 in [Figure 4.19a](#)) indicate that the galaxy disk is receding in the W and approaching in the E. However, the bulk motions of the wind, as determined by the v_{50} residuals (Column 4 in [Figure 4.19a](#)), are oriented in the opposite direction of the disk rotation with approaching velocities in the W and receding velocities in the E. In [O I] 63, the largest approaching $\Delta v_{50 \text{ wind}}$ velocities ($\sim -85 \text{ km s}^{-1}$) are in a compact feature just W of the nucleus while moderate receding velocities are in the E ($\sim 35 \text{ km s}^{-1}$). [O III] 88 $\Delta v_{50 \text{ wind}}$ residuals show moderate approaching values in the W (~ -20

NGC 1068



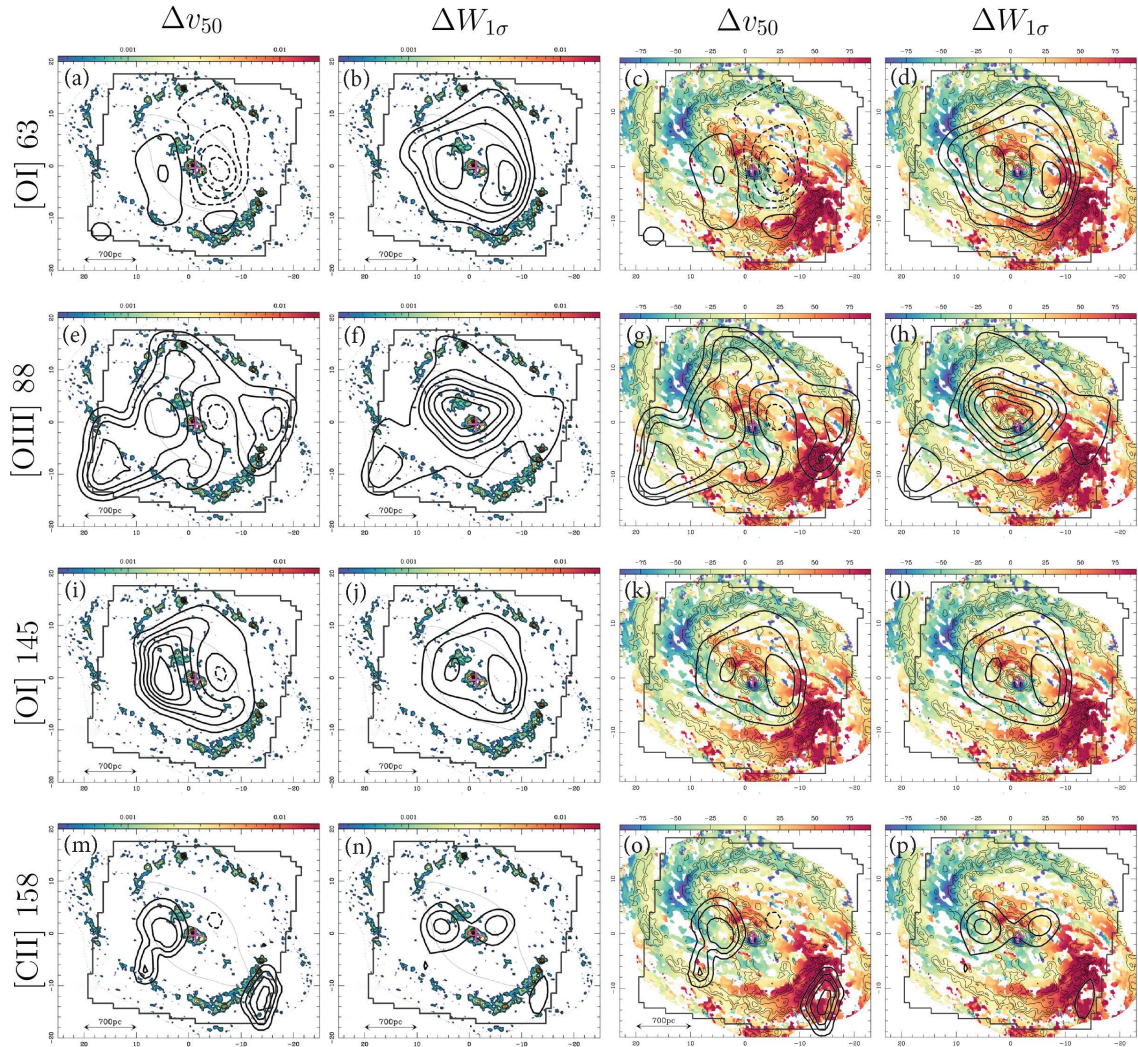


Figure 4.20 NGC 1068: PACS contours overlaid on 349 GHz continuum and CO(3-2) residual mean-velocity field from [García-Burillo et al. \(2014\)](#).

NGC 1068

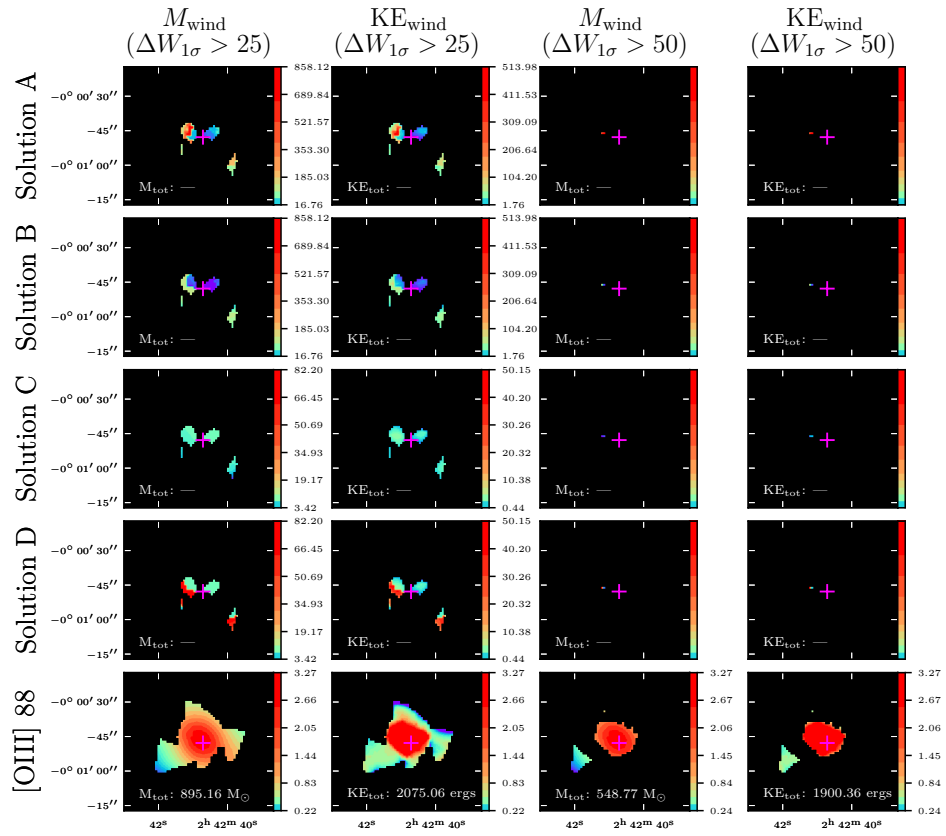


Figure 4.21 Mass and KE in the wind derived from the PDR solutions and the [O III] 88 flux. Symbols, units, and plots are the same as those in Figure 4.10.

km s⁻¹) and fast receding velocities in the E (~ 65 km s⁻¹). [O I] 145 and [C II] 158 show mostly systemic velocities in the W (~ -5 km s⁻¹). However, [O I] 145 shows fast receding velocities in the E (~ 90 km s⁻¹) while [C II] 158 shows moderate receding velocities of ~ 30 km s⁻¹.

The largest residual velocity dispersions in the wind ($\Delta W_{1\sigma \text{ wind}} \sim 200$ km s⁻¹; see [Figure 4.19b](#)) are detected in [O III] 88 and are in a central compact region that is elongated towards the NE along the direction of the nuclear bar. This region is spatially coincident with the molecular outflow seen in CO(3-2) ([García-Burillo et al., 2014](#)). It is also spatially coincident with H α and [O III] 5007 line emission which extends NE of the nucleus ([Cecil et al., 1990](#); [Veilleux et al., 2003](#)). In the NLR, the deprojected intrinsic ionized gas velocities associated with optical [NII] emission are ~ 1500 km s⁻¹ with respect to systemic ([Cecil et al., 1990](#)).

In [O I] 63, [O I] 145, and [C II] 158, there are two knots which flank the galaxy nucleus. The W knot contains the larger $\Delta W_{1\sigma \text{ wind}}$ residuals with $\Delta W_{1\sigma \text{ wind}} 170$ km s⁻¹ in [O I] 63 and $\Delta W_{1\sigma \text{ wind}} \sim 100$ km s⁻¹ in [O I] 145. The E knot contains $\Delta W_{1\sigma \text{ wind}}$ residuals of ~ 120 km s⁻¹ and ~ 70 km s⁻¹ for [O I] 63 and [O I] 145, respectively. In [C II] 158, the knots have similar dispersion residuals with $\Delta W_{1\sigma \text{ wind}} \sim 70$ km s⁻¹. The $\Delta W_{1\sigma \text{ wind}}$ knots seen in [O I] 63, [O I] 145, and [C II] 158 are most likely non-circular motions due to the presence of NGC 1068's nuclear bar and spiral arms (features which are not accounted for in our simple disk velocity field model), as opposed to an outflow.

The ionized gas mass follows the morphological structure of the [O III] 88 flux (i.e. an ellipse spanning from the NE to the SW) with the greatest masses (~ 4000

M_{\odot}) concentrated around the galaxy center. The largest energies are concentrated around the nucleus, while there may be some structure following the spiral arms.

4.9.6 NGC 3079

Column 1 of [Figure 4.22a](#) shows the [C II] 158 v_{50} map of NGC 3079. The range of velocities are between ~ -120 and $\sim +160$ km s^{-1} and indicate that the gas on the N side is approaching us while the gas on the S side is receding from us, consistent with observations of H α ([Veilleux et al., 1999](#)) and H $_2$ O maser spots in the disk ([Yamauchi et al., 2004](#)).

The [C II] 158 v_{50} residuals in the wind region east of the nucleus ([Figure 4.22a](#), Column 4) show redshifted velocities in the N and blueshifted velocities in the S. W of the nucleus, most of the redshifted velocities lie close to the galaxy plane while blueshifted velocities begin to appear further below the plane at $\sim 10''$. The [C II] 158 $\Delta W_{1\sigma \text{ wind}}$ map ([Figure 4.22b](#), Column 4) shows an elongated feature $\sim 10''$ in length just S of the nucleus with $\Delta W_{1\sigma \text{ wind}} \sim 100$ km s^{-1} . A more extended structure lies E to W around the elongated feature and has $\Delta W_{1\sigma \text{ wind}} \sim 75$ km s^{-1} .

The contours of these [C II] 158 residuals are overlaid on the 1.4 GHz image from [Sebastian et al. \(2019\)](#) (see the top row of [Figure 4.23](#)), where the double-lobed radio morphology of the wind is outlined by bright filaments. At the base of the W lobe, where the filaments are brightest, $\Delta v_{50 \text{ wind}}$ appears to trace the lobe's edges. The velocities along the southern edge are receding with $\Delta v_{50 \text{ wind}} \sim 35$ km s^{-1} and

NGC 3079

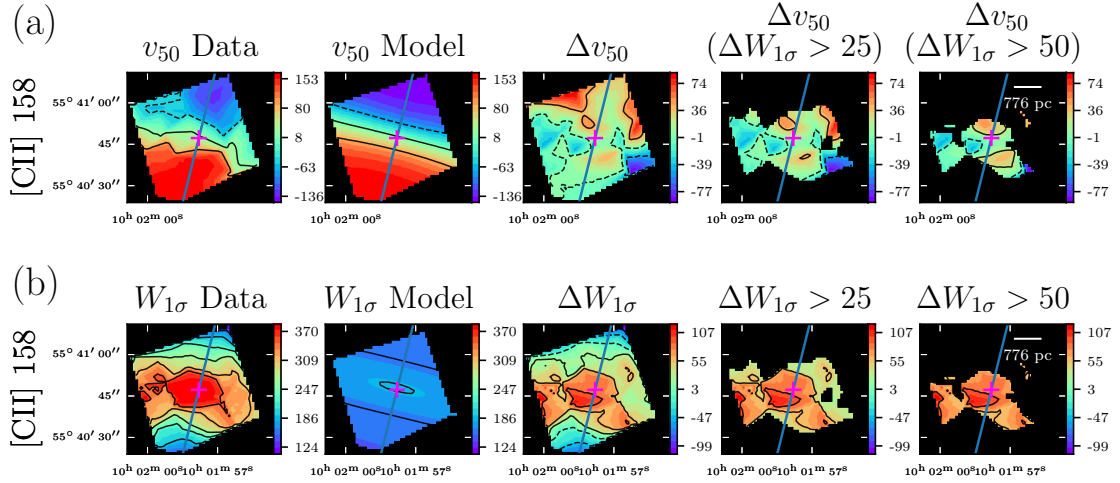


Figure 4.22 NGC 3079: Results from modeling the disk velocity field with 3^{D} BAROLO. Symbols, units, and plots are the same as those in Figure 4.8.

the velocities along the northern edge are approaching with $\Delta v_{50 \text{ wind}} \sim -15 \text{ km s}^{-1}$.

The middle row of Figure 4.23 shows the same contours as above, but overlaid on the continuum subtracted $\text{H}\alpha + [\text{N II}]$ image from Cecil et al. (2001) where only the eastern bubble is visible (the western lobe lies behind the disk of galaxy and is therefore extinguished). In the E lobe, there is a lack of radio emission along the southern edge of the bubble, extending out to $\sim 1 \text{ kpc}$ above the disk. However, there is optical emission along this edge where approaching velocities in $[\text{C II}] 158$ are $\Delta v_{50 \text{ wind}} \sim -35 \text{ km s}^{-1}$ and where the largest velocities of $\Delta W_{1\sigma \text{ wind}} (\sim 100 \text{ km s}^{-1})$. Cecil et al. (2001) has shown that this filament aligns with the axis of the jet observed at 8 GHz (Trotter et al., 1998). The larger dispersion residuals observed here are most likely due to the presence of this jet interacting with the ISM of the galaxy disk.

At $\sim 1 \text{ kpc}$, the optical filament appears to disperse at the location where the

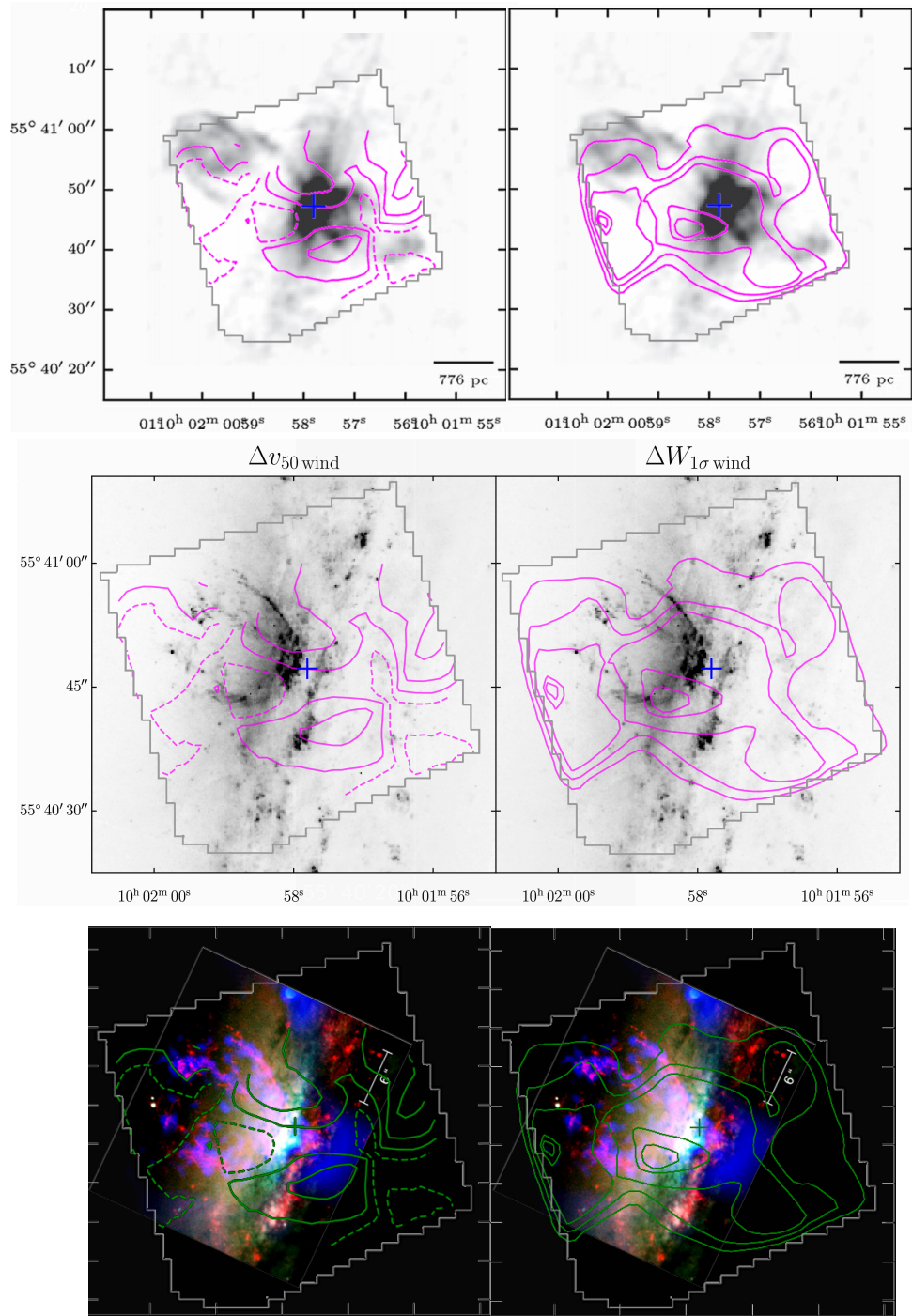


Figure 4.23 Top row: PACS contours of the [C II] 158 v_{50} and $W_{1\sigma}$ residuals in the wind in NGC 3079 overlaid on 1.4GHz observations from Sebastian et al. (2019). Middle row: PACS contours of the [C II] 158 v_{50} and $W_{1\sigma}$ residuals in the wind in NGC 3079 overlaid on H α + [N II] image from Cecil et al. (2001). Bottom row: *Chandra* image (blue) + *HST* (red and green).

radio emission begins and extends ~ 1 kpc to the top of the bubble. The $\Delta v_{50 \text{ wind}}$ along this filament is $\sim -20 \text{ km s}^{-1}$. The base of the northern edge is seen in both optical and radio where receding velocities are $\Delta v_{50 \text{ wind}} \sim 45 \text{ km s}^{-1}$.

The bottom row of [Figure 4.23](#) shows the [C II] 158 $\Delta W_{1\sigma \text{ wind}}$ contours overlaid on the *HST* image from above (red and green) and the *Chandra* data from [Cecil et al. \(2001\)](#). Notice that in the E, the (soft) X-ray filaments spatially correlate with the optical filaments, while in the W, the (soft) X-ray emission fills the second lobe, but lacks any of the filamentous structures seen at 1.4 GHz.

4.9.7 NGC 4945

Column 1 of [Figure 4.24a](#) shows the v_{50} maps of NGC 4945 which range in velocity from $\sim -90 \text{ km s}^{-1}$ to $\sim +100 \text{ km s}^{-1}$ for [O III] 88, [O I] 145, and [C II] 158. As discussed in [Section 4.8.3](#), the [O I] 63 emission in NGC 4945 shows significant self-absorption along the galaxy major axis and is excluded from this analysis. The v_{50} maps indicate that the NE part of the disk is receding from us and the SW part of the disk is approaching us, consistent with previous observations ([Venturi et al., 2017](#)).

The maps of the residuals in the wind in Column 4 of [Figure 4.24](#) show in [O III] 88 a SE to NW collimated structure aligned with NGC 4945's biconical outflow. The presence of the SE lobe is clearly seen in the [O I] 145 wind residuals, with perhaps some detection of the inner NW lobe. No outflow is detected in [C II] 158.

In [Figure 4.25](#), the contours of the wind residuals (magenta lines) are overlaid

NGC 4945

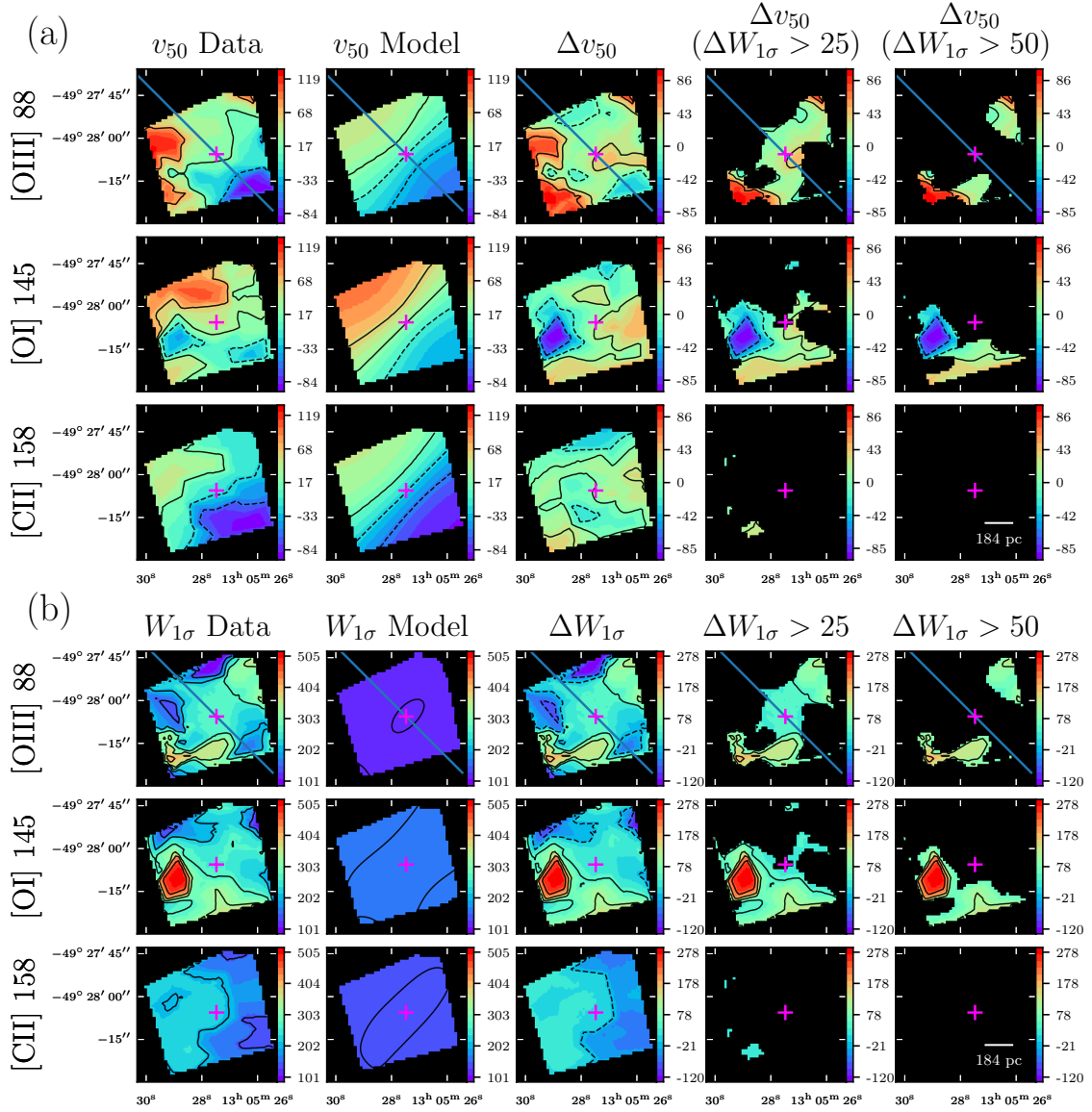


Figure 4.24 NGC 4945: Results from modeling the disk velocity field with $3D$ BAROLO. Symbols, units, and plots are the same as those in Figure 4.8.

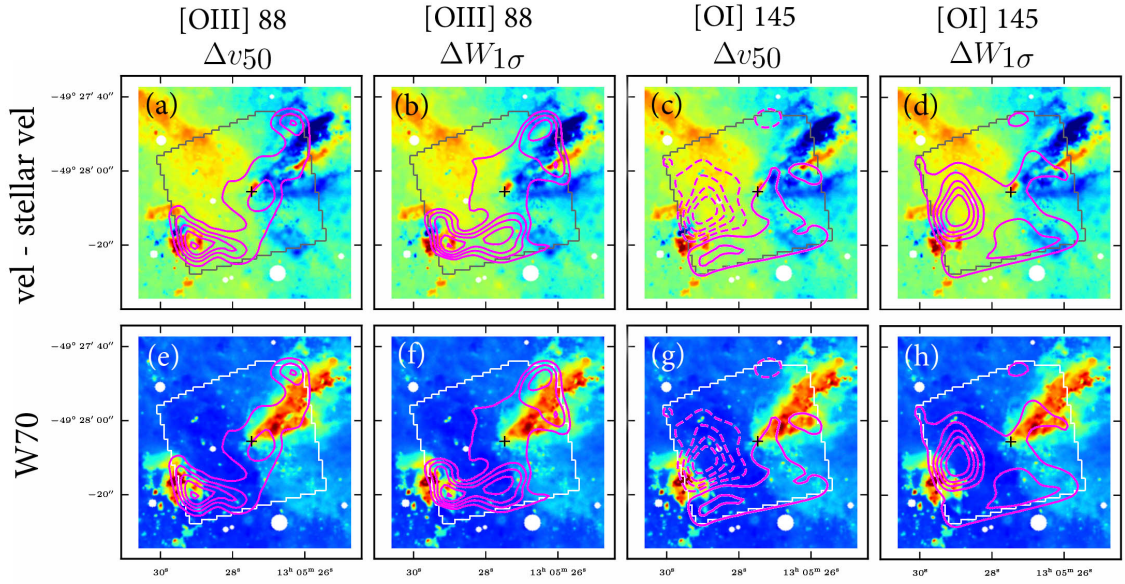


Figure 4.25 Top row: PACS contours overlaid on the [NII] residual velocity field of NGC 4945 from Venturi et al. (2017). Bottom row: PACS contours overlaid on the [NII] W70 of NGC 4945 from Venturi et al. (2017).

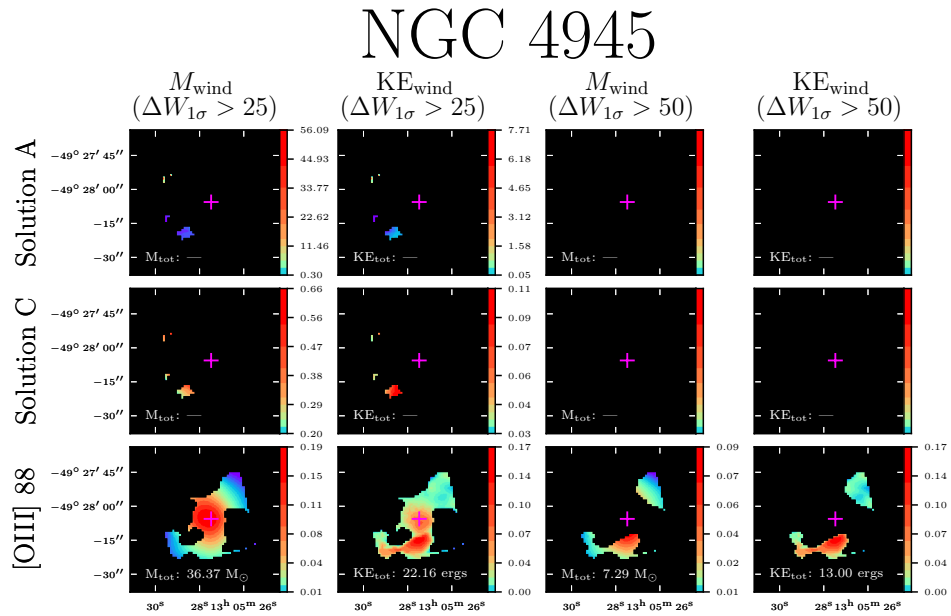


Figure 4.26 Mass and KE in the wind derived from the PDR solutions and the [O III] 88 flux. Symbols, units, and plots are the same as those in Figure 4.10.

on the optical [N II] 6583 Å images from [Venturi et al. \(2017\)](#) (top row) and the X-ray images from [Marinucci et al. \(2012\)](#) (bottom row). Residual velocities and dispersions in the ionized gas as traced by [O III] 88 are largest along the edges of the outflow lobes, this is most evident in [Figure 4.25\(a,c\)](#), with receding velocities up to $\Delta v_{50\text{ wind}} \sim +95 \text{ km s}^{-1}$ and up to $\Delta v_{50\text{ wind}} \sim +50 \text{ km s}^{-1}$ for the SE and NW lobes, respectively. [O III] 88 residual dispersions at the base of the SE lobe are in the range $\Delta W_{1\sigma\text{ wind}} \sim 100 \text{ km s}^{-1}$ to $\sim 160 \text{ km s}^{-1}$, while $\Delta W_{1\sigma\text{ wind}}$ ranges from $\sim 90 - 100 \text{ km s}^{-1}$ on the edges of the NW lobe.

The [O I] 145 v_{50} wind residuals (see Column 1 of [Figure 4.24a](#)) are located mostly below the plane of the galaxy. In the optical, the SE lobe only appears at $\sim 15''$ from the nucleus, but in [O I] 145, the strongest feature of the SE lobe begins to emerge at $\sim 10''$, demonstrating the advantage of the FIR to penetrate further through the galaxy disk. The [O I] 145 feature in the SE lobe is approaching with $\Delta v_{50\text{ wind}} \sim -90 \text{ km s}^{-1}$ and contains large dispersions in the range of $\Delta W_{1\sigma\text{ wind}} \sim 250 - 280 \text{ km s}^{-1}$.

The NW outflow cone in NGC 4945 opens towards us and lies in front of the galactic disk, while the SE cone is oriented in the opposite geometry ([Venturi et al., 2017](#)) and is partially obstructed by foreground dust located in the galactic plane ([Heckman et al., 1990](#); [Koornneef, 1993](#)). The kinematics of the SE lobe as seen in [O III] 88 and [O I] 145 are consistent with the MUSE [N II] observations from [Venturi et al. \(2017\)](#). The center of the SE lobe is approaching us (seen in [O I] 145) and the edges are receding (seen in [O III] 88). The $\Delta v_{50\text{ wind}}$ of the ionized gas in the NW lobe however, only indicates that the outflow is receding from us. [Venturi et al.](#)

(2017) suggests that the edges of the NW lobe are approaching and the inner region of the NW lobe is receding, however we do not detect any approaching velocities in the NW lobe.

There is no significant detection of the neutral gas in the outflow of NGC 4945 (see Figure 4.26), but there is a prominent detection of the ionized gas. The largest ionized masses are concentrated around the galaxy nucleus while the largest KE in the outflow lie S of the nucleus in a $\sim 20''$ long structure elongated E to W. The most eastern part of this structure spatially coincides with the SE outflow cone. Some western portions of this structure may also be attributed to the outflow, but the most W edge of the structure may be contamination from disk emission.

4.10 Summary

We have analyzed archival *Herschel*-PACS data of five fine structure lines ([O III] 88, [O I] 63, [N II] 122, [O I] 145, and [C II] 158) in seven nearby galaxies (Cen A, Circinus, M 82, NGC 253, NGC 1068, NGC 3079, and NGC 4945). While the galactic-scale outflows in these objects have been studied extensively at wavelengths spanning the entire electromagnetic spectrum, they are relatively unexplored in the FIR wavelength regime, $55 - 210 \mu\text{m}$, studied here. Thanks to the unique combination of angular resolution, sensitivity, and two-dimensional coverage in the FIR of *Herschel* PACS, we have been able to spatially and kinematically resolve the neutral atomic and ionized gas in the outflow of each galaxy in our sample. The main results are summarized as follows:

1. We have derived velocity-integrated fluxes, radial velocities, and $1-\sigma$ line width maps of all five atomic fine-structure lines. Radial velocity maps indicate that the kinematics within the galaxy disks are dominated by rotation. For some objects (e.g. M 82 and Cen A), the observed line dispersion maps alone can delineate the collimated outflow from the galaxy disk.

2. Analysis of the emission line ratio maps confirm earlier results in the literature (e.g. the prominent ionization cone in Circinus, the jet in Cen A, and the ionized outflow in NGC 1068). These ratios are insightful tools to diagnose the physical conditions of the ionized and neutral gas within the outflows and near the AGN or SB regions. Compact shapes of the line ratios near the galaxy center reveal effects of ionizing radiation (e.g. [O I] 63 / [C II] 158).

3. Modeling of the PDRs near the AGN and/or SB and within the outflow has constrained the physical parameters of the neutral atomic gas, namely the UV interstellar radiation field, G_0 , and the hydrogen gas density, n_{H} . In general, the highest densities are compact structures that surround the galaxy center. Exceptions are seen in M 82 and NGC 253, where the structures are more extended and irregular in shape. For the most part, the largest ISRFs are also compact structures centered on the galaxy nucleus; exceptions are M 82 where the shape of the highest radiation is extended and elongated in the direction of the galaxy disk, and in NGC 4945 where the extended ISRF is elongated to the E. Additionally, although the shape of G_0 in NGC 253 is compact and spherical, it is off center to the W. Two objects show obvious structures in G_0 and/or n_{H} which are spatially coincident with the known outflow. Higher densities and radiation are seen elongated NE in the direction of

the jet in Cen A. For NGC 4945, the highest densities are found not around the galaxy center, but are located SE of the nucleus in the S outflow.

4. We have modeled the gas velocity field of the galaxy disks via a “tilted-ring” model. Subsequently, the excess residual between the observed and modeled $1\text{-}\sigma$ line widths was used to define the spatial location of the wind (e.g. regions where the $1\text{-}\sigma$ line width residuals were $> 25 \text{ km s}^{-1}$).

5. We have derived properties of the outflow such as bulk motions, masses, and kinetic energies based on our definition of a wind. We find that excess line widths are a better indicator of outflow compared to excess radial velocities.

6. We have compared our results with other wavelength data and find that our definition of a wind results in features (morphological and kinematic) consistent with the literature. For example, bulk motions in the wind region of M 82 indicate that the N cone is receding from us and the S cone is approaching us, in agreement with the literature. Inspection of the excess line widths inside the wind region show that larger line width residuals coincide with known features in an outflow. For example, the largest excess line widths in NGC 3079 spatially coincide with the known radio jet and an optical filament E of the nucleus. Morphology of the wind is also consistent with the literature. M 82 shows line width residuals extending SE to NW in a collimated feature which spatially coincides with a known SiO chimney.

7. We have demonstrated the advantage of the FIR wavelength range over that of the optical and UV when exploring SB or AGN regions. This is most obvious in NGC 3079 where the outflow W of the nucleus lies behind the disk and is extinguished in the optical, but the superbubble is detected in [C II] 158.

8. For completeness, we also present the results of the analysis of the molecular gas traced by OH 119 in [Appendix B](#).

We have pushed the boundaries of the capabilities of *Herschel*-PACS in this work, but higher resolution observations of AGN and SB regions are necessary to clearly disentangle the outflow from the galaxy disk. JWST will be able to observe out to $\sim 28 \mu\text{m}$ but with better than $\sim 1''$ angular resolution, and therefore out to distances an order of magnitude larger ($\sim 100 \text{ Mpc}$; $z \sim 0.03$). There are many ionized, neutral, and molecular gas diagnostics in the MIR and this will allow studies of the multi-phase winds in exquisite details. Moreover, line ratios in the MIR, such as $[\text{O IV}] 25.6 / [\text{Ne II}] 12.8$ and $[\text{Ne V}] 14.3 / [\text{Ne II}] 12.8$ will nicely complement the FIR, providing powerful diagnostics to discriminate AGNs from star formation activity (e.g. [Veilleux et al., 2009](#)).

Chapter 5: Summary and Future Work

The goal of this thesis was to study and explore the cool component of galactic-scale winds in nearby SBs and AGNs. This research is based on archival FIR and MIR spectroscopic data obtained with *Herschel*–PACS and *Spitzer*–IRS, respectively. In this chapter, we briefly summarize the main results of the work discussed in this thesis.

5.1 Main Results

In Chapter 2 we presented the results of our analysis of spectroscopic data of OH at $119 \mu\text{m}$ obtained with *Herschel*–PACS of 52 local ($d < 50$ Mpc) BAT AGN selected from the very hard X-ray (14 – 195 keV) 58 month *Swift*–BAT Survey. These data were combined with *Herschel*–PACS observations of 43 nearby ($z < 0.3$) ULIRG/QSOs from (Veilleux et al., 2013). The inclusion of the BAT AGN sample with the ULIRG/QSO sample extended the range of AGN properties (luminosities, star formation rates, and stellar masses) to lower values by 1 – 2 orders of magnitude compared to the ULIRG/QSO sample alone. We measure the frequency of occurrence of the wind in the BAT AGN. We also look for correlations between the properties of the wind and that of the host galaxy.

Evidence for molecular outflows as traced by OH at 119 μm , was seen in only four of the 52 BAT AGN. This corresponds to a 24% outflow detection rate in the BAT AGN where the search for outflows was possible (i.e. 12 objects were seen in pure absorption and 5 were seen with absorption+emission composite profiles). Evidence for molecular inflows is seen in seven objects, corresponding to a $\sim 40\%$ inflow detection rate in the BAT AGN.

When the BAT AGN are combined with the ULIRG/QSOs, the total sample covers a range of ~ 3 dex in SFR and AGN luminosity and ~ 2 dex in stellar mass. The combined sample shows positive trends between outflow velocities and the host galaxy properties: stellar mass, SFR, and AGN luminosity. The correlation between wind velocity and AGN luminosity is the strongest of these three. Our results strongly suggest that at higher AGN luminosities ($\log(L_{\text{AGN}}/L_{\odot} \gtrsim 11.5$) the AGN dominates over star formation in driving the outflow. At lower luminosities the AGN may not have the energetics required to drive fast molecular outflows, but stellar processes could dominate if the AGN were weak or absent. It is clear that SF plays a crucial role in driving winds, but the presence of an AGN is needed to drive the fastest winds in our sample.

In Chapter 3 we presented the analysis of *Spitzer*–IRS observations of OH at 35 μm in 15 nearby ($z \lesssim 0.06$) U/LIRGs. The estimation of molecular outflow properties, such as mass, from radiative–transfer models, (such as those in [González-Alfonso et al., 2017](#)), are dependent on the estimation of the OH–to–H abundance ratio, X_{OH} . Thus, constraining the value of this parameter will result in more accurate predictions when employed. Therefore, we exploited the fact that the

ground–state OH absorption feature at 35 μm is optically thinner than the other OH doublets in the FIR to provide an independent constraint on the estimation of X_{OH} . We computed the OH column densities in our sample and compared them to the hydrogen column density for a typical optical depth at 35 μm of ~ 0.5 . Assuming a gas–to–dust ratio of ~ 125 , we find a mean of $X_{\text{OH}} = 1.01 \pm 0.15 \times 10^{-6}$ for our sample. We attempt to verify that the radiative transfer models from [González-Alfonso et al. \(2017\)](#) predict a realistic OH 35 line profile by comparing the shape of the predicted line profile with the shape of the line profile fitted to observed data. The agreement between the two is generally very good in terms of overall strength (equivalent width) of the feature, and this adds some confidence in the energetics derived from these models.

In Chapter 4 we presented the analysis of archival *Herschel*-PACS data of five atomic fine structure lines ([O I] 63, [O III] 88, [N II] 122, [O I] 145, and [C II] 158) in seven nearby galaxies (M 82, Cen A, Circinus, NGC 253, NGC 1068, NGC 3079, and NGC 4945). Included is also the preliminary analysis of OH 119 in these objects.

We derived velocity–integrated fluxes, radial velocities, and 1- σ line width maps of the fine structure lines in each object. For some objects (e.g. M 82) the observed line dispersion maps alone can delineate the collimated outflow from the galaxy disk. We computed emission line ratios and detect well known features in some of the objects (e.g. the ionization cone in Circinus). We employ PDR models to estimate the strength of the radiation field and the hydrogen density in our objects. For some objects higher densities and radiation field strengths are spatially coincident with the known outflow (e.g. the jet in Cen A). We model the gas

velocity fields in our sample with ^{3D}BAROLO and use the excess residual between the observed and modeled line widths to define the spatial location of the wind. Once the wind is defined, residual radial velocities can trace bulk motions of the outflow. For example, in M 82, for all atomic lines, the N cone is receding from us and the S cone is approaching us. The significant advantage of the FIR over optical or UV wavelengths was underscored while defining the wind location. In particular for NGC 3079, the FIR captures the W superbubble which lies behind the disk and is extinguished in the optical. We also estimate masses and kinetic energies for the neutral and ionized gas in the wind for objects with a wind detection. We also compare the results of our analysis with other wavelength data and find remarkable consistency in the comparisons. For example, the largest residual line widths in NGC 3079 spatially coincide with the known radio jet indicating that the larger residuals are due to the presence of the jet interacting with the ISM of the galaxy disk. The preliminary analysis of OH 119 in our sample shows unambiguous extended outflows in NGC 253 in the form of P–Cygni profiles and unambiguous extended inflows in Circinus and NGC 4945 in the form of inverted P–Cygni profiles.

5.2 Future Work

We have pushed the boundaries of the capabilities of *Herschel*-PACS in Chapter 4, but higher resolution observations of AGN and SB regions are necessary to clearly disentangle the outflow from the galaxy disk. The high resolution ($\sim 1''$) and sensitivity of the James Webb Space Telescope (JWST) will be able to resolve the

SB and/or AGN activity inside the central spaxel of our PACS observations, thus providing the opportunity to study the energy mechanisms of winds in great detail. In the MIR alone, there are many ionized, neutral, and molecular gas diagnostics that will allow for studies of multiphase winds and the MIR range of JWST will also be a nice compliment to the FIR since the combination of these wavelength ranges will expand the possible line ratios such as $[\text{O IV}] 25.6 / [\text{O III}] 88$ which has been proposed as a powerful diagnostic to discriminate AGNs from SF activity.

Also of particular interest will be *SPace Infrared telescope for Cosmology and Astrophysics* (SPICA; [Swinyard et al., 2009](#)) whose unprecedented spectroscopic sensitivity in the FIR will be able shed light on the role of molecular outflows at high z (currently, only a few detections have been reported). At higher redshifts, the star formation rate density and AGN activity increase which points to an increasing importance of feedback processes earlier in the Universe. SPICA will be able to measure outflow properties of distant AGN with unprecedented accuracy and depth, and provide us with a greater understanding of galaxy formation and evolution.

Appendix A: *Spitzer* MIR SPECTRA

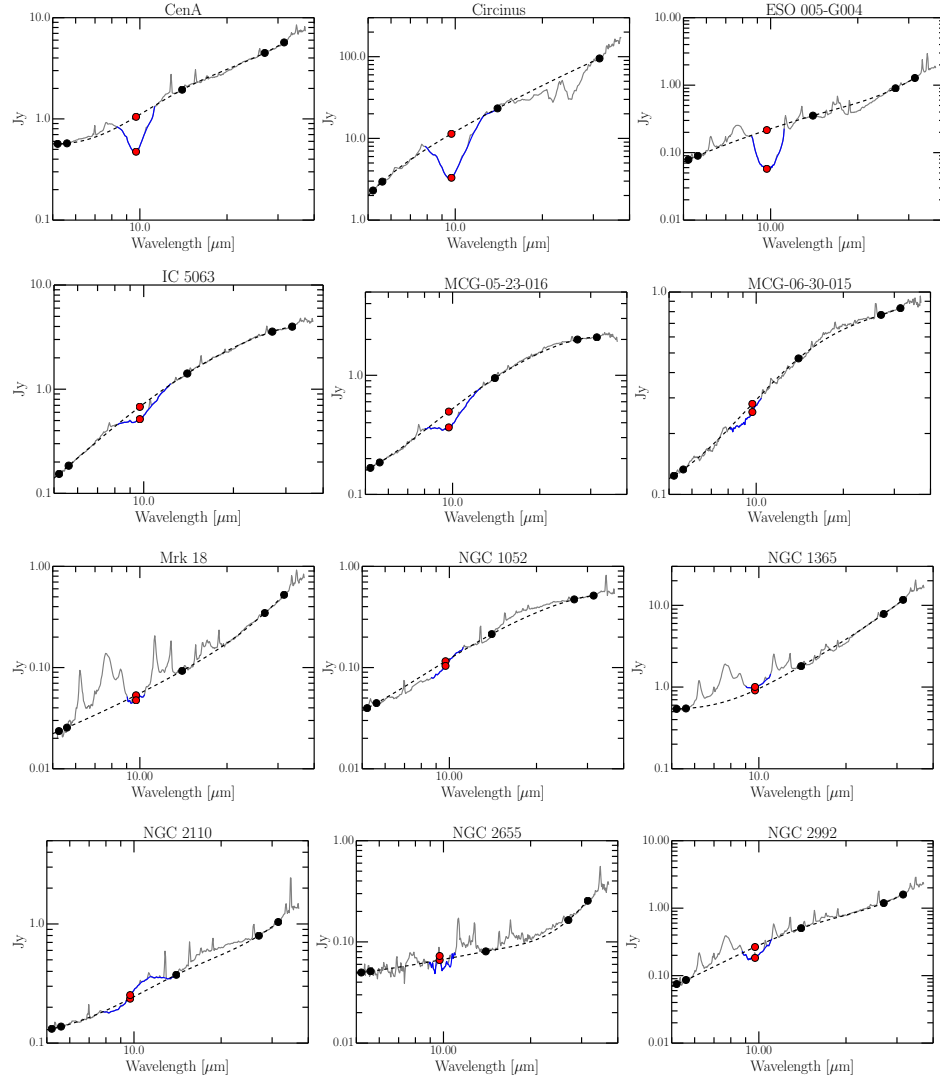


Figure A.1 Mid-infrared ($5\text{--}37\mu\text{m}$) spectra used to measure $S_{9.7\mu\text{m}}$. The dashed line is the continuum calculated from the cubic spline interpolation fitted to the pivot points shown as black dots. Red dots show $f_{cont}(9.7\mu\text{m})$ (located on dashed continuum line) and $f_{obs}(9.7\mu\text{m})$ (located on the solid black line or the observed flux density). The blue line shows the integration range used to calculate the flux and total equivalent width of the $9.7\mu\text{m}$ silicate feature (see [Table 2.4](#) and [Table 2.5](#)).

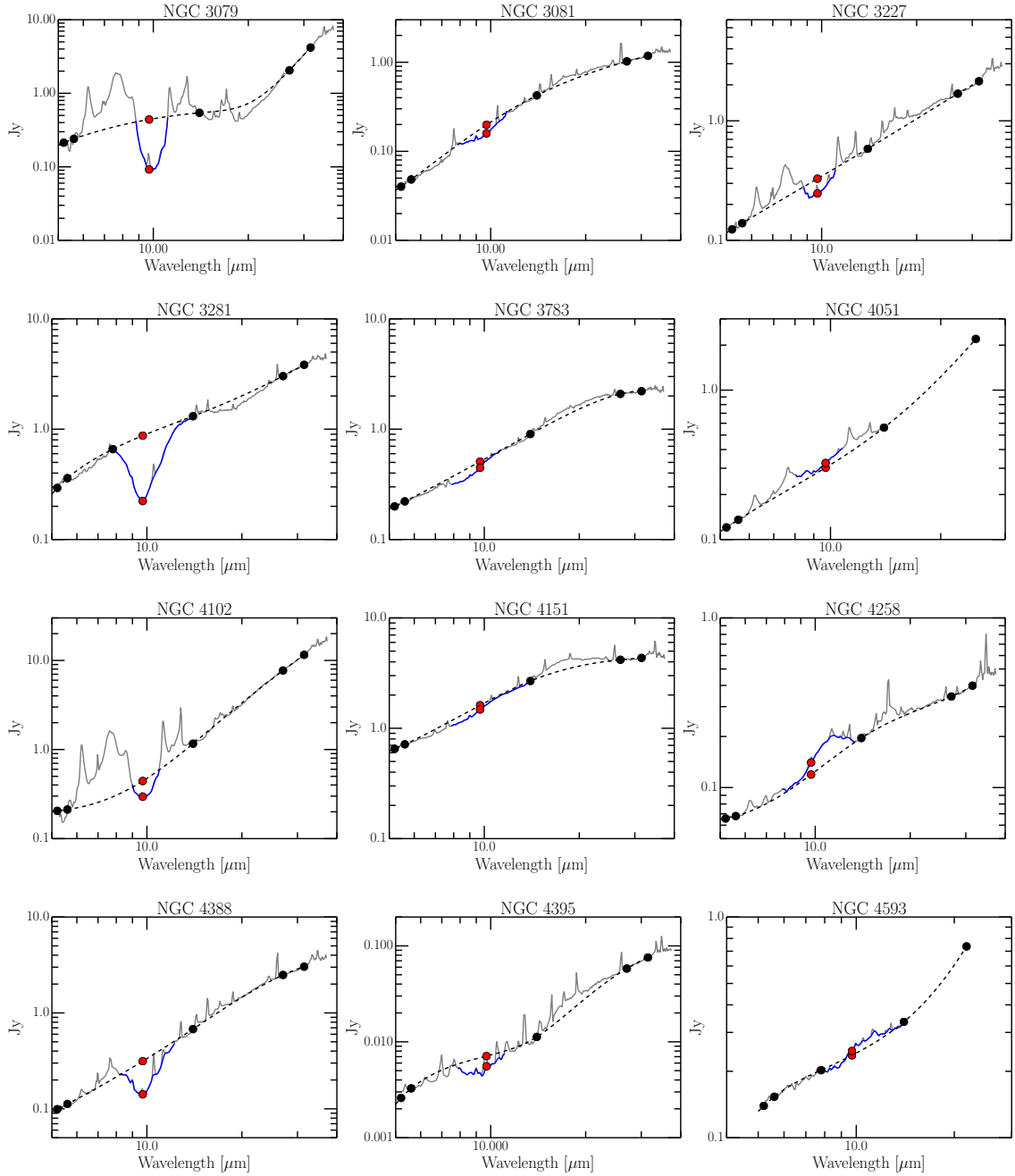


Figure A.2 (Continued)

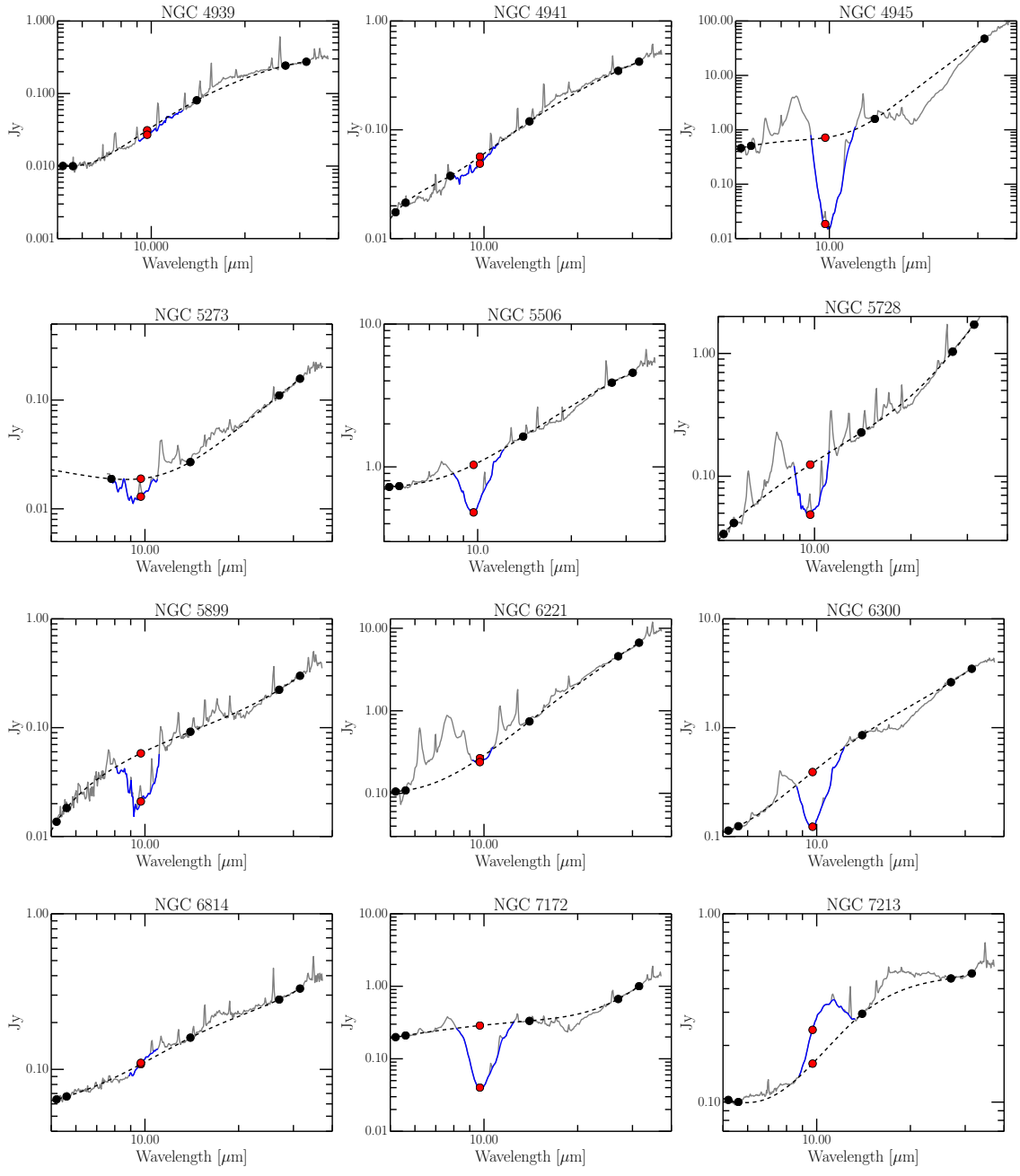


Figure A.3 (Continued)

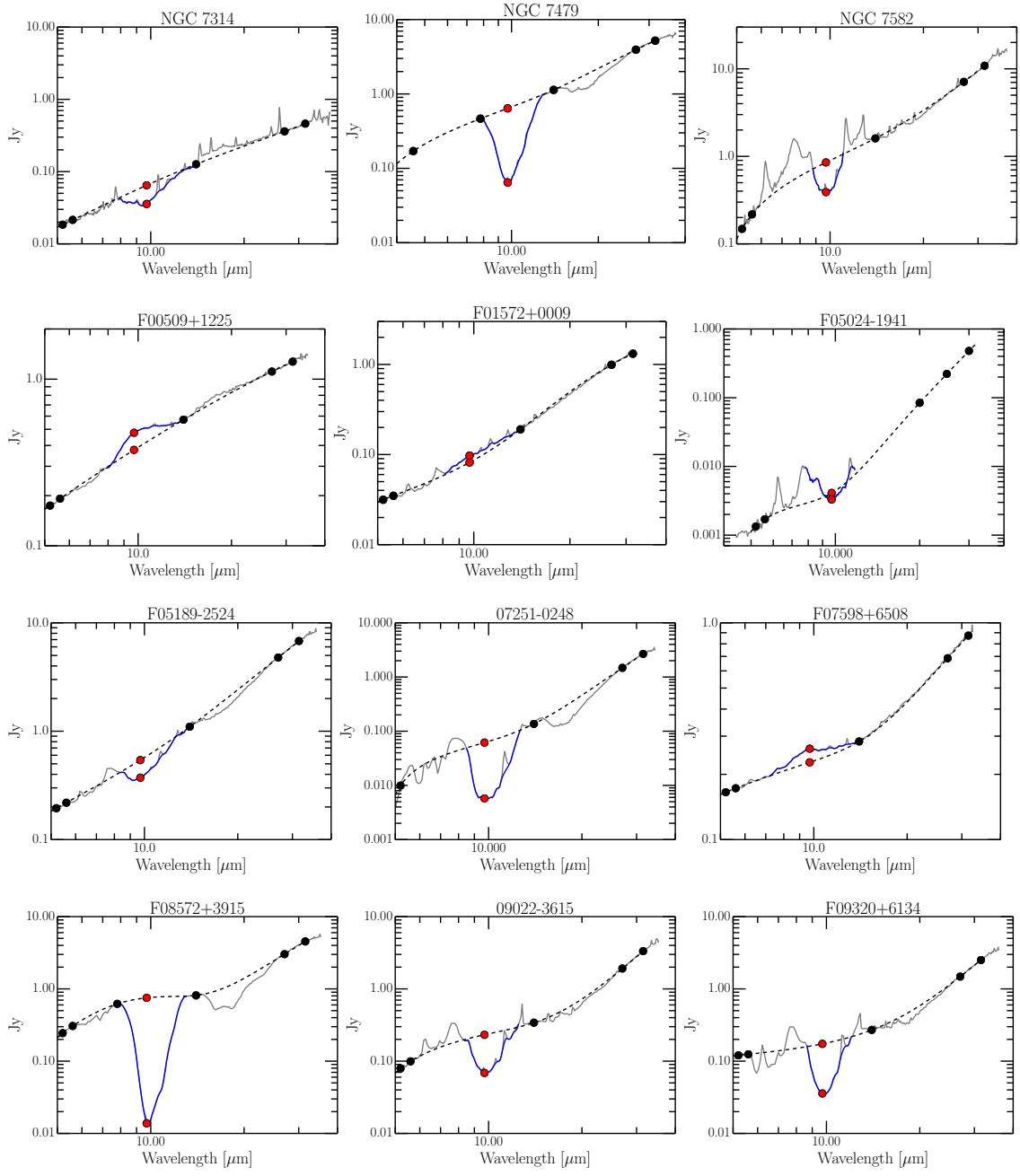


Figure A.4 (Continued)

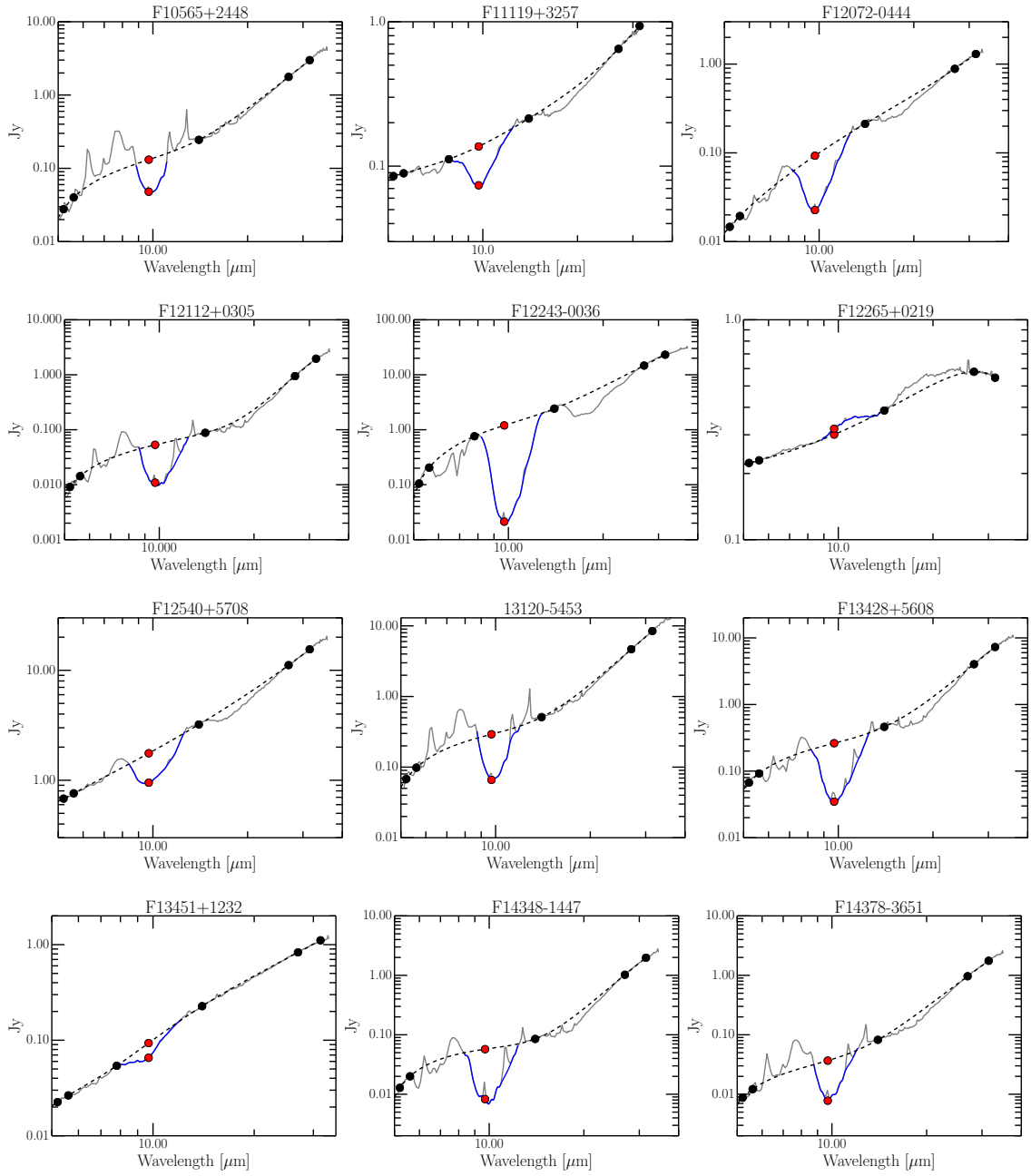


Figure A.5 (Continued)

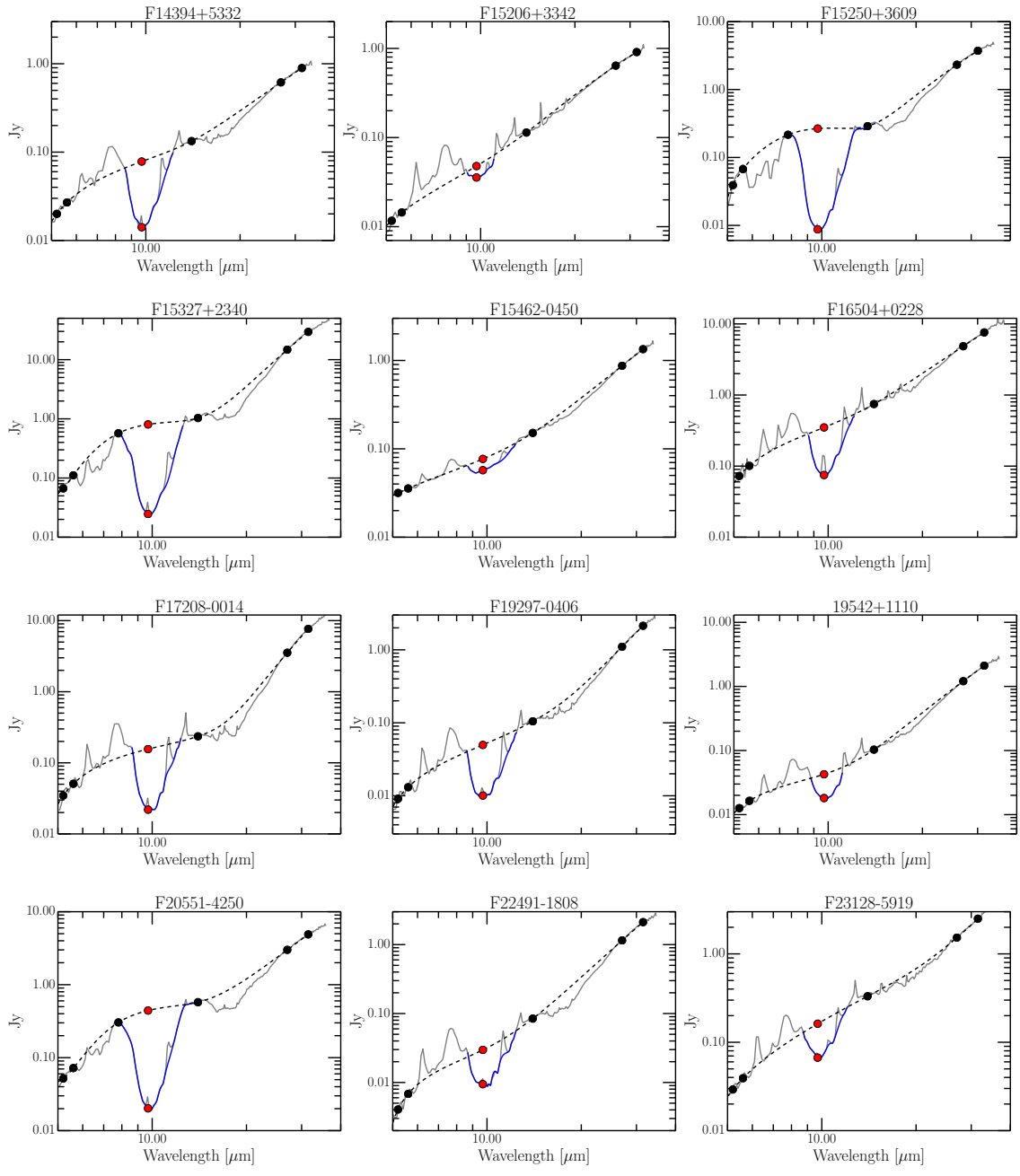


Figure A.6 (Continued)

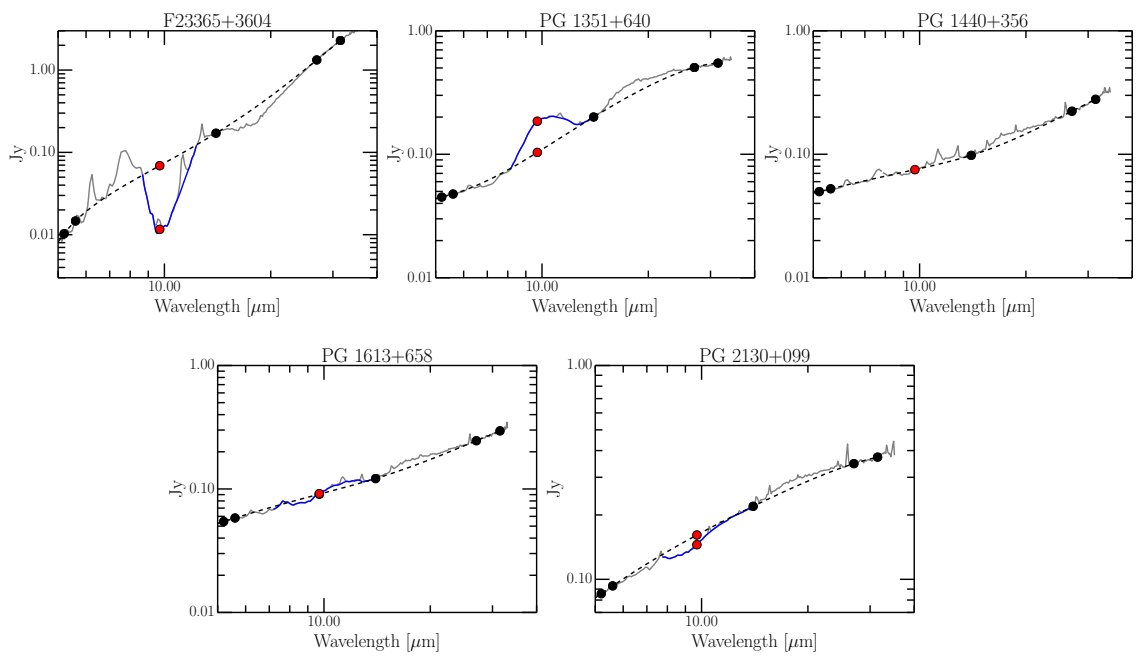


Figure A.7 (Continued)

Appendix B: Results on OH 119 μm

PACS observations of the OH 119.233, 119.441 μm doublet were retrieved and reduced in the same manner as the atomic FIR data (see [Section 4.4](#)). The PACS resolution at 119 μm is $\sim 270 \text{ km s}^{-1}$. Details of the OH observations are in [Table B.1](#). To reduce noise, the OH data have been smoothed with a Gaussian kernel of width 0.05 μm (this step was excluded for the spectra in NGC 253). For each spaxel, a first-order spline was fit to the continuum and subtracted from the spectra. Profile fitting of the OH doublet followed a similar procedure from [Veilleux et al. \(2013\)](#) and [Stone et al. \(2016\)](#). The OH profile is modeled using four Gaussian components (two for each line of the doublet). The separation between the two lines of the doublet was set to 0.208 μm in the rest frame ($\sim 520 \text{ km s}^{-1}$) and the amplitude and standard deviation were fixed to be the same for each component in the doublet.

We characterize the OH line profile properties in the same manner as the atomic lines (e.g. v_{50} and $W_{1\sigma}$) and present here our preliminary results of the spectral analysis of OH 119 for each object. Four figures are presented for each object (see [Figure B.1](#)). The top left shows the PACS IFU footprint on the sky (black lines and squares) and the outline of the ionized wind traced by [O III] 88 (white line).

Table B.1. PACS OH 119 μm Observations

Object Name	ObsId	t_{exp} (s)	Proposal ID
M 82	1342232257	958	OT1_shaileyd_1
Cen A	1342225989	976	OT1_shaileyd_1
Circinus	1342225147	958	OT1_shaileyd_1
NGC 253	1342237604	976	OT1_shaileyd_1
NGC 1068	1342203128	3330	KPGT_esturm_1
NGC 3079	1342221391	8045	DDT_esturm_4
NGC 4945	1342247792	958	OT1_shaileyd_1

Note. — Column 1: Galaxy Name. Column 2: Observation Id. Column 3: Exposure time. Column 4: Proposal ID.

Top right shows the spline fits to the continuum while bottom left shows the line profile fits to the continuum subtracted spectrum. Finally, bottom right shows maps of the line profile properties for the absorption and/or emission components fitted to the spectra. The $1\text{-}\sigma$ line width maps have not been corrected for instrumental broadening.

When pure emission and/or pure absorption (e.g. M 82 and NGC 1068) is observed in the OH 119 line profile, the rotation of the galaxy disk is discernible in the v_{50} maps (see [Figure B.1](#) and [Figure B.5](#)). The rotation is consistent with the results from the analysis of the ionized and neutral gas traced by the fine structure lines. However, when there is a combination of absorption and emission components in an OH line profile, the physical interpretation of v_{50} is not so clear.

For all of objects, there is no detection of an outflow in the central spaxel. Only Circinus (see [Figure B.3](#)) shows a wind in the central spaxel in the form of an unambiguous inflow (e.g. an inverted P-Cygni profile is observed). Cen A shows no

discernible detection of a wind in OH 119. NGC 1068 is seen in pure emission with no detection of an outflow.

The largest line widths ($\sim 500 \text{ km s}^{-1}$) in M 82 (see [Figure B.1](#)) appear in pure absorption in spaxels (3,0) and (2,3). The absorption lines have blue-shifted wings and are spatially coincident with the ionized outflow detected in [O III] 88, suggesting there is also outflow in the molecular gas.

NGC 253 shows detections of unambiguous outflow outside of the central spaxel (see [Figure B.4](#)) which extend N, S, and NW of the nucleus. The P-Cygni profiles lie in good spatial agreement with the ionized outflow traced by [O III] 88 .

NGC 4945 (see [Figure B.7](#)) shows pure absorption above and below the disk at the edges of the PACS FOV. Unambiguous inflow is seen mostly S of the nucleus in spaxels (2,1), (4,2), and (4,3). These spaxels are spatially coincident with the edges of the ionized outflow traced by [O III] 88 . There is also unambiguous inflow W of the nucleus in spaxel (3,3), but the spaxel lies outside of the ionized outflow. There is also a possible detection of a blue absorption wing E of the nucleus in spaxel (1,1).

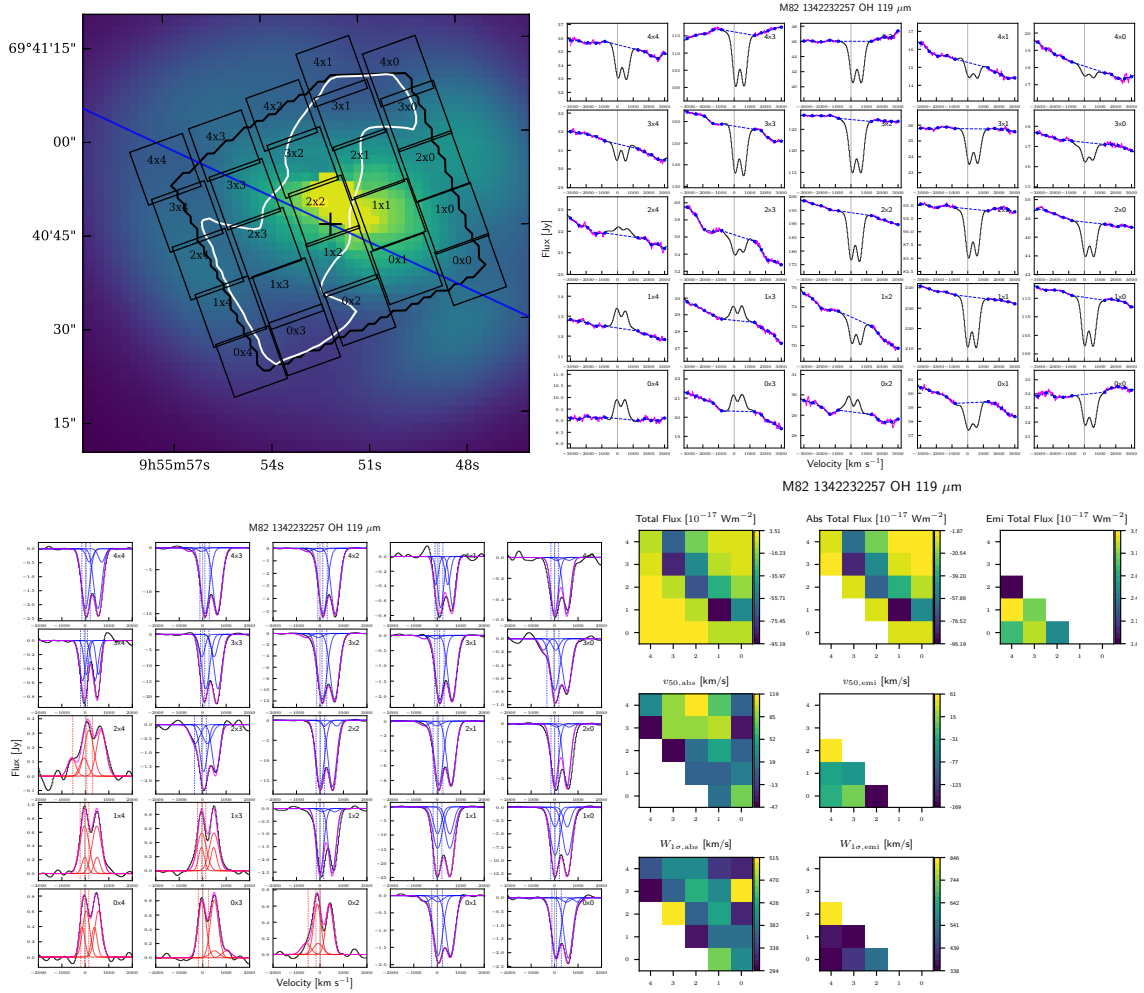


Figure B.1 Top left: PACS IFU footprint of OH 119 (black squares) overlaid on the 22 μm WISE image of M 82. The white contour marks the spatial extent of the [O III] 88 wind. The black contour outlines the PACS footprint of the [O III] 88 observation. The black cross marks the adopted galaxy center and the blue line marks the galaxy major axis. Top right: Spline fits to the OH 119 continuum (blue dashed lines). Black lines are the observed data. Magenta areas indicate the regions used to fit the continuum. Blue dots mark the pivot points used to fit the spline. Bottom left: Line profile fitting results of the continuum-subtracted spectra. Solid blue lines indicate gaussian absorption components. Solid red lines indicate gaussian emission components. Vertical dashed blue (red) lines mark the v_{16} , v_{50} , and v_{84} velocities in absorption (emission). Bottom right: Top row, from left to right shows the total velocity-integrated flux of the fitted OH line profiles, the total flux in the absorption components only, and the total flux in the emission components only. Middle row shows v_{50} for the absorption (left) and emission components (right). Bottom row shows the $1-\sigma$ line widths of the absorption (left) and emission (right) components.

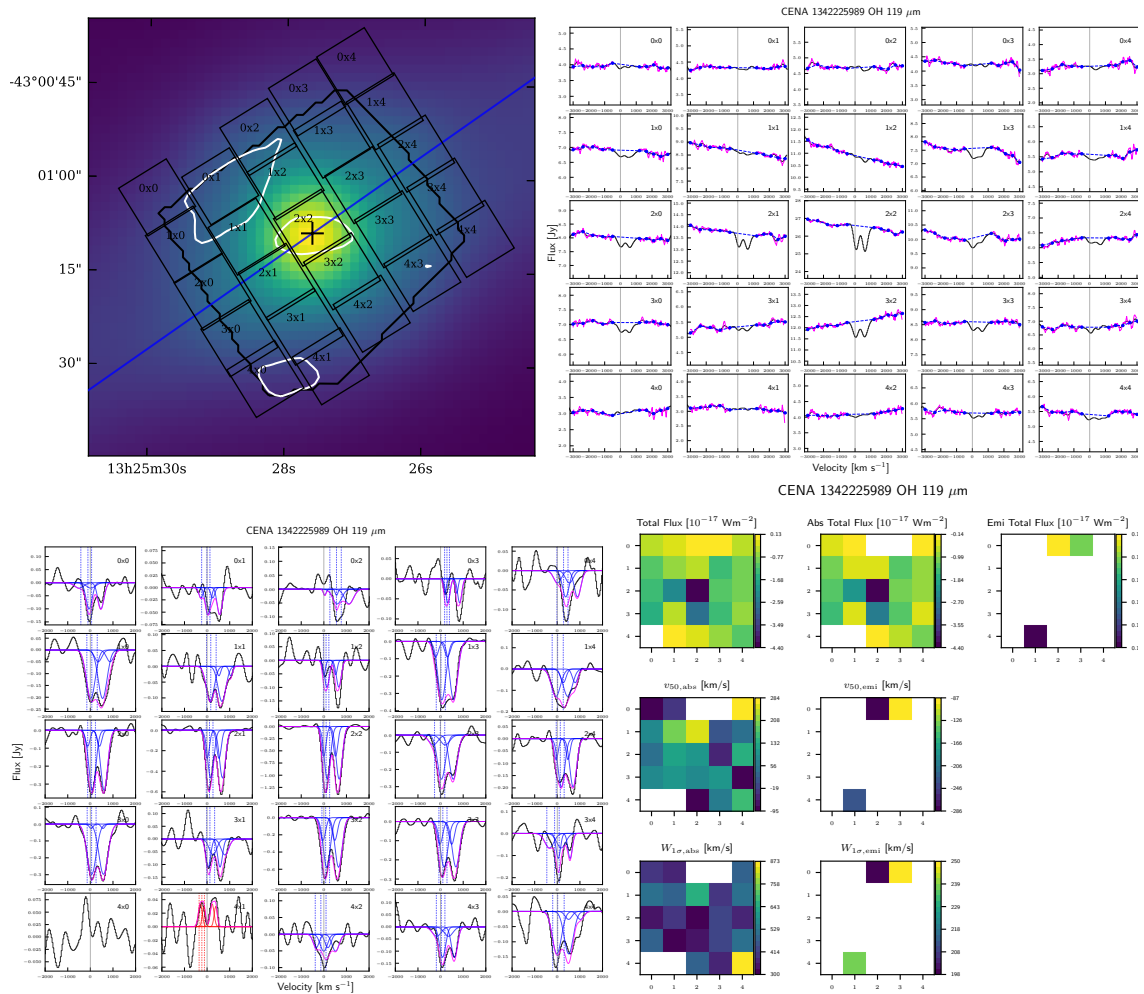


Figure B.2 Cen A. Lines and symbols are the same as those in Figure B.1.

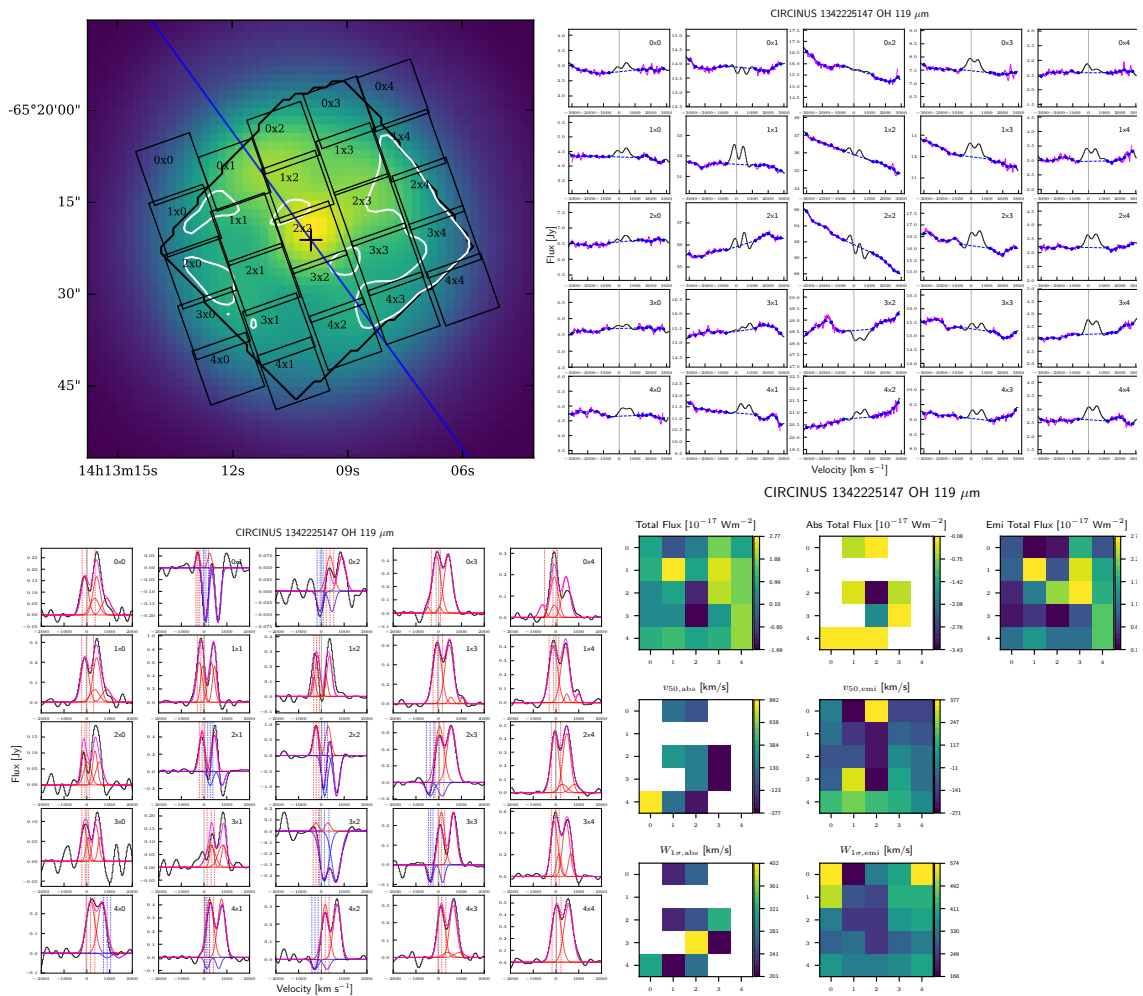


Figure B.3 Circinus. Lines and symbols are the same as those in Figure B.1.

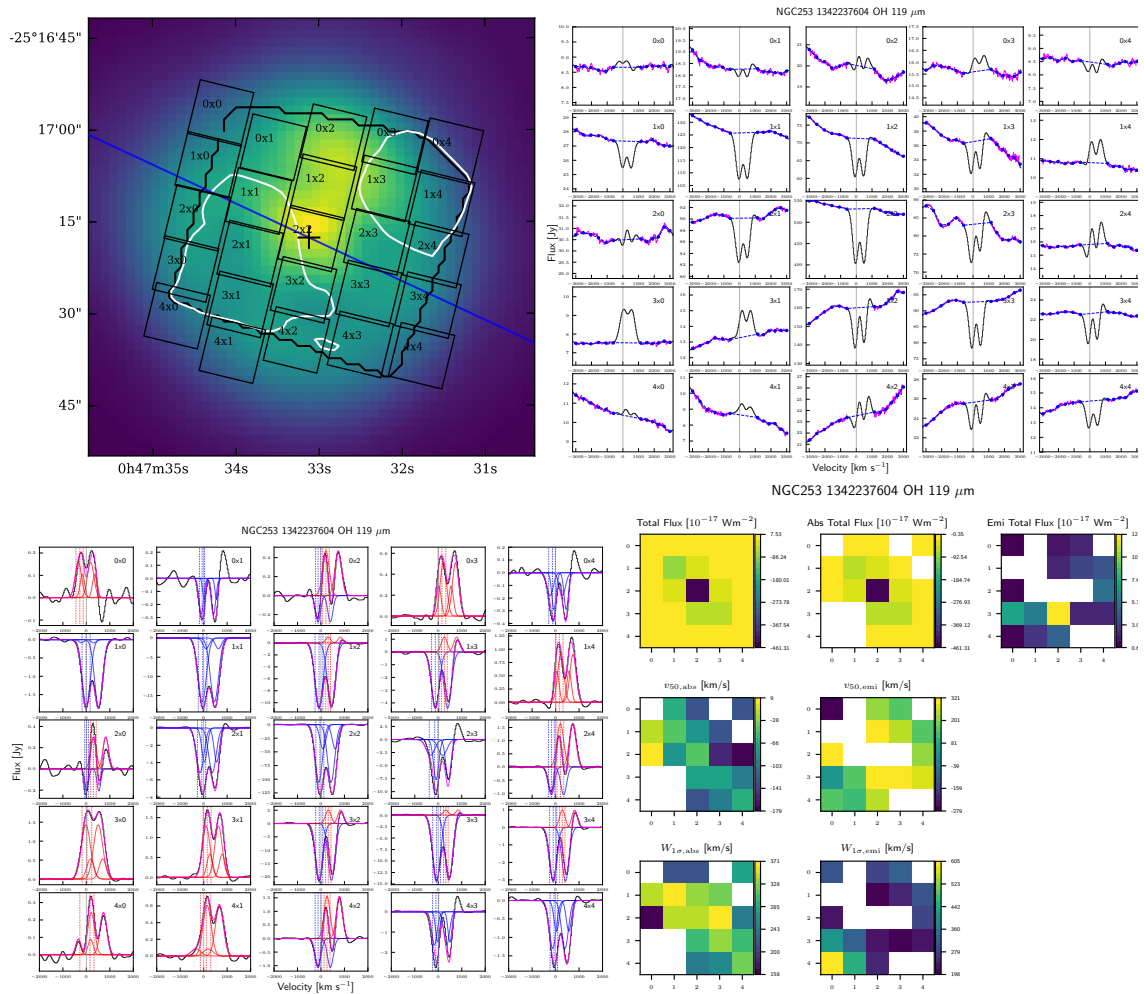


Figure B.4 NGC 253. Lines and symbols are the same as those in Figure B.1.

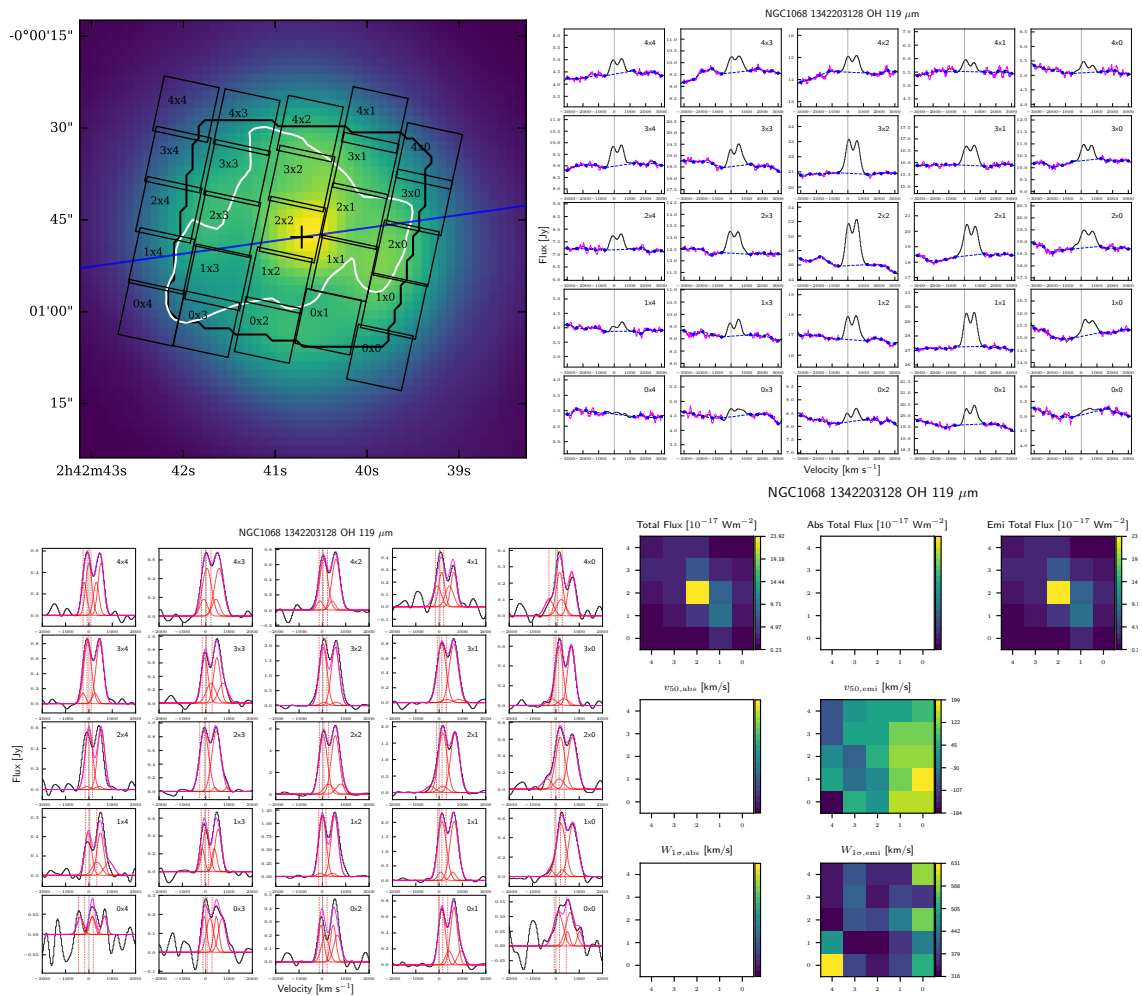


Figure B.5 NGC 1068. Lines and symbols are the same as those in Figure B.1.

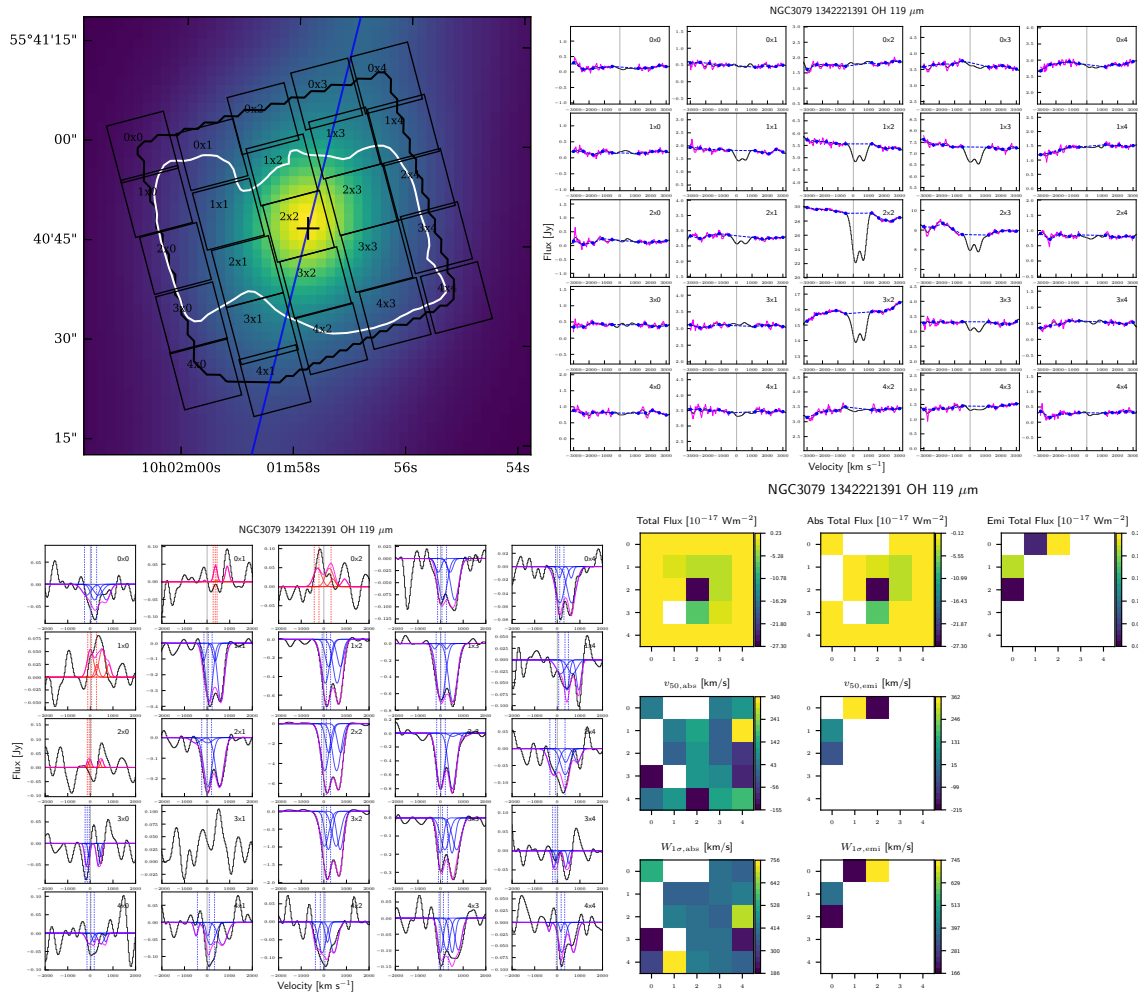


Figure B.6 NGC 3079. Top left: The white contour marks the spatial extent of the [C II] 158 wind. Lines and symbols are the same as those in Figure B.1.

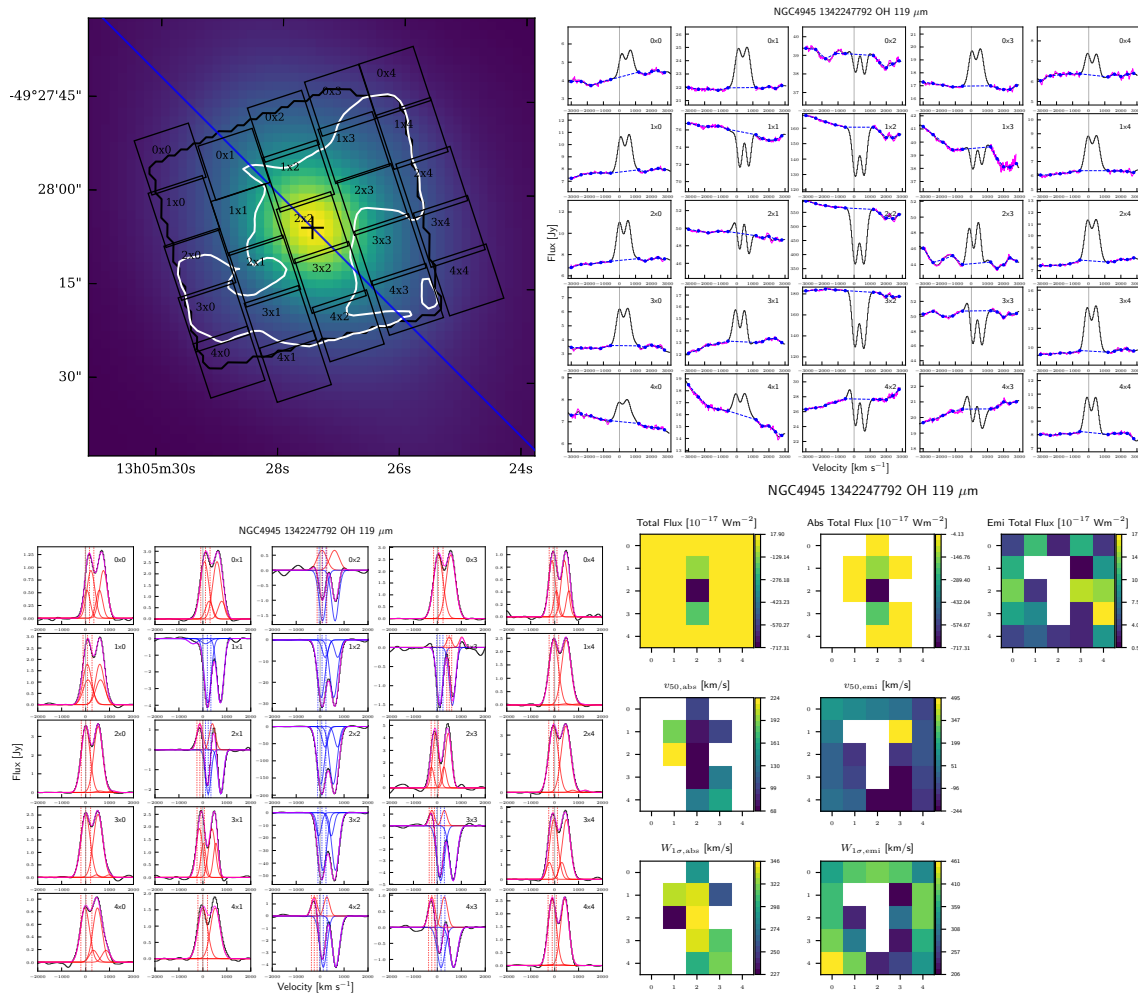


Figure B.7 NGC 4945. Lines and symbols are the same as those in Figure B.1.

Bibliography

- Abel, N. P., Dudley, C., Fischer, J., Satyapal, S., & van Hoof, P. A. M. 2009, *ApJ*, 701, 1147
- Aguirre, A., Hernquist, L., Schaye, J., et al. 2001, *ApJ*, 561, 521
- Alatalo, K., Blitz, L., Young, L. M., et al. 2011, *ApJ*, 735, 88
- Alexander, D. M., Swinbank, A. M., Smail, I., McDermid, R., & Nesvadba, N. P. H. 2010, in *Astronomical Society of the Pacific Conference Series*, Vol. 427, *Accretion and Ejection in AGN: a Global View*, ed. L. Maraschi, G. Ghisellini, R. Della Ceca, & F. Tavecchio, 74
- Alton, P. B., Davies, J. I., & Bianchi, S. 1999, *A&A*, 343, 51
- Armus, L., Mazzarella, J. M., Evans, A. S., et al. 2009, *PASP*, 121, 559
- Baldry, I. K., Glazebrook, K., Brinkmann, J., et al. 2004, *ApJ*, 600, 681
- Banerji, M., Chapman, S. C., Smail, I., et al. 2011, *MNRAS*, 418, 1071
- Barbosa, F. K. B., Storchi-Bergmann, T., McGregor, P., Vale, T. B., & Rogemar Riffel, A. 2014, *MNRAS*, 445, 2353
- Barnes, J. E., & Hernquist, L. 1996, *ApJ*, 471, 115
- Bassani, L., Dadina, M., Maiolino, R., et al. 1999, *ApJS*, 121, 473
- Baumgartner, W. H., Mushotzky, R., & Tueller, J. 2011, in *Bulletin of the American Astronomical Society*, Vol. 43, *American Astronomical Society Meeting Abstracts #217, #125.01*
- Bell, E. F., & de Jong, R. S. 2001, *ApJ*, 550, 212
- Benson, A. J., Bower, R. G., Frenk, C. S., et al. 2003, *ApJ*, 599, 38
- Bertone, S., De Lucia, G., & Thomas, P. A. 2007, *MNRAS*, 379, 1143
- Blanco, V. M., Graham, J. A., Lasker, B. M., & Osmer, P. S. 1975, *ApJ*, 198, L63

- Bland, J., Taylor, K., & Atherton, P. D. 1987, *MNRAS*, 228, 595
- Blanton, M. R., & Moustakas, J. 2009, *ARA&A*, 47, 159
- Bolatto, A. D., Warren, S. R., Leroy, A. K., et al. 2013, *Nature*, 499, 450
- Bosma, A. 1978, in *IAU Symposium, Vol. 77, Structure and Properties of Nearby Galaxies*, ed. E. M. Berkhuijsen & R. Wielebinski, 28
- Bower, R. G., Benson, A. J., Malbon, R., et al. 2006, *MNRAS*, 370, 645
- Bradford, C. M., Stacey, G. J., Fischer, J., et al. 1999, in *ESA Special Publication, Vol. 427, The Universe as Seen by ISO*, ed. P. Cox & M. Kessler, 861
- Bravo-Guerrero, J., & Stevens, I. R. 2017, *MNRAS*, 467, 3788
- Brusa, M., Perna, M., Cresci, G., et al. 2016, *A&A*, 588, A58
- Burns, J. O., Feigelson, E. D., & Schreier, E. J. 1983, *ApJ*, 273, 128
- Calzetti, D., Wu, S.-Y., Hong, S., et al. 2010, *ApJ*, 714, 1256
- Cano-Díaz, M., Maiolino, R., Marconi, A., et al. 2012, *A&A*, 537, L8
- Carilli, C. L., & Walter, F. 2013, *ARA&A*, 51, 105
- Carniani, S., Marconi, A., Maiolino, R., et al. 2015, *A&A*, 580, A102
- . 2016, *A&A*, 591, A28
- Cecil, G., Bland, J., & Tully, R. B. 1990, *ApJ*, 355, 70
- Cecil, G., Bland-Hawthorn, J., & Veilleux, S. 2002, *ApJ*, 576, 745
- Cecil, G., Bland-Hawthorn, J., Veilleux, S., & Filippenko, A. V. 2001, *ApJ*, 555, 338
- Chevalier, R. A., & Clegg, A. W. 1985, *Nature*, 317, 44
- Cicone, C., Brusa, M., Ramos Almeida, C., et al. 2018, *Nature Astronomy*, 2, 176
- Cicone, C., Feruglio, C., Maiolino, R., et al. 2012, *A&A*, 543, A99
- Cicone, C., Maiolino, R., Sturm, E., et al. 2014, *A&A*, 562, A21
- Cicone, C., Maiolino, R., Gallerani, S., et al. 2015, *A&A*, 574, A14
- Cielo, S., Bieri, R., Volonteri, M., Wagner, A. Y., & Dubois, Y. 2018, *MNRAS*, 477, 1336
- Clarke, D. A., Burns, J. O., & Norman, M. L. 1992, *ApJ*, 395, 444

- Cohen, M., Megeath, S. T., Hammersley, P. L., Martín-Luis, F., & Stauffer, J. 2003, *AJ*, 125, 2645
- Cole, S., Norberg, P., Baugh, C. M., et al. 2001, *MNRAS*, 326, 255
- Combes, F. 2014, *Proceedings of the International Astronomical Union*, 10, 182189
- Combes, F., & Charmandaris, V. 2000, *A&A*, 357, 75
- Contursi, A., Poglitsch, A., Grácia Carpio, J., et al. 2013, *A&A*, 549, A118
- Cooper, J. L., Bicknell, G. V., Sutherland, R. S., & Bland-Hawthorn, J. 2008, *ApJ*, 674, 157
- . 2009, *ApJ*, 703, 330
- Costa, T., Sijacki, D., & Haehnelt, M. G. 2014, *MNRAS*, 444, 2355
- Crenshaw, D. M., Kraemer, S. B., Boggess, A., et al. 1999, *ApJ*, 516, 750
- Cresci, G., Mainieri, V., Brusa, M., et al. 2015, *ApJ*, 799, 82
- Croton, D. J., Springel, V., White, S. D. M., et al. 2006, *MNRAS*, 365, 11
- Croxall, K. V., Smith, J. D., Wolfire, M. G., et al. 2012, *ApJ*, 747, 81
- Dale, D. A., Helou, G., Brauher, J. R., et al. 2004, *ApJ*, 604, 565
- Dale, D. A., Helou, G., Contursi, A., Silbermann, N. A., & Kolhatkar, S. 2001, *ApJ*, 549, 215
- Darling, J. 2007, in *IAU Symposium, Vol. 242, Astrophysical Masers and their Environments*, ed. J. M. Chapman & W. A. Baan, 417–426
- Darling, J., & Giovanelli, R. 2006, *AJ*, 132, 2596
- Das, V., Crenshaw, D. M., Kraemer, S. B., & Deo, R. P. 2006, *AJ*, 132, 620
- Dasyra, K. M., Tacconi, L. J., Davies, R. I., et al. 2006a, *ApJ*, 638, 745
- . 2006b, *ApJ*, 651, 835
- . 2007, *ApJ*, 657, 102
- de Grijs, R. 2001, *Astronomy and Geophysics*, 42, 4.12
- Destombes, J. L., Marliere, C., Baudry, A., & Brillet, J. 1977, *A&A*, 60, 55
- Di Matteo, T., Springel, V., & Hernquist, L. 2005, *Nature*, 433, 604
- Di Teodoro, E. M., & Fraternali, F. 2015, *MNRAS*, 451, 3021
- Diamond-Stanic, A. M., Moustakas, J., Tremonti, C. A., et al. 2012, *ApJ*, 755, L26

- Díaz-Santos, T., Armus, L., Charmandaris, V., et al. 2017, *ApJ*, 846, 32
- Dinerstein, H. L., Lester, D. F., & Werner, M. W. 1985, *ApJ*, 291, 561
- Draine, B. T. 2011, *Physics of the Interstellar and Intergalactic Medium*
- Dunn, J. P., Crenshaw, D. M., Kraemer, S. B., & Trippe, M. L. 2008, *AJ*, 136, 1201
- Duric, N., Seaquist, E. R., Crane, P. C., Bignell, R. C., & Davis, L. E. 1983, *ApJ*, 273, L11
- Elbaz, D., Daddi, E., Le Borgne, D., et al. 2007, *A&A*, 468, 33
- Elmouttie, M., Haynes, R. F., Jones, K. L., Sadler, E. M., & Ehle, M. 1998a, *MNRAS*, 297, 1202
- Elmouttie, M., Koribalski, B., Gordon, S., et al. 1998b, *MNRAS*, 297, 49
- Engelbracht, C. W., Kundurthy, P., Gordon, K. D., et al. 2006, *ApJ*, 642, L127
- Espada, D., Matsushita, S., Peck, A., et al. 2009, *ApJ*, 695, 116
- Fabian, A. C. 2012, *ARA&A*, 50, 455
- Fabian, A. C., Sanders, J. S., Haehnelt, M., Rees, M. J., & Miller, J. M. 2013, *MNRAS*, 431, L38
- Falstad, N., González-Alfonso, E., Aalto, S., et al. 2015, *A&A*, 580, A52
- Farrah, D., Lebouteiller, V., Spoon, H. W. W., et al. 2013, *ApJ*, 776, 38
- Ferkinhoff, C., Hailey-Dunsheath, S., Nikola, T., et al. 2010, *ApJ*, 714, L147
- Ferkinhoff, C., Brisbin, D., Nikola, T., et al. 2011, *ApJ*, 740, L29
- Fernández-Ontiveros, J. A., Spinoglio, L., Pereira-Santaella, M., et al. 2016, *ApJS*, 226, 19
- Feruglio, C., Maiolino, R., Piconcelli, E., et al. 2010, *A&A*, 518, L155
- Filippenko, A. V., & Sargent, W. L. W. 1992, *AJ*, 103, 28
- Fischer, J., Abel, N. P., González-Alfonso, E., et al. 2014, *ApJ*, 795, 117
- Fischer, J., Sturm, E., González-Alfonso, E., et al. 2010, *A&A*, 518, L41
- Flower, D. R., Pineau des Forets, G., Field, D., & May, P. W. 1996, *MNRAS*, 280, 447
- Förster Schreiber, N. M., Genzel, R., Newman, S. F., et al. 2014, *ApJ*, 787, 38
- García-Burillo, S., Martín-Pintado, J., Fuente, A., & Neri, R. 2001, *ApJ*, 563, L27

- García-Burillo, S., Combes, F., Usero, A., et al. 2014, *A&A*, 567, A125
- Genzel, R., Förster Schreiber, N. M., Rosario, D., et al. 2014, *ApJ*, 796, 7
- Ginsburg, A., & Mirocha, J. 2011, *PySpecKit: Python Spectroscopic Toolkit*, Astrophysics Source Code Library, , ascl:1109.001
- Goicoechea, J. R., & Cernicharo, J. 2002, *ApJ*, 576, L77
- Goicoechea, J. R., Cernicharo, J., Lerate, M. R., et al. 2006, *ApJ*, 641, L49
- Goldsmith, P. F., Yıldız, U. A., Langer, W. D., & Pineda, J. L. 2015, *ApJ*, 814, 133
- González-Alfonso, E., & Cernicharo, J. 1999, in *ESA Special Publication, Vol. 427, The Universe as Seen by ISO*, ed. P. Cox & M. Kessler, 325
- González-Alfonso, E., Fischer, J., Aalto, S., & Falstad, N. 2014a, *A&A*, 567, A91
- González-Alfonso, E., Fischer, J., Graciá-Carpio, J., et al. 2012, *A&A*, 541, A4
- . 2014b, *A&A*, 561, A27
- González-Alfonso, E., Fischer, J., Sturm, E., et al. 2015, *ApJ*, 800, 69
- González-Alfonso, E., Fischer, J., Spoon, H. W. W., et al. 2017, *ApJ*, 836, 11
- Goulding, A. D., Alexander, D. M., Bauer, F. E., et al. 2012, *ApJ*, 755, 5
- Greene, J. E., Zakamska, N. L., & Smith, P. S. 2012, *ApJ*, 746, 86
- Griffiths, R. E., Ptak, A., Feigelson, E. D., et al. 2000, *Science*, 290, 1325
- Gültekin, K., Richstone, D. O., Gebhardt, K., et al. 2009, *ApJ*, 698, 198
- Habing, H. J. 1968, *Bull. Astron. Inst. Netherlands*, 19, 421
- Hailey-Dunsheath, S., Nikola, T., Stacey, G. J., et al. 2010, *ApJ*, 714, L162
- Hardcastle, M. J., Worrall, D. M., Kraft, R. P., et al. 2003, *ApJ*, 593, 169
- Harris, G. L. H., Rejkuba, M., & Harris, W. E. 2010, *PASA*, 27, 457
- Harrison, C. M., Alexander, D. M., Mullaney, J. R., & Swinbank, A. M. 2014, *MNRAS*, 441, 3306
- Harrison, C. M., Alexander, D. M., Swinbank, A. M., et al. 2012, *MNRAS*, 426, 1073
- Harrison, C. M., Alexander, D. M., Mullaney, J. R., et al. 2016, *MNRAS*, 456, 1195
- Hashimoto, T., Laporte, N., Mawatari, K., et al. 2018, *Nature*, 557, 392

- Heckman, T. M., Alexandroff, R. M., Borthakur, S., Overzier, R., & Leitherer, C. 2015, *ApJ*, 809, 147
- Heckman, T. M., Armus, L., & Miley, G. K. 1990, *ApJS*, 74, 833
- Heckman, T. M., Lehnert, M. D., Strickland, D. K., & Armus, L. 2000, *ApJS*, 129, 493
- Heckman, T. M., & Thompson, T. A. 2017, arXiv e-prints, arXiv:1701.09062
- Heesen, V., Beck, R., Krause, M., & Dettmar, R. J. 2011, *A&A*, 535, A79
- Helou, G., Khan, I. R., Malek, L., & Boehmer, L. 1988, *ApJS*, 68, 151
- Herrera-Camus, R., Bolatto, A., Smith, J. D., et al. 2016, *ApJ*, 826, 175
- Herrera-Camus, R., Sturm, E., Graciá-Carpio, J., et al. 2018a, *ApJ*, 861, 94
- . 2018b, *ApJ*, 861, 95
- Higdon, S. J. U., Devost, D., Higdon, J. L., et al. 2004, *PASP*, 116, 975
- Hlavacek-Larrondo, J., Carignan, C., Daigle, O., et al. 2011, *MNRAS*, 411, 71
- Hollenbach, D. J., Takahashi, T., & Tielens, A. G. G. M. 1991, *ApJ*, 377, 192
- Hollenbach, D. J., & Tielens, A. G. G. M. 1997, *ARA&A*, 35, 179
- . 1999, *Reviews of Modern Physics*, 71, 173
- Hoopes, C. G., Heckman, T. M., Strickland, D. K., et al. 2005, *ApJ*, 619, L99
- Hopkins, P. F., Cox, T. J., Kereš, D., & Hernquist, L. 2008, *ApJS*, 175, 390
- Hopkins, P. F., Somerville, R. S., Hernquist, L., et al. 2006, *ApJ*, 652, 864
- Houck, J. R., Roellig, T. L., van Cleve, J., et al. 2004, *ApJS*, 154, 18
- Hutton, S., Ferreras, I., Wu, K., et al. 2014, *MNRAS*, 440, 150
- Irwin, J., Wiegert, T., Merritt, A., et al. 2019, *AJ*, 158, 21
- Israel, F. P., Güsten, R., Meijerink, R., Requena-Torres, M. A., & Stutzki, J. 2017, *A&A*, 599, A53
- Itoh, T., Done, C., Makishima, K., et al. 2008, *PASJ*, 60, S251
- Izumi, T., Wada, K., Fukushige, R., Hamamura, S., & Kohno, K. 2018, *ApJ*, 867, 48
- Janssen, A. W., Christopher, N., Sturm, E., et al. 2016, *ApJ*, 822, 43

- Jarrett, T. H., Chester, T., Cutri, R., Schneider, S. E., & Huchra, J. P. 2003, *AJ*, 125, 525
- Kaufman, M. J., Wolfire, M. G., & Hollenbach, D. J. 2006, *ApJ*, 644, 283
- Kaufman, M. J., Wolfire, M. G., Hollenbach, D. J., & Luhman, M. L. 1999, *ApJ*, 527, 795
- Kennicutt, Jr., R. C. 1998, *ApJ*, 498, 541
- Kimm, T., Somerville, R. S., Yi, S. K., et al. 2009, *MNRAS*, 394, 1131
- King, A. R. 2010, in *Astronomical Society of the Pacific Conference Series*, Vol. 427, *Accretion and Ejection in AGN: a Global View*, ed. L. Maraschi, G. Ghisellini, R. Della Ceca, & F. Tavecchio, 315
- King, A. R., Zubovas, K., & Power, C. 2011, *MNRAS*, 415, L6
- Koornneef, J. 1993, *ApJ*, 403, 581
- Kormendy, J., & Ho, L. C. 2013, *ARA&A*, 51, 511
- Kormendy, J., & Richstone, D. 1995, *ARA&A*, 33, 581
- Kornei, K. A., Shapley, A. E., Martin, C. L., et al. 2012, *ApJ*, 758, 135
- . 2013, *ApJ*, 774, 50
- Koss, M., Mushotzky, R., Baumgartner, W., et al. 2013, *ApJ*, 765, L26
- Koss, M., Mushotzky, R., Veilleux, S., et al. 2011, *ApJ*, 739, 57
- Kraft, R. P., Forman, W. R., Jones, C., et al. 2002, *ApJ*, 569, 54
- Krieger, N., Bolatto, A. D., Walter, F., et al. 2019, *ApJ*, 881, 43
- Krips, M., Martín, S., Eckart, A., et al. 2011, *ApJ*, 736, 37
- Krug, H. B., Rupke, D. S. N., & Veilleux, S. 2010, *ApJ*, 708, 1145
- Laine, S., & Beck, R. 2008, *ApJ*, 673, 128
- Lehnert, M. D., & Heckman, T. M. 1996, *ApJ*, 462, 651
- Leroy, A. K., Walter, F., Martini, P., et al. 2015, *ApJ*, 814, 83
- Liseau, R., Justtanont, K., & Tielens, A. G. G. M. 2006, *A&A*, 446, 561
- Lutz, D., Sturm, E., Genzel, R., et al. 2003, *A&A*, 409, 867
- Lutz, D., Berta, S., Contursi, A., et al. 2015, *ArXiv e-prints*, arXiv:1511.02075
- Madau, P., Ferrara, A., & Rees, M. J. 2001, *ApJ*, 555, 92

Maiolino, R., Alonso-Herrero, A., Anders, S., et al. 2000, *ApJ*, 531, 219

Maiolino, R., Gallerani, S., Neri, R., et al. 2012, *MNRAS*, 425, L66

Malkan, M. A., Gorjian, V., & Tam, R. 1998, *ApJS*, 117, 25

Marconi, A., & Hunt, L. K. 2003, *ApJ*, 589, L21

Marconi, A., Moorwood, A. F. M., Origlia, L., & Oliva, E. 1994, *The Messenger*, 78, 20

Marconi, A., Oliva, E., van der Werf, P. P., et al. 2000a, *A&A*, 357, 24

Marconi, A., Schreier, E. J., Koekemoer, A., et al. 2000b, *ApJ*, 528, 276

Marinucci, A., Risaliti, G., Wang, J., et al. 2012, *MNRAS*, 423, L6

Martin, C. L. 2005, *ApJ*, 621, 227

—. 2006, *ApJ*, 647, 222

Martin, C. L., Shapley, A. E., Coil, A. L., et al. 2012, *ApJ*, 760, 127

—. 2013, *ApJ*, 770, 41

Martin, C. L., & Soto, K. T. 2016, *ApJ*, 819, 49

Matsuta, K., Gandhi, P., Dotani, T., et al. 2012, *ApJ*, 753, 104

McCormick, A., Veilleux, S., Meléndez, M., et al. 2018, *MNRAS*, 477, 699

McElroy, R., Croom, S. M., Pracy, M., et al. 2015, *MNRAS*, 446, 2186

McKinley, B., Briggs, F., Gaensler, B. M., et al. 2013, *MNRAS*, 436, 1286

McKinley, B., Tingay, S. J., Carretti, E., et al. 2018, *MNRAS*, 474, 4056

Meijerink, R., Spaans, M., & Israel, F. P. 2007, *A&A*, 461, 793

Meijerink, R., Spaans, M., Loenen, A. F., & van der Werf, P. P. 2011, *A&A*, 525, A119

Meléndez, M., Mushotzky, R. F., Shimizu, T. T., Barger, A. J., & Cowie, L. L. 2014, *ApJ*, 794, 152

Meléndez, M., Veilleux, S., Martin, C., et al. 2015, *ApJ*, 804, 46

Middelberg, E., Krichbaum, T. P., Roy, A. L., Witzel, A., & Zensus, J. A. 2005, *Astronomical Society of the Pacific Conference Series*, Vol. 340, *Approaching NGC 3079 with VLBI*, ed. J. Romney & M. Reid, 140

Middelberg, E., Roy, A. L., Nagar, N. M., et al. 2004, *A&A*, 417, 925

- Mingo, B., Hardcastle, M. J., Croston, J. H., et al. 2012, *ApJ*, 758, 95
- Moorwood, A. F. M., van der Werf, P. P., Kotilainen, J. K., Marconi, A., & Oliva, E. 1996, *A&A*, 308, L1
- Morganti, R., Frieswijk, W., Oonk, R. J. B., Oosterloo, T., & Tadhunter, C. 2013, *A&A*, 552, L4
- Morganti, R., Killeen, N. E. B., Ekers, R. D., & Oosterloo, T. A. 1999, *MNRAS*, 307, 750
- Morganti, R., Veilleux, S., Oosterloo, T., Teng, S. H., & Rupke, D. 2016, *A&A*, 593, A30
- Mushotzky, R. F., Shimizu, T. T., Meléndez, M., & Koss, M. 2014, *ApJ*, 781, L34
- Naab, T., & Ostriker, J. P. 2017, *ARA&A*, 55, 59
- Nardini, E., Reeves, J. N., Gofford, J., et al. 2015, *Science*, 347, 860
- Nenkova, M., Ivezić, Ž., & Elitzur, M. 2002, *ApJ*, 570, L9
- Nenkova, M., Sirocky, M. M., Nikutta, R., Ivezić, Ž., & Elitzur, M. 2008, *ApJ*, 685, 160
- Nesvadba, N. P. H., Polletta, M., Lehnert, M. D., et al. 2011, *MNRAS*, 415, 2359
- Netzer, H., Lutz, D., Schweitzer, M., et al. 2007, *ApJ*, 666, 806
- Offer, A. R., & van Dishoeck, E. F. 1992, *MNRAS*, 257, 377
- Ott, S. 2010, in *Astronomical Society of the Pacific Conference Series*, Vol. 434, *Astronomical Data Analysis Software and Systems XIX*, ed. Y. Mizumoto, K.-I. Morita, & M. Ohishi, 139
- Parkin, T. J., Wilson, C. D., Schirm, M. R. P., et al. 2014, *ApJ*, 787, 16
- Pedlar, A., Muxlow, T. W. B., Garrett, M. A., et al. 1999, *MNRAS*, 307, 761
- Peng, Y.-j., Lilly, S. J., Kovač, K., et al. 2010, *ApJ*, 721, 193
- Pereira-Santaella, M., Colina, L., García-Burillo, S., et al. 2016, *A&A*, 594, A81
- Pilbratt, G. L., Riedinger, J. R., Passvogel, T., et al. 2010, *A&A*, 518, 7. <http://arxiv.org/abs/1005.5331>
- Poglitsch, A., Waelkens, C., Geis, N., et al. 2010, *A&A*, 518, L2. <http://arxiv.org/abs/1005.1487>
- Pound, M. W., & Wolfire, M. G. 2008, in *APSC*, Vol. 394, *Astronomical Data Analysis Software and Systems XVII*, ed. R. W. Argyle, P. S. Bunclark, & J. R. Lewis, 654

- Puccetti, S., Comastri, A., Fiore, F., et al. 2014, *ApJ*, 793, 26
- Quillen, A. C., Brookes, M. H., Keene, J., et al. 2006, *ApJ*, 645, 1092
- Radomski, J. T., Packham, C., Levenson, N. A., et al. 2008, *ApJ*, 681, 141
- Renzini, A., & Peng, Y.-j. 2015, *ApJ*, 801, L29
- Richings, A. J., & Faucher-Giguere, C.-A. 2017, ArXiv e-prints, arXiv:1706.03784
- Roche, P. F., Whitmore, B., Aitken, D. K., & Phillips, M. M. 1984, *MNRAS*, 207, 35
- Rogstad, D. H., Lockhart, I. A., & Wright, M. C. H. 1974, *ApJ*, 193, 309
- Roussel, H., Wilson, C. D., Vigroux, L., et al. 2010, *A&A*, 518, L66
- Rubin, K. H. R., Prochaska, J. X., Koo, D. C., et al. 2014, *ApJ*, 794, 156
- Rubin, K. H. R., Weiner, B. J., Koo, D. C., et al. 2010, *ApJ*, 719, 1503
- Rubin, R. H., Dufour, R. J., & Walter, D. K. 1993, *ApJ*, 413, 242
- Rubin, R. H., Simpson, J. P., Erickson, E. F., & Haas, M. R. 1988, *ApJ*, 327, 377
- Rupke, D. 2018, *Galaxies*, 6, 138
- Rupke, D., Gültekin, K., & Veilleux, S. 2017, ArXiv e-prints, arXiv:1708.05139
- Rupke, D. S., Veilleux, S., & Sanders, D. B. 2002, *ApJ*, 570, 588
- . 2005a, *ApJS*, 160, 115
- . 2005b, *ApJS*, 160, 87
- . 2005c, *ApJ*, 632, 751
- Rupke, D. S. N., & Veilleux, S. 2011, *ApJ*, 729, L27
- . 2013, *ApJ*, 768, 75
- Rupke, D. S. N., & Veilleux, S. 2015, *ApJ*, 801, 126
- Sanders, D. B., & Mirabel, I. F. 1996, *ARA&A*, 34, 749
- Savage, B. D., & Sembach, K. R. 1996, *ARA&A*, 34, 279
- Scheuer, P. A. G. 1974, *MNRAS*, 166, 513
- Schiano, A. V. R. 1985, *ApJ*, 299, 24
- Schinnerer, E., Eckart, A., Tacconi, L. J., Genzel, R., & Downes, D. 2000, *ApJ*, 533, 850

- Schöier, F. L., van der Tak, F. F. S., van Dishoeck, E. F., & Black, J. H. 2005, *A&A*, 432, 369
- Schreier, E. J., Burns, J. O., & Feigelson, E. D. 1981, *ApJ*, 251, 523
- Schurch, N. J., Roberts, T. P., & Warwick, R. S. 2002, *MNRAS*, 335, 241
- Schwartz, C. M., & Martin, C. L. 2004, *ApJ*, 610, 201
- Scoville, N. Z., Soifer, B. T., Neugebauer, G., et al. 1985, *ApJ*, 289, 129
- Sebastian, B., Kharb, P., O'Dea, C. P., Colbert, E. J. M., & Baum, S. A. 2019, *ApJ*, 883, 189
- Sharp, R. G., & Bland-Hawthorn, J. 2010, *ApJ*, 711, 818
- Shimizu, T. T., Meléndez, M., Mushotzky, R. F., et al. 2016, *MNRAS*, 456, 3335
- Shimizu, T. T., Mushotzky, R. F., Meléndez, M., Koss, M., & Rosario, D. J. 2015, *MNRAS*, 452, 1841
- Shopbell, P. L., & Bland-Hawthorn, J. 1998, *ApJ*, 493, 129
- Skinner, C. J., Smith, H. A., Sturm, E., et al. 1997, *Nature*, 386, 472
- Smajić, S., Fischer, S., Zuther, J., & Eckart, A. 2012, *A&A*, 544, A105
- Sofia, U. J., Lauroesch, J. T., Meyer, D. M., & Cartledge, S. I. B. 2004, *ApJ*, 605, 272
- Solomon, P. M., Downes, D., & Radford, S. J. E. 1992, *ApJ*, 398, L29
- Somerville, R. S., & Davé, R. 2015, *ARA&A*, 53, 51
- Somerville, R. S., Hopkins, P. F., Cox, T. J., Robertson, B. E., & Hernquist, L. 2008, *MNRAS*, 391, 481
- Spinoglio, L., & Malkan, M. A. 1992, *ApJ*, 399, 504
- Spinoglio, L., Malkan, M. A., Smith, H. A., González-Alfonso, E., & Fischer, J. 2005, *ApJ*, 623, 123
- Spinoglio, L., Pereira-Santaella, M., Dasyra, K. M., et al. 2015, *ApJ*, 799, 21
- Spoon, H. W. W., Armus, L., Marshall, J. A., et al. 2009, *ApJ*, 693, 1223
- Spoon, H. W. W., & Holt, J. 2009, *ApJ*, 702, L42
- Spoon, H. W. W., Marshall, J. A., Houck, J. R., et al. 2007, *ApJ*, 654, L49
- Spoon, H. W. W., Farrah, D., Lebouteiller, V., et al. 2013, *ApJ*, 775, 127

- Springel, V. 2005, MNRAS, 364, 1105
- Stasińska, G., Izotov, Y., Morisset, C., & Guseva, N. 2015, A&A, 576, A83
- Sternberg, A., & Dalgarno, A. 1995, ApJS, 99, 565
- Stone, M., Veilleux, S., Meléndez, M., et al. 2016, ApJ, 826, 111
- Storey, J. W. V., Watson, D. M., & Townes, C. H. 1981, ApJ, 244, L27
- Strateva, I., Ivezić, Ž., Knapp, G. R., et al. 2001, AJ, 122, 1861
- Strickland, D. K., & Heckman, T. M. 2007, ApJ, 658, 258
- Strickland, D. K., Heckman, T. M., Weaver, K. A., Hoopes, C. G., & Dahlem, M. 2002, ApJ, 568, 689
- Strickland, D. K., & Stevens, I. R. 2000, MNRAS, 314, 511
- Sturm, E., Rupke, D., Contursi, A., et al. 2006, ApJ, 653, L13
- Sturm, E., González-Alfonso, E., Veilleux, S., et al. 2011, ApJ, 733, L16
- Swinyard, B., Nakagawa, T., Merken, P., et al. 2009, Experimental Astronomy, 23, 193
- Tadhunter, C., Morganti, R., Rose, M., Oonk, J. B. R., & Oosterloo, T. 2014, Nature, 511, 440
- Tielens, A. G. G. M., & Hollenbach, D. 1985, ApJ, 291, 722
- Tingay, S. J., Jauncey, D. L., Reynolds, J. E., et al. 1998, AJ, 115, 960
- Tommasin, S., Spinoglio, L., Malkan, M. A., & Fazio, G. 2010, ApJ, 709, 1257
- Tremonti, C. A., Moustakas, J., & Diamond-Stanic, A. M. 2007, ApJ, 663, L77
- Trotter, A. S., Greenhill, L. J., Moran, J. M., et al. 1998, ApJ, 495, 740
- Tully, R. B., Rizzi, L., Shaya, E. J., et al. 2009, AJ, 138, 323
- Turner, B. E. 1985, ApJ, 299, 312
- Turner, T. J., & Pounds, K. A. 1989, MNRAS, 240, 833
- Vasudevan, R. V., & Fabian, A. C. 2007, MNRAS, 381, 1235
- . 2009, MNRAS, 392, 1124
- Vasudevan, R. V., Fabian, A. C., Gandhi, P., Winter, L. M., & Mushotzky, R. F. 2010, MNRAS, 402, 1081
- Veilleux, S. 1991a, ApJS, 75, 357

- . 1991b, *ApJS*, 75, 383
- . 1991c, *ApJ*, 369, 331
- Veilleux, S. 2006, in *Astronomical Society of the Pacific Conference Series*, Vol. 357, *Astronomical Society of the Pacific Conference Series*, ed. L. Armus & W. T. Reach, 231
- Veilleux, S., & Bland-Hawthorn, J. 1997, *ApJ*, 479, L105
- Veilleux, S., Bolatto, A., Tombesi, F., et al. 2017, *ApJ*, 843, 18
- Veilleux, S., Cecil, G., & Bland-Hawthorn, J. 2005, *ARA&A*, 43, 769
- Veilleux, S., Cecil, G., Bland-Hawthorn, J., et al. 1994, *ApJ*, 433, 48
- Veilleux, S., Kim, D.-C., & Sanders, D. B. 1999, *ApJ*, 522, 113
- Veilleux, S., Kim, D. C., & Sanders, D. B. 2002, *ApJS*, 143, 42. <http://arxiv.org/abs/astro-ph/0207401>
- Veilleux, S., Maiolino, R., Bolatto, A. D., & Aalto, S. 2020, arXiv e-prints, arXiv:2002.07765
- Veilleux, S., Shopbell, P. L., Rupke, D. S., Bland -Hawthorn, J., & Cecil, G. 2003, *AJ*, 126, 2185
- Veilleux, S., Rupke, D. S. N., Kim, D.-C., et al. 2009, *ApJS*, 182, 628
- Veilleux, S., Meléndez, M., Sturm, E., et al. 2013, *ApJ*, 776, 27
- Venturi, G., Marconi, A., Mingozzi, M., et al. 2017, *Frontiers in Astronomy and Space Sciences*, 4, 46
- Véron-Cetty, M.-P., & Véron, P. 2006, *A&A*, 455, 773
- Voit, G. M. 1992, *ApJ*, 399, 495
- Walter, F., Weiss, A., & Scoville, N. 2002, *ApJ*, 580, L21
- Walter, F., Bolatto, A. D., Leroy, A. K., et al. 2017, *ApJ*, 835, 265
- Weiner, B. J., Coil, A. L., Prochaska, J. X., et al. 2009, *ApJ*, 692, 187
- Werner, M. W., Roellig, T. L., Low, F. J., et al. 2004, *ApJS*, 154, 1
- Westmoquette, M. S., Smith, L. J., Gallagher, J. S., & Walter, F. 2013, *MNRAS*, 428, 1743
- Westmoquette, M. S., Smith, L. J., & Gallagher, III, J. S. 2011, *MNRAS*, 414, 3719
- Whitaker, K. E., Franx, M., Leja, J., et al. 2014, *ApJ*, 795, 104

- Wills, K. A., Redman, M. P., Muxlow, T. W. B., & Pedlar, A. 1999, MNRAS, 309, 395
- Wilson, A. S., & Ulvestad, J. S. 1987, ApJ, 319, 105
- Wilson, C. D., Petitpas, G. R., Iono, D., et al. 2008, ApJS, 178, 189
- Winter, L. M., Veilleux, S., McKernan, B., & Kallman, T. R. 2012, ApJ, 745, 107
- Wolfire, M. G., Tielens, A. G. G. M., & Hollenbach, D. 1990, ApJ, 358, 116
- Wright, E. L. 2006, PASP, 118, 1711
- Yamauchi, A., Nakai, N., Sato, N., & Diamond, P. 2004, PASJ, 56, 605
- Zakamska, N. L., Hamann, F., Pâris, I., et al. 2016, MNRAS, 459, 3144
- Zhang, D. 2018, Galaxies, 6, 114
- Zschaechner, L. K., Walter, F., Bolatto, A., et al. 2016, ApJ, 832, 142
- Zschaechner, L. K., Bolatto, A. D., Walter, F., et al. 2018, ApJ, 867, 111
- Zubovas, K., & Nayakshin, S. 2014, MNRAS, 440, 2625